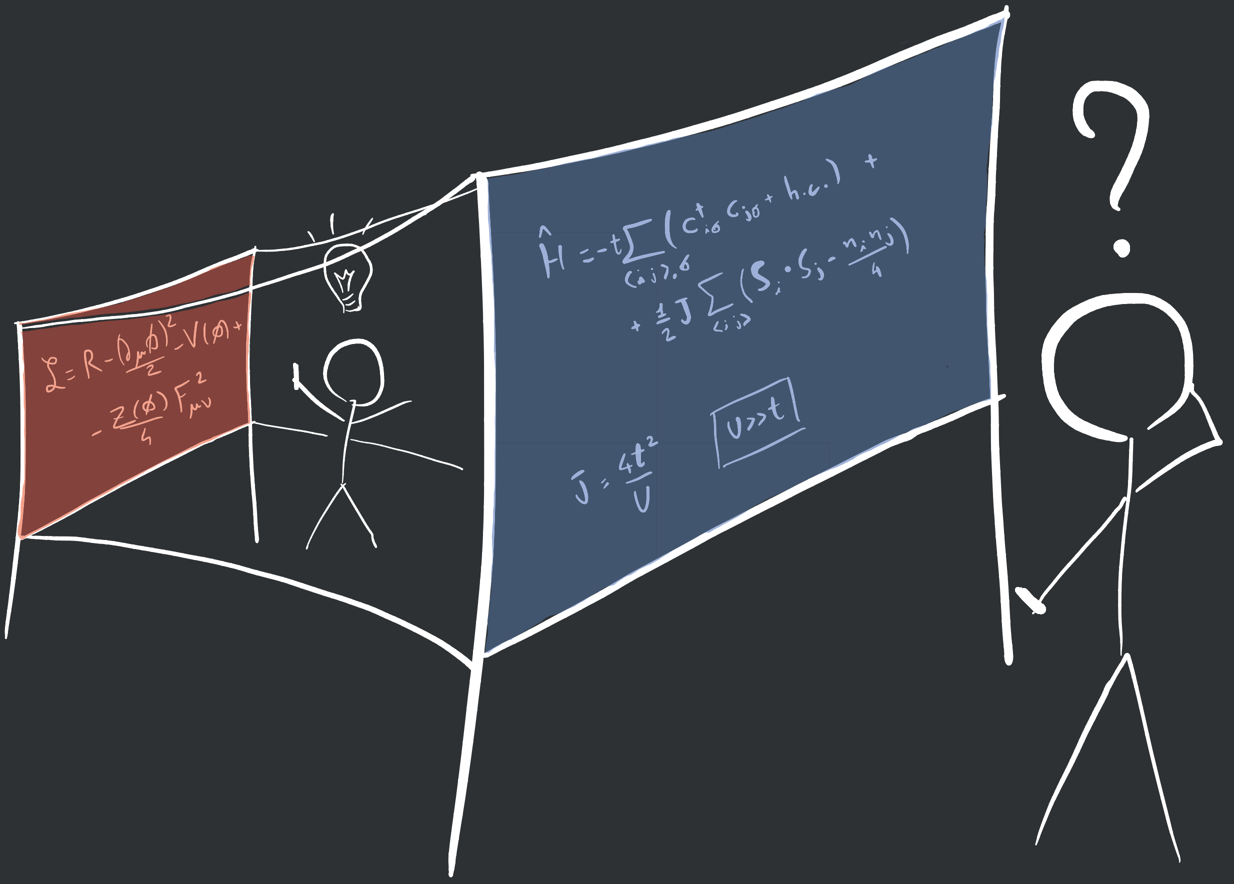

Applications of the gauge/gravity duality to the cuprate strange metal

Applications of the gauge/gravity duality to the cuprate strange metal

Enea Mauri

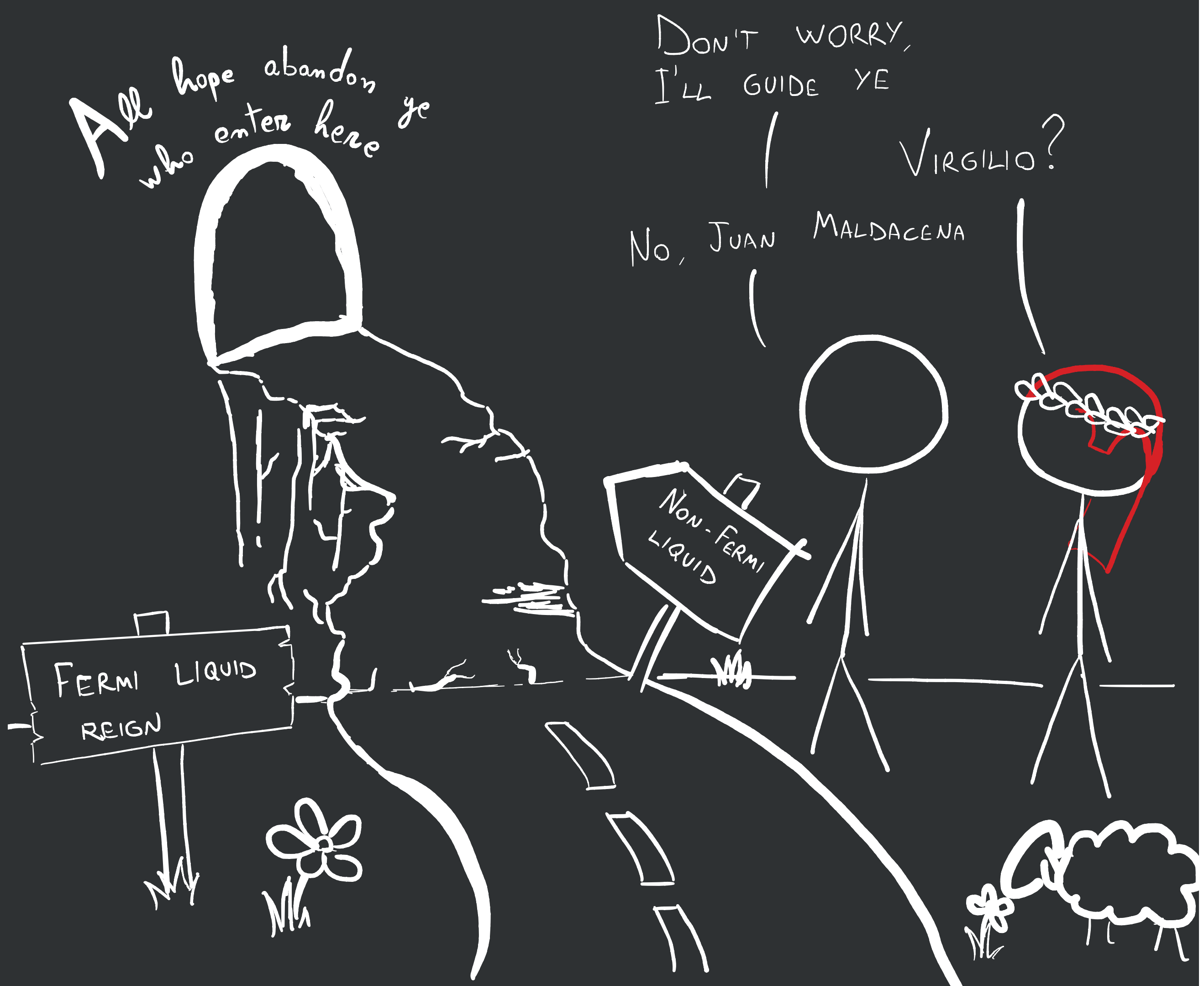

Applications of the gauge/gravity duality to the cuprate strange metal

Toepassingen van de dualiteit tussen ijktheorie en zwaartekracht op het vreemde metaal in de koperoxides

(met een samenvatting in het Nederlands)

Proefschrift

ter verkrijging van de graad van Doctor aan de
Universiteit Utrecht,
op gezag van de
Rector Magnificus prof. dr. H.R.B.M. Kummeling,
ingevolge het besluit van het college voor promoties
in het openbaar te verdedigen op
woensdag 21 december 2022 des middags te 2.15 uur

door

Enea Mauri

geboren op 29 juli 1992
te Giussano, Italië

Promotor: prof. dr. ir. H.T.C. Stoof

Contents

List of publications

The chapters of this thesis are based on the following manuscripts:

- E. Mauri and H. T. C. Stoof. Screening of coulomb interactions in holography. *Journal of High Energy Physics*, 2019 (https://doi.org/10.1007/JHEP04(2019)035)
- E. Mauri and H. T. C. Stoof. Coulomb drag between two strange metals. *Phys. Rev. B*, 2021 (https://doi.org/10.1103/PhysRevB.106.205116)
- S. Smit, E. Mauri, L. Bawden, F. Heringa, F. Gerritsen, E. van Heumen, Y. K. Huang, T. Kondo, T. Takeuchi, N. E. Hussey, T. K. Kim, C. Cacho, A. Krikun, K. Schalm, H. T. C. Stoof, and M. S. Golden. Momentum-dependent scaling exponents of nodal self-energies measured in strange metal cuprates and modelled using semi-holography, *submitted for publication to Nature Physics*, 2021 (https://doi.org/10.48550/arXiv.2112.06576)
- E. Mauri, S. Smit, M. S. Golden and H. T. C. Stoof. Gauge/gravity duality comes to the lab: evidence of momentum-dependent scaling exponents in the nodal electron self-energy of cuprate strange metals, *submitted for publication to Phys. Rev. B*, 2022

Other contributions by the author:

- R. Rodgers, E. Mauri, U. Gürsoy and H. T. C. Stoof. Thermodynamics and transport of holographic nodal line semimetals. *Journal of High Energy Physics*, 2021 (https://doi.org/10.1007/JHEP11(2021)191)

Chapter 1

Introduction

1.1 The strangeness of the strange metal

With the first copper tools dating back more than 10000 years, metals have played a key role in the development of civilization all throughout human history, with their fascinating physical properties being exploited in a large variety of applications. To name just a few, their structural behavior has been extensively used to engineer ever more complex tools, machines, and buildings, the rare optical traits of gold, silver, and other metals were used already by ancient Romans (and other civilizations before them) as a base for their monetary system, and, in more recent times, it is their ability to conduct electricity that drove the second industrial revolution and ultimately brought us to the technology-dominated world we live in. It is, then, hardly a surprise that the study of metals has played a major role in condensed-matter physics, leading to the proposal of the *Fermi-liquid theory* that explained the phenomenology of many of the known metals. What, perhaps, comes more as a surprise, is that nowadays we still find "strange" metallic systems that elude our understanding and call for the need for new physical theories. These *strange metals*, as they have been very descriptively named, are the topic of this thesis. We explore what a modern computational technique, called *gauge/gravity* or *holographic duality*, can teach us about the complicated physics of these materials.

In order to understand the reasons behind such a name, we have to define what we mean by "normal" metals. In a simplified picture, a metal is, from a microscopic point of view, a lattice of fixed atoms with conduction electrons that are loosely bound and can easily hop from one site to the other. Our current understanding of how the metallic behavior arises from the interactions among the electrons is based, as mentioned, on the very successful framework of the Fermi-liquid theory. Contrary to what its name suggests, it was developed in the 1950s by Lev Landau and explains why we can get a good understanding of metals by treating them as a gas of Fermi particles, i.e., particles subject to Pauli's exclusion principle stating that there cannot be two electrons in the same quantum state. Due to this restriction, in a non-interacting fermion gas particles build up a Fermi surface, with the low-energy excitations corresponding to adding or removing a fermion from this Fermi sea. What Landau realized is that, irrespectively of the details and strength of the interaction at the lattice (ultraviolet) scale, the low-energy (infrared) physics of the interacting system still admits an effective description in terms of fermionic electrons and holes, although they are not the original particles of the free theory. Due to interactions, these emergent particle-like collective excitations have different properties compared to the elementary particles (e.g., a renormalized mass and a different energy distribution), and are hence called *quasiparticles*. The Fermi-liquid framework then provides for a weakly interacting picture to study the physical properties of metals, even when at the lattice scale the interactions are strong. This led to an understanding of many metallic properties such as, for instance, the specific heat and magnetic susceptibility, the T^2 dependence of the resistivity at low temperatures T and, together with the Bardeen–Cooper–Schrieffer (BCS) theory of superconductivity, it helped to explain why common metals become superconductors when cooled to near absolute zero.

In 1986, however, an experiment on a copper-oxide compound [9] brought to light the phenomenon of high-temperature superconductivity, sparking a new experimental and theoretical research interest in this class of materials—also referred to as *cuprates*—leading in the following years to the discovery of ever higher critical temperatures up to 135 K at ambient pressure. While not quite "high-temperature" enough to be of use in everyday devices at room temperature, it owes its name to the fact that it greatly exceeds the temperature limit for a transition to a superconducting phase according to the BCS theory (around 39 K [101]), pointing at a different mechanism at play and the need for a new physical theory. As the mechanism behind this kind of superconducting transition is still unclear, there is also not yet a clear way to give an upper limit on the critical temperature T_c, giving hope for the possibility of room-temperature superconductivity and making this problem of particular practical appeal. Our strange metal is the normal (i.e., non-superconducting) phase of these high-T_c superconductors, and it is an example of a non-Fermi-liquid metal, showing a very different behavior compared to the normal metals that fall under Landau's successful framework, as we will highlight with some examples in what follows.

In general, cuprates compounds share a layered structure of CuO_2 planes, usually separated by an insulating layer with an inter-layer distance varying between 6–15Å. In a simplified picture, the plane is formed by a square lattice with a Cu atom in each corner and an oxygen atom at the center of each side of the unit cell (see Fig. 1.1), with a lattice constant around 3.8–4Å. This leaves one hole per Cu atom when there is no doping. Contrary to what one might expect from the odd number of electrons in the valence shell, cuprates are insulators. They are an instance of what are known as *Mott insulators*, where the strong repulsion between electrons makes it energetically expensive for an electron to hop onto the neighboring site, hence effectively confining each electron to its unit cell with an antiferromagnetic ordering (i.e., with an alternating spin on each site). It is only through doping—by either adding or removing electrons—that the mobility of charge carriers is re-established, and at high doping levels, the cuprates behave like normal metals as shown in the phase diagram in Fig. 1.2. While the details of the phase diagram depend on the particular cuprate considered, it shares some generic features such as the "dome-shaped" superconducting region with a maximum critical temperature at a value of doping, p^*, that is hence referred to as *optimal*, and with the strange-metal phase sitting above this optimal doping. With the aforementioned phase being the focus of this thesis, we will not discuss here the other regions of the phase diagram—as it is a topic that would deserve an entire chapter on its own—and instead refer the reader to the good review on the topic in Ref. [110].

Perhaps the most famous among the strangeness of this phase is the anomalous behavior of the resistivity, which is exactly linear in T from the low temperatures reached when the superconducting dome is suppressed (e.g., by a high magnetic field) to the highest temperature, as, contrary to normal metals, it does not saturate above the Ioffe-Mott-Regel limit. The low-temperature linear resistivity is a universal feature of all the cuprates and, furthermore, there appears to be a link between the linear-in-T scattering rate and the pairing mechanism behind superconductivity as deviations from the Fermi-liquid-T^2 scaling of the resistivity at low temperatures and high doping appear in conjunction with superconductivity when doping is lowered [110]. For this reason, we focus on the study of holographic models dual to field theories with

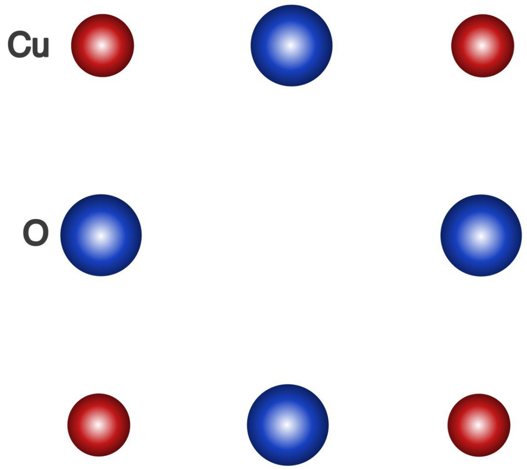

Figure 1.1: Unit cell for the cuprate square lattice in the CuO layers.

this linear behavior, although there are other anomalous features that characterize the strange-metal phase, such as, for example, the temperature behavior of the Hall angle [18] and the Hall effect [63].

There is not yet a consensus on the origin of this low-energy scaling behavior, but experimental results seem to point to the fact that cuprates' physics is governed by a quantum critical **phase**. Measurement performed in a high magnetic field, to suppress superconductivity and access the low-temperature regime, point to the fact that the linear-in-T resistivity is a feature of the strange metal across an **extended** range of doping. Moreover, this view is reinforced by recent angle-resolved photoemission spectroscopy (ARPES) measurements of the spectral function along the nodal direction, suggesting that the strange-metal phenomenology is governed by a particular (quasi-)local quantum critical phase, i.e., a phase that is, in first approximation, local in space and featureless in momentum.

What is interesting, is that some of the simplest holographic theories dual to nonzero-density field theories naturally describe the physics of these (quasi-)local quantum critical phases. It is, then, in this context that we employ the gauge/gravity duality as we explain in the next section. From the practical point of view, it is a tool that allows for an effective description of the emergent low-energy physics of a strongly interacting system showing quantum critical behavior, making it possible to study the

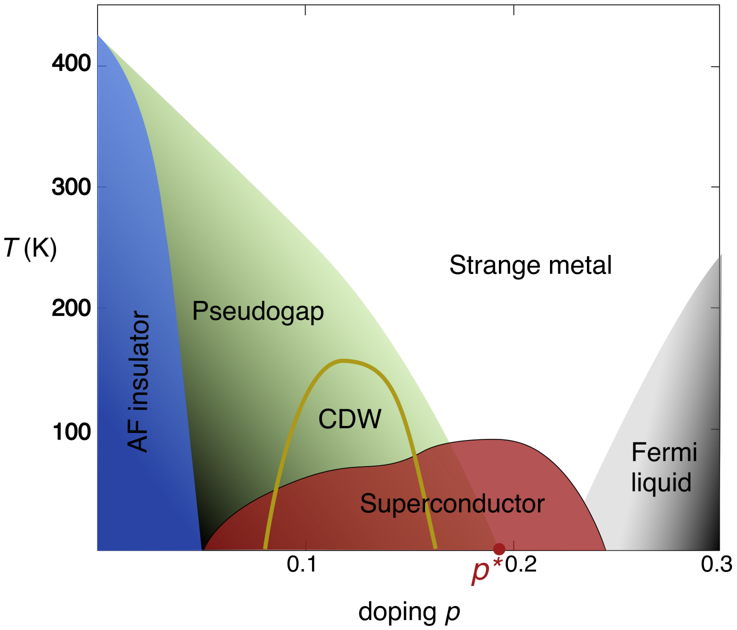

Figure 1.2: Typical phase diagram for a hole-doped cuprate. Above the superconducting dome at optimal doping, p^*, we find the strange-metal phase, while at high doping the cuprate behaves like a normal Fermi liquid.

scaling of transport coefficients as well as the fermion spectral function of relevance to ARPES experiments.

1.2 A brief tour of holographic metals

As mentioned above, many of the results presented in this thesis follow from the application to condensed matter of what is most commonly known under the names of holographic duality, gauge/gravity duality, or AdS/CFT correspondence. For the condensed-matter physicist, the relevance of this correspondence is due to the fact that it allows for the computation of the thermodynamics and transport properties of a class of strongly interacting electron systems that elude a description in terms of the established Fermi-liquid theory based on the quasiparticle picture. The key aspect of this approach resides in the word "duality", which simply tells us that we have two different but equivalent ways to describe a system. While one can argue that redundancy is not always useful, the power of this correspondence lies in the fact that it is an example of a *strong-weak duality*, meaning that if we look at a system with strong interactions on one side, its equivalent description on the other side of the correspondence is going to be a weakly interacting one that lends itself to the use of perturbation methods. For our purposes, in short, it implies that properties of the strongly interacting metals we are interested in can be understood by a (computationally speaking) simpler theory of classical gravity, albeit in one dimension higher.

There are, of course, other approaches to try to understand the physics of these systems (see for example Ch. 3 of Ref. [133] for an overview), but most other analytical and numerical techniques rely on constraints such as low-dimensionality of the system or the assumption of zero density in order to be computationally tractable. What, instead, sets holography apart is the easiness to deal with both nonzero temperature and density in any number of spatial dimensions, allowing us to handily compute response functions in the *real-time* domain (as opposed to the imaginary-time formalism on which many field-theoretic or numerical methods are based). On the other hand, holography provides us with an effective description of the emergent low-energy physics governing the system, but it fails to deliver a microscopic understanding of the underlying mechanism at play that leads to this emergent physics. It is important to stress this concept of emergence, as the ultraviolet (UV) physics described by the holographic model we consider is a highly symmetric one and with an infinite number of degrees of freedom (the so-called "large-N" limit, with N^2 being the number of degrees of freedom of the matrix-valued fields in the field theory). This is quite different from the atomic lattice of a real cuprate. In particular, for the models used in this thesis, the UV physics is that of a conformal field theory (CFT)—that is a theory invariant under the set of transformations of the spacetime that preserve angles (and in particular, this implies that the theory is scale invariant). Nevertheless, despite these striking differences on the high end of the energy scale, the correspondence may deliver us the correct physics in the low-energy regime as—much like for the Fermi liquid—the emergent infrared physics does not dependent on the UV details of the theory it flows from. Due to this, in condensed-matter applications of the duality, we often adopt a "bottom-up" approach. It means that, instead of starting from a known theory of quantum gravity and reducing it to an effective classical action[1] by taking the appropriate large-N and strong coupling limits, we build—guided by the symme-

---

[1] For the reader unfamiliar with the concept, the action is the central player of field theories. It is a functional, $S[\phi(t, \boldsymbol{x})]$, whose saddle point, $\delta S[\phi] = 0$, defines the classical equations of motion of the fields $\phi(t, \boldsymbol{x})$.

try of the quantum critical system we want to study—a classical gravitational action from scratch to include all the elements we need to describe the system of interests.

For these reasons, however, we find it extremely important that predictions from holography can be confronted with experimental measurements for validation. This is why one of the main objectives of the work presented in this thesis is to strengthen the link between the “holographic metal” and experimentally observed features of the strange-metal phase of cuprate high-T_c superconductors. Given this premise, we would like to make the work presented in the next chapters accessible to a varied audience, and in what follow we will hence try our best to give a quick but practical introduction to holography. By now there are plenty of very good introductions to the topic, see for example Refs. [57, 53, 133], so we will not indulge much in explaining the nitty-gritty details of the duality but we focus on providing a conceptual understanding of the use of this peculiar correspondence in the study of the seemingly unrelated physics of electrons in copper-oxide materials.

In short, the holographic correspondence gives a prescription to obtain the generating functional[2]

$$Z_{\mathrm{QFT}}\left[J(t,\boldsymbol{x})\right] = \left\langle e^{i\int \mathrm{d}t\mathrm{d}^d\boldsymbol{x}\, J_I(t,\boldsymbol{x})O_I(t,\boldsymbol{x})}\right\rangle \ , \tag{1.1}$$

for a certain quantum field theory effectively described, in the limit of strong interactions, by a set of collective *single-trace* operators $\{O_I(t,\boldsymbol{x})\}$, with $(t,\boldsymbol{x})$ the coordinates of the $(d+1)$-dimensional (flat) spacetime[3], and with sources $\{J_I(t,\boldsymbol{x})\}$, where a summation over repeated indices is implied. The term “single-trace” highlights the fact that the operators in the field theory of the correspondence are traces of $N\times N$ matrix-valued fields, with the strong interaction limit going hand-in-hand with the limit of $N\to\infty$, allowing for a saddle-point description of the theory (see for example section 1.4 of Ref. [57] for more details). For our purposes we always work in this large-N, strongly interacting limit, hence, it will often be implicitly assumed from now on.

In this limit, on the other side of the correspondence we have a gravitational theory

---

[2] The *partition function*, Z_{QFT}, is the central object of a quantum field theory in the path integral formalism. It acts as a generating functional for the theory, meaning that we can obtain the Green’s functions of the system (and in general any connected n-point function) by taking functional derivatives of $\log Z_{\mathrm{QFT}}$ with respect to the sources.

[3] In the convention adopted here d refers to the number of spatial dimensions of the field theory. However, it is often also used to denote the number of spacetime dimensions of the field theory (or equivalently the number of spatial dimensions of the dual gravitational theory). These different conventions for d can often be a source of confusion, we will try to make clear in each chapter which convention we are using.

described by the *bulk* action $S_{\text{bulk}}[\Phi(t,\boldsymbol{x},r)]$, with r denoting the extra spatial dimension. In our conventions, this extra dimension runs perpendicular to the boundary of the spacetime located at $r=\infty$, and it is on this boundary that the dual quantum field theory is defined. The (classical) fields Φ_I in the gravitational theory act as sources for the dual operators O_I of the boundary theory so that (upon proper normalization of the fields) $J_I(t,\boldsymbol{x}) \equiv \lim_{r\to\infty}\Phi_I(t,\boldsymbol{x},r)$. In a sense then, the quantum theory is described through a projection on the lower dimensional boundary of the gravitational theory, giving justice to the name "holography". This extra physical dimension geometrizes the energy scaling of the quantum critical boundary theory [133], such that the deep interior of the spacetime encodes the low-energy scaling of the field theory, while ultraviolet physics is represented by the near-boundary geometry as depicted in Fig. 1.3.

The heart of the duality is thus given by the Gubser-Klebanov-Polyakov-Witten (GKPW) rule, providing the link between the two sides by stating the equivalence between the quantum field theory partition function and the gravitational path integral:

$$Z_{\text{QFT}}\left[J(t,\boldsymbol{x})\right] = \int \mathcal{D}\Phi e^{iS_{\text{bulk}}[\Phi(t,\boldsymbol{x},r)]}\Big|_{\Phi(t,\boldsymbol{x},r=\infty)=J(t,\boldsymbol{x})} \,. \tag{1.2}$$

The goal of the condensed-matter physicist is then to find the right gravitational theory that gives rise to the effective infrared description of interesting phases of matter. In what follows we briefly explain what is needed on the gravity side to build a minimal model of a cuprate in the above-mentioned bottom-up approach.

The gravitational theories used in this thesis are characterized by being asymptotically Anti-de-Sitter (AdS), whose symmetries dictate that the dual theory in the high-energy limit is then a conformal field theory. We can, hence, define the conformal scaling dimension Δ_I of each operator $O_I(t,\boldsymbol{x})$ through its properties under the scaling $(t,\boldsymbol{x}) \to (t',\boldsymbol{x}') = (\lambda t, \lambda \boldsymbol{x})$ according to $\langle O_I(t,\boldsymbol{x})\rangle \to \langle O_I'(t',\boldsymbol{x}')\rangle = \lambda^{-\Delta_I} O_I(t,\boldsymbol{x})$. For a pure AdS spacetime, this conformal scaling completely characterizes the behavior of the correlation functions at all energies. In order to model the more interesting low-energy physics of a cuprate strange metal—described by a nonzero particle density as well as nonzero temperature—we, therefore, need to introduce new elements in the spacetime that modifies the pure AdS structure for small values of r, hence breaking the UV conformal invariance. We summarize below the relevant "dictionary entries" for a minimal holographic model of a strongly interacting strange metal

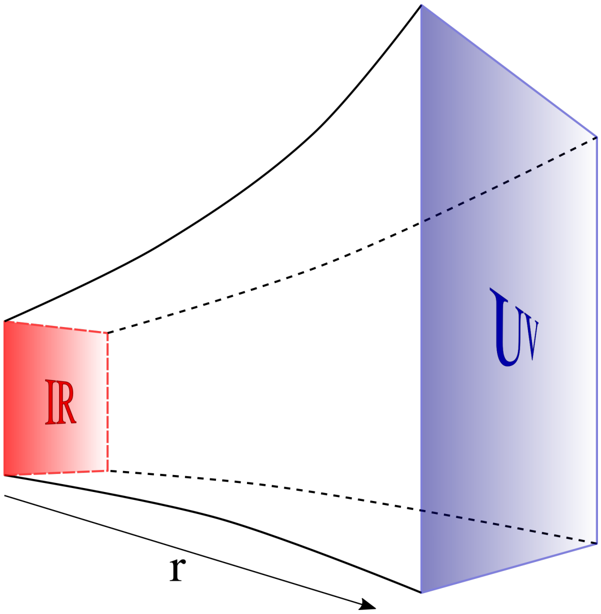

Figure 1.3: Pictorial representation of the AdS spacetime, with the extra radial dimension encoding for the energy scaling of the dual field theory.

- the metric tensor $g_{\mu\nu}$ describing the spacetime geometry of the gravitational theory is dual to the energy-momentum tensor $T_{\mu\nu}$ of the flat field theory on the spacetime boundary,
- the Hawking temperature and entropy of a black hole in the deep interior of the spacetime—whose nonzero radius sets a cutoff in the radial direction—encodes the nonzero temperature T and entropy density s of the dual field theory,
- a Maxwell gauge field A_μ with a nonzero time component in the bulk gravitational action introduces a chemical potential $\mu \equiv \lim_{r\to\infty} A_t$ that acts as a source for a nonzero density of particles ρ in the field theory,
- a scalar field ϕ, the dilaton, allows for the description of a quantum critical phase with Lifshitz scaling and hyperscaling violation, i.e., with diverse values of the exponents (z, θ), the *dynamical critical exponent* and the *hyperscaling violation exponent*, respectively, that characterize the quantum critical theory (and will be defined in a moment).

In the next chapters, we will be mainly concerned with two models. One is the Reissner-Nordström (RN) gravitational background that includes the first three dictionary entries, and it is thus given by the Einstein-Maxwell action that we discuss in detail in chapter 2

$$S_{\mathrm{EM}} = \frac{1}{16\pi G}\int \mathrm{d}r\mathrm{d}t\mathrm{d}^d\boldsymbol{x}\,\sqrt{-g}\Bigg[\underbrace{R-2\Lambda}_{\text{Einstein}}-\underbrace{\frac{1}{4g_F^2}F_{\mu\nu}^2}_{\text{Maxwell}}\Bigg]\,, \tag{1.3}$$

with R the Ricci scalar, Λ the cosmological constant and $F_{\mu\nu} \equiv \partial_\mu A_\nu - \partial_\nu A_\mu$ the electromagnetic tensor. The second is an instance of Einstein-Maxwell-Dilaton (EMD) gravity—generically described by an action as in Eq. (1.4) below—proposed by Gubser and Rocha [50] where the addition of the dilaton allows for a scaling of the resistivity that is linear in temperature $\rho \sim T$, characteristic of the strange metal cuprates.

The RN model is a well-studied example as it allows for an analytical solution for the background (i.e., the classical equations of motion resulting from variation of the action are exactly solvable) and hence it serves as a simple starting point to study thermodynamics and transport properties of holographic quantum matter at nonzero density and temperatures. The compelling aspect of the RN black-hole model is that it shows the existence of an emergent **local** quantum critical phase in the infrared of the dual field theory. With the term local we mean that the quantum critical phase is characterized by a scaling that is, in first instance, momentum independent.

If we separate space and time dimensions, a scale transformation acts mathematically by taking $\boldsymbol{x} \to \lambda \boldsymbol{x}$ and $t \to \lambda^z t$, with the exponent z characterizing the different scaling of space and time known as the *dynamical critical exponent*. Relativistic theories, for example, have $z = 1$, while the emergent critical phase described by the RN inner spacetime is one with $z = \infty$. This is—as we will discuss in more detail in a moment—the (quasi-)local quantum critical phase believed to govern the strange-metal phenomenology.

One drawback of the RN model, however, is that the entropy density presents a low-temperature scaling of the form $s \sim s_0 + s_2 T^2$, implying a residual entropy at zero temperature that hints at an instability of the model. One way to overcome this limitation is by employing the last dictionary entry presented above, that is, with the addition of a dilaton (scalar) field.

The effect of the dilaton, $\phi(t, \boldsymbol{x}, r)$, is to further modify the inner spacetime geometry allowing for a variety of emergent quantum critical phases that are now characterized by two exponents (z, θ), with θ the hyperscaling-violating exponent that defines how the metric transform under scaling, $\mathrm{d}s^2 \to \lambda^{2\theta/d}\mathrm{d}s^2$. The action now takes the general form

$$S_{\mathrm{EMD}} = \frac{1}{16\pi G}\int \mathrm{d}r\mathrm{d}t\mathrm{d}^d\boldsymbol{x}\,\sqrt{-g}\left[R - (\partial_\mu\phi)^2 - V(\phi) - \frac{Z(\phi)}{4g_F^2}F_{\mu\nu}^2\right]\,. \tag{1.4}$$

and through different choices of $Z(\phi)$ and $V(\phi)$ we can tune the values of z and θ (within some bounds, see e.g. Sec. 4.2 of Ref. [57]) and hence the low-energy and low-temperature physics of the dual field theory. In particular, we have for the entropy

$$s \sim T^{\frac{d-\theta}{z}}\,, \tag{1.5}$$

and we see that in a $z = \infty$ theory, for any finite θ, we obtain a nonzero entropy at zero temperature as in the RN model. However, an interesting class of dilaton models is given by taking $z \to \infty$ and $\theta \to -\infty$ such that its ratio is finite and equal to $\eta \equiv -\theta/z$. Here we recover local quantum criticality while resolving the problem of residual entropy in the $T \to 0$ limit. The Gubser-Rocha model is of this kind, with $\eta = 1$ and hence $s \sim T$. This is important as in theories with $z = \infty$ there is a universal viscous contribution to the DC resistivity, which is proportional to the entropy of the state [26], consequently $\rho \sim s \sim T$ reproducing the famous linear resistivity of the normal state of the cuprates.

Now that we argued what $z = \infty$ holographic metals have in common with the cuprate strange metals, we briefly show in the next sections how to use the correspondence for computational purposes. Especially, after explaining how the thermodynamic properties of the field theory are obtained from the equilibrium solution, we show how to compute response functions—that can be used to study transport properties of the strange metal—and we discuss the holographic fermionic spectral function, for comparison with the Fermi surface measured by ARPES experiments on cuprates.

1.2.1 Equilibrium and thermodynamics

Starting from a gravitational theory, the equilibrium properties of the quantum system are given by the solution to the classical equations of motion obtained by variation of the **Euclidean** gravitational action (derived from the bulk action upon the substitution $\tau \equiv it$, i.e., by performing a *Wick rotation*). However, there are some subtleties we first need to take care of. The action evaluated *on-shell*, i.e., on the classical solution of the equations of motion for the fields, Φ_{cl}, is divergent for $r \to \infty$ and it hence needs to be renormalized. This is done by introducing counterterms defined on a cut-off surface at $r = r_{\text{UV}}$, with $r_{\text{UV}} \to \infty$ at the end of the calculation. Moreover, in a spacetime with a boundary, the action needs to be supplemented with a boundary term, named the Gibbson-Hawking-York term, in order to have a well-defined boundary problem where the metric is held fixed. In the rest of this introduction, whenever we refer to the gravitational action we implicitly refer to the action containing all the necessary counterterms and boundary terms. It then follows immediately from the GKPW rule that the thermodynamic potential of the field theory is given by

$$\Omega \equiv -k_B T \log Z_{\text{QFT}} = k_B T S_{\text{E}}[\Phi_{\text{cl}}] \ , \tag{1.6}$$

where S_{E} is the Euclidean classical gravitational action.

1.2.2 Linear response and transport

Obtaining real-time response functions at nonzero temperatures is where the holographic framework really shows its power. What we are after is the response of the system to small external perturbations, i.e., the change in the expectation value of the quantum operator $O_I(\omega, \boldsymbol{k})$ dual to the field $\phi_I(r, \omega, \boldsymbol{k})$ due to the change in the source $J_J(\omega, \boldsymbol{k})$ dual to $\phi_J(r, \omega, \boldsymbol{k})$, that are related by the *retarded Green's function* as

$$\delta\langle O_J\rangle\,(\omega, \boldsymbol{k}) = \sum_{I=1}^{M} G^R_{O_J O_I}(\omega, \boldsymbol{k}) \delta J^I(\omega, \boldsymbol{k}) \ , \tag{1.7}$$

where the Fourier-space retarded Green's function for the operators O_I and O_J is defined by

$$G^R_{O_J O_I}(\omega, \boldsymbol{k}) \equiv -i \int \mathrm{d}t \mathrm{d}^d\boldsymbol{x}\, e^{-i\omega t + \boldsymbol{k}\cdot\boldsymbol{x}} \theta(t) \left\langle [O_I(t, \boldsymbol{x}), O_J(0, \boldsymbol{0})] \right\rangle \ , \tag{1.8}$$

where $\theta(t)$ is the Heaviside step function. In holography, the computation of the real-time Green's function for the strongly interacting quantum critical theory is mapped, in the large-N limit, to a perturbative problem for the classical fields in the bulk in Lorentzian signature (as opposed to Euclidean signature for the computation of thermodynamics quantities)

$$\mathcal{S}_{\text{gravity}}[\Phi_J + \delta\Phi_J] \Rightarrow \delta\langle O_J\rangle\,(\omega, \boldsymbol{k}) = \sum_{I=1}^{M} G^R_{O_J O_I}(\omega, \boldsymbol{k}) \delta J^I(\omega, \boldsymbol{k}) \ . \tag{1.9}$$

To be more precise, by perturbing the bulk action we find the *linearized equations of motion* (LEOM) for the set of field fluctuations $\delta\Phi_I$. In order to solve this set of (usually coupled) differential equations for the fluctuations in a nonzero temperature background, we need to impose boundary conditions at the black-hole horizon and we are faced with two possible choices, *infalling-wave* or *outgoing-wave* boundary condition. The first describes modes that carry energy *into* the horizon, encoding for dissipation and ultimately corresponding to the computation of the *retarded* Green's function, and it is, therefore, the boundary condition of choice for the computation performed in this thesis[4]. Using the GKPW rule and the holographic dictionary we can then show that the change in the expectation value of the operators O_I and their corresponding sources J_I are encoded in the asymptotic behavior of the dual field fluctuations according to (after an eventual redefinition of the field so that its leading near boundary behavior is constant)

$$\delta\Phi_I(r,\omega,\boldsymbol{k}) \to \delta J_I(\omega,\boldsymbol{k}) + \cdots + \mathcal{C}\delta\left\langle O_I(\omega,\boldsymbol{k})\right\rangle r^{(d+1-2\Delta_I)} \text{ , as } r\to\infty \tag{1.10}$$

with $\delta\Phi_I(r,\omega,\boldsymbol{k})$ the solution to the linearized equations of motion with an infalling-wave boundary condition at the horizon, Δ_I the conformal scaling dimension of the operator O_I, the "..." stands for eventual terms that need regularization and the coefficient $\mathcal{C}$ is completely determined by the solution to the LEOM.

To summarize, we can compute the retarded Green's function by taking the following steps

- perturb the gravitational bulk action $\mathcal{S}_{\text{gravity}}[\Phi_J+\delta\Phi_J]$ to obtain a set of (usually coupled) linearized equations of motion for the set of fluctuations $\delta\Phi_J$,
- find all the independent solutions to the set of linearized differential equations for the fluctuations after imposing infalling-wave boundary condition at the black-hole horizon (in most cases this can only be done numerically),
- extract the change in the source δJ_J and the change in the expectation value of the operator $\delta\left\langle O_J\right\rangle$ by studying the near-boundary behavior of the solution to the LEOM for the dual field fluctuations $\delta\Phi_J$,
- after computing the changes in expectation values and sources solve for the matrix of retarded Green's function according to $\delta\left\langle O_J\right\rangle(\omega,\boldsymbol{k}) = \sum_{I=1}^{M} G^R_{O_J O_I}(\omega,\boldsymbol{k})\delta\Phi^I_s(\omega,\boldsymbol{k})$.

---

[4] As you might have guessed, the outgoing-wave boundary conditions allows for the computation of the *advanced* Green's function

Of particular physical interest are the pole structure of the retarded Green's function and its imaginary part that defines the *spectral weight* $\mathcal{A}_I$ for an operator O_I as $\mathcal{A}_I \equiv -\mathrm{Im}[G^R_{O_I O_I}]$. In analogy with the single-particle Green's function whose poles define the quasiparticle excitations of the system, with the spectral weight containing all the information about their decay rate, the pole structure of the holographic Green's function defines the *quasinormal modes* describing the collective excitations of the strongly interacting quantum critical system in response to the external perturbation.

In the rest of the thesis, we will especially focus on the spectral functions of the current density operator J^μ, dual to the bulk gauge field A_μ, as it is a quantity of particular experimental interest. The spectral function of the time component $\rho \equiv J^t$, in fact, defines the response of the holographic strange metal to charge density fluctuations, while the one for the spatial component J^x (where we arbitrarily fixed the momentum of the perturbation in our isotropic system along the x-axis) is particularly relevant to transport experiments as it is related to the *optical conductivity* by

$$\sigma(\omega) = \frac{G^R_{J^x J^x}(\omega, \mathbf{0})}{i\omega} \ . \tag{1.11}$$

1.2.3 Infrared Green's function

As we stressed already several times, what we are trying to capture with holography is the effective description of a metal at low energies without worrying too much about its precise form in the UV. However, one might have noticed from the previous section that, in order to obtain the Green's function, we need to integrate the equations for the fluctuations over the entire spacetime. One is then left to wonder why we can be so careless about the UV details. What role do they play in the low-energy Green's function we are interested in? What information can be reliably computed from the inner region of the spacetime independently on the large-r UV region?

The answer to the above questions lies in the fact that dissipative physics is completely encoded by the near-horizon (inner) geometry. It can indeed be shown that

$$\mathrm{Im}[G^R(\omega, \boldsymbol{k}; T)] \propto \mathrm{Im}[G^R_{\mathrm{IR}}(\omega, \boldsymbol{k}; T)] \qquad \text{for} \qquad T, \omega, |\boldsymbol{k}| \ll \mu \ , \tag{1.12}$$

where $\mathrm{Im}[G^R_{\mathrm{IR}}(\omega, \boldsymbol{k}; T)]$ is completely determined by the near-horizon geometry alone and, hence, so is the low-energy limit of the full Green's function up to a constant coefficient that depends on the UV. In the following, we briefly sketch why this is the case (for a more complete treatment, see e.g. Sec. 4.3 of Ref. [57]).

For the sake of simplicity, let us set $T = 0$ and forget about momentum $\boldsymbol{k}$ so that the only energy scale of the field theory to compare with the chemical potential is set by the frequency (the argument can also be generalized to include nonzero temperature and momentum). We are interested in the behavior of the full Green's function in the low-energy limit $\omega \ll \mu$, but the problem is that we cannot simply send $\omega \to 0$ to find the leading order as this limit does not commute with the small-r limit[5]. What we can do is solve the wave equations for the fluctuations in two regimes, one with $r \ll \mu$—that defines the above-mentioned *inner* region (or *near-horizon* region in the presence of a black-hole)—and the other for $r \gg \omega$ where the solution to leading order can be safely found by setting $\omega = 0$. The trick is that for $\omega \ll \mu$ there is a large region of overlap between these two regimes where the solutions can be matched, as depicted in Fig. 1.4. The frequency-dependent solution in the inner region, in analogy with the procedure in the full spacetime, defines the infrared Green's function $G^R_{\mathrm{IR}}(\omega)$ introduced above, and by matching with the outer solution we find to leading order

$$G^R(\omega) = \frac{a + bG^R_{\mathrm{IR}}(\omega)}{c + dG^R_{\mathrm{IR}}(\omega)} \qquad a, b, c, d \in \mathbb{R} \ . \tag{1.13}$$

The coefficients, $\{a, b, c, d\}$, are determined by the solution in the outer region where we could set $\omega = 0$ and are, hence, frequency-independent and real. More in general, these coefficients are functions of ω, k, T that admit an analytical expansion in $\omega/\mu, k/\mu, T/\mu$ that starts from order zero. To lowest order then, the imaginary part of the full Green's function is just a (UV-dependent) constant times the imaginary part of the IR Green's function.

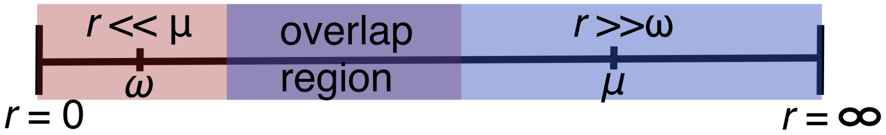

Figure 1.4: Pictorial representation of the two regimes in which we solve the wave equations. For $\omega \ll \mu$ there is an overlap region with $\omega \ll r \ll \mu$ where we can match the solutions.

---

[5] In the presence of a black-hole horizon r would then be the distance from the horizon

1.2.4 Hydrodynamic modes and plasmons

In the low-energy regime, we should expect the modes of the system to coincide with what is obtained with another low-energy phenomenological approach, *hydrodynamics*. Due to strong interactions the equilibration time of the system after a small perturbation is fast enough (compared to the hydrodynamic characteristic scale) that the only long-lived excitations are the ones associated with (quasi)conserved quantities that cannot relax. There is a lot that can be said about hydrodynamics, and in this section, we only give a short introduction in order to show that, in a neutral system with conserved momentum, we find linear low-energy excitations, the *sound modes*, that also appears in the response of our holographic models, as shown in Fig. 1.5. Furthermore, we present here how screening effects due to the long-range Coulomb interaction are going to change these modes giving rise to *plasmon excitations*. The relevance of these excitations is due to the fact that they appear to play an important role in cuprates [59, 100] and have been proposed as a possible mechanism mediating the superconducting phase transition. Introducing them into the holographic description of the strange metal is the main topic of Ch. 2 of this thesis. For a more extensive introduction to hydrodynamics, we suggest Ref. [83], or Sec. 5.4 of Ref. [57] and Ch. 7 of Ref. [133] for an introduction with a view towards holography.

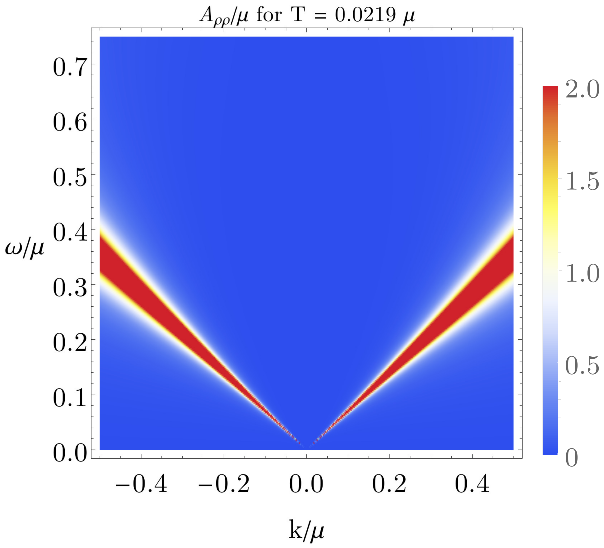

Figure 1.5: Linear sound modes in the holographic density spectral function.

For our CFT deformed by temperature T and chemical potential μ, the equations of motion of relativistic[6] hydrodynamics are:

$$\begin{aligned} \partial_\mu T^{\mu\nu} &= F^{\mu\nu}_{\text{ext}} J_\mu \ , \\ \partial_\mu J^\mu &= 0 \ , \end{aligned} \tag{1.14}$$

with $T^{\mu\nu}$ the expectation value of the field theory stress tensor, J_μ a charge current, and $F^{\mu\nu}_{\text{ext}}$ describing an (eventual) external electromagnetic field. These equations are exact, but in order to close the system of equations, we need to find a local expression for $T^{\mu\nu}$ and J^μ in terms of the hydrodynamic variables. These are called *constitutive relations*, and the hydrodynamic approximation consists in writing them in a derivative expansion. To zeroth order we have

$$\begin{aligned} T^{\mu\nu} &= (\epsilon + P) u^\mu u^\nu + P \eta^{\mu\nu} \ , \\ J^\mu &= \rho u^\mu \ , \end{aligned} \tag{1.15}$$

with u^μ the velocity vector given by $u^\mu = (1, 0)$ as we consider a fluid at rest. Furthermore, ϵ, P, and ρ are the equilibrium energy density, pressure, and particle density of the system respectively, that can be expressed in terms of the hydrodynamic variables through the equilibrium equation of state $P(\mu, T)$.

What we want to find are the collective modes of the system under small perturbations around equilibrium

$$u^\mu = (1, \delta u^i), \qquad T \to T + \delta T, \qquad \mu \to \mu + \delta\mu \ . \tag{1.16}$$

The perturbation of the energy-momentum tensor and current are then [57]

$$\begin{aligned} \delta J^t =& \delta\rho, \quad \delta J^i = \rho \delta u^i, \quad \delta T^{tt} = \delta\epsilon \ , \\ \delta T^{ij} =& \delta^{ij} (\partial_\epsilon P \delta\epsilon + \partial_\rho P \delta\rho) \ , \quad \delta T^{ti} = (\epsilon + P) \delta u^i \ . \end{aligned} \tag{1.17}$$

In a medium with conservation of energy and momentum, $\partial_\mu T^{\mu\nu} = 0$, we find from

---

[6] Notice that holography defines a relativistic theory. In application to a condensed-matter system it is hence used as an effective description of a theory with linear dispersion by replacing the speed of light c with the characteristic velocity of the system $v \ll c$.

Eqs. (1.17) and the conservation equations in Eqs. (1.14) for the fluctuations

$$\omega\delta\rho - k\rho\delta u = 0 \ , \tag{1.18}$$

$$\omega(\epsilon + P)\delta u = k(\partial_\epsilon P\delta\epsilon + \partial_\rho P\delta\rho) \ , \tag{1.19}$$

$$\omega\delta\epsilon = k(\epsilon + P)\delta u \ , \tag{1.20}$$

where $\delta u = \delta u_x$ and, given that we are considering a homogeneous and isotropic background, we wrote the space and time dependence of the fluctuations as $e^{-i\omega t+ikx}$, fixing the momentum along the x direction, without loss of generality. This then gives an equation of motion for the density fluctuations

$$\left[\omega^2 - k^2\left(\partial_\epsilon P + \frac{\rho}{(\epsilon + P)}\partial_\rho P\right)\right]\delta\rho = 0 \ , \tag{1.21}$$

where we recognize the linearly-dispersing sound excitations with the speed of sound determined by

$$v_s^2 \equiv \partial_\epsilon P + \frac{\rho}{(\epsilon + P)}\partial_\rho P = (\partial_\epsilon P)_{S,\mathcal{N}} \ , \tag{1.22}$$

with the notation $(\cdot)_{S,\mathcal{N}}$ meaning that the derivative is evaluated at constant entropy and particle number $\mathcal{N}$.

What we want to see now, is what happens to the sound mode if the charges are subject to screening effects due to the long-range Coulomb interaction.
From Gauss' law, in a medium with dielectric constant ε, we now have

$$\nabla \cdot \boldsymbol{E} = \frac{\rho}{\varepsilon} \Rightarrow ikE_x = \frac{\rho}{\varepsilon} \ , \tag{1.23}$$

leading to an effective $F^{\mu\nu}_{\text{ext}}$ in Eqs. (1.14). The equations for the fluctuations of the energy-momentum tensor then become

$$\omega(\epsilon + P)\delta u = k(\partial_\epsilon P\delta\epsilon + \partial_\rho P\delta\rho) + \frac{2}{k}\frac{\rho^2}{\varepsilon}\delta\rho \ , \tag{1.24}$$

$$\omega\delta\epsilon = \left[k(\epsilon + P) - \frac{1}{k}\frac{\rho^2}{\varepsilon}\right]\delta u \ . \tag{1.25}$$

Using, as before, the equation for current conservation we then find that the equation for the density fluctuations becomes

$$\left[\omega^2 - \frac{\rho^2}{\varepsilon(\epsilon + P)} - v_s^2 k^2\right] \delta\rho = 0 \ , \tag{1.26}$$

and we see that the linear sound modes turned into a **gapped** plasmon mode, with

$$\omega_{\mathrm{pl}} = \sqrt{\frac{\rho^2}{\varepsilon(\epsilon + P)}} \tag{1.27}$$

the characteristic plasma frequency for a relativistic fluid.

Before concluding this section, let us emphasize a distinction between the hydrodynamic approach and holography even in the regime of overlap of the two approaches. We only discussed here the modes of the systems, however, a key physical quantity is the lifetime of these excitations. This is captured by the imaginary part of the Green's function and can be described by phenomenological coefficients whose values cannot be determined from hydrodynamics alone. On the other hand, holography also contains all the information on the decay of the excitations, controlled by the quantum critical nature of the system.

1.2.5 Double-trace deformation

As of now we always talked about changing the infrared of the theory by introducing relevant single-trace operators O dual to some classical field ϕ in the bulk that alters the inner geometry of the spacetime. We can, however, also introduce a *double-trace* deformation

$$S = S_{\mathrm{QFT}} + \frac{\lambda}{2} \int \mathrm{d}t \mathrm{d}^d \boldsymbol{x} \, O^2 \ , \tag{1.28}$$

that modifies the response of the system leaving, nonetheless, the spacetime geometry unchanged. From the gravitational side, it can be shown that the multi-trace deformation corresponds to changing the boundary conditions for the dual field [129]. This has the effect of modifying the Green's function for the operator O, and it will play a key role in introducing screening effects in the holographic strange metal. In the theory deformed by the double-trace operator in Eq. (1.28) the Green's function for

O becomes

$$G_{\text{d.t.}}(\omega,\boldsymbol{k}) = \frac{G_{\text{s.t.}}(\omega,\boldsymbol{k})}{1+\lambda G_{\text{s.t.}}(\omega,\boldsymbol{k})} \ , \tag{1.29}$$

with $G_{\text{s.t.}}(\omega,k)$ the response function for O in the un-deformed theory.

The reader with a background in condensed-matter theory will notice that this takes a familiar form reminiscent of the *random-phase approximation* (RPA). It is important, though, to keep in mind that $G_{\text{s.t.}}$ in Eq. (1.29) has a very different nature from the free electron Green's function of condensed-matter RPA, as it is a Green's function for a collective excitation of a system governed by strong interactions.

1.2.6 Fermions and the Fermi surface of a non-Fermi liquid

In the previous sections, we focused on the effective description of the collective, bosonic, modes of the system governing its transport properties. However there is another quantity of great experimental interest, the fermionic self-energy near the Fermi surface, $\Sigma(\omega,k) = \Sigma'(\omega,k) - i\Sigma''(\omega,k)$, as its imaginary part can be probed by ARPES experiments. In particular, we will be interested in analyzing slices of the cuprate spectral function at fixed energy, aka momentum-dependent cuts (MDC), along the nodal direction (see Fig. 1.6). These show a peak near the Fermi surface, as shown in Fig. 1.7, that can be fitted with a function

$$\mathcal{A}(k;\omega) = \frac{W(\omega)}{\pi}\frac{\Gamma(\omega,k)/2}{(k-k_*(\omega))^2+(\Gamma(\omega,k)/2)^2} \ , \tag{1.30}$$

where $\Gamma(\omega,k) = 2\Sigma''(\omega,k)/v_F + G_0(\omega)$ and $G_0(\omega)$ includes all the contributions that are not determined by the electron self-energy (for example, due to phonons, impurities or instrument sensitivity). Moreover, v_F is the renormalized Fermi velocity, $k_*(\omega)$ determines the peak position $k_*(\omega) \simeq k_F + \omega/v_F$ with k_F the Fermi wave number, and $W(\omega)$ is an overall normalization factor. Experimentally, it was observed that the self-energy of cuprates near the Fermi surface is dominated by the frequency dependence, as the MDC curves are well described by a Lorentzian lineshape with

$$\Sigma''(\omega,k) \sim (\omega^2)^\alpha \ , \tag{1.31}$$

where the power α depends on doping.

Our goal is to use holography to compute $\Sigma''(\omega,k)$ and compare the (semi-)holographic

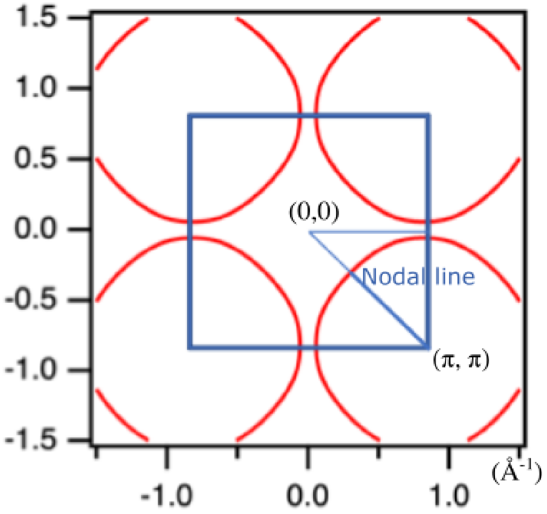

Figure 1.6: Momentum-space structure of the Fermi surface for a strange metal cuprate. The blue square represents a unit cell, with the red line showing the position of the Fermi surface. The so-called nodal direction is represented by the line connecting the $(0, 0)$ and (π, π) points.

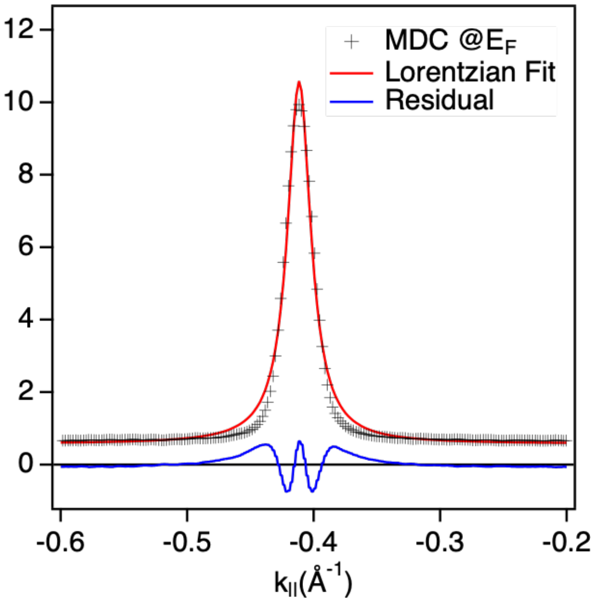

Figure 1.7: Peak in an MDC of the nodal fermionic spectral function near the Fermi energy, signaling the presence of a Fermi surface.

prediction with the experimental line-shape from ARPES measurements. The holographic computation involves solving the Dirac action in the curved background to extract the fermionic Green's function, and the details of the procedure will be introduced extensively in Ch. 5. Here we want to highlight the relationship between the $z = \infty$ scaling of our holographic models and the electronic self-energy of cuprates.

In an approach called *semi-holography* [33, 52], the electron self-energy in the nodal direction can be directly related to the infrared fermionic Green's function obtained from the near-horizon geometry as mentioned in Sec. 1.2.3, hence,

$$\Sigma''(\omega, k) \propto \mathrm{Im}[G^R_{\mathrm{IR}}(\omega, k)] \ . \tag{1.32}$$

The interesting part is that our holographic model is characterized by the $z = \infty$ near-horizon scaling

$$t \to \lambda t, \quad r \to \lambda r, \quad x \to x \ , \tag{1.33}$$

where space (and thus momentum) is dimensionless under scaling. The key implication is that in the low-energy limit momentum dependence can, hence, only appear in the exponent and the IR Green's function is given by a power law in frequency

$$G^R_{\mathrm{IR}}(\omega, k) \sim \omega^{2\alpha(k)} \ . \tag{1.34}$$

For sharp peaks near the Fermi surface $\alpha(k) \approx \alpha(k_F)$ we recover—upon tuning the parameters in the Dirac equation to match the experimental doping dependence—the local self-energy conjectured for the cuprates.

On the other hand, since the semi-holographic self-energy still implicitly depends on momentum through $\alpha(k)$ (this is the reason why these theories are sometimes called *semi-local* quantum critical) we expect small deviations from the Lorentzian lineshape as we look at MDCs away from the Fermi surface. Showing that deviations compatible with the semi-holographic prediction are indeed observed in ARPES measurement of the Fermi surface of a cuprate strange metal is one of the main results of this thesis, which will be presented in Ch. 4 and Ch. 5.

1.3 Overview of the rest of the thesis

The chapters that follow are a collection of the papers—either published, under review, or in preparation for submission—that resulted from the research performed in these last few years. Here we give a brief overview of the topic of each chapter.

- In **Chapter 2** we introduce Coulomb interactions in the holographic description of strongly interacting systems, by means of a (current-current) double-trace deformation. We then proceed to show—using as an example the Reissner-Nordström background—that this leads to gapped plasmon modes in the density-density response. We then generalize the procedure to describe layered systems, where for a single layer we recover the expected plasmon dispersion proportional to $\sqrt{k}$, while in a multi-layer system we find the linear 'acoustic plasmon' modes that have been observed experimentally in a layered cuprate high-temperature superconductors. Finally, we compute the optical conductivity of the deformed theory in a three-dimensional metal, where a logarithmic correction is present and we show how this can be related to the conductivity measured in Dirac and Weyl semimetals.

- In **Chapter 3** we study the Coulomb drag in a two-layer system with strong in-plane interaction modeled with the holographic framework using the Einstein-Maxwell-Dilaton background. We show that the low-temperature dependence of the drag resistivity is $\rho_D \propto T^4$, which strongly deviates from the quadratic dependence of Fermi liquids. Furthermore, we present numerical results at room temperature and above, using typical parameters of the cuprates, to provide an estimate of the magnitude of this effect for future experiments. At this higher temperature, we find that the drag resistivity is enhanced by the plasmons characteristic of the two-layer system.

- The work presented in **Chapter 4** resulted from a collaboration between experimental and theoretical physicists, and it has a more experimental inclination. Here we present a highly precise experimental determination of the cuprate electronic self-energy obtained by angle-resolved photoemission. In particular, we show that constant energy cuts through the nodal spectral function in $(\mathrm{Pb,Bi})_2\mathrm{Sr}_{2-x}\mathrm{La}_x\mathrm{CuO}_{6+\delta}$ have a non-Lorentzian lineshape, meaning the nodal self-energy contains a momentum dependence. We then present how the experimental data are captured remarkably well by a power law with a k-dependent scaling exponent that emerges naturally from semi-holography.

The main share of the experimental work was performed by S. Smit of the University of Amsterdam, and this chapter can also be found in his doctoral thesis. It is, instead, the theoretical part that formally pertains to this dissertation.

- In **Chapter 5** we delve deeper into the theory behind the finding presented in Chapter 4. We show that the momentum-dependent scaling exponents of the holographic fermion self-energy of the Gubser-Rocha model for a strange metal are able to describe the deviation from the Lorentzian line shape that is expected from the power-law-liquid (PLL) model proposed for the cuprates' electronic self-energy $\Sigma''_{\mathrm{PLL}}(\omega) \propto (\omega^2)^\alpha$. More precisely, by direct comparison with experimental results, we provide evidence that this departure from either a Fermi liquid or the power-law liquid, resulting in an asymmetry of the spectral function as a function of momentum around the central peak, is captured at low temperature and all dopings by a semi-holographic model that predicts a momentum-dependent scaling exponent in the electron self-energy as $\Sigma(\omega, k) \propto \omega(-\omega^2)^{\alpha(1-(k-k_F)/k_F)-1/2}$, with $\hbar k_F$ the Fermi momentum.

Chapter 2

Screening of Coulomb interactions in holography

2.1 Introduction

The AdS/CFT correspondence [94, 48, 128] has become an important tool for studying strongly coupled quantum field theories, and, in the last decade, it found an ever-increasing range of applications into the realm of condensed-matter physics [60, 53, 133, 57]. Many recent experiments demonstrate that in strongly interacting systems as, for example, the cuprates high-temperature superconductors, the observed behavior can deviate quite drastically from well known condensed-matter results based on weakly coupled theories that admit a quasiparticles description. In particular, these materials exhibit a strange-metal phase for temperatures higher than the superconducting critical temperature, where quasiparticle excitations appear to be absent (see e.g. ref. [57]). The promising aspect of the gauge/gravity duality is that it allows us to study systems without quasiparticle excitations. It can be used to compute thermodynamic quantities and response functions with relatively little effort by mapping strongly interacting quantum field theories on the boundary of an asymptotically AdS spacetime, to classical gravity in the curved bulk spacetime. Trying to tune holographic models such that they reproduce the properties of laboratory condensed-matter systems as closely as possible is, therefore, one important goal of ongoing research in holographic applications to condensed matter.

A common feature in conventional holographic calculations is that they describe neutral systems, where the low-energy hydrodynamic excitations in the longitudinal channel contain sound modes. However, it is well established that in metals the density fluctuations of the charged electrons give rise to a different type of collective excitations known as plasmons [121]. In order to have more realistic models of strongly interacting metals and superconductors, it is thus important to modify the holographic theory to include the effect of the long-range Coulomb interaction that turns the linear sound modes into plasmon modes.

In textbook condensed-matter response calculations the electron-electron interaction is introduced in the description through a self-consisted field method known as the random-phase approximation (RPA) [14, 106, 15, 105], where the induced charge without Coulomb interaction is replaced with the screened charge. In a translational invariant system the density-density response function $\chi(\omega, \boldsymbol{k})$ then becomes, in terms of the non-interacting response function $\chi_0(\omega, \boldsymbol{k})$, equal to

$$\chi(\omega, \boldsymbol{k}) = \frac{\chi_0(\omega, \boldsymbol{k})}{1 - V(\omega, \boldsymbol{k})\chi_0(\omega, \boldsymbol{k})} \equiv \frac{\chi_0(\omega, \boldsymbol{k})}{\epsilon(\omega, \boldsymbol{k})} \ , \tag{2.1}$$

where $\epsilon(\omega, \boldsymbol{k})$ is the dynamical dielectric function, and $V(\omega, \boldsymbol{k})$ the Fourier transform of the Coulomb potential. In non-relativistic systems, where the Fermi velocity is much smaller than the speed of light, the latter is only a function of the magnitude of the momentum $|\boldsymbol{k}|$. In particular, for 2D and 3D materials, where here we refer to the spatial dimension of a system living in the usual $(3+1)$-dimensional spacetime, we have that

$$\begin{cases} V(\omega, \boldsymbol{k}) = \frac{e^2}{2\epsilon_0 |\boldsymbol{k}|}, & \text{2D} \\ V(\omega, \boldsymbol{k}) = \frac{e^2}{\epsilon_0 \boldsymbol{k}^2}, & \text{3D} \ , \end{cases} \tag{2.2}$$

with $-e$ the charge of the electron, and ϵ_0 the dielectric constant.

In this paper, we develop a generic procedure to include the above RPA correction, and hence the effect of Coulomb interactions, into holographic models at nonzero density. A first step towards studying plasmon modes in holography was recently made in refs. [43, 46, 42, 45], where it was shown that plasmon quasinormal-modes can be studied by imposing a new type of boundary conditions on the bulk linearized equations of motion. Here we explain how these boundary conditions naturally arise by introducing a (current-current) double-trace deformation of the boundary theory, and how this gives rise to an RPA-like form of the response function. Using also the example of the Reissner-Nordström metal, we numerically study the full frequency and momentum dependence of the spectral functions and show how the prescribed procedure turns the low-energy sound modes into gapped plasmon modes.

In the particular case of a $(3+1)$-dimensional theory, we also show that by introducing long-range Coulomb interactions in the holographic theory, we obtain an anomalous cutoff-dependent logarithmic behavior in the real part of the optical conductivity, analogous to the one observed in the conductivity of Dirac and Weyl semimetals [115].

In $(2+1)$-dimensions, we adapt our procedure to correctly describe a system where electrons are constrained to two spatial dimensions, but where the Coulomb potential exists in three spatial dimensions. This allows us to obtain a low-energy dispersion relation $\omega \propto \sqrt{|\boldsymbol{k}|}$ as expected in charged (spatially) two-dimensional system as, for example, graphene [92, 93]. Furthermore, since experiments on $(2+1)$-dimensional materials are often performed on a multi-layer system, we propose a toy model describing an infinite stack of $(2+1)$-dimensional layers, where the dynamics in each layer is determined holographically through a dual Reissner-Nordström theory and where the coupling between the layers is given only by the long-range Coulomb interaction. A recent example of the interest in these multi-layered systems is given in ref. [59], where the spectral function for a layered copper-oxide high-temperature superconductor has been measured. These experimental results suggest that it is indeed the Coulomb interaction that governs the coupling between different layers, validating the assumptions of our toy model, and hinting at the fact that low-energy charge fluctuations might be very relevant for the description of the dynamics of high-T_c superconductors. We, therefore, show how our toy model qualitatively reproduces the observed spectral functions, with low-energy linear excitations, often referred to as 'acoustic plasmons', believed to possibly play an important role in the mechanism of high-temperature superconductivity [69, 85, 11].

The structure of the paper is as follow. In section 2.2 we briefly summarize the Reissner-Nordström model and its spectral functions containing the sound modes. In section 2.3 we explain how to deform the theory to describe a charged system with plasmon excitations and show how the density-density response function obtains the RPA-like form. In section 2.4 we present the numerical results for the spectral functions with plasmon excitations in a $(2+1)$-dimensional theory and propose a toy model for a layered system in $3+1$ dimensions. Finally, section 2.5 contains the results for the optical conductivity for a $(3+1)$-dimensional system with Coulomb interactions.

2.2 Reissner-Nordström black brane

In this section we introduce the Reissner-Nordström model that we use throughout the paper as a concrete example of the proposed procedure, that we introduce in detail in section 2.3. The dynamics of this holographic model has been thoroughly studied in refs. [29, 28, 24, 25]. In order to be able to compare directly with our later results, however, we briefly review its dynamical properties by computing the spectral functions. We then recover that the low-energy excitations of the theory in the longitudinal sector are linear sound modes and a diffusive mode.

Throughout the paper, we call d the spacetime dimension of the boundary theory, dual to a gravitational $(d+1)$-dimensional bulk theory and we use the mostly-plus metric. We denote with r the coordinate of the extra spatial dimension of the bulk theory, with the boundary at $r \to \infty$ unless explicitly stated otherwise. When Fourier transforming in the direction orthogonal to r, we denote with $k = (\omega/c, \boldsymbol{k})$ the d-dimensional momentum. We use, with a slight abuse of notation, greek lower-case tensor indices for both the $(d+1)$-dimensional bulk and the d-dimensional boundary, as the range of the indices is clear from the context. Moreover, in computing dynamical quantities, we always use a gauge in which all the r-components of the field fluctuations are zero, so that no confusion should arise.

2.2.1 Gravity action

The simplest holographic model with a nonzero-density boundary theory is the Reissner-Nordström model, described by a bulk Einstein-Maxwell action, that in SI units reads

$$S_{EM} = \int \mathrm{d}^{d+1}x \, \sqrt{-g} \left(\frac{c^3}{16\pi G}(R - 2\Lambda) - \frac{1}{4\lambda c} F_{\mu\nu}F^{\mu\nu} \right) \,, \tag{2.3}$$

where $x = (r, ct, \boldsymbol{x})$, with r the bulk coordinate, G is Newton's gravitational constant in $d+1$ dimensions, and λ is a coupling constant with dimension $[\lambda] = \mathrm{m}^{d-2}\,\mathrm{kg}$, such that $[A_\mu] = \mathrm{m\,kg\,s}^{-1}$. Defining $A_t \equiv cA_0$, we then see that $[A_t] = \mathrm{m}^2\,\mathrm{kg\,s}^{-2} = [\mu]$, i.e., the bulk field A_t has the dimensions of a chemical potential. Since we want to describe a homogeneous and isotropic boundary theory, i.e., the chemical potential and the energy-momentum tensor do not depend on the spacetime coordinates and there is no preferred direction, we look for a solution of the form $A_\mu = (0, A_0(r), \boldsymbol{0})$ and $g_{\mu\nu} = g_{\mu\nu}(r)$.

For notational convenience, we first rewrite the action in terms of dimensionless fields and coordinates, by redefining the fields as

$$\begin{aligned}
\tilde{A}_t =& \frac{L}{2r_0}\sqrt{\frac{16\pi G}{\lambda c^4}}\frac{A_t}{c} \ , \\
\tilde{A}_x =& \frac{L}{2r_0}\sqrt{\frac{16\pi G}{\lambda c^4}}A_x \ , \\
\tilde{A}_r =& \frac{r_0}{2L}\sqrt{\frac{16\pi G}{\lambda c^4}}A_r \ , \\
\tilde{g}_{\mu\nu} =& \frac{L^2}{r_0^2}g_{\mu\nu} \ , \\
(\tilde{t}, \tilde{\boldsymbol{x}}, \tilde{r}) =& \left(\frac{ctr_0}{L^2}, \frac{xr_0}{L^2}, \frac{r}{r_0}\right) \ ,
\end{aligned} \tag{2.4}$$

with $L^2 = -d(d-1)/2\Lambda$ the AdS radius squared and r_0 denotes the position of the black-brane (outer) horizon. Notice that this rescaling thus fixes the horizon at $\tilde{r}_0 = 1$. However, using the scaling symmetry of the action

$$\tilde{r} \to a\tilde{r}, \ (\tilde{t}, \tilde{\boldsymbol{x}}) \to (\tilde{t}, \tilde{\boldsymbol{x}})/a, \ \tilde{A}_\mu \to a\tilde{A}_\mu, \tag{2.5}$$

we can obtain any solution from the solution with $\tilde{r}_0 = 1$. From now on we only use dimensionless variables and omit the tildes. In the end, the theory we are going to study, including boundary terms, is described by the action:

$$\begin{aligned}
S/\hbar = \frac{c^3 L^{d-1}}{4\pi\hbar G}\Bigg(&\frac{1}{4}\int_{\mathcal{M}} \mathrm{d}^{d+1}x\,\sqrt{-g}\,[R - d(d-1) - F_{\mu\nu}F^{\mu\nu}] + \frac{1}{2}\int_{\partial\mathcal{M}} \mathrm{d}^d x\sqrt{-\gamma}K \\
&+ \int_{\partial\mathcal{M}} \mathrm{d}^d x \mathcal{L}_{c.t.}^{(d)}\Bigg) \ ,
\end{aligned} \tag{2.6}$$

where now every field and coordinate is dimensionless, as is the prefactor in front of the integral that for now we take to be equal to one, by an appropriate scaling of the action, but we briefly come back to this prefactor later on. The second term is the Gibbons-Hawking-York boundary term, with $\gamma_{\mu\nu} \equiv g_{\mu\nu} - n_\mu n_\nu$ the induced metric on the boundary, n_μ the unit vector normal to the boundary, and the determinant γ of $\gamma_{\mu\nu}$ is taken only in the directions orthogonal to n^μ. Finally, K is the trace of the second fundamental form $K = \gamma^{\mu\nu}\nabla_\mu n_\nu$. This boundary term is necessary to have a well-defined Dirichlet problem on the boundary [131, 39, 58]. In the case at hand (see below Eq. (2.7) where the asymptotically AdS spacetime is a foliation of flat Minkowski spacetime) we have $n_\nu = \sqrt{g_{rr}}\delta^r_\mu$ and K reduces to $K = -\sqrt{g_{rr}}\gamma^{\mu\nu}\Gamma^r_{\mu\nu}$, with $\Gamma^r_{\mu\nu}$ the bulk Christoffel symbols. The last term in the action contains the counterterms necessary to regulate the divergences in the theory, and its explicit form depends on the dimension d of the boundary spacetime. We present later the counterterms in the case of $d = 2+1$ and $d = 3+1$. For a detailed treatment see, for instance, ref. [27].

The classical equations of motion derived from the above action are solved by the Reissner-Nordström background, describing an asymptotically AdS charged black brane, that in the units we introduced takes the form

$$\begin{aligned} \mathrm{d}s^2 =& - f(r)\mathrm{d}t^2 + \frac{1}{f(r)}\mathrm{d}r^2 + r^2 \mathrm{d}\boldsymbol{x}^2 \ , \\ A_t(r) =& \mu\left(1 - r^{2-d}\right) \ , \\ f(r) =& r^2\left[1 - \left(1 + \frac{2(d-2)}{d-1}\mu^2\right) r^{-d} + \frac{2(d-2)}{d-1}\mu^2 r^{2(1-d)}\right] \ , \end{aligned} \tag{2.7}$$

where we defined $\lim_{r\to\infty} A_t(r) = \mu \equiv A_t'(1)/(d-2)$ for $d > 2$, that, according to the holographic dictionary, we interpret as the chemical potential of the boundary theory. Here and below, the prime denotes derivatives with respect to the radial coordinate. From the solution of $f(r)$, we can see that the mass M and charge Q of the black brane are expressed in terms of μ as

$$Q = \sqrt{\frac{2(d-2)}{d-1}}\mu \ , \tag{2.8}$$

$$M = 1 + \frac{2(d-2)}{d-1}\mu^2 = 1 + Q^2 \ . \tag{2.9}$$

The solution is then completely characterized by one dimensionless parameter, that we take to be T/μ, with the black-brane temperature given by

$$T(\mu) = \frac{f'(1)}{4\pi} = \frac{d - \frac{2(d-2)^2}{d-1}\mu^2}{4\pi} \ . \tag{2.10}$$

The equilibrium properties of the theory are well known (see e.g. ref. [133]) and can be derived from the GKPW rule after regularizing the action at the cutoff scale $r = r_{\text{UV}}$ by inserting the boundary counterterm

$$S_{c.t.} = -\frac{(d-1)}{2}\int_{r=r_{\text{UV}}} \mathrm{d}^d x\sqrt{-\gamma} \ . \tag{2.11}$$

We give here for later convenience the nonzero components of the equilibrium expectation values in the chosen units, that for $d > 2$, are:

$$\delta^{ij}\left\langle P\right\rangle \equiv \left\langle T^{ij}\right\rangle = \lim_{r_{\rm UV}\to\infty} 2r_{\rm UV}^2 \frac{\delta S^{cl}|_{r=r_{\rm UV}}}{\delta g_{ij}^{(0)}} = \frac{1}{4}\delta^{ij}\left(1+\frac{2(d-2)}{d-1}\mu^2\right) = \frac{1}{4}\delta^{ij}M \ , \tag{2.12}$$

$$\left\langle \epsilon\right\rangle \equiv \left\langle T^{00}\right\rangle = \lim_{r_{\rm UV}\to\infty} 2r_{\rm UV}^2 \frac{\delta S^{cl}|_{r=r_{\rm UV}}}{\delta g_{00}^{(0)}} = \frac{(d-1)}{4}\left(1+\frac{2(d-2)}{d-1}\mu^2\right) = \frac{(d-1)}{4}M \ , \tag{2.13}$$

$$\left\langle \rho\right\rangle \equiv \left\langle J^{0}\right\rangle = \lim_{r_{\rm UV}\to\infty} \frac{\delta S^{cl}|_{r=r_{\rm UV}}}{\delta A_{0}^{(0)}} = (d-2)\mu \ . \tag{2.14}$$

Here S^{cl} is a reminder that the action is evaluated at the classical solution and the superscript in $\delta g_{\mu\nu}^{(0)}$ and $\delta A_{\mu}^{(0)}$ means that we are deriving with respect to the leading-order term in the asymptotic expansion of the field for large r. We see here that, in order to compare holographic results to experiments, we should choose, in this bottom-up approach, the prefactor in front of the action in Eq. (2.6), that we conveniently scaled away, such to tune the thermodynamic quantities to values close to the experimental ones.

2.2.2 Fluctuations and response functions

The background solution of the gravity action in Eq. (2.6) defines the equilibrium properties of the boundary theory. In order to study the response of the field theory to small perturbations, we have to consider fluctuations of the classical fields on top of the background solution:

$$\begin{aligned} A_\mu &\to A_\mu + a_\mu \\ g_{\mu\nu} &\to g_{\mu\nu} + h_{\mu\nu} \ . \end{aligned} \tag{2.15}$$

Exploiting rotational invariance to fix the momentum along the x direction, so that $k = (\omega, \pm|\boldsymbol{k}|, 0, \ldots, 0)$, the fluctuations decouple according to their parity under $O(d-2)$ acting on $x^2, \ldots, x^{d-1}$ [84]. In particular, we are interested in the longitudinal channel associated with spin 0, as it is the one containing the density-density response function that in $d = 3+1$ and $d = 2+1$ are described by the components

$$\delta\boldsymbol{\Phi} \equiv \left(a_t, a_x, a_r, h_{xt}, h_{tt}, h_{xx}, h_{yy} = h_{zz}, h_{rr}, h_{tr}, h_{xr}\right) \ , \tag{2.16}$$

and will ultimately lead to hydrodynamic diffusion and sound modes. It is convenient to work in a gauge where $h_{r\mu} = 0$, as well as $A_r = a_r = 0$. The set of coupled fluctuations then becomes

$$\delta\boldsymbol{\Phi} = (a_t, a_x, h_{xt}, h_{tt}, h_{xx}, h_{yy} = h_{zz}) \ . \tag{2.17}$$

Solving the coupled set of linearized equations of motion for these fluctuations, with infalling boundary conditions at the black-brane horizon, allows us, after eventual renormalization of boundary divergences (see ref. [118] for a detailed treatment), to compute the retarded Green's functions of the dual boundary theory. To do so, we follow the procedure in ref. [78]. A caveat is that to extract the matrix of Green's functions for a set of M coupled fields we need M independent solutions. In the case at hand, however, our choice to work in a gauge where all the radial components are zero does not completely fix the gauge freedom of a_μ and $h_{\mu\nu}$, and we are left with four gauge degrees of freedom. This implies that we can only find two independent solutions of the linearized equations of motion, corresponding to the two physical degrees of freedom. The remaining solutions needed to compute the full Green's function matrix are pure gauge solutions that can be constructed analytically. In appendix 2.A, we show how to construct these gauge solutions and we provide their explicit form for the theory at hand. From the retarded Green's function $G^R(\omega, \boldsymbol{k})$ we can obtain the spectral function defined as

$$A(\omega, \boldsymbol{k}) \equiv -\frac{2}{\pi}\mathrm{Im}[G^R(\omega, \boldsymbol{k})] \ . \tag{2.18}$$

The spectral function is an interesting quantity as it tells us the rate of work done on the system by a small external perturbation at a given frequency [121]. Sharp peaks in the spectral function, that correspond to poles in the Green's function, denote long-lived collective modes, with a lifetime determined by the width of the peak.

In figures 2.1 and 2.2 we present the spectral functions of a $(2+1)$-dimensional system for the density response $A_{\rho\rho}$ as well as for the energy-density response $A_{\epsilon\epsilon}$ for two different values of the temperature. Here, as in the rest of the paper, we work in the grand-canonical ensemble, hence all the plots are rescaled to a solution with unit chemical potential. Since we are describing a strongly interacting system, we expect from hydrodynamics considerations (see e.g. ref. [83]) to find two linear sound modes due to energy-momentum conservation. As the poles are shared by all Green's functions, although the residues differ, in both spectral functions the low-energy linear sound modes $\omega = \pm v_s|\boldsymbol{k}|$ are evident. In particular, up to the numerical precision obtained, the speed of sound satisfies the relation $v_s = 1/\sqrt{d-1}$ in the low-energy regime [107, 24]. These hydrodynamic sound modes, known as first sound, are present even in the low-temperature limit as long as $\omega, k \ll \mu$, with the nonzero chemical potential setting an effective hydrodynamic scale [28, 24, 25]. This is similar to an ultra-cold Fermi gas at unitarity where, in the limit $T \to 0$, hydrodynamic first sound exists at long wavelengths in a range set by the Fermi energy, and where this first sound mode crosses over to collisionless zeroth sound at shorter wavelengths. In the density spectral function we observe, in addition to the sound modes, the expected diffusive mode due to charge conservation that corresponds to the broad quadratic band. Here the linear modes become less sharply peaked when the temperature is raised as part of the spectral weight shifts into the diffusive mode. Note that the diffusive mode is absent in $A_{\epsilon\epsilon}$, because in that mode the charge fluctuations do not induce a velocity field $\boldsymbol{v}(t, \boldsymbol{x})$ in the fluid, hence also no energy transport. A thorough analysis of these modes has been presented for $(2+1)$-dimensional systems in ref. [24]. In the next section, we turn to the problem of deforming the holographic theory in order to describe a charged quantum field theory with plasmon excitations.

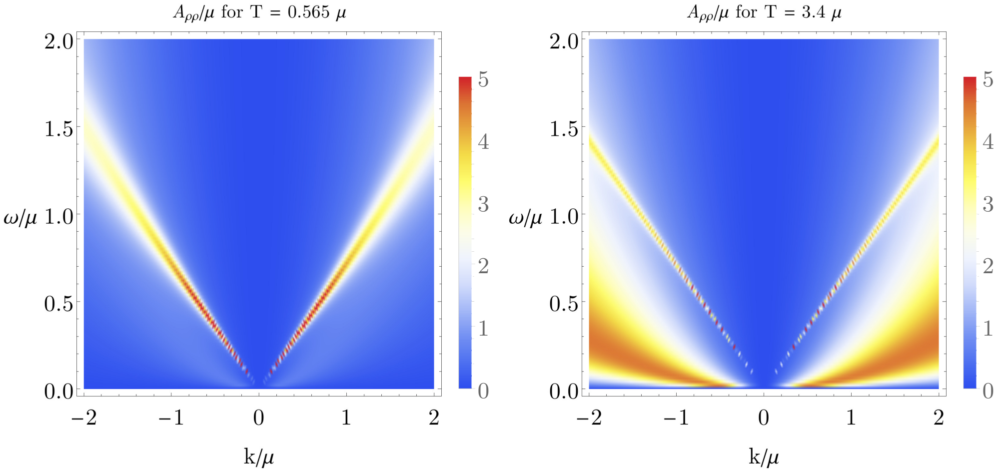

Figure 2.1: The density spectral function for two different values of the temperature in $2+1$ dimensions. Notice that in addition to the linear sound modes with a low-energy behavior of the dispersion given by $\omega = \pm|\boldsymbol{k}|/\sqrt{2}$, we can clearly observe the diffusive mode, that becomes more dominant as we increase T/μ.

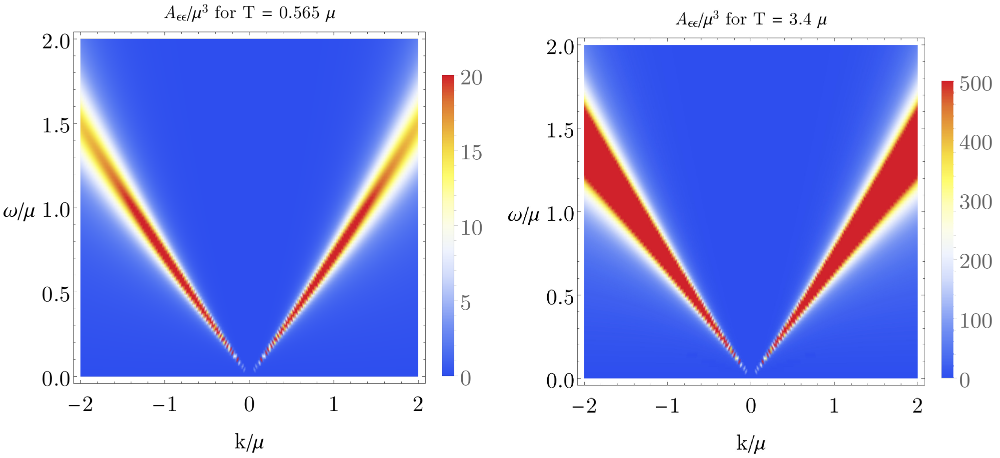

Figure 2.2: The energy-density spectral function for two different values of the temperature in 2+1 dimensions. The sound modes are clearly visible and we can notice that the associated peaks become higher for a higher value of the temperature.

2.3 Plasmon modes in holographic theories

In this section we explain how to introduce Coulomb interactions in the boundary quantum field theory, and show how this gives rise to an RPA-like form of the response functions that turns the linear modes observed in the Reissner-Nordström spectral function into long-lived plasmon excitations.

The holographic theory presented in the previous section is dual to a charge-neutral boundary theory, that is, the Maxwell field in the bulk acts only as a source for the current operator J^μ in the boundary theory, and there is no dynamical photon [54]. However, in condensed matter we are often interested in describing charged systems, i.e., systems with a long-range Coulomb interaction. We, therefore, need to modify the boundary theory to add dynamical photons coupled to the conserved current $\langle J^\mu \rangle$ obtained from holography in the large-N limit, which are described by the Maxwell action

$$S_{\mathrm{M}} = \int \mathrm{d}^d x \left(-\frac{1}{4\mu_0 e^2} F_{\mu\nu} F^{\mu\nu} + A_\mu \langle J^\mu \rangle \right) , \tag{2.19}$$

with μ_0 the magnetic permeability and $-e$ the electron charge. Note that we also used the fact that our boundary theory is defined on flat Minkowski spacetime, so that $\sqrt{-\eta} = 1$. Integrating out the A_μ field from Eq. (2.19), using the standard ξ

procedure to account for the gauge freedom, we obtain in momentum space (see for example ref. [117])

$$S = -\frac{1}{2}\int \frac{\mathrm{d}^d k}{(2\pi)^d}\mu_0 e^2 \langle J^\mu(k)\rangle \left[\frac{\eta_{\mu\nu} - (1-\xi)k_\mu k_\nu/k^2}{k^2}\right]\langle J^\nu(-k)\rangle \ . \tag{2.20}$$

Notice that Eq. (2.20) assumes the form of a double-trace deformation of the boundary theory for the current operator.

As first described in refs. [129, 98], a double-trace deformation in the large-N limit can be incorporated in the holographic dual simply as a change in the boundary conditions for the corresponding fields. In the gauge/gravity duality without multi-trace deformation, we can obtain the response to small fluctuations from the asymptotic behavior of the field fluctuations. For example in the case of the Maxwell-field fluctuations we have

$$a_\mu = a_\mu^{(0)} + \cdots + \frac{\eta_{\mu\nu}}{(d-2)}\delta\langle J^\nu\rangle r^{-d+2} + \mathcal{O}(r^{-d-2}) \ , \tag{2.21}$$

and according to the holographic dictionary, we interpret the leading-order coefficient $a_\mu^{(0)}$ as the source a_μ^{s} of the fluctuations $\delta\langle J^\mu\rangle$. Following the prescription in ref. [129], in order to include a multi-trace deformation of the response $\int \mathrm{d}^d x\, \delta\langle J^\mu\rangle \mathcal{M}_{\mu\nu}\delta\langle J^\nu\rangle \equiv W(\delta\langle J^\mu\rangle)$, we still interpret the subleading term in equation (2.21) as the response to the source fluctuations, but we impose the boundary condition

$$\lim_{r\to\infty} a_\mu = a_\mu^{\mathrm{s}} + \frac{\delta W}{\delta\langle J^\mu\rangle} \ . \tag{2.22}$$

The reason for this boundary condition can be easily understood by looking at the boundary behavior of the holographic theory. The boundary contribution from the Maxwell-field fluctuations in the renormalized holographic action, Eq. (2.6), evaluated on-shell is given, at second order in fluctuations, by

$$\delta S^{(2)} = \frac{1}{2}\int_{r=\infty}\frac{\mathrm{d}^d k}{(2\pi)^d} a_\mu^{\mathrm{s}}(k)\delta\langle J^\mu(-k)\rangle \ , \tag{2.23}$$

with

$$\lim_{r\to\infty} a_\mu = a_\mu^{(0)} = a_\mu^{\mathrm{s}} \ . \tag{2.24}$$

By introducing a boundary contribution of the form of Eq. (2.19) at infinity, that, in the saddle point approximation of the large-N limit, we write in dimensionless units as

$$
\begin{aligned}
S_{d.t.} &= \int \mathrm{d}^d x \left(-\frac{1}{4\alpha^2} \left[F_{\mu\nu} F^{\mu\nu} + \frac{2}{\xi} \left(\partial_\mu A^\mu \right)^2 \right] + A_\mu \left\langle J^\mu \right\rangle \right) \\
&= -\frac{1}{2} \int_{r=\infty} \frac{\mathrm{d}^d k}{(2\pi)^d} \alpha^2 \left\langle J^\mu(k) \right\rangle \left[\frac{\eta_{\mu\nu} - (1-\xi) k_\mu k_\nu / k^2}{k^2} \right] \left\langle J^\nu(-k) \right\rangle \ ,
\end{aligned}
\tag{2.25}
$$

with α^2 a dimensionless constant that depends on the charge of the system, its permittivity and on the prefactor of the action in Eq. (2.6), the boundary term for the fluctuations now becomes

$$
\delta S^{(2)} = \frac{1}{2} \int_{r=\infty} \frac{\mathrm{d}^d k}{(2\pi)^d} \left[a^s_\mu(k) - \alpha^2 \left(\frac{\eta_{\mu\nu} - (1-\xi) k_\mu k_\nu / k_\mu k^\mu}{k_\mu k^\mu} \right) \delta \left\langle J^\nu(k) \right\rangle \right] \delta \left\langle J^\mu(-k) \right\rangle \ .
\tag{2.26}
$$

Since the double-trace deformation does not modify the bulk theory, we see that this is equivalent to the Reissner-Nordström theory described above, where we simply modify the boundary conditions

$$
\lim_{r\to\infty} a_\mu = a^{(0)}_\mu \equiv a^{\mathrm{s}}_\mu - \alpha^2 \left(\frac{\eta_{\mu\nu} - (1-\xi) k_\mu k_\nu / k^2}{k^2} \right) \delta \left\langle J^\nu \right\rangle \ ,
\tag{2.27}
$$

that are of the form of Eq. (2.22). Notice that these boundary conditions are equivalent to the ones used in ref. [46] to study plasmonic quasi-normal modes in a $d = 2+1$ holographic theory, but that were obtained differently by looking for zeros of the dielectric function.

The effect of the deformation in Eq. (2.25) on the response functions is easily derived, and in practice there is no need to solve the boundary value problem anew (e.g. by shooting). In fact, ignoring for the moment the gravitational part, as it does not influence the procedure for the density-density and current-current spectral functions we are interested in, we have from linear-response theory without the double-trace deformation

$$
\delta \left\langle J^\mu \right\rangle = G^{\mu\nu} a^{\mathrm{s}}_\nu = G^{\mu\nu} a^{(0)}_\nu \ .
\tag{2.28}
$$

Since the bulk theory is left unchanged by the deformation, the Maxwell-field fluctuations a_μ satisfies the same linearized equations of motion with the same near-boundary behavior, the only difference is that now we interpret the leading-order coefficient $a^{(0)}_\nu$

not as the source alone but according to the right-hand side of Eq. (2.27). In terms of the source a^{s}_{μ} in the presence of a double-trace deformation, expression (2.28) now becomes

$$\delta \langle J^{\mu} \rangle = G^{\mu\nu} \left(a^{\mathrm{s}}_{\nu} - \alpha^2 V_{\nu\sigma} \delta \langle J^{\sigma} \rangle \right) \ , \tag{2.29}$$

where for convenience we defined $V_{\mu\nu} = (\eta_{\mu\nu} - (1-\xi)k_{\mu}k_{\nu}/k^2)/k^2$. Rearranging the equation in order to put it into the form $\delta \langle J^{\mu} \rangle = \chi^{\mu\nu} a^{\mathrm{s}}_{\nu}$ to extract the response function $\chi^{\mu\nu}$ we have that

$$\left(\delta^{\mu}_{\sigma} + \alpha^2 G^{\mu\nu} V_{\nu\sigma} \right) \delta \langle J^{\sigma} \rangle = G^{\mu\nu} a^{\mathrm{s}}_{\nu} \ , \tag{2.30}$$

and we see that the response function assumes the RPA-like form

$$\chi = \left(I + \alpha^2 G V \right)^{-1} G \ . \tag{2.31}$$

Explicitly, introducing Π by means of

$$G(\omega, \boldsymbol{k}) = \begin{pmatrix} \boldsymbol{k}^2 \Pi(\omega, \boldsymbol{k}) & \omega \boldsymbol{k} \Pi(\omega, \boldsymbol{k}) \\ \omega \boldsymbol{k} \Pi(\omega, \boldsymbol{k}) & \omega^2 \Pi(\omega, \boldsymbol{k}) \end{pmatrix} \ , \tag{2.32}$$

we obtain

$$\chi(\omega, \boldsymbol{k}) =$$
$$\left[\begin{pmatrix} 1 & 0 \\ 0 & 1 \end{pmatrix} + \frac{\alpha^2}{-\omega^2 + \boldsymbol{k}^2} \begin{pmatrix} \boldsymbol{k}^2 \Pi & \omega \boldsymbol{k} \Pi \\ \omega \boldsymbol{k} \Pi & \omega^2 \Pi \end{pmatrix} \begin{pmatrix} -1 - (1-\xi) \frac{\omega^2}{-\omega^2 + \boldsymbol{k}^2} & (1-\xi) \frac{\omega \boldsymbol{k}}{-\omega^2 + \boldsymbol{k}^2} \\ (1-\xi) \frac{\omega \boldsymbol{k}}{-\omega^2 + \boldsymbol{k}^2} & 1 - (1-\xi) \frac{\boldsymbol{k}^2}{-\omega^2 + \boldsymbol{k}^2} \end{pmatrix} \right]^{-1}$$

$$\cdot \begin{pmatrix} \boldsymbol{k}^2 \Pi & \omega \boldsymbol{k} \Pi \\ \omega \boldsymbol{k} \Pi & \omega^2 \Pi \end{pmatrix} = \frac{1}{1 - \alpha^2 \Pi(\omega, \boldsymbol{k})} \begin{pmatrix} \boldsymbol{k}^2 \Pi(\omega, \boldsymbol{k}) & \omega \boldsymbol{k} \Pi(\omega, \boldsymbol{k}) \\ \omega \boldsymbol{k} \Pi(\omega, \boldsymbol{k}) & \omega^2 \Pi(\omega, \boldsymbol{k}) \end{pmatrix} \ , \tag{2.33}$$

that is of course independent of the gauge-choice parameter ξ. In particular, we can see that the density-density response function is

$$\chi^{00}(\omega, \boldsymbol{k}) = \frac{\boldsymbol{k}^2 \Pi(\omega, \boldsymbol{k})}{1 - \alpha^2 \Pi(\omega, \boldsymbol{k})} = \frac{G^{00}(\omega, \boldsymbol{k})}{1 - \frac{\alpha^2}{\boldsymbol{k}^2} G^{00}(\omega, \boldsymbol{k})} \ , \tag{2.34}$$

as expected from RPA calculations.

From relativistic hydrodynamics we know that in the low-energy limit G^{00} assumes the form ([83])

$$G^{00}(\omega, \boldsymbol{k}) \simeq \frac{\langle\rho\rangle^2}{\langle\epsilon\rangle + \langle P\rangle} \frac{\boldsymbol{k}^2}{\omega^2 - \boldsymbol{k}^2 v_s^2} \qquad \text{for} \quad \omega \gtrsim \boldsymbol{k} \ , \tag{2.35}$$

with the equilibrium quantities defined in Eqs. (2.12)-(2.14), and v_s^2 the speed of sound squared $v_s^2 = \partial P/\partial\epsilon = 1/(d-1)$. This suggest that the RPA-like response function in Eq. (2.34) contains a gapped plasmon mode, with the plasma frequency determined by

$$\omega_p^2 = \alpha^2 \frac{(d-1)\,\langle\rho\rangle^2}{d\,\langle\epsilon\rangle} = \alpha^2 \lim_{\omega\to 0} G^{xx}(\omega, \boldsymbol{k} = \boldsymbol{0}) \ . \tag{2.36}$$

In figure 2.3, we show side by side the density-density spectral function with and without double-trace deformation, for two different values of the parameter T/μ, where we see that the linear sound modes turn into a gapped plasmon mode. The dashed black line represent the hydrodynamic approximation of the plasmon mode from Eq. (2.35). We can think of higher values of T/μ as moving towards the zero chemical potential limit, where there is no plasmon mode. By comparing the two figures we can indeed observe that for higher values of T/μ the low-energy gapped mode becomes less visible in the spectral function. This can be seen in more details by comparing with figure 2.4, where we show some slices of the spectral function for different fixed values of momentum $|\boldsymbol{k}|/\mu$. Here we also notice that the height of the peak of the plasmon modes is lower than the corresponding peak in the Reissner-Nordström solution. This is due to the screening effect of the charged particles that opposes density fluctuations. Moreover, we see that the plasmon peak initially increases as we move to smaller values of $|\boldsymbol{k}|/\mu$, as was the case for the linear modes, but it then starts to decrease for small value of $|\boldsymbol{k}|/\mu$, due to the $\boldsymbol{k}^2$ factor in the low-energy limit of the density-density spectral function. Even though in this paper we mainly focus on the density-density response, the plasmon modes are of course also present in the current-current spectral function as we show in figure 2.5. Here the plasmon mode is more easily visible as there is no $\boldsymbol{k}^2$ suppression, since from Ward's identities we know that $\boldsymbol{k}^2 G^{xx} = \omega^2 G^{00}$.

This gapped plasmon mode is observed in $(3+1)$-dimensional metals, however, in an experimental $(2+1)$-dimensional system we expect to find plasmon modes of the form $\omega \propto \sqrt{|\boldsymbol{k}|}$. Notice that the expression for the RPA-like correction to the response function in Eq. (2.34) has been derived in an arbitrary spacetime dimension and it

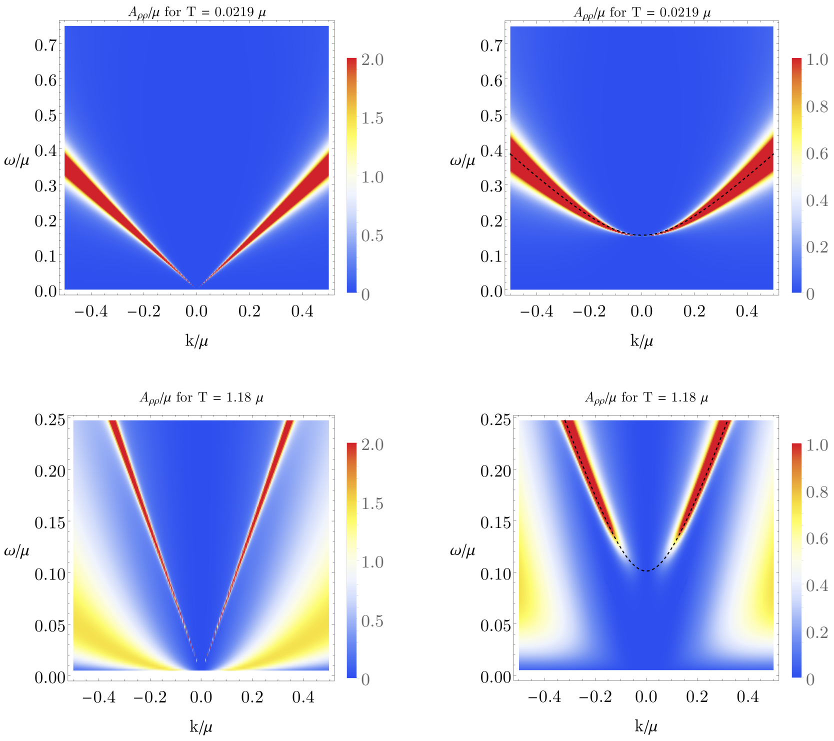

Figure 2.3: The density spectral function for $T \simeq 0.02\mu$ (top) and $T \simeq 1.18\mu$ (bottom) without (left) and with (right) double-trace deformation. Here we have taken $\alpha^2 = 1/25$. The black dashed line represents the plasmon modes computed in the hydrodynamic approximation. We see that the double-trace deformation turns the low-energy sound modes into a gapped plasmon mode, although the low-energy excitation are less visible as the height of the peak for low $|\boldsymbol{k}|/\mu$ becomes smaller for higher values of T/μ.

is independent of the value of d. This implies that in any dimension, the qualitative behavior of the spectral function looks the same as the one in figure 2.3, although the position and residue of the poles of course change. In the next section we show how to modify the double-trace deformation to, from an experimental point of view, correctly describe plasmon modes in $(2+1)$-dimensional systems.

2.4 Plasmon modes in $d = 2 + 1$

As already noted in ref. [46], the presence of a gapped mode is due to the fact that in the holographic theory of a $(2+1)$-dimensional model, we also constrain the boundary dynamical photons to live in $2 + 1$ dimensions, while in layered materials studied

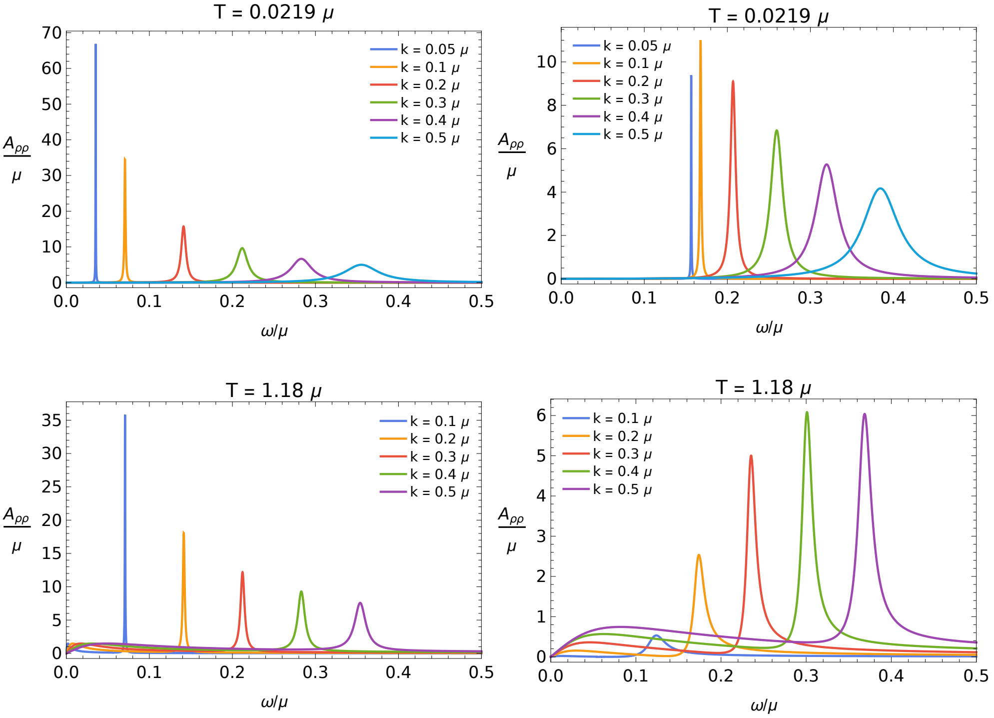

Figure 2.4: The density spectral function for $T \simeq 0.02\mu$ (top) and $T \simeq 1.18\mu$ (bottom) without (left) and with (right) double-trace deformation for different values of k/μ ($\alpha^2 = 1/25$). We see that the height of the peak of the plasmon modes is lower than in the corresponding sound modes due to screening of the charged particles. Moreover we observe that for low momenta, the peak in the RPA response function decreases as we move towards smaller values of $|\boldsymbol{k}|/\mu$.

in laboratories, the current is constrained on the $(2+1)$-dimensional layer, but the photons are free to move in all the spacetime dimensions, giving rise to an effective Coulomb potential $V(\boldsymbol{k}) \propto 1/|\boldsymbol{k}|$. Put differently, the Coulomb potential between charges at positions $\boldsymbol{x}$ and $\boldsymbol{x}'$ behaves as $1/|\boldsymbol{x} - \boldsymbol{x}'|$ and not as $\log|\boldsymbol{x} - \boldsymbol{x}'|$.

2.4.1 Single Layer

In order to model a more realistic $(2+1)$-dimensional system, where photons that mediate the Coulomb interaction are free to move in the whole three-dimensional space, we consider a $d = 2 + 1$ boundary theory, dual to the $(d+1)$-dimensional bulk theory from Eq. (2.6), but we define the deformation of the boundary theory by starting from a $(d+1)$-dimensional boundary term. Defining the $(d+1)$-dimensional

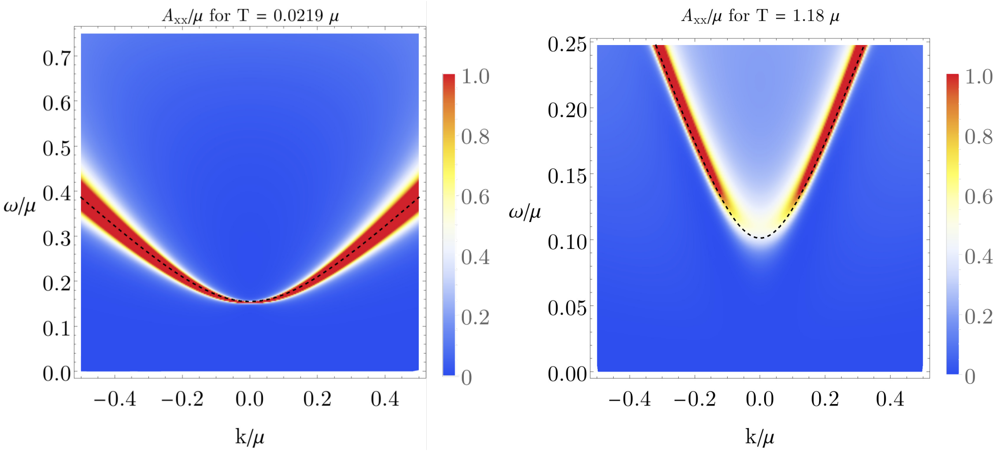

Figure 2.5: The current spectral function for $T \simeq 0.02\mu$ (left) and $T \simeq 1.18\mu$ (right) with a double-trace deformation ($\alpha^2 = 1/25$). Here we can clearly see the gapped plasmon mode, as the height of the peak does not go to zero as $\boldsymbol{k} \to \boldsymbol{0}$.

vector (x, z) and momentum (k, k_z), with x and k living in d spacetime dimensions while z and k_z represent the extra spatial dimension normal to the layer and the associated momentum respectively, we restrict the current operator to a plane as

$$\begin{cases} J^\mu(x,z) = J^\mu(x)\delta(z), \quad \mu = 0, \dots, d-1 \\ J^z(x,z) = 0 \end{cases} . \tag{2.37}$$

Inserting this expression into Eq. (2.25), Fourier transforming and performing the Gaussian integral over the Maxwell field we obtain

$$S_{\mathrm{M}} = -\frac{1}{2}\int \frac{\mathrm{d}^d k}{(2\pi)^d}\int \frac{\mathrm{d}k_z}{2\pi}\,\alpha^2 \left(\langle J^\mu(k)\rangle \frac{\eta_{\mu\nu}}{k^2+k_z^2} \langle J^\nu(-k)\rangle \right) , \tag{2.38}$$

that can be integrated over k_z to obtain the d-dimensional boundary deformation

$$-\frac{1}{2}\int \frac{\mathrm{d}^d k}{(2\pi)^d}\frac{\alpha^2}{2} \left(\langle J^\mu(\omega,\boldsymbol{k})\rangle \frac{\eta_{\mu\nu}}{\sqrt{-\omega^2+\boldsymbol{k}^2}} \langle J^\nu(-\omega,-\boldsymbol{k})\rangle \right) \qquad \text{for } \boldsymbol{k}^2 > \omega^2 . \tag{2.39}$$

This in particular implies that the response function now takes the form:

$$\chi(\omega,\boldsymbol{k}) = \frac{1}{1-\frac{\alpha^2}{2}\sqrt{-\omega^2+\boldsymbol{k}^2}\Pi(\omega,\boldsymbol{k})} \begin{pmatrix} \boldsymbol{k}^2\Pi(\omega,\boldsymbol{k}) & \omega\boldsymbol{k}\Pi(\omega,\boldsymbol{k}) \\ \omega\boldsymbol{k}\Pi(\omega,\boldsymbol{k}) & \omega^2\Pi(\omega,\boldsymbol{k}) \end{pmatrix} . \tag{2.40}$$

However, we are ultimately interested in describing condensed-matter systems, where the Fermi velocity is considerably smaller than the speed of light, so $v_F \ll c$ and we look into a regime where $|\boldsymbol{k}| \gg \omega$ in Eq. (2.40). As a result, the density-density response function is well approximated by the familiar form

$$\chi^{00}(\omega, \boldsymbol{k}) = \frac{G^{00}(\omega, \boldsymbol{k})}{1 - \frac{\alpha^2}{2|\boldsymbol{k}|} G^{00}(\omega, \boldsymbol{k})} \ , \tag{2.41}$$

that is expressed in terms of the static Coulomb potential expected in two-dimensional metals. Notice that the coupling constant for the single layer is $\alpha^2/2$, in accordance with Eq. (2.2).

In figure 2.6 we see, for two different values of T/μ, how this form of the potential does indeed give rise to $\omega \propto \sqrt{|\boldsymbol{k}|}$ modes observed in a (spatially) two-dimensional system such as graphene [93]. As before, the black dashed lines show the hydrodynamic plasmon modes

$$\omega_p^2 = \frac{\alpha^2}{2} \frac{2 \langle \rho \rangle^2}{3 \langle \epsilon \rangle} |\boldsymbol{k}| \ . \tag{2.42}$$

In figure 2.7, we observe the momentum dependence of the peak for $T \simeq 0.02\mu$, where again we notice that the height of the peak in the charged system is less pronounced with respect to the one in the Reissner-Nordström solution, due to the screening effect of charged particles. Furthermore, in figure 2.8, we study the temperature dependence of this mode for a fixed value of $|\boldsymbol{k}|/\mu$. In the Reissner-Nordström solution, the position of the peak for low enough momenta is independent of the temperature and given by the speed of sound $\omega = v_s|\boldsymbol{k}| = |\boldsymbol{k}|/\sqrt{2}$. In contrast, when we introduce Coulomb interactions we can see that, while the peak still gets sharper and the height increases as we lower the temperature, the position of the peak is temperature dependent. For high temperatures, as the temperature is raised the mode shifts towards the position of the peak of the neutral solution ($\omega/\mu \simeq 0.035$ for $|\boldsymbol{k}|/\mu = 0.05$), since temperature fluctuations start to dominate over the effect of Coulomb interactions. As we decrease the temperature, however, while the peak initially shifts to higher frequencies, it reaches a maximum frequency for $T/\mu = 1/2\pi$ (purple line in the plots) before starting to move back on the frequency axis as we further lower the temperature. This behavior is in accordance with the hydrodynamic prediction for the plasma frequency in Eq. (2.42). In figure 2.9 we show the temperature dependence of this hydrodynamic prediction in the grand-canonical ensemble, that is given by the temperature dependence of the thermodynamic quantities in Eqs. (2.12)-(2.14). The green line includes the higher-order correction expressed in terms of the temperature-independent sound velocity $v_s = 1/\sqrt{2}$

$$\omega_p^2 = \frac{\alpha^2}{2}\frac{2\left\langle\rho\right\rangle^2}{3\left\langle\epsilon\right\rangle}|\boldsymbol{k}| + v_s^2\boldsymbol{k}^2 \ . \tag{2.43}$$

The hydrodynamic plasma frequency shows a maximum at $T/\mu = 1/2\pi$, given by

$$\omega_p = \sqrt{\frac{\alpha^2}{3}|\boldsymbol{k}|\mu + \frac{\boldsymbol{k}^2}{2}} \ , \tag{2.44}$$

that, for $\alpha^2/2 = 1/10$ and $|\boldsymbol{k}| = \mu/100$, gives $\omega_p \simeq 0.0268\mu$, in agreement with the holographic results shown in figure 2.8. On the other hand, as $T/\mu \to \infty$, $\left\langle\rho\right\rangle^2/\left\langle\epsilon\right\rangle \to 0$ and we recover the sound dispersion.

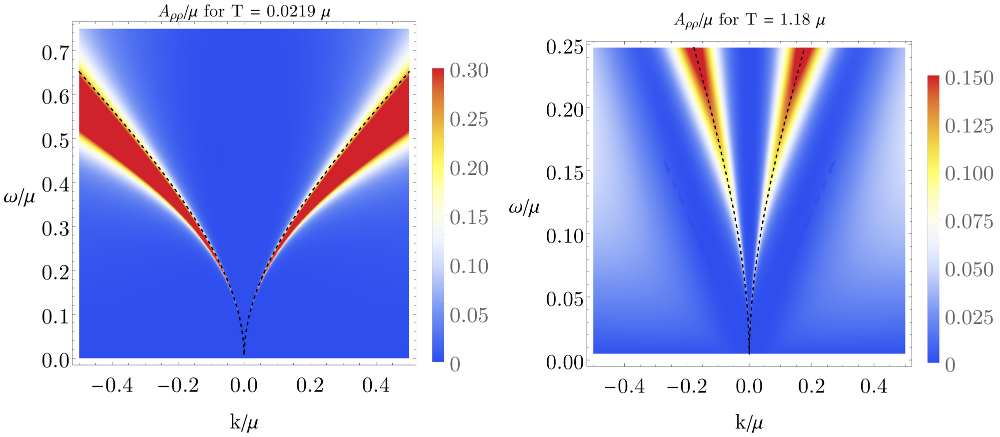

Figure 2.6: The density spectral function for $T \simeq 0.02\mu$ (left) and $T \simeq 1.2\mu$ (right). We have taken $\alpha^2/2 = 1$. Here we see that the sound modes from the Reissner-Nordström solution turn into $\omega \propto \sqrt{|\boldsymbol{k}|}$ modes at low energies. The dashed black line represent the hydrodynamic solution for the dispersion relation $\omega^2 = 2\left\langle\rho\right\rangle^2|\boldsymbol{k}|/3\left\langle\epsilon\right\rangle$

2.4.2 Layered system

In a similar fashion to what we did in the last section, we present here a toy model for an infinite stack of $(2+1)$-dimensional layers. We show that we recover the form of the Coulomb potential for a layered electron gas [122, 35], and we present the density spectral function for a double-trace deformation of this form. The latter shows a dispersion relation for the low-energy plasmon excitations that changes from linear to

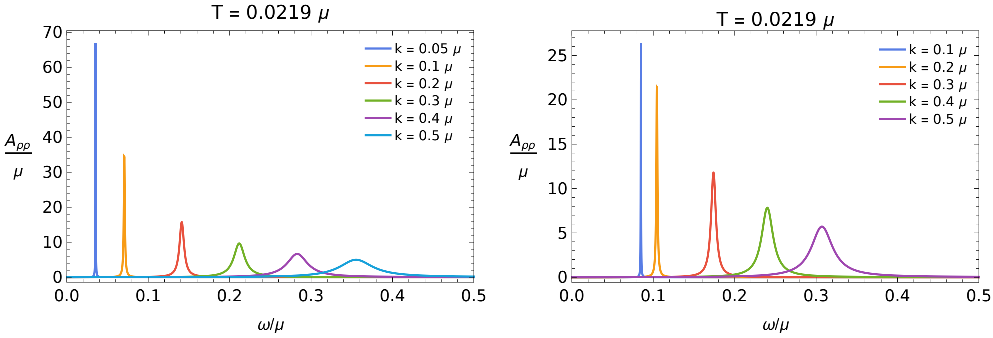

Figure 2.7: The density spectral function for different values of $|\boldsymbol{k}|/\mu$ in the Reissner-Nordström solution (left) and with Coulomb corrections (right). We see that due to screening in the charged system the plasmon peaks shift towards higher frequencies and are lower in height than the corresponding peak of the sound mode.

a gapped mode as a function of Bloch momentum p in the direction perpendicular to the layers. This behavior of the plasmon modes has very recently been observed in high-temperature cuprate superconductors consisting of stacked conducting copper-oxide layers [59].

For our toy model, we make the approximation that there are both strong in-plane short-range interactions and a long-range Coulomb interaction that couples the different layers. We, therefore, model each single layer as an independent $d = 2 + 1$ boundary system dual to the $3 + 1$ Reissner-Nordström bulk theory, but we define a $(3 + 1)$-dimensional current as

$$\begin{cases} J^\mu(x,z) = \sum_n J^\mu(x,z)\delta(z - n\ell), & \mu = 0,\dots,d-1 \\ J^z(x,z) = 0 \end{cases}, \tag{2.45}$$

with $n \in \mathbb{Z}$ the layer index. The layers are stacked along the z axis with ℓ the distance between each layer, and $J^\mu(x, n\ell)$ is the boundary operator computed from holographic calculations with sources $a_n^{(0)}$ not necessarily equal to each other.

Using Eq. (2.45) into the boundary deformation in Eq. (2.25) and choosing the gauge $\xi = 1$ for convenience, we obtain the action

$$\int \mathrm{d}^d x \int \mathrm{d}z \left(\frac{1}{2\alpha^2} A_\mu(x,z) \left[\eta^{\mu\nu}\partial^2\right] A_\nu(x,z) - \sum_n A_\mu(x,z) \left\langle J^\mu(x,z) \right\rangle \delta(z - n\ell) \right), \tag{2.46}$$

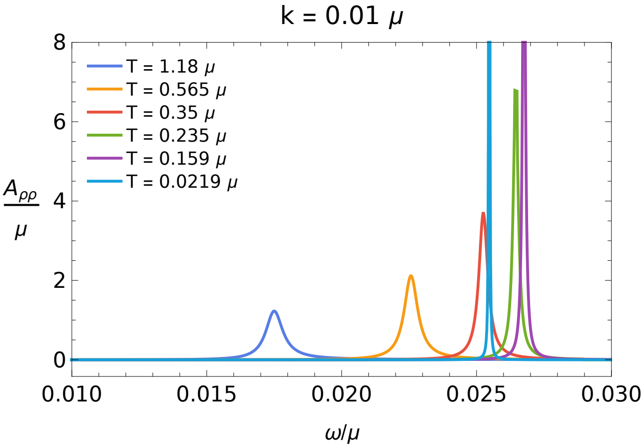

Figure 2.8: Temperature dependence of the plasmon mode for $|\boldsymbol{k}|/\mu = 0.01$ and $\alpha^2/2 = 1/10$. We see that the peaks become less pronounced as we raise the temperature due to the effect of temperature fluctuations. Moreover, for high temperatures, the position of the plasmon mode shifts towards the position of the sound mode in the neutral system, as temperature fluctuations start dominating over the Coulomb interaction. As we lower the temperature we see that the plasma frequency reaches a maximum at $T/\mu = 1/2\pi$ (purple), before moving to lower values as the temperature is decreased further.

with $\mu = 0, \ldots, d-1$, and we have integrated out $A_z(x, z)$. Fourier transforming and integrating out the Maxwell field, we obtain

$$-\frac{\alpha^2}{2} \int \frac{\mathrm{d}^d k}{(2\pi)^d} \int \frac{\mathrm{d}k_z}{2\pi} \left(\sum_{n,m} \langle J^\mu(-k, n\ell) \rangle \, \eta_{\mu\nu} \frac{e^{-ik_z(n-m)\ell}}{k^2 + k_z^2} \langle J^\nu(k, m\ell) \rangle \right) . \tag{2.47}$$

We can next perform the integral over the momentum k_z and further Fourier transform

$$J^\mu(k, n\ell) = \frac{\ell}{2\pi} \int_{-\pi/\ell}^{\pi/\ell} \mathrm{d}p \, J^\mu(k, p) e^{ipn\ell} \ ,$$

so that we can then sum over the layer indices to obtain the desired double-trace deformation (see appendix 2.B for the detailed computation)

$$-\frac{\alpha^2}{2} \int \frac{\mathrm{d}^d k}{(2\pi)^d} \int_{-\pi/\ell}^{\pi/\ell} \frac{\mathrm{d}p}{2\pi} \langle J^\mu(-k, -p) \rangle \, \eta_{\mu\nu} \frac{\ell}{2|k|} \frac{\sinh(|k|\ell)}{\cosh(|k|\ell) - \cos(p\ell)} \langle J^\nu(k, p) \rangle \ , \tag{2.48}$$

that gives the Coulomb potential for a layered electron gas. Notice that when the layer sources are in phase, i.e., $\cos(p\ell) = 1$, we recover the potential for a (3+1)-dimensional

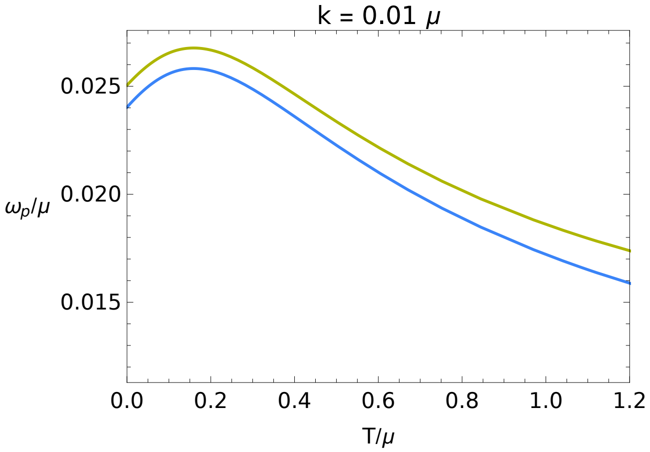

Figure 2.9: Temperature dependence of the hydrodynamic plasma frequency for $|\boldsymbol{k}|/\mu = 0.01$ and $\alpha^2/2 = 1/10$, with (green) and without (blue) a higher-order momentum correction $v_s^2\boldsymbol{k}^2$. We see that the plasma frequency has a maximum at $T/\mu = 1/2\pi$, corresponding to $\omega_p \simeq 0.0268\mu$.

system proportional to $1/k^2$ for $|k| \ll 1$ and ℓ such that $|k|\ell \ll 1$, since

$$\frac{\ell}{2|k|}\frac{\sinh\left(|k|\ell\right)}{\cosh\left(|k|\ell\right)-1} = \frac{1}{k^2} + \mathcal{O}(\ell^2)\ . \tag{2.49}$$

The spectral function then contains, for $p\ell = 0$, a gapped plasmon mode, as it is shown in figure 2.10a, where we plot the density spectral function at $T \simeq 0.02\mu$ for a Reissner-Nordström solution with a double-trace deformation of the form of Eq. (2.48). However, as the only coupling between the layers is due to the Coulomb interaction, the Green's functions of each single layer without the double-trace deformation contain linear modes typical of a $(2+1)$-dimensional system and with a dispersion $\omega = |\boldsymbol{k}|/\sqrt{2}$ for low energies, and the resulting gapped mode is therefore different from the one in a $(3+1)$-dimensional material with the same characteristics. On the other hand for any $\cos(p\ell) \neq 0$ we can distinguish three different regimes. For $|k|\ell \ll |\cos(p\ell)|$ we obtain a constant potential

$$\frac{\ell}{2|k|}\frac{\sinh\left(|k|\ell\right)}{\cosh\left(|k|\ell\right)-\cos(p\ell)} = \frac{\ell^2/2}{1-\cos(p\ell)} + \mathcal{O}\left(|k|^2\ell^4\right)\ . \tag{2.50}$$

In the Reissner-Nordström system with a linear low-energy dispersion relation, this has the effect of renormalizing the speed of these sound modes. However, for $|\cos(p\ell)| \ll |k|\ell \ll 1$, we recover the $1/k^2$ potential. Finally, for $|k|\ell \gg 1$ we obtain a $\ell/2|k|$

potential. As for the $(2+1)$-dimensional case, in condensed-matter systems we are interested in the limit where ω in the potential satisfies $\omega \ll |\boldsymbol{k}|$ as it is suppressed by a factor of $v_{\mathrm{F}}/c \ll 1$, with v_{F} the Fermi velocity. In this limit, the latter potential gives rise to a dispersion relation $\omega \propto \sqrt{|\boldsymbol{k}|}$. This behavior can be seen in figures 2.10b-2.10d. In particular, by looking at the hydrodynamic approximation

$$G^{00}(\omega, \boldsymbol{k}) \simeq \frac{2\left<\rho\right>^2}{3\left<\epsilon\right>}\frac{\boldsymbol{k}^2/\ell}{\omega^2 - \boldsymbol{k}^2 v_s^2} \qquad \text{for} \qquad \omega \gtrsim \boldsymbol{k}\ , \tag{2.51}$$

we can see that, by introducing a double-trace deformation as in Eq. (2.48), we obtain a response function

$$\chi(\omega, \boldsymbol{k}) = \frac{\boldsymbol{k}^2/\ell}{\omega^2 - v_s^2\boldsymbol{k}^2 - \frac{\alpha^2}{2|\boldsymbol{k}|}\left(\frac{2\left<\rho\right>^2}{3\left<\epsilon\right>}\right)\frac{\sinh(|\boldsymbol{k}|\ell)}{\cosh\left(|\boldsymbol{k}|\ell\right) - cos(p\ell)}\boldsymbol{k}^2}\ , \tag{2.52}$$

whose poles are shown in figure 2.11 for several value of $p\ell$, from $p\ell = 0$, that gives the gapped plasmon mode, to $p\ell = \pi$ that leads to the lowest speed of sound, since in the hydrodynamic limit the renormalized speed of sound is given by

$$\tilde{v}_s^2 = \frac{1}{2} + \frac{\alpha^2}{2}\left(\frac{2\left<\rho\right>^2}{3\left<\epsilon\right>}\right)\frac{\ell}{1 - \cos p\ell}\ . \tag{2.53}$$

In figures 2.10a-2.10d we see that the low-energy behavior of the acoustic plasmon modes is well described by the hydrodynamics approximation (shown as a black dashed line). As we move to higher frequencies, however, we observe a discrepancy between the holographic result and the hydrodynamic approximation. This is not unexpected as hydrodynamics is only a long-wavelength theory.

2.5 Plasmons in $3+1$ dimensions and conductivity

In this section we apply the double-trace deformation to the holographic calculation of the $(3+1)$-dimensional optical conductivity in the Reissner-Nordström metal. Although it would seem straightforward to extend the results of the previous section to a $(3+1)$-dimensional model, there is an important subtlety as, in all even boundary dimensions, the theory contains a logarithmic divergence that introduces a scale into the theory that needs to be determined experimentally. Without a double-trace deformation this scale only enters the real part of the Green's functions, and it, therefore, does not modify the spectral functions. However, when introducing the double-trace

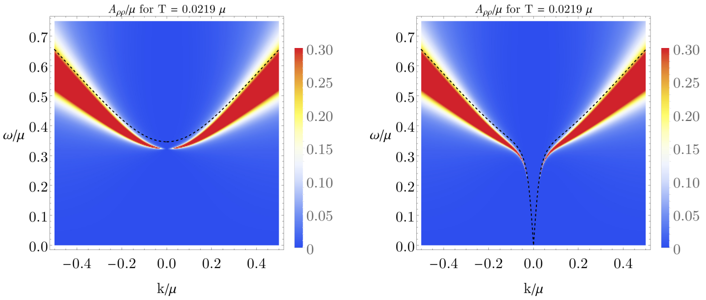

(a) $p\ell = 0$ **(b)** $p\ell = \pi/10$

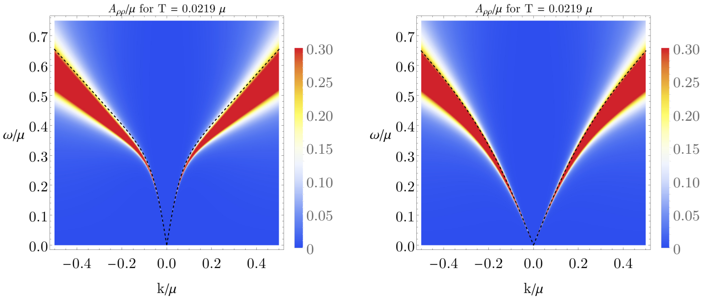

(c) $p\ell = \pi/4$ **(d)** $p\ell = \pi$

Figure 2.10: The density spectral function for a layered system at $T \simeq 0.02\mu$. When the sources are in phase (a), i.e., $\cos(p\ell) = 1$, we recover the gapped mode of $(3+1)$-dimensional materials. However, if the sources are out of phase, for $k\ell \ll |\cos(p\ell)|$ the dispersion relation is linear. We can also observe that for $|\cos(p\ell)| \ll k\ell \ll 1$, we recover the quadratic modes (b). For $k\ell \gg 1$ we instead recover the dispersion relation $\omega \propto \sqrt{|\boldsymbol{k}|}$, as more noticeable in (c)-(d). The black dashed line represent the plasmon modes computed in the hydrodynamic approximation. In all the plots we used $\alpha^2 = 1$ and $\ell = 10$.

deformation the scale affects the imaginary part of the Green's functions as well, and can be observed in the spectral function, or equivalently, in the real part of the (longitudinal) conductivity. We show that this gives rise to a form of the conductivity that resembles the one measured in Weyl and Dirac semimetals.

2.5.1 Renormalization and anomaly

In order to study the properties of the boundary theory we need to regularize the divergences of the boundary action. The necessary counterterms depend on the spacetime dimension of the theory, and for the gravitational part of the action they are treated in detail in ref. [27] up to $d = 6$.

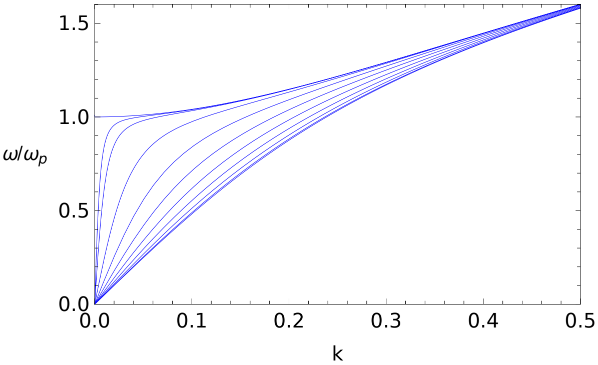

Figure 2.11: Effect of the double-trace deformation for a layered system on a response function with low-energy sound modes. For $p\ell = 0$ we obtain a gapped plasmon mode, while for any value of $p\ell \in (0, \pi]$ the low-energy dispersion relation is linear, with $p\ell = \pi$ having the lowest speed. The plot shows the plasmon dispersion for $p\ell = \{0, \pi/50, \pi/25, n\pi/8\}$, with $n \in [1, 8]$ an integer.

In the case of $d = 2 + 1$ treated above, the Maxwell term is finite as $r \to \infty$, and the only UV divergence comes from the gravitational part that we regularized by adding the counterterm in Eq. (2.11). More interesting, however, is the case of even boundary spacetime dimension, as the $3 + 1$-dimensional system we are interested in. The asymptotic expansion of the fields as $r \to \infty$ is

$$\begin{aligned} h_{\mu\nu} \to & r^2 \left(h^{(0)}_{\mu\nu} + h^{(2)}_{\mu\nu} r^{-2} + \cdots + h^{(d)}_{\mu\nu} r^{-d} + \mathrm{h}_{\mu\nu} r^{-d} \log\left(r/|k|\right) + \mathcal{O}(r^{-d-2}\log r) \right) \\ a_\mu \to & a^{(0)}_\mu + a^{(2)}_\mu r^{-2} + \cdots + a^{(d-2)}_\mu r^{-d+2} + \mathrm{a}_\mu r^{-d+2} \log\left(r/|k|\right) + \mathcal{O}(r^{-d}\log r) \ , \end{aligned} \tag{2.54}$$

where the expansion coefficients are functions of k, and the logarithmic terms only appear in even dimensions. All the higher-order coefficients as well as the coefficient of the logarithmic term are local functions of the leading-order coefficients $a^{(0)}_\mu$ and $h^{(0)}_{\mu\nu}$ and can be determined by a near-boundary analysis. The exceptions are the coefficients related to the field theory response, $h^{(d)}_{\mu\nu}$ and $a^{(d-2)}_\mu$ in the present case, that require the full solution of the linearized equations of motion.[1] In $d = 3 + 1$, we see that in addition to the divergence regulated by the counterterm in (2.11), both the Maxwell and the gravitational field then present a logarithmic divergence, related to

---

[1] In the asymptotic expansion in Eq. (2.54) it is usually convention to include all the momentum dependence in the coefficients, hence to adsorb the $\log(1/|k|)$ term into the coefficient with the same power of r. However, here we keep the momentum dependence in the term $\log(r/|k|)$, as it makes the following argument more clear.

the conformal anomaly of the boundary theory [118].

As we show below, the regularization of the logarithm introduce a renormalization scale, $k_{\rm UV}$, that cannot be determined from the theory but enters as an experimental parameter. Since we are mostly interested in studying the density-density response function, here we focus on the logarithmic term coming from the expansion of the Maxwell field. The case of the metric field is analogous. The boundary term relevant for the $\langle J^\mu J^\nu\rangle$ correlation functions is

$$\delta S^{(2)}_{A,bdy} = -\lim_{r_{\rm UV}\to\infty}\frac{1}{2}\int_{r=r_{\rm UV}} \mathrm{d}^d x\,\sqrt{-\gamma}n^\mu\gamma^{\nu\sigma}a_\sigma\partial_\mu a_\nu\ . \tag{2.55}$$

Inserting the asymptotic expansion of Eq. (2.54) in $d=3+1$, and the expressions for the induced boundary metric and the vector normal to the boundary, we obtain

$$\delta S^{(2)}_{A,bdy} = -\lim_{r_{\rm UV}\to\infty}\frac{1}{2}\int_{r=r_{\rm UV}} \mathrm{d}^4 x\,\eta^{\nu\sigma}a^{(0)}_\sigma\left(-2a^{(2)}_\nu + \mathrm{a}_\nu - 2\mathrm{a}_\nu\log\left(r/|k|\right)\right)\ . \tag{2.56}$$

So, in order to take the limit we need to regularize the logarithmic divergence. This can be done by inserting a scale-dependent counterterm

$$S_{c.t.} = -\frac{\log(r_{\rm UV}/\tilde{k}_{\rm UV})}{4}\int_{r=r_{\rm UV}} \mathrm{d}^d x\,\sqrt{-\gamma}F_{\mu\nu}F^{\mu\nu} \tag{2.57}$$

that gives us the regularized boundary term

$$\delta S^{(2)}_{A,bdy} = \frac{1}{2}\int \mathrm{d}^4 x\,\eta^{\nu\sigma}a^{(0)}_\sigma 2\left[a^{(2)}_\nu + \mathrm{a}_\nu\log\left(\frac{k_{\rm UV}}{|k|}\right)\right]\ , \tag{2.58}$$

where we defined $k_{\rm UV} = \tilde{k}_{\rm UV}\sqrt{e}$. We, therefore, see that the response of the current operator to small fluctuations depends on the choice of scale:

$$\delta\left\langle J^\mu\right\rangle = \frac{\delta S^{(2)}_{A,bdy}}{\delta a^{(0)}_\mu} = 2\eta^{\mu\nu}\left[a^{(2)}_\nu + \mathrm{a}_\nu\log\left(\frac{k_{\rm UV}}{|k|}\right)\right]\ . \tag{2.59}$$

The coefficients a_ν can be expressed in terms of the source term by matching coefficients in a near-boundary expansion, and we obtain

$$\begin{aligned}\mathrm{a}_0 &= -\frac{|\boldsymbol{k}|}{2}(\omega a^{(0)}_x + |\boldsymbol{k}|a^{(0)}_0)\ ,\\ \mathrm{a}_x &= \frac{\omega}{2}(\omega a^{(0)}_x + |\boldsymbol{k}|a^{(0)}_0)\ .\end{aligned} \tag{2.60}$$

This implies that the dependence of the Maxwell Green's functions on the renormalization scale k_{UV} appears in a purely real term

$$G^{\mu\nu} = \widetilde{G}^{\mu\nu} - k^{\mu}k^{\nu}\log\left(\frac{k_{\text{UV}}}{|k|}\right) \;, \tag{2.61}$$

were we denoted with $\widetilde{G}^{\mu\nu}$ the part of the Green's functions independent of k_{UV}. The logarithmic correction is thus not visible in the spectral function, nor in the real part of the conductivity. However, due to the form of the RPA-like response function in Eq. (2.33), this is not the case anymore when we introduce the double-trace deformation, and the scale-dependent term can also be observed in the real part of the optical conductivity

$$\sigma(\omega) = \frac{\chi^{xx}(\omega, \boldsymbol{k} = \boldsymbol{0})}{-i\omega} \;. \tag{2.62}$$

In particular for $\boldsymbol{k} = \boldsymbol{0}$, the a_x fluctuations decouples from all the others, and the current-current Green's function takes the form

$$G^{xx}(\omega, \boldsymbol{k} = \boldsymbol{0}) = -\frac{2a_x^{(2)}(\omega)}{a_x^{(0)}(\omega)} - \omega^2\log\left(\frac{\omega_{\text{UV}}}{|\omega|}\right) \equiv \widetilde{G}^{xx}(\omega, \boldsymbol{k} = \boldsymbol{0}) - \omega^2\log\left(\frac{\omega_{\text{UV}}}{|\omega|}\right) \;, \tag{2.63}$$

and, as mentioned previously, for the neutral system the scale-dependent logarithm only affects the imaginary part of the optical conductivity

$$\sigma_0(\omega) = \frac{\widetilde{G}^{xx}(\omega, \boldsymbol{k} = \boldsymbol{0})}{-i\omega} - i\omega\log\left(\frac{\omega_{\text{UV}}}{|\omega|}\right) \equiv \widetilde{\sigma}_0 - i\omega\log\left(\frac{\omega_{\text{UV}}}{|\omega|}\right) \;. \tag{2.64}$$

When we include the double-trace deformation we see from Eq. (2.29) that the optical conductivity for a system with Coulomb interactions becomes

$$\sigma(\omega) = \frac{\sigma_0(\omega)}{1 - \frac{\alpha^2}{i\omega}\sigma_0(\omega)} \;, \tag{2.65}$$

so that the real part of the conductivity now contains a signature of the scale-dependent logarithm

$$\text{Re}[\sigma(\omega)] = \frac{\text{Re}[\widetilde{\sigma}_0(\omega)]}{\left(1 - \frac{\alpha^2}{\omega}\text{Im}[\widetilde{\sigma}_0(\omega)] + \alpha^2\log\left(\omega_{\text{UV}}/|\omega|\right)\right)^2 + \frac{\alpha^2}{\omega}\text{Re}[\widetilde{\sigma}_0(\omega)]} \;. \tag{2.66}$$

This form of the conductivity, with a logarithmic term depending on a scale ω_{UV} to be determined experimentally, resembles the optical conductivity of Dirac and Weyl semimetals [115]. In the next sections, we give some explicit examples of conductivities in $3+1$ dimensions with the double-trace correction. In particular, in section 2.5.2 we compute the optical conductivity in pure AdS$_5$, without backreaction, that can be found analytically. In section 2.5.3 we instead study the effects of the double-trace deformation on the optical conductivity of the Reissner-Nordström metal.

2.5.2 Exact solution in AdS$_5$ background

In the simple case of a Maxwell action on a AdS$_5$ background without backreaction, which is the probe limit where the coupling constant $\lambda \to \infty$, we can compute the optical conductivity analytically. We use this example to show the importance of the logarithmic term in the optical conductivity when adding a double-trace deformation. In particular, we find that the optical conductivity in the neutral theory matches the results for a non-interacting Weyl or Dirac semimetal obtained from condensed-matter calculations [71, 72]. Inserting the deformation then gives us the optical conductivity expected from Weyl and Dirac semimetals with only long-range Coulomb interactions in the RPA approximation.

Since we consider the limit of no backreaction on the metric, we are only interested in the Maxwell action

$$S = -\frac{1}{4}\int \mathrm{d}^{d+1}\sqrt{-g}F_{\mu\nu}F^{\mu\nu} \ , \tag{2.67}$$

with the AdS background metric (we use the variable $\rho \equiv 1/r$ for notational convenience)

$$\mathrm{d}s^2 = \frac{1}{\rho^2}\left(\mathrm{d}\rho^2 + \eta_{\mu\nu}dx^\mu dx^\nu\right) \ . \tag{2.68}$$

The linearized equations of motion of the theory are solved, after fixing the momentum in the x direction, by

$$a_x(\omega,\boldsymbol{k}) = \begin{cases} C_1 J_{d/2-1}(-ik\rho) + C_2 Y_{d/2-1}(-ik\rho), & -\omega^2+\boldsymbol{k}^2>0 \\ \tilde{C}_1 H^{(1)}_{d/2-1}(\tilde{k}\rho) + \tilde{C}_2 H^{(2)}_{d/2-1}(\tilde{k}\rho), & -\omega^2+\boldsymbol{k}^2<0 \end{cases} , \tag{2.69}$$

with $\tilde{k} \equiv \sqrt{-(-\omega^2+\boldsymbol{k}^2)} \in \mathbb{R}$, and $H^{(1)}$ and $H^{(2)}$ are the Hankel functions of the first and second kind, respectively. From now on we focus on the case $-\omega^2 + \boldsymbol{k}^2 < 0$ as we are ultimately interested in the conductivity for $\boldsymbol{k} = \boldsymbol{0}$. The solution with $\tilde{C}_2 = 0$ correspond to the infalling boundary condition and can be used to compute the retarded Green's function. We thus set $\tilde{C}_2 = 0$ in the following.

For $d = 3 + 1$, we can then study the near boundary ($\rho \to 0$) behavior of the field fluctuations

$$a_x = \tilde{C}_1 \left(-\frac{2i}{\tilde{k}\pi} + \frac{\tilde{k}\rho^2}{2} + \frac{i\tilde{k}(2\gamma_{\text{E}} - 1)}{2\pi}\rho^2 + \frac{i\tilde{k}}{\pi} \log\left(\frac{\tilde{k}\rho}{2}\right)\rho^2 \right) \tag{2.70}$$

that shows the logarithmic term that gives rise to a divergence on the boundary, with $\gamma_{\text{E}} \simeq 0.577$ the Euler's gamma constant. After regularizing the boundary action with a counterterm of the form

$$S_{c.t.} = -\frac{\log\left(\rho_{\text{UV}} k_{\text{UV}} e^{(2\gamma_{\text{E}}-1)/2}/2\right)}{4} \int_{\rho=\rho_{\text{UV}}} \mathrm{d}^d x \sqrt{-\gamma} F_{\mu\nu} F^{\mu\nu} \tag{2.71}$$

we can extract the optical conductivity

$$\sigma_0(\omega) = \frac{G^{xx}(\omega, \boldsymbol{k} = \boldsymbol{0})}{-i\omega} = \frac{\pi}{2}\omega + i\omega \log\left(\frac{|\omega|}{\omega_{\text{UV}}}\right) = \frac{i\omega}{2} \log\left(-\left(\frac{\omega}{\omega_{\text{UV}}}\right)^2\right) , \tag{2.72}$$

that exactly reproduces the zero-temperature optical conductivity for a non-interacting Weyl or Dirac semimetal, up to a prefactor [71]. In particular, the holographic result in (2.72) describes a system with strong interactions, and, contrary to the non-interacting Dirac semimetal calculation, the prefactor that for convenience we have set to one by a rescaling of the action, depends on the coupling constant. The frequency dependence, however, is the same as it is set by the conformal symmetry of the theory.

When introducing a double-trace deformation the new response function takes the form

$$\chi^{xx}(\omega, \boldsymbol{k}) = \frac{G^{xx}(\omega, \boldsymbol{k})}{1 - \frac{\alpha^2}{\omega^2} G^{xx}(\omega, \boldsymbol{k})} , \tag{2.73}$$

so that the real part of the conductivity in the modified boundary theory with Coulomb interaction becomes:

$$\text{Re}[\sigma(\omega)] = \text{Re}\left[\frac{\chi^{xx}(\omega, \boldsymbol{k} = \boldsymbol{0})}{-i\omega}\right] = \frac{\frac{\pi}{2}\omega}{\left(1 + \alpha^2 \log(|\omega|/\omega_{\text{UV}})\right)^2 + \frac{\alpha^4 \pi^2}{4}} . \tag{2.74}$$

The logarithmic term in the denominator of the conductivity is reminiscent of the conductivity of Weyl semimetals [115]. From (2.74), we can see that for $\omega \to 0$ and $\omega \to \infty$, $\sigma \sim \omega/\log^2(\omega)$, and in both limits we have $\mathrm{Re}[\sigma] < \mathrm{Re}[\sigma_0]$. However, there is a range of values for the coupling constant α^2 where we can have $\mathrm{Re}[\sigma] > \mathrm{Re}[\sigma_0]$ (considering only $\omega > 0$, where the real part of the conductivity is always positive). Explicitly:

$$\begin{aligned}
&\alpha^2 < \frac{2}{\pi}: \quad \begin{cases} \sigma(\omega) > \sigma_0(\omega), & \exp\left(-\frac{1}{\alpha^2} - \sqrt{\frac{1}{\alpha^4} - \frac{\pi^2}{4}}\right) < \frac{\omega}{\omega_{\mathrm{UV}}} < \exp\left(-\frac{1}{\alpha^2} + \sqrt{\frac{1}{\alpha^4} - \frac{\pi^2}{4}}\right) , \\ \sigma(\omega) < \sigma_0(\omega), & \text{otherwise} \end{cases} \\
&\alpha^2 > \frac{2}{\pi}: \quad \sigma(\omega) < \sigma_0(\omega), \quad \forall \omega \in \mathbb{R}^+ .
\end{aligned} \tag{2.75}$$

This behavior can be observed in figure 2.12, were we plot the conductivity with and without double-trace deformation for different values of the coupling constant. In all the plots we fixed the renormalization scale $\omega_{\mathrm{UV}} = 100$. Note however that, being the only scale in the theory, a change in the value of ω_{UV} simply amounts to a change of scale. Notice also, that there is no plasmon peak in the conductivity. This is an effect of the probe limit, where the Maxwell field decouples from the gravitational background and does not backreact on the geometry. This in turns suppresses the sound modes in a neutral theory, and hence the plasmon modes in a charged system.

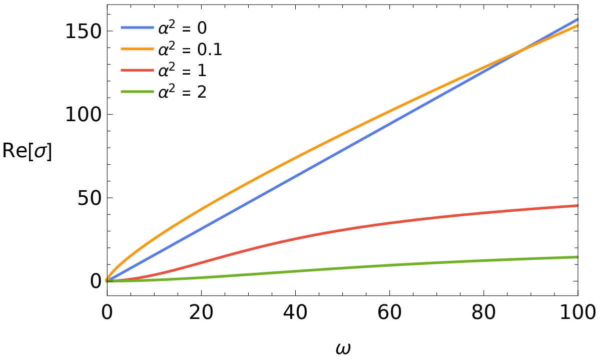

Figure 2.12: Conductivity for a Maxwell field in AdS$_5$ without backreaction, but with a double-trace boundary deformation. The value of the coupling constant α^2 determines the importance of the effect of the double-trace deformation. The case $\alpha^2 = 0$ corresponds to the standard solution $\mathrm{Re}[\sigma(\omega)] = \omega\pi/2$.

2.5.3 Conductivity with Coulomb interactions

Here we compute the optical conductivity in $d = 3+1$ boundary spacetime dimensions for the Reissner-Nordström metal with and without double-trace deformation.

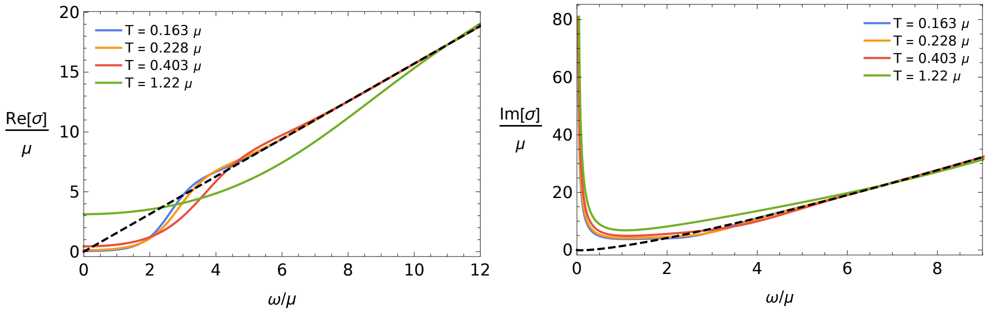

Figure 2.13: Real (left) and imaginary (right) part of the optical conductivity for the Reissner-Nordström metal in $d = 3+1$ for different values of the temperature. The black dashed line is the AdS$_5$ analytical solution. For large frequency we see that both the real and the imaginary parts go to the AdS$_5$ results, where for the imaginary part we choose the cutoff scale ω_{UV} to be the same for different values of T/μ. In particular, in the imaginary part, we can observe the logarithmic behavior for large frequency, as well as the $1/\omega$ behavior for small ω. This implies that the real part of the conductivity contains a delta function $Z\delta(\omega)$, with Z the Drude weight that in this case is given by $Z = 2\langle\rho\rangle^2/3\langle\epsilon\rangle$.

In figure 2.13, we show the optical conductivity for a neutral system for different values of T/μ and compare it with the AdS$_5$ analytical solution obtained in the previous section. In particular, the short-wavelength limit of the theory is determined by the geometry of the bulk spacetime for large r, and we therefore expect to recover the AdS$_5$ result for high frequencies. This is indeed what we observe in figure 2.13, and we can notice the logarithmic behavior at large frequencies in the imaginary part of the conductivity, were we chose the value of the cutoff-scale ω_{UV} to be the same for different values of T/μ, since the asymptotic behavior depends on the choice of scale. Moreover, we can see that at small frequencies the imaginary part of the optical conductivity of the Reissner-Nordström solution diverges as $1/\omega$, signaling the presence of a delta function at the origin for Re$[\sigma(\omega)]$. This delta function is expected since we are dealing with a system with translation invariance, but it is suppressed in the probe limit for the AdS$_5$ solution as the background is kept fixed [55].

By introducing the double-trace deformation the delta function in the origin disappears, as it is turned into a peak at the plasma frequency by Coulomb interactions. In figure 2.14, we can clearly observe this peak, that becomes sharper and higher as we lower the temperature. In figure 2.15 we plot the imaginary part of the conductivity,

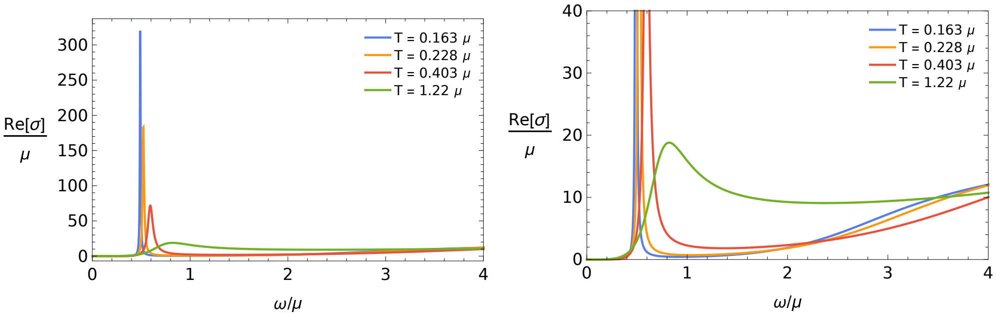

Figure 2.14: Real part of the optical conductivity for the Reissner-Nordström metal in $d = 3 + 1$ with a double-trace deformation ($\alpha^2 = 1/10$). On the right we show an enlarged version of the figure on the left. We clearly see a peak at the plasma frequency, that becomes increasingly higher (left) and sharper (right) as we lower the temperature. Moreover, we notice that the conductivity goes to zero as $\omega \to 0$, contrary to the neutral system.

where we see that the pole in the origin present in the optical conductivity of a neutral system is shifted to the nonzero plasma frequency. Moreover, with the double-trace deformation, the real part of the conductivity goes to zero as $\omega \to 0$, as is expected from Eq. (2.66).

2.6 Conclusion and Outlook

In summary, we proposed a general procedure to introduce screening effects of the Coulomb interaction in the holographic description of strongly interacting system. This allows us to study spectral functions of systems with charged particles that contain plasmon excitations, as it is the case in many condensed-matter systems of interest. In particular, we numerically studied the effect of this procedure in a Reissner-Nordström theory, where we observed properties expected from traditional condensed-matter calculations.

In $d = 3 + 1$ we obtained a gapped plasmon mode in the density-density response function, and we showed that the optical conductivity with Coulomb interactions contains scale-dependent logarithms, resembling the conductivities predicted in Dirac and Weyl semimetals.

In $d = 2+1$, our main result is a toy model of a system composed of a stack of (spatially) two-dimensional layers, with strong in-plane interaction and with coupling between layers governed by the Coulomb interaction. In this model we see that the behavior of the low-energy dynamics depends on the out-of-plane Bloch momentum p. When

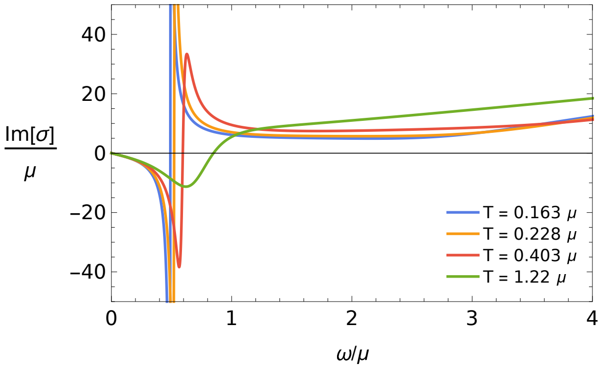

Figure 2.15: Imaginary part of the optical conductivity for the Reissner-Nordström metal in $d = 3+1$ with a double-trace deformation ($\alpha^2 = 1/10$). We see that $\mathrm{Im}[\sigma(\omega)] \to 0$ for $\omega \to 0$. This implies that there is no pole at the origin, as screening effects shift the pole to the nonzero plasma frequency.

$p\ell = 0$, with ℓ the inter-plane distance the density-density spectral function contains a gapped plasmon mode. However, for $p\ell \neq 0$, we obtain an 'acoustic plasmon', with a linear low-energy dispersion relation with a renormalized speed of sound. These results show that the model qualitatively reproduces recent experimental results [59]. This suggests that the Coulomb interaction between layers might play a key role in high-temperature cuprate superconductors, proving the necessity of incorporating this interaction in holographic models if we want to study properties of these layered high-T_c materials. In a single layer, we instead showed that the dispersion relation assume the form $\omega \propto \sqrt{|\boldsymbol{k}|}$, as observed in graphene.

In conclusion, we have seen that, even with a relatively simple holographic model as the Reissner-Nordström background, the addition of long-range Coulomb interactions presents interesting features that can more closely reproduce experimental results in strongly interacting materials. Therefore, it would be very interesting in future work to apply the double-trace deformation introduced here to different holographic backgrounds, such as the holographic superconductor model and Lifshitz solutions, in order to study the behavior of their longitudinal low-energy excitations in the presence of Coulomb interactions. These gravitational theories, contrary to the Reissner-Nordström model, allow for the description of systems with zero entropy at zero temperature. As the ultimate goal is to describe laboratory condensed-matter system, a next important step is to relax the assumption of momentum conservation, as impurities in experimental materials necessarily break momentum conservation.

Finally, the addition of a hyperscaling-violation factor to the metric of the Lifshitz solution can be used to study the effect of Coulomb interactions on quantum phases with hyperscaling violation [86].

2.A Gauge Solutions

In the theory considered in this paper, we have two gauge fields, the one-form A_μ and the metric tensor $g_{\mu\nu}$. In order to compute the Green's function, we then introduce fluctuations of these fields $\delta A_\mu \equiv a_\mu$ and $\delta g_{\mu\nu} \equiv h_{\mu\nu}$. As explained in section 2.2, using rotational invariance to fix the momentum along the x direction $k^\mu = (\omega, \pm|\boldsymbol{k}|, 0, \ldots, 0)$, the remaining fluctuations decouple according to their parity under $O(d-2)$ acting on $x^2, \ldots, x^{d-1}$ [84]. In the longitudinal channel, in both $d = 3+1$ and $d = 2+1$, we are then left with (where obviously in $d = 2+1$ there is no h_{zz})

$$\delta\boldsymbol{\Phi} = (a_t, a_x, a_r, h_{xt}, h_{tt}, h_{xx}, h_{yy} = h_{zz}, h_{rr}, h_{tr}, h_{xr}) \ . \tag{2.76}$$

Using the gauge freedom to choose a gauge where $h_{r\mu} = 0$, as well as $A_r = a_r = 0$, the set of coupled fluctuations reduces to

$$\delta\boldsymbol{\Phi} = (a_t, a_x, h_{xt}, h_{tt}, h_{xx}, h_{yy} = h_{zz}) \ . \tag{2.77}$$

This set of fluctuations contains only two physical degrees of freedom, therefore, we can only find two independent solutions to the coupled system of linearized equations of motion. However, after setting the r components to zero, we still have some leftover gauge freedom, and the remaining solutions necessary to compute the Green's functions are pure gauge solutions that can be extracted once we know the residual gauge freedom we are left with, as we explain below.

The fields are invariant under the gauge transformation

$$A_\mu + a_\mu \to A_\mu + a_\mu - \partial_\mu \Lambda \ , \tag{2.78}$$

and diffeomorphisms. The latter gives

$$\begin{aligned} a_\mu &\to a_\mu - \xi^\nu \nabla_\nu A_\mu - (\nabla_\mu \xi^\nu) A_\nu \\ h_{\mu\nu} &\to h_{\mu\nu} - \nabla_\mu \xi_\nu - \nabla_\nu \xi_\mu \ . \end{aligned} \tag{2.79}$$

In order to set the r-components of the metric fluctuations to zero we have to choose a vector $\bar{\xi}^{\nu}$ such that

$$h_{r\mu} = \nabla_r \bar{\xi}_\mu - \nabla_\mu \bar{\xi}_r = \partial_r \bar{\xi}_\mu - 2\Gamma^{\lambda}_{r\mu}\bar{\xi}_\lambda + \partial_\mu \bar{\xi}_r \ . \tag{2.80}$$

This defines a set of partial differential equations. Working in Fourier space and using rotational invariance to fix the momentum in the x direction, we obtain a set of coupled ordinary differential equations of the form

$$\xi'(r,\omega,k) + A(r)\xi(r,\omega,k) = B(r,\omega,k) \ , \tag{2.81}$$

that has the general solution

$$\bar{\xi}(r,\omega,k) = \left(\int \mathrm{d}r \left[B(r,\omega,k)e^{\int \mathrm{d}r A(r)}\right] + C(\omega,k)\right) e^{-\int \mathrm{d}r A(r)} \ . \tag{2.82}$$

We therefore see that ξ_μ is determined up to an arbitrary factor $C_\mu(\omega,k)e^{-\int \mathrm{d}r A_\mu(r)}$, that corresponds to the left over gauge freedom. In particular from Eq. (2.80) we find that the residual gauge transformations are given by

$$\xi_r = C_r(\omega,k)e^{2\int \mathrm{d}r \Gamma^{r}_{rr}} \ , \tag{2.83}$$

$$\xi_\alpha = C_\alpha(\omega,k)e^{2\int \mathrm{d}r \Gamma^{\alpha}_{r\alpha}} \ , \tag{2.84}$$

where $\alpha = t,x,y$ and there is no summation on the two repeated indices in $\Gamma^{\alpha}_{r\alpha}$. In the same way, we want to choose the scalar Λ in (2.78) in order to set the r component of the gauge field to zero. Under the diffeomorphism used to set $h_{r\mu} = 0$, we have that $A_r + a_r$ transformed as

$$A_r + a_r \to A_r + a_r + 2g^{tt}\bar{\xi}_t \Gamma^{t}_{rt} A_t - g^{tt}\bar{\xi}'_t A_t \ , \tag{2.85}$$

so we need to choose Λ to be

$$\Lambda(r,\omega,k) = \int \mathrm{d}r \left(A_r + a_r + 2g^{tt}\bar{\xi}_t \Gamma^{t}_{rt} A_t - g^{tt}\bar{\xi}'_t A_t\right) + \lambda(\omega,k) \tag{2.86}$$

where $\lambda(\omega,k)$ is an arbitrary constant in r. Notice that this expression is also invariant under the residual gauge transformation $\bar{\xi}_t \to \bar{\xi}_t + c_t e^{2\int \mathrm{d}r \Gamma^{t}_{rt}}$. Since we have some gauge freedom left, and we know that the linearized equations of motion are invariant under all allowed gauge transformation, we have, given a solution $\bar{\Phi}$ of the linearized equations of motion, that $\bar{\Phi}$ transformed under all residual gauge transformation is also a solution. Moreover, we know that $\Phi = 0$ is a solution. We can thus construct pure gauge solutions by choosing n independent residual gauge transformation, i.e., by fixing n linearly independent values of the vector $\boldsymbol{C} = (\lambda, C_\alpha)$.

For example, in $d = 2 + 1$ we have from Eqs. (2.80) and (2.82) that the gauge where there are no r-components of the fluctuations is defined by

$$\begin{aligned}
\bar{\xi}_r &= \left(\frac{1}{2}\int \mathrm{d}r \left[h_{rr} e^{-\int \mathrm{d}r \Gamma^r_{rr}}\right] + C_r\right) e^{\int \mathrm{d}r \Gamma^r_{rr}} \ , \\
\bar{\xi}_t &= \left(\int \mathrm{d}r \left[(h_{rt} + i\omega\xi_r) e^{-2\int \mathrm{d}r \Gamma^t_{rt}}\right] + C_t\right) e^{2\int \mathrm{d}r \Gamma^t_{rt}} \ , \\
\bar{\xi}_x &= \left(\int \mathrm{d}r \left[(h_{rx} - ik\xi_r) e^{-2\int \mathrm{d}r \Gamma^x_{rx}}\right] + C_x\right) e^{2\int \mathrm{d}r \Gamma^x_{rx}} \ , \\
\bar{\xi}_y &= \left(\int \mathrm{d}r \left[h_{ry} + e^{-2\int \mathrm{d}r \Gamma^y_{yt}}\right] + C_y\right) e^{2\int \mathrm{d}r \Gamma^y_{ry}} \ ,
\end{aligned} \tag{2.87}$$

and we are left with the gauge transformations defined by

$$\begin{aligned}
\Lambda =& \lambda(\omega, k) \ , \\
\xi_i =& C_i(\omega, k) e^{2\int \mathrm{d}r/r} = r^2 C_i(\omega, k) \ , \\
\xi_t =& C_t(\omega, k) e^{\int \mathrm{d}r \frac{f'}{f}} = f C_t(\omega, k) \ , \\
\xi_r =& C_r(\omega, k) e^{-\int \mathrm{d}r \frac{f'}{2f}} = \frac{1}{\sqrt{f}} C_r(\omega, k) \ .
\end{aligned} \tag{2.88}$$

Remembering that the behavior of the considered field fluctuations under a gauge transformation is given, in Fourier space, by

$$\begin{aligned}
a_x \to& a_x - ik\Lambda \ , \\
a_t \to& a_t + i\omega\Lambda \ ,
\end{aligned} \tag{2.89}$$

and

$$\begin{aligned} a_x &\to a_x + ikA_t/f\xi_t \ , \\ a_t &\to a_t - fA_t'\xi_r - i\omega/fA_t\xi_t \ , \\ h_{xt} &\to h_{xt} - ik\xi_t + i\omega\xi_x \ , \\ h_{tt} &\to h_{tt} + 2i\omega\xi_t + ff'\xi_r \ , \\ h_{xx} &\to h_{xx} - 2ik\xi_x - 2fr\xi_r \ , \\ h_{yy} &\to h_{yy} - 2fr\xi_r \ , \end{aligned} \tag{2.90}$$

we can generate 4 independent pure gauge solutions by setting the fluctuations to zero on the right-hand side of (2.89) and (2.90) and plugging in the expressions for the residual gauge freedom (2.88) with $\boldsymbol{C} = C_\mu \delta^\mu_{\bar{\nu}}$ and $\bar{\nu}$ ranging over the 4 indices.

Notice that in (2.87), $\bar{\xi}_t$ and $\bar{\xi}_x$ depends on ξ_r, therefore, when performing a residual gauge transformation $\bar{\xi}_r \to \bar{\xi}_r + 1/\sqrt{f}C_r$, $\bar{\xi}_t$ and $\bar{\xi}_x$ will change as well. We ultimately find that the pure gauge solutions are:

$$\begin{aligned} \delta\boldsymbol{\Phi}^{(1)} =& (-\omega, k, 0, 0, 0, 0) \\ \delta\boldsymbol{\Phi}^{(2)} =& \big(0, 0, i\omega r^2, 0, -2ikr^2, 0\big) \\ \delta\boldsymbol{\Phi}^{(3)} =& (-i\omega A_t, ikA_t, -ikf, 2i\omega f, 0, 0) \\ \delta\boldsymbol{\Phi}^{(4)} =& \bigg(- \sqrt{f}A_t' + \omega^2 A_t \int \frac{\mathrm{d}r}{f\sqrt{f}}, -\omega k \int \frac{\mathrm{d}r A_t}{f\sqrt{f}} + \omega k \int \frac{\mathrm{d}r A_t}{f\sqrt{f}}, \\ & \omega k \left[f \int \frac{\mathrm{d}r}{f\sqrt{f}} + r^2 \int \frac{\mathrm{d}r}{r^2\sqrt{f}} \right], -2\omega^2 f \int \frac{\mathrm{d}r}{f\sqrt{f}} + \sqrt{f}f', \\ & - 2k^2r^2 \int \frac{\mathrm{d}r}{r^2\sqrt{f}} - 2\sqrt{f}r, -2\sqrt{f}r \bigg) \end{aligned} \tag{2.91}$$

This results can now easily be checked by substitution in the linerarized equations of motion.

2.B Details of the calculations for the layered system

Using the notation of section 2.4.2, with $d = 2+1$, the $(3+1)$-dimensional boundary deformation in Fourier space, after integrating out the Maxwell field, is, up to a factor of $-\alpha^2/2$ that we neglect here for notational convenience

$$\int \frac{\mathrm{d}^d k}{(2\pi)^d} \int \frac{\mathrm{d}k_z}{2\pi} \left\langle J^\mu(-k,-k_z)\right\rangle \frac{\eta_{\mu\nu}}{k^2+k_z^2} \left\langle J^\nu(k,k_z)\right\rangle \ , \tag{2.92}$$

with $J^\mu(k,k_z)$ the Fourier transform of $J^\mu(x,z)$ defined as

$$J^\mu(x,z) = \sum_n J^\mu(x,z)\delta(z-n\ell) \ . \tag{2.93}$$

The Fourier transform along the z direction can easily be computed as

$$J(x,k_z) = \sum_n \int \mathrm{d}z \int J(x,z)\delta(z-n\ell)e^{-ik_z z} = \sum_n J(x,n\ell)e^{-ik_z n\ell} \ . \tag{2.94}$$

Inserting this into (2.92) we then have

$$\int \frac{\mathrm{d}^d k}{(2\pi)^d} \int \frac{\mathrm{d}k_z}{2\pi} \left(\sum_{n,m} \left\langle J^\mu(-k,n\ell)\right\rangle \eta_{\mu\nu} \frac{e^{-ik_z(n-m)\ell}}{k^2+k_z^2} \left\langle J^\nu(k,m\ell)\right\rangle \right) \ , \tag{2.95}$$

and we can perform the integral over k_z that gives

$$\int \frac{\mathrm{d}^d k}{(2\pi)^d} \left(\sum_{n,m} \left\langle J^\mu(-k,n\ell)\right\rangle \eta_{\mu\nu} \frac{e^{-|n-m||k|\ell}}{2|k|} \left\langle J^\nu(k,m\ell)\right\rangle \right) \ . \tag{2.96}$$

In order to perform the summation, we first Fourier transform $J(k,n\ell)$ in the first Brillouin zone, that is, we can write

$$J(k,n\ell) = \frac{\ell}{2\pi} \int_{-\pi/\ell}^{\pi/\ell} \mathrm{d}p \, J(k,p) e^{ipn\ell} \ , \tag{2.97}$$

to obtain

$$\int \frac{\mathrm{d}^d k}{(2\pi)^d} \sum_{n,m} \frac{\ell^2}{(2\pi)^2} \int_{-\pi/\ell}^{\pi/\ell} \mathrm{d}p \, \mathrm{d}p' \ \left\langle J^\mu(-k,p)\right\rangle \eta_{\mu\nu} \frac{e^{-|n-m||k|\ell}}{2|k|} \left\langle J^\nu(k,p')\right\rangle e^{in\ell p + im\ell p'} \ . \tag{2.98}$$

We can now perform the summations

$$\begin{aligned}
&\sum_{n,m} e^{-|n-m||k|\ell} e^{in\ell p+im\ell p'} \\
&= \sum_m e^{-m|k|\ell+im\ell p'} \sum_{n<m} e^{n|k|\ell+in\ell p} + \sum_m e^{m|k|\ell+im\ell p'} \sum_{n>m} e^{-n|k|\ell+in\ell p} + \sum_m e^{im\ell(p+p')} \\
&= \sum_m e^{im\ell(p+p')} \left(\sum_{n<0} e^{n|k|\ell+in\ell p} + \sum_{n>0} e^{-n|k|\ell+in\ell p} + 1 \right) \\
&= \frac{2\pi}{\ell}\delta(p+p') \left(2\sum_{n>0} e^{-n|k|\ell}\cos(p\ell) + 1 \right) = \frac{2\pi}{\ell}\delta(p+p') \frac{\sinh(|k|\ell)}{\cosh(|k|\ell) - \cos(p\ell)} \ ,
\end{aligned} \tag{2.99}$$

to finally obtain

$$\int \frac{\mathrm{d}^d k}{(2\pi)^d} \int_{-\pi/\ell}^{\pi/\ell} \frac{\mathrm{d}p}{2\pi} \, \langle J^\mu(-k,-p) \rangle \, \eta_{\mu\nu} \frac{\ell}{2|k|} \frac{\sinh(|k|\ell)}{\cosh(|k|\ell) - \cos(p\ell)} \, \langle J^\nu(k,p) \rangle \ . \tag{2.100}$$

For the boundary theory coming from holography, we use a set of d-dimensional solutions dual to a $d+1$ bulk theory, whose boundary terms read, up to a factor of 1/2

$$\int \mathrm{d}^d x \, A_\mu^{(n)}(x) \left\langle J^\mu_{(n)}(x) \right\rangle \ , \tag{2.101}$$

so that the $(d+1)$-dimensional stack of layers can be modelled as

$$\sum_n \int \mathrm{d}^d x \, A_\mu^{(n)}(x) \left\langle J^\mu_{(n)}(x) \right\rangle = \int \mathrm{d}^d x \int \mathrm{d}z \, \sum_n A_\mu(x,z) \, \langle J^\mu(x,z) \rangle \, \delta(z - nl) \ . \tag{2.102}$$

Fourier transforming as described above, we can rewrite this last integral as

$$\begin{aligned}
&\int \frac{\mathrm{d}^d k}{(2\pi)^d} \int \frac{\mathrm{d}k_z}{2\pi} \int_{-\pi/\ell}^{\pi/\ell} \frac{\mathrm{d}p}{2\pi} \, \ell A_\mu(k,k_z) \, \langle J^\mu(-k,p) \rangle \, e^{i(p+k_z)n\ell} \\
&= \int \frac{\mathrm{d}^d k}{(2\pi)^d} \int_{-\pi/\ell}^{\pi/\ell} \frac{\mathrm{d}p}{2\pi} \, \ell A_\mu(k,p) \, \langle J^\mu(-k,-p) \rangle \ .
\end{aligned} \tag{2.103}$$

Studying the second-order variation to extract the Green's function, we have

$$\begin{aligned}
&\int \frac{\mathrm{d}^d k}{(2\pi)^d} \int_{-\pi/\ell}^{\pi/\ell} \frac{\mathrm{d}p}{2\pi}\, \ell a_\mu^{\mathrm{s}}(k,p) \delta \left\langle J^\mu(-k,-p)\right\rangle \\
&= \int \frac{\mathrm{d}^d k}{(2\pi)^d} \int_{-\pi/\ell}^{\pi/\ell} \frac{\mathrm{d}p}{2\pi} \left(\ell a_\mu^{\mathrm{s}}(k,p)\right) \frac{G^{\mu\nu}(k)}{\ell} \left(\ell a_\nu^{\mathrm{s}}(-k,-p)\right) \\
&= \int \frac{\mathrm{d}^d k}{(2\pi)^d} \int_{-\pi/\ell}^{\pi/\ell} \frac{\mathrm{d}p}{2\pi}\, \delta \left\langle J^\mu(k,p)\right\rangle \left[\ell G^{-1}(k)\right]_{\mu\nu} \delta \left\langle J^\nu(k,p)\right\rangle \ ,
\end{aligned} \tag{2.104}$$

where $\ell a_\mu^{\mathrm{s}}(k,p)$ is the $(d+1)$-dimensional source. In addition, $G(k)$, which is independent of the Bloch momentum p, is the Green's function coming from a holographic calculation for a d-dimensional boundary theory, so that $G(k)/\ell$ has the dimensions of a $(d+1)$-dimensional response. When we introduce the double-trace deformation that couples the layers, the total boundary action, second order in fluctuations, then reads

$$\begin{aligned}
&\int \frac{\mathrm{d}^d k}{(2\pi)^d} \int_{-\pi/\ell}^{\pi/\ell} \frac{\mathrm{d}p}{2\pi}\, \delta \left\langle J^\mu(-k,-p)\right\rangle \left[\ell a_\mu(k,p) - \eta_{\mu\nu} \frac{\alpha^2 \ell}{2|k|} \frac{\sinh\left(|k|\ell\right)}{\cosh\left(|k|\ell\right) - \cos(p\ell)} \delta \left\langle J^\nu(k,p)\right\rangle\right] \\
&= \int \frac{\mathrm{d}^d k}{(2\pi)^d} \int_{-\pi/\ell}^{\pi/\ell} \frac{\mathrm{d}p}{2\pi}\, \delta \left\langle J^\mu(-k,-p)\right\rangle \left[\ell G^{-1}_{\mu\nu}(k) - \eta_{\mu\nu} \frac{\alpha^2 \ell}{2|k|} \frac{\sinh\left(|k|\ell\right)}{\cosh\left(|k|\ell\right) - \cos(p\ell)}\right] \delta \left\langle J^\nu(k,p)\right\rangle ,
\end{aligned} \tag{2.105}$$

that gives a $(d+1)$-dimensional density-density response function of the form

$$\chi^{00}(k,p) = \frac{G^{00}(k)/\ell}{1 - \frac{\alpha^2}{2|k|} \frac{\sinh\left(|k|\ell\right)}{\cosh\left(|k|\ell\right) - \cos(p\ell)} k^2 G^{00}(k)/\boldsymbol{k}^2} \ . \tag{2.106}$$

Notice that in the limit $\ell \to \infty$ the above boundary action, Eq. (2.105), becomes

$$\int \frac{\mathrm{d}^d k}{(2\pi)^d} \delta \left\langle J^\mu(-k)\right\rangle \left[G^{-1}_{\mu\nu}(k) - \eta_{\mu\nu} \frac{\alpha^2}{2|k|}\right] \delta \left\langle J^\nu(k)\right\rangle \ , \tag{2.107}$$

giving the effective two-dimensional response for a single layer.

Chapter 3

Coulomb Drag between Two Strange Metals

3.1 Introduction

The cuprates have been of interest to both the experimental and theoretical physics community for the past three decades due to their peculiar metallic properties that cannot be explained within the standard Fermi-liquid framework [110, 80]. In this class of materials, that have in common a layered structure of CuO_2 planes, strong Coulomb interactions between the electrons give rise to unusual and still unclear quantum behavior, of which the high-temperature superconducting phase is of most technological importance. Above the maximum critical temperature of the superconducting phase, we find the so-called strange metal, whose anomalous linear-in-T resistivity [23, 20, 16, 2, 88, 90] characterizes its non-Fermi-liquid behavior, even if the superconductivity is suppressed by a magnetic field [64]. Given the importance of understanding the physics at play in the strange-metal phase in order to also get a better grasp on the instability towards high-temperature superconductivity, there have been a variety of attempts to model the strongly interacting cuprates [87, 104, 99, 75, 81, 132, 30, 10, 127, 135]. One technique, in particular, is the application of the AdS/CFT correspondence, or holographic duality [94], conjectured and first developed by the string-theory community, but that has proven to be a powerful tool to qualitatively study low-energy properties of strongly interacting quantum matter as well [57, 133, 1]. In fact, the more easily tractable classical limit of a gravitational theory allows for an effective description of the generic behavior of a strongly interacting system in one lower spatial dimension, such as a cuprate strange metal layer with its strong (on-site Hubbard U) electromagnetic repulsion.

In this paper we use a holographic Einstein-Maxwell-Dilaton model (EMD) of the strange metal [50] to study a two-layer system where the interaction among the different layers is only mediated by the long-range Coulomb force. The importance of such a setting is motivated by the experimental relevance of multi-layered systems. For simplicity most of the holographic studies of the cuprates focus on describing the behavior of a single-layer, however, there has been recent experimental interest in probing also the bulk response of the cuprates [59, 100]. Experimental results in both hole- and electron-doped cuprates show that the density response is governed by the inter-layer Coulomb interaction, giving rise to low-energy acoustic plasmon modes. Plasmons are ubiquitous in condensed-matter materials due to the electric charge of the electron, but only recently a way to capture dynamical Coulomb interactions and, hence, screening effects due to the charged nature of the system, has been proposed in holography [43, 46, 44, 96, 114], opening the door to the possibility of studying 'holographic' plasmons and providing a simplified framework to test experimental results on acoustic plasmons in multi-layered cuprates [96].

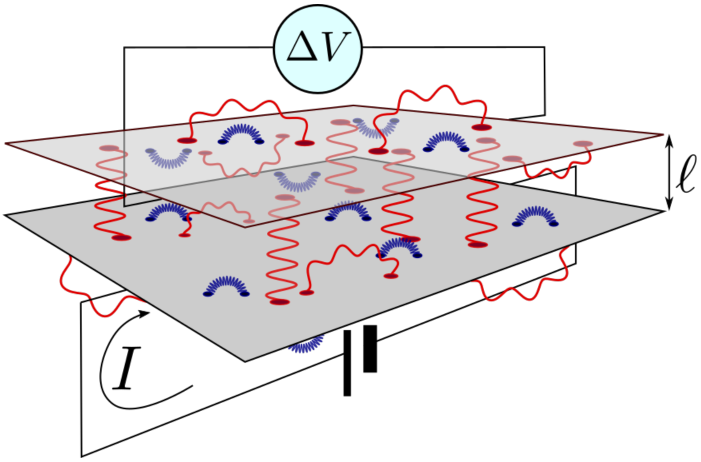

Figure 3.1: Experimental set-up for a Coulomb drag measurement. A current I flows through the active layer and the voltage drop $\Delta V = -R_D I$ induced in the passive layer is observed to measure the drag resistance. In the holographic description under study we have two types of interactions, i.e., strong in-plane interactions leading to strange-metal behavior (blue) and the long-range Coulomb interactions (red).

In view of these developments, our main aim is here to present a link between holographic predictions and experimental results by studying the density response of two holographic strange-metal layers. In particular, by considering the Coulomb drag resistivity, we are able to obtain also quantitative estimates of the drag effect in the hope to provide a verifiable prediction to either validate the holographic model or to show its shortcomings. Here Coulomb drag refers to a transport phenomenon of a system of closely spaced but electrically isolated layers, where a current driven through the 'active' layer gives rise to a current in the nearby 'passive' layer due to inter-layer scattering of the charge carriers mediated by the long-range Coulomb interaction that couples density fluctuations among the different layers [102]. A typical experimental set-up is shown in Fig. 3.1, where a known current is driven through one layer and the drag effect, parametrized by the drag resistivity ρ_D, is studied by measuring the voltage drop in the passive layer.

In the holographic description we are using, the system is characterized by two kinds of interactions, a strong one that is of short range and therefore does not contribute to the inter-layer scattering, and the long-range Coulomb interaction that instead also gives rise to the coupling between the separate layers. The success of the holographic duality relies on the fact that it naturally describes a strongly interacting system, such as a strange metal [53], and we thus can take two copies of such a model to describe the two layers. On the other hand, it is important to realize that holographic models present always a 'neutral' response, where there are no photons in the system. However, by performing a so-called double-trace deformation [129, 130, 95], we have recently shown how to add within holography also the long-range Coulomb screening effects to multi-layered models on top of the strong neutral interactions [96]. We use this procedure here to couple the holographic strange-metal layers in order to study the Coulomb drag resistivity, as we explain in detail in the following.

3.2 Einstein-Maxwell-Dilaton theory

Let us briefly review how we obtain the strange-metal response function for a single layer from holography. The holographic duality states the equivalence between a strongly interacting quantum theory and a classical gravitational theory with one additional spatial dimension, where the coordinate r of this additional dimension parametrizes the energy scale of the quantum field theory. In particular low-energy physics is described by the geometry in the deep interior ($r \to 0$) of the spacetime, while the near-boundary geometry ($r \to \infty$) characterizes the ultra-violet details of the dual field theory.

As a holographic model of a single-layer cuprate strange metal, we use a $(3+1)$-dimensional Einstein-Maxwell-Dilaton theory proposed by Gubser *et al.* [50]. This is one model in a class of holographic theories dual to a quantum field theory characterized at low energies by a 'semi-local' quantum critical phase with a dynamical critical exponent $z = \infty$, with the important implication that the scaling of the electron self-energy is then dominated by its frequency dependence $\hbar\Sigma(\omega, \boldsymbol{k}) \simeq \omega(-\omega^2)^{\nu_k - 1/2}$, with momentum dependence only entering through the exponent ν_k. The relevance of this result is due to the fact that, upon tuning the adjustable parameters in the holographic model, the holographic result reproduces the 'power-law liquid' model, with $\hbar\Sigma''(\omega, \boldsymbol{k}) \propto \omega^{2\alpha}$ that is found to accurately describes the experimentally observed electron self-energy in angle-resolved photoemission spectroscopy (ARPES) measurements near the Fermi surface [113]. Here, α is a doping-dependent constant, with $\alpha = 1/2$ at optimal doping and the holographic model reducing to the famous marginal Fermi liquid [75, 81] proposed for the qualitative description of the optimally-doped strange metal. Moreover, the momentum-dependence in the exponent predicted by the Gubser-Rocha model used here has been recently shown to accurately describe deviations from the power-law liquid model away from the Fermi surface in high-quality ARPES measurements [119, 97], providing further support for the usefulness of the model in studying the response function of the strange metal. On the other hand, it is also important to keep in mind that the strange metal is further characterized by an anomalous scaling of some quantities at nonzero magnetic field, such as the Hall angle, and, while of no relevance for the results presented in this paper, the holographic model used here might fail to reproduce such a scaling [12].

The gravitational action for the model is

$$\begin{aligned} S_{\text{EMD}} = \frac{c^3}{16\pi G} \int & \mathrm{d}r \mathrm{d}(ct) \mathrm{d}^2 x \sqrt{-g} \left[R - \frac{(\partial_\mu \phi)^2}{2} \right. \\ & \left. + \frac{6}{L^2} \cosh\left(\frac{\phi}{\sqrt{3}}\right) - \frac{e^{\phi/\sqrt{3}}}{4 g_F^2} F_{\mu\nu}^2 \right] \\ & + S_{\text{ct}} \ , \end{aligned} \tag{3.1}$$

with r denoting the additional spacial direction of the curved bulk spacetime, R the Ricci scalar, ϕ a dimensionless scalar field known as the dilaton [17, 40], and $F_{\mu\nu}$ the electromagnetic tensor with coupling constant

$$g_F^2 = \frac{c^4 \mu_0}{16\pi G} \ , \tag{3.2}$$

where $[\mu_0] = \mathrm{m\ kg/C^2}$ is a constant with the dimension of a magnetic permittivity. Finally, L is the anti-de Sitter (AdS) radius and S_{ct} contains the boundary counterterms necessary to have a well-defined boundary problem, and that are specified in the appendix. The dilaton field is such that the emergent low-energy theory is described by a semi-local quantum critical phase with both the dynamical critical exponent $z = \infty$ and the hyperscaling violation exponent $\theta = -\infty$ divergent but with a fixed ratio equal to -1. As previously mentioned, the dynamical exponent $z = \infty$ implies that at energies well below the Fermi energy, quantum critical correlations can only depend on momentum through the power of the frequency dependence, while $\theta/z = -1$ ensures that the entropy goes linearly to zero at zero temperature [57]. Ultimately, this scaling allows for the description of a quantum critical phase with a linear-in-T resistivity and entropy [3] and an electron self-energy that is dominated by its frequency dependence as desired for a strange metal [49]. On the field-theory side, the dilaton is dual to a scalar operator $\mathcal{O}$ sourced by $\phi^{(0)}$, that leads to a nonzero trace of the energy-momentum tensor according to $\langle T^{\mu}{}_{\mu} \rangle = \phi^{(0)} \langle \mathcal{O} \rangle$. This in turn implies, as we will see, that the speed of sound of the low-energy excitations of the system differs from that of a conformal invariant liquid.

For computational purposes it is convenient to re-write the action in Eq. (3.1) in dimensionless quantities by expressing everything in terms of physical constants and the dimensionful scale L of the theory, that is by measuring distances in units of L and energies in terms of $\hbar c/L$. We, therefore, define the dimensionless coordinates $(\tilde{r}, \tilde{t}, \tilde{\boldsymbol{x}}) \equiv (r, ct, \boldsymbol{x})/L$, and we absorb the gauge coupling into the field $\tilde{A}_\mu \equiv A_\mu / g_F$. The action then becomes

$$\begin{aligned} \tilde{S}_{\mathrm{EMD}} = \frac{c^3 L^2}{16\pi\hbar G} \int \mathrm{d}\tilde{r}\, \mathrm{d}\tilde{t}\, \mathrm{d}^2\tilde{x} \sqrt{-g} \Bigg[R - \frac{(\partial_\mu \phi)^2}{2} \\ + 6\cosh\left(\frac{\phi}{\sqrt{3}}\right) - \frac{e^{\phi/\sqrt{3}}}{4} \tilde{F}_{\mu\nu}^2 \Bigg] \ . \end{aligned} \tag{3.3}$$

From now on, we will mostly use dimensionless quantities and we will drop the tilde for notational convenience and explicitly state when we write expressions in terms of dimensionful quantities. Moreover, we follow the convention of setting the prefactor of the integral, $N_G \equiv c^3L^2/16\pi\hbar G$, to unity for computational convenience, but we will comment extensively on its role in fixing the plasma frequency in a later section. This prefactor is related to the large-N number of species of the boundary quantum field theory [133].

The thermodynamics of this holographic strange-metal model is described by a solution to the coupled set of Einstein equations for the metric $g_{\mu\nu}$, Maxwell equations for the $U(1)$ gauge field A_μ, and the Klein-Gordon equation for the real scalar field ϕ as obtained from the variation of the action:

$$\begin{aligned} R_{\mu\nu} - \frac{1}{2}Rg_{\mu\nu} = T_{\mu\nu}\ ,\ \ \nabla_\mu(e^{\phi/\sqrt{3}}F^{\mu\nu}) = 0\ ,\\ \nabla_\mu\nabla^\mu\phi = \frac{e^{\phi/\sqrt{3}}}{4\sqrt{3}}F^2 - \frac{2\sqrt{3}}{L^2}\sinh(\phi/\sqrt{3})\ , \end{aligned} \tag{3.4}$$

where $R_{\mu\nu}$ and R are the Ricci tensor and scalar, respectively, and the energy-momentum tensor equals

$$\begin{aligned} T_{\mu\nu} =& \frac{1}{2}\partial_\mu\phi\partial_\nu\phi + \frac{e^{\phi/\sqrt{3}}}{2}F_\mu{}^\sigma F_{\nu\sigma} \\ &- g_{\mu\nu}\left(\frac{e^{\phi/\sqrt{3}}}{8}F^2 + \frac{(\partial_\sigma\phi)^2}{4} + \frac{3}{L^2}\cosh(\phi/\sqrt{3})\right)\ . \end{aligned} \tag{3.5}$$

In particular, we are looking at long-wavelength excitations in the nodal direction, neglecting possible anisotropy, so that the fields in Eq. (3.4) are a function of the radial coordinate r only. This set of equations for $(g_{tt} = -1/g_{rr}, g_{xx} = g_{yy}, A_t, \phi)$ then support a fully analytical black-hole solution [50], with a non-zero temperature and entropy, and with $A_t(r)$ setting a non-zero density in the dual boundary theory through the radially conserved quantity $n \equiv \sqrt{-g(r)}\ e^{\phi(r)/\sqrt{3}}F^{rt}(r)$, $g(r)$ being the determinant of the metric. It is important to notice that the definition of the density given here is related to the density of the boundary field theory by the unknown dimensionless prefactor N_G in the action in Eq. (3.3) that we set to unity, as explicitly shown in the appendix. This holds true for all operators and response functions so that, while with a 'bottom-up' holographic computation we are able to study the qualitative response of the system, we cannot make a quantitative comparison between the holographic model and the response measured experimentally. However, as we argue in a later section, the introduction of screening effects allows us to fix this constant by matching the experimental plasma frequency, opening up the opportunity for a further, quantitative, test of holographic predictions.

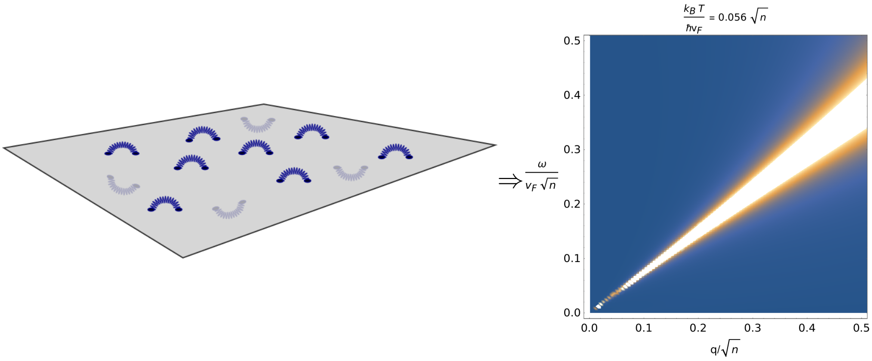

Figure 3.2: (Left) Picture of a single-layer with strong short-range interactions and (right) the imaginary part of the holographic density-density response, $\Pi''(\omega, q)$, at a fixed temperature $k_B T/\hbar v_F\sqrt{n} \simeq 0.038$. We see that the density-density response contains a linear sound mode with $\omega = v_s q$.

In order to also compute the response of the holographic strange metal to small external perturbations, we have to linearize the gravitational equations in Eq. (3.4) around the black-hole solution. We obtain in this way a set of coupled equations for the fluctuations $(\delta g_{tt}, \delta g_{tx}, \delta g_{xx}, \delta g_{yy}, \delta A_t, \delta A_x, \delta\phi)$ that can only be solved numerically. According to the holographic dictionary [53, 57, 1, 133], finding such a solution with infalling-wave boundary conditions at the black-hole horizon, allows us to extract all the retarded Green's function of the system, and hence the density-density response function $\Pi(\omega, \boldsymbol{q})$, by studying the near-boundary behavior of the field fluctuations. This is a response of a two-dimensional layer with strong in-plane interactions but without screening effects due to the long-range Coulomb interactions, as depicted in Fig. 3.2 and evident from the density-density response function that shows a linear sound mode $\omega = v_s q$ instead of the typical plasmon mode expected in the presence of screening $\omega \propto \sqrt{q}$. Here we used rotational invariance to fix $\boldsymbol{q} = (q, 0)$ without loss of generality.

In order to introduce screening effects, we need to couple dynamical photons to the current operator $\langle J^\mu \rangle$. To do so, as shown in Refs. [96, 114], we introduce a boundary "double-trace" deformation for the electromagnetic field, i.e., we add to the gravitational action in Eq. (3.1) a boundary term

$$
\begin{aligned}
S = &\int \mathrm{d}r\mathrm{d}^2x\mathrm{d}t\,\mathcal{L}_{\text{gravity}} + \\
&+ \int \mathrm{d}^2x\mathrm{d}t \int \mathrm{d}z \left(-\frac{\epsilon}{4}F_{\mu\nu}F^{\mu\nu} + A_\mu \langle J^\mu\rangle\right) \ ,
\end{aligned}
\tag{3.6}
$$

with z the spatial direction orthogonal to the x-y plane, and we used the convention of omitting the tilde on the dimensionless coupling $\tilde{\epsilon} \equiv \hbar c\epsilon/e^2$, with ϵ the dielectric constant of the material surrounding the layer and e the electric charge. The addition of this boundary term does not change the linearized equations of motions needed to compute the response function, but it only changes the boundary conditions [43, 44] for the field fluctuations. In particular, by restricting the current operator to the x-y plane where the holographic boundary theory is defined we can see that, with the addition of the boundary double-trace deformation, the density-density response function is related to the 'neutral' response function $\Pi(\omega, \boldsymbol{q})$ by

$$
\chi_{2\mathrm{D}}(\omega, \boldsymbol{q}) = \frac{\Pi(\omega, \boldsymbol{q})}{1 - \frac{\Pi(\omega,\boldsymbol{q})}{2\epsilon|\boldsymbol{q}|}} \equiv \frac{\Pi(\omega, \boldsymbol{q})}{\epsilon(\omega, \boldsymbol{q})} \ , \tag{3.7}
$$

and we recognize a RPA-like form with a Coulomb potential $V(\boldsymbol{q}) = 1/2\epsilon|\boldsymbol{q}|$, where we neglect retardation effects, i.e., a frequency dependence in the potential, by assuming $v_F \ll c$ (see Ref. [96] for details). Two things to keep in mind here are that, contrary to textbook RPA, $\Pi(\omega, \boldsymbol{q})$ is the density-density correlation function of a strongly interacting system computed from holography, and it hence accounts for the effect of strong interactions as can be seen in Fig. 3.2 where we show that Π'' contains a linear sound mode. Moreover, these interactions are effectively two-dimensional, living only in the plane, and should then be thought of as strong interactions that are short-ranged compared to the inter-layer distance, as depicted in Fig. 3.1. On the other hand, the long-range Coulomb interactions described by the addition of the boundary action in Eq. (3.6) are three-dimensional, as depicted in Fig. 3.3, where we also show that this induces the expected plasmon dispersion for a single layer.

In order to obtain a simple model of a two-layer cuprate strange metal where the long-range Coulomb interaction is the dominant inter-layer interaction [59], we take two independent copies of a two-dimensional holographic strange metal described by the action in Eq. (3.1) and couple them through the three-dimensional boundary double-

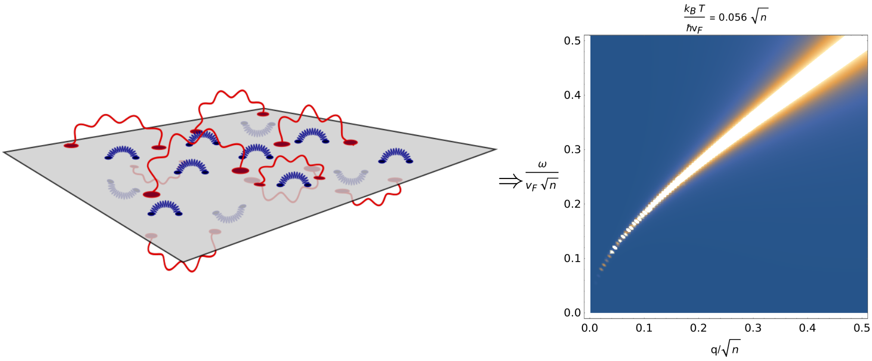

Figure 3.3: (Left) Picture of a single-layer with in-plane short-range strong interactions (blue) and long-range Coulomb interactions (red) and (right) the holographic density-density response $\Pi''(\omega, q)$ at a fixed temperature $k_B T/\hbar v_F\sqrt{n} \simeq 0.038$. We see that the density-density response contains the plasmon mode with $\omega \propto \sqrt{q}$.

trace deformation, where the current J^μ takes the form

$$J^\mu(\boldsymbol{x}, z) = J^\mu_{(1)}(\boldsymbol{x}, z)\delta(z + \ell/2) + J^\mu_{(2)}(\boldsymbol{x}, z)\delta(z - \ell/2) \ , \tag{3.8}$$

hence describing two layers laying parallel to the x-y plane and separated by a distance ℓ along the z-axis orthogonal to the x-y plane. This again, gives rise to an RPA-like form of the inter-layer density-density response, as we briefly show here.

First of all, let us remark that, as we want to describe the physics of the strange metal where the linear dispersion has a Fermi velocity v_F, we replace from now on the speed of light in the gravitational theory with the Fermi velocity $c \to v_F$. From holography, the effective boundary action for the field fluctuations in Fourier space takes the form

$$\frac{1}{2}\int \frac{\mathrm{d}^2q\mathrm{d}\omega}{(2\pi)^3} \sum_{i=1}^{2} a^{i(0)}_\mu(\omega, \boldsymbol{q}) j^\mu_i(-\omega, -\boldsymbol{q}) \ , \tag{3.9}$$

where $a^{i(0)}_\mu \equiv \lim_{r\to\infty} \delta A^i_\mu(r)$ and $j^\mu_i \equiv \delta\left\langle J^\mu_i \right\rangle$. Adding the boundary term from Eq. (3.6) and using the Fourier transform of the current in Eq. (3.8), $J(\omega, \boldsymbol{q}, q_z) = J^\mu_{(1)}(\omega, \boldsymbol{q})e^{iq_z\ell/2} + J^\mu_{(2)}(\omega, \boldsymbol{q})e^{-iq_z\ell/2}$, we can integrate out the Maxwell field fluctuations to obtain an effective boundary action for the currents. We define the absolute value of the four-vector $k \equiv |\boldsymbol{k}| = \sqrt{q^2 - \omega^2 v_F^2/c^2}$, where the factor of v_F^2/c^2 is due to the above-mentioned fact that the holographic theory is dual to a quantum field theory describing excitations with bare velocity v_F and the dimensionless ω then contains a factor of v_F while the Coulomb interactions propagate at the speed of light c. Then, the three-dimensional double-trace deformation gives a boundary term

$$\frac{1}{2}\int \frac{\mathrm{d}^2q\mathrm{d}\omega}{(2\pi)^3}\left(j_1^{\mu}(\omega,\boldsymbol{q})\, j_2^{\mu}(\omega,\boldsymbol{q})\right)\begin{pmatrix} \frac{\eta_{\mu\nu}}{2\epsilon k} & \frac{\eta_{\mu\nu}e^{-k\ell}}{2\epsilon k} \\ \frac{\eta_{\mu\nu}e^{-k\ell}}{2\epsilon k} & \frac{\eta_{\mu\nu}}{2\epsilon k}\end{pmatrix}\begin{pmatrix} j_1^{\nu}(-\omega,-\boldsymbol{q}) \\ j_2^{\nu}(-\omega,-\boldsymbol{q})\end{pmatrix} . \tag{3.10}$$

As we are interested in the limit $v_F/c \to 0$, upon a redefinition of $\epsilon c/v_F \to \epsilon$, we then obtain the effective action for the current fluctuations

$$\frac{1}{2}\int \frac{\mathrm{d}^2q\mathrm{d}\omega}{(2\pi^3)}\left(j_1^{\mu}\, j_2^{\mu}\right)\underbrace{\begin{pmatrix} {\Pi_1}_{\mu\nu}^{-1} + \frac{\eta_{\mu\nu}}{2\epsilon q} & \frac{\eta_{\mu\nu}e^{-q\ell}}{2\epsilon q} \\ \frac{\eta_{\mu\nu}e^{-q\ell}}{2\epsilon q} & {\Pi_2}_{\mu\nu}^{-1} + \frac{\eta_{\mu\nu}}{2\epsilon q}\end{pmatrix}}_{\chi^{-1}}\begin{pmatrix} j_1^{\nu} \\ j_2^{\nu}\end{pmatrix} , \tag{3.11}$$

with $\chi(\omega, q)$ the two-layer response and $q \equiv |\boldsymbol{q}|$. The coupling ϵ here plays an important role. As mentioned above, in bottom-up computations of holographic theories we can study the behavior of the response function up to an undetermined constant, meaning that we cannot provide a *quantitative* estimate of the magnitude of the effect, as this is only possible from a top-down construction from a known string theory that fixes the prefactor of the action N_G. With the introduction of plasmons and hence a known scale ϵ, we can fix this unknown constant to match the plasma dispersion defined by the low-energy pole of Eq. (3.7). This allows us a novel check for the holographic framework. Namely, we can further verify if the dual gravitational theory and the proposed plasmon set-up provide also a quantitative agreement with experimental measurements. Looking at it the other way around, studying the plasmon response in cuprates could give insight into the dual string theory needed to match the correct prefactor. We give further details on the relationship between N_G and the plasmon dispersion, and how to translate the dimensionless results from holography into physical units in the appendix.

3.3 Coulomb Drag resistivity

Our starting point is the drag resistivity within the random-phase approximation that is given in dimensionful units by the expression [73, 136, 38, 76]

$$\begin{aligned}\rho_D =&\frac{\hbar^2}{16\pi^3 e^2 n_1 n_2 k_B T}\int_{-\infty}^{+\infty}\frac{\mathrm{d}\omega}{\sinh^2(\hbar\omega/2k_BT)}\int \mathrm{d}\boldsymbol{q}\,\boldsymbol{q}^2\frac{\mathrm{Im}[\Pi_1(\omega,\boldsymbol{q})]}{|\Pi_1(\omega,\boldsymbol{q})|^2}|\chi_{12}(\omega,\boldsymbol{q})|^2\frac{\mathrm{Im}[\Pi_2(\omega,\boldsymbol{q})]}{|\Pi_2(\omega,\boldsymbol{q})|^2}\\ \equiv&\frac{\hbar^2}{e^2}\int_{-\infty}^{+\infty}\mathrm{d}\omega\int_0^{\infty}\mathrm{d}q\,\mathcal{I}(\omega,q)\end{aligned}, \tag{3.12}$$

where in the second line we defined the dimensionless integrand $\mathcal{I}(\omega, q)$ and use rotational invariance to choose, without loss of generality, a direction for the in-plane momentum. Here, n_1 and n_2 are the densities of the active and passive layers, respectively, $\Pi_i(\omega,\boldsymbol{q})$ are the corresponding intra-layer density-density response functions, and the dynamically screened inter-layer density response is given by the off-diagonal element of $\chi(\omega, q)$ defined through Eq. (3.11), that is

$$\chi_{12} = -\frac{\Pi_1\Pi_2}{\Pi_1\Pi_2\frac{e^2}{\epsilon q}\sinh(q\ell) + \left[\frac{2q\epsilon}{e^2} - \Pi_1 - \Pi_2\right]e^{q\ell}}\ . \tag{3.13}$$

This approximation ignores the effect of vertex corrections. However, as mentioned above, the electron self-energy in cuprates depends mostly on frequency. This feature is also captured in our holographic model where the low-energy theory is described by a 'semi-local' quantum critical phase, where the electron self-energy $\hbar\Sigma(\omega,\boldsymbol{k})$ scales like $\omega^{2\nu_k}$, with the momentum dependence only entering in the power ν_k [50, 3]. We, therefore, expect Eq. (3.12) to be a valid approximation for the Coulomb drag resistivity for a cuprate two-layer system in the strange-metal regime.

From Eqs. (3.12) and (3.13) we see that the only input we need to compute the drag resistivity are the single-layer response functions $\Pi_i(\omega,\boldsymbol{q})$. The power of our holographic approach now lies in the fact that it allows us to compute this response in a strongly interacting system. Here in particular, we focus on a regime where the length scale characterizing the strong interaction is much smaller than the lattice scale and, to first order, the behavior of the drag resistivity depends solely on the nature of the inter-layer interactions and not on disorder that would only give higher-order corrections to the drag. This may reveal interesting features of the cuprates, and possibly verify if the proposed holographic model of the strange metal correctly describes this phenomenon.

3.4 Results

We work in each layer with electrons at the same fixed equilibrium density n, separately conserved in each layer, and we study the holographic density-density response function that is anticipated to describe the physics of the strange metal near the Fermi momentum, in the regime where the dispersion of the electrons can be linearized. In the low-temperature regime and at energies and momenta much smaller than the Fermi energy and Fermi momentum, respectively, we find that the response function is well approximated by a hydrodynamic model, that takes the form (see Ref. [83] for details on the derivation)

$$\Pi(\omega, q) = \frac{q^2\left(\omega\mathcal{D} + iv_s^2 D_d \chi q^2\right)}{\omega^3 + i\omega^2 q^2(2D_s + D_d) - \omega q^2 v_s^2 - iv_s^2 D_d q^4} \ . \tag{3.14}$$

Analyzing its pole structure, we see that $\Pi(\omega, k)$ contains a linear sound mode at $\omega = \pm v_s q - iD_s q^2 + \mathcal{O}(q^4)$, and a diffusive mode at $\omega = -iD_d q^2 + \mathcal{O}(q^4)$, with $\mathcal{D}$ the Drude weight, and $\chi = -\lim_{q\to 0,\,\omega\to 0}\Pi(\omega, \boldsymbol{q})$ the (hydrodynamic) compressibility. This form of Π implies that the integrand in Eq. (3.12), *i.e.* $\mathcal{I}(\omega, q)$, contains, for our symmetric case $\Pi_i \equiv \Pi$ (it is straightforward to generalize the results to layers with different densities and three different surrounding dielectric constants [7]), in addition to a diffusive mode $\omega = -iD_d q^2$, the out-of-phase acoustic plasmon mode and the in-phase optical plasmon characteristic of a two-layer system [65, 125, 109, 120, 7]. The plasmon modes have been shown to play a key role in the drag resistivity in two-dimensional electron gases [36, 37, 61]. The latter frequencies are

$$\omega = \pm\sqrt{v_s^2 + \frac{\mathcal{D}\ell}{2\epsilon}}q + \mathcal{O}\left(q^2\right) \tag{3.15}$$

$$\omega = \pm\sqrt{\frac{e^2\mathcal{D}q}{\epsilon}}\left(1 + e^2\frac{v_s^2 - e^2\mathcal{D}\ell/2\epsilon}{2\mathcal{D}\epsilon}q\right) + \mathcal{O}\left(q^2\right) \ . \tag{3.16}$$

All three modes are clearly visible in the numerical result for the integrand in Fig. 3.4. These modes thus determine the low-temperature behavior of the drag resistivity. We emphasize here that compared to a purely hydrodynamic approach as in Refs. [5, 62], the holographic model gives also a prediction for the coefficients in Eq. (3.14) and for their temperature dependence, allowing us to fully determine the dominant low-temperature behavior of ρ_D. In particular, we numerically explored the pole

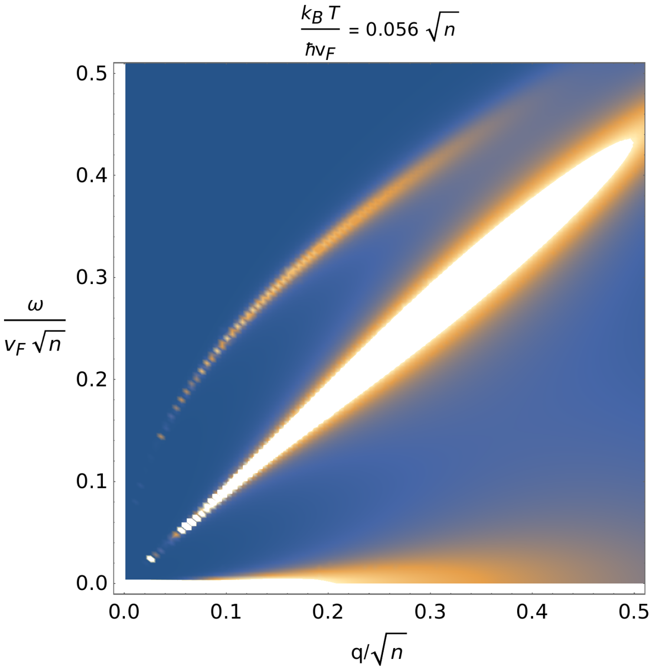

Figure 3.4: Typical integrand $\mathcal{I}(\omega, q)$ in Eq. (3.12), showing the in-phase and out-of-phase plasmon modes, and the low-energy diffusive mode.

structure of the retarded density-density correlators in the limit of $T \to 0$ to find that in this low-temperature hydrodynamics [28, 79, 24], the sound diffusion coefficient equals $D_s = (1/6\sqrt{3})k_B T/\hbar n$, whereas the charge diffusion constant obeys [57] $D_d = (4\pi/\sqrt{3})k_B T/\hbar n$. Notice that these scalings differs from the one found in the Reissner-Nordström background where there is no linear-in-T resistivity (see, e.g., Ref. [133]). Both coefficients are fully determined by background (thermodynamic) quantities, as is the zero-temperature 'Drude weight' $\mathcal{D} = (1/3^{1/4})v_F\sqrt{n}/\hbar$, where we use a slight abuse of terminology since the Drude weight for a system with translation invariance usually refers to the strength of the delta function in the zero-frequency limit of the optical conductivity $\sigma(\omega)$. As it is defined here $\mathcal{D}$ is such that $\lim_{\omega\to 0}\sigma(\omega) = \pi e^2\mathcal{D}\delta(\omega)$. The factor $v_F/3^{1/4}$ appearing in the Drude weight is, as expected, the low-energy speed of sound v_s, as we verified numerically finding $v_s \approx 0.76 v_F$. This differs from the $v_F/\sqrt{2}$ of a conformal field theory as conformal invariance is broken in the low-energy limit by the dilaton field. It is also slightly higher than expected from the thermodynamic potential Ω via $v_s = (-\partial\Omega/\partial\varepsilon)^{1/2} = \sqrt{17/31}v_F$, with the Ω defined as the gravitational action in Eq. (3.3) evaluated on-shell, and the equilibrium energy density ε such that it satisfies the thermodynamic relation $-\Omega/V = -\epsilon + sT + \mu n$, with s the entropy density. Accordingly, to zeroth order in T, $\chi = \mathcal{D}/v_s^2 \approx 1.32\sqrt{n}/\hbar v_F$ so that the height of the diffusive peak is determined by the subleading behavior $(\mathcal{D}/v_s^2 - \chi)/2 \approx 2.56(k_B T)^2/\sqrt{n}(\hbar v_F)^3$, with the proportionality constant obtained numerically.

The hydrodynamic model in Eq. (3.14), together with the above results, can be integrated to compute the drag resistivity according to Eq. (3.12). In general, this can only be done numerically, however, we can look at the dominant behavior in the low-temperature and large ℓ limit. In this regime, the dominant contribution to the drag resistivity is determined by the diffusive modes, and we can make the approximation

$$\mathrm{Im}[\Pi] = -\frac{\omega q^2 D_d (\mathcal{D}/v_s^2 - \chi)}{\omega^2 + D_d^2 q^4} \ . \tag{3.17}$$

Moreover, for large ℓ the contributions to the drag from the diffusive mode lie at low-energies $\omega \approx D_d q^2$, as the integration range is controlled by a factor $e^{-2q\ell}$ in χ_{12} from Eq. (3.13). Hence, $\sinh(\omega/2T)^{-2} \approx 4T^2/\omega^2$ and $\Pi \approx -\chi$, and we can then perform the frequency integral to obtain

$$\begin{aligned} \rho_D =& \frac{(\mathcal{D}/v_s^2 - \chi)^2 \hbar^2 k_B T}{4\pi D_d n^2 e^2} \int_0^\infty \mathrm{d}q \ \frac{e^{-2q\ell}}{|\frac{2q\epsilon}{e^2} + 2\chi + \frac{e^2(1-e^{2q\ell})}{2q\epsilon}\chi^2|^2} \\ \approx& \frac{(\mathcal{D}/v_s^2 - \chi)^2 \hbar^2 k_B T}{4\pi D_d n^2 e^2} \int_0^\infty \mathrm{d}q \ \frac{e^{-2q\ell}}{|2\chi + \frac{e^2(1-e^{2q\ell})}{2q\epsilon}\chi^2|^2} \ . \end{aligned} \tag{3.18}$$

Given the scaling of the coefficients presented above, this shows that–in the low-temperature limit–$\rho_D(T) \propto T^4$, strikingly different from the Fermi liquid result $\rho_D(T) \propto T^2$ due to thermal broadening of the Fermi surface [41, 73, 136]. In Fig. 3.5 we show a plot of $\rho_D/(k_B T)^3$ at low temperature for $\ell = 75$Å with the numerical integration of the full hydrodynamic model from Eq. (3.14) (blue line) and the diffusive-mode expression in Eq. (3.18), that shows the validity of the approximation in this regime. The dashed black line gives an upper-bound analytical estimate of the resistivity given by

$$\begin{aligned} \rho_D \lesssim& \frac{(\mathcal{D}/v_s^2 - \chi)^2 \hbar^2 k_B T}{4\pi D_d n^2 e^2} \int_0^\infty \mathrm{d}q \ \frac{e^{-2q\ell}}{|\frac{e^2(1-e^{2q\ell})}{2q\epsilon}\chi^2|^2} \\ =& \frac{3\zeta(3)\hbar^2}{8\pi n^2 e^2 \alpha^4} \frac{(\mathcal{D}/v_s^2 - \chi)^2 k_B T}{D_d \chi^4 \ell^4} \propto \frac{T^4}{\ell^4} \ . \end{aligned} \tag{3.19}$$

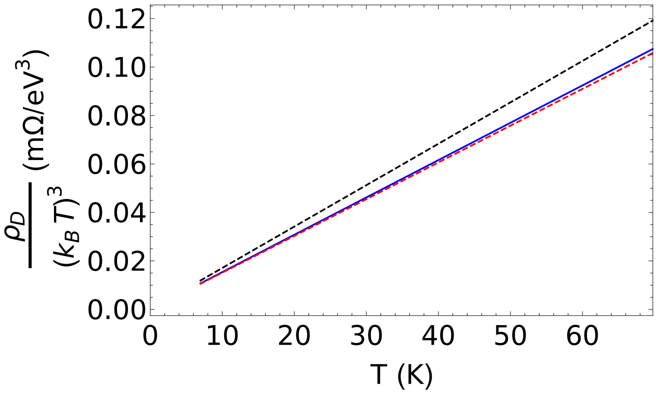

Figure 3.5: Low-temperature scaling of the resistivity in the hydrodynamic approximation (blue line) that shows $\rho_D \propto T^4$ and comparison with the model that only accounts for a diffusive mode as in Eq. (3.18) (red dashed line). The dashed black line shows the upper-bound estimate in Eq. (3.19) that can be computed analytically.

For the realistic system we want to model, we use the density $n = 6.25 \times 10^{14}\,\mathrm{cm}^{-2}$, the Fermi velocity obeying $\hbar v_F = 3\,\mathrm{eV\AA}$ as typical in the cuprates, and the inter-layer spacing $\ell = 6.2\,\mathrm{\AA}$, that is of the order of the effective inter-layer distance of LCCO planes used in the experiment on plasmons by Hepting *et al.* [59], and we assumed a dielectric constant of the insulating material between the layers of $\epsilon = 2\epsilon_0$. Further, we are able to give a quantitative result thanks to the above-mentioned matching of the prefactor N_G, otherwise undetermined in a bottom-up approach, with the experimentally determined plasma dispersion (see appendix for the details). For this smaller value of the interlayer distance, the full hydrodynamic result is considerably larger than expected from the response function with only a diffusive mode. Nonetheless, it shows the same T^4 dependence at small temperatures, where the contribution of the plasmon modes is still irrelevant, as shown in Fig. 3.6. It is important to notice that the temperature dependence of the dissipative coefficients D_d and D_s, that ultimately leads to the T^4 scaling of the drag resistivity, is characteristic of the particular holographic model used. However, the linear dependence on T of these coefficients comes from the linear-in-T resistivity, which is a fundamental requirement of any strange-metal model.

While the T^4 scaling controls the low-temperature behavior, at room temperature and higher temperatures, the above approximation breaks down. In this regime, the contribution of both the optical and the acoustic plasmon modes cannot be neglected and the drag resistivity grows faster with temperature. This is shown in Figs. 3.7 for the hydrodynamic approximation, where we plot for different temperatures the result

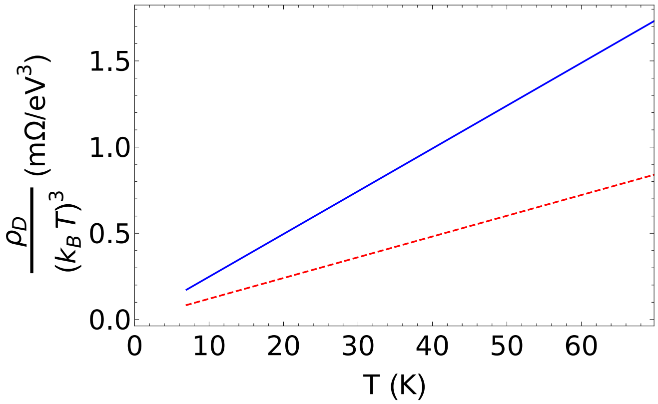

Figure 3.6: Low-temperature scaling of the resistivity in the hydrodynamic approximation (blue line) that shows $\rho_D \propto T^4$. Here we used the parameters of the cuprate modeled in this paper, that we introduced above. This shows that in this regime the resistivity presents the scaling expected from the diffusive mode (dashed red line), even though considering the diffusive mode alone underestimates its magnitude.

of the frequency integral in Eq. (3.12), i.e. $\mathcal{I}(q) \equiv \int \mathrm{d}\omega\, \mathcal{I}(\omega, q)$, rescaled with a factor $(k_B T)^4$. We see that at low temperatures the contribution from the plasmon modes is negligible and the integrand scales as expected from the argument presented above. As the temperature is increased the function develops a peak at low momenta, which is due to the contribution of the plasmon modes and does not scale with T^4. The effect of the plasmons and the change of the scaling behavior can also be seen in the log-log plot in Fig. 3.8. With the cuprate we are modeling in this paper, characterized by the quantities specified above, the system at higher temperatures enters a regime where both plasmon modes are relevant and we cannot simply neglect the contribution of one or the other. For this reason, together with the fact that at the higher values of T the exponential factor $\sinh(\omega/2T)^{-2}$ in Eq. (3.12) starts to dominate, the scaling of the resistivity in this regime cannot be described by a simple power law.

As of now, we looked at a hydrodynamic model, where the input from holography comes in the form of a prediction for the temperature dependence of the coefficients in the model. While we expect a deviation between the hydrodynamic model and the holographic response at larger temperatures, we show below that in the low-temperature limit we do not expect such a deviation to change the drag resistivity significantly. The low-energy physics described by the holographic EMD model is, in fact, not fully described by hydrodynamics, as it contains a quantum critical contribution characterized by a dynamical critical exponent $z = \infty$. In particular, this implies

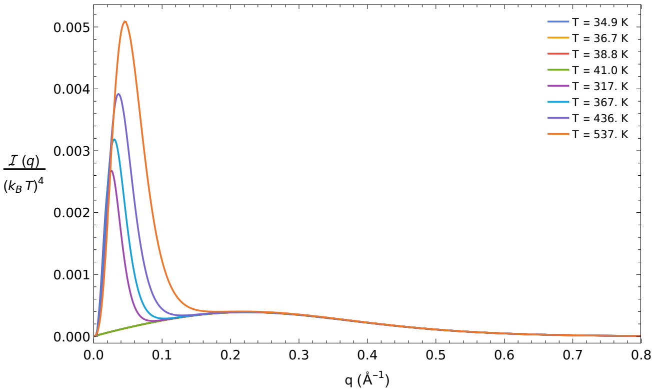

Figure 3.7: Result of the integral over frequency in Eq. (3.12) for the drag resistivity as a function of momenta rescaled with $(k_B T)^4$. We see that at low temperatures the contribution from the plasmon modes is negligible and the resistivity scale as $\rho_D \propto T^4$, while as the temperature is raised the contribution to the drag of the plasmon modes becomes more and more dominant.

that there is a quantum critical contribution to the low-energy spectral function, with $\hbar\omega \ll k_B T$, that scales with temperature as $\Pi \propto T^{2\nu_q}$, with ν_q a momentum dependent exponent [56]. One might then wonder if this low-energy scaling could affect the low-temperature scaling of the drag resistivity. However, in the holographic model used in this paper, we found, for the lowest temperatures accessible to our numerics where the drag resistivity is determined mostly by the low-frequency behavior of Π, that the temperature dependence of the modes in the integrand in Eq. (3.12) is well described by the hydrodynamic model, and corrections due to the momentum-dependent temperature scaling from the quantum critical sector can be neglected. This is pictured in Fig. 3.9 and 3.10 where we show, for some fixed momenta in our range of interest, that the diffusive mode in Im[Π] computed from holography scales as expected from the hydrodynamic model (dashed red line in the plots), with deviations that are only of higher order in temperature. It might be nonetheless an interesting point for future studies to check if there might be a setting where the quantum critical scaling becomes relevant to the drag resistivity even at low temperatures and if it could then be possible to observe it experimentally.

At higher temperatures, however, the relevant energy range for the computation of the drag resistivity becomes large enough that the deviation of the holographic solution from its approximation with the hydrodynamic model cannot be neglected, and we hence need a full numerical solution of the holographic model to compute the resistiv-

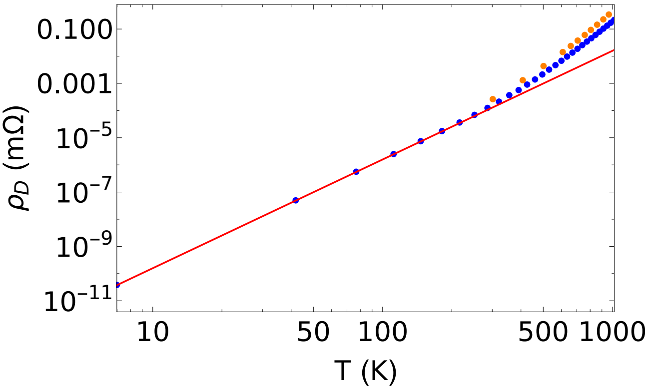

Figure 3.8: Log-log plot of the drag resistivity in the hydrodynamic approximation (blue dots) where we can clearly see the deviation from the T^4 behavior (represented by the red line) above room temperatures. We also show the results for the drag resistivity obtained from the holographic model (orange dots), as explained below.

ity integral. In particular, there is an enhancement of the plasmon modes contribution in the holographic solution, due to higher-order corrections neglected in the hydrodynamic model, as well as the quantum critical contribution. A distinction between the roles of these two contributions goes beyond the scope of this paper, but it can be an interesting problem to address in future studies. The greater contribution from the plasmon mode is shown for example in Fig. 3.11, where we plot the acoustic plasmon peak in the integrand $\mathcal{I}(\omega, q)$ at a fixed value of $q = 0.066\sqrt{n}$ for both the holographic model and its hydrodynamic approximation. As highlighted in Fig. 3.12, where we look at the integral over frequency rescaled with temperature, $\mathcal{I}(q)/(k_B T)^4$, the T^4 scaling that governs the low-temperature resistivity follows closely the hydrodynamic approximation (dashed blue line). Hence we expect the holographic drag resistivity to deviate more significantly from the hydrodynamic result at higher temperatures, as the contribution from the plasmon modes becomes more and more dominant. This is shown in Fig. 3.13 where we present the result for $\rho_D(T)$ up to high temperatures in holography (solid blue line) and hydrodynamics (dashed blue line). In particular, we see that in the holographic model just above room temperature there is a regime with a contribution to the temperature dependence coming from the different lifetimes of plasmon excitations at different temperatures. On the other hand, as we increase the temperature further, we enter a regime where the behavior of the drag resistivity is determined by the $\sinh(\omega/2T)^{-2}$ factor, hence $\rho_D(T) \propto e^{-\Delta/T}$, (dashed red curve in the plot). We found $\Delta \approx 6240$K, consistent with the acoustic plasmon energy.

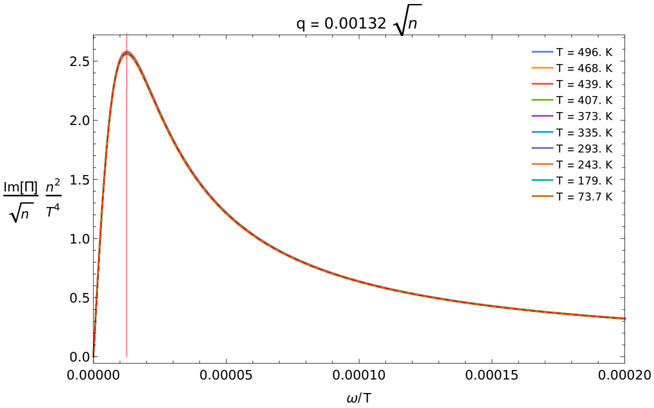

Figure 3.9: Data collapse of the imaginary part of the density-density response function at low energies - that determines the low-temperature drag resistivity - for several temperatures, together with the behavior expected from the hydrodynamic model (dashed black line), for one value of momentum relevant to the low-temperature resistivity $q = 0.00132\sqrt{n}$

3.5 Conclusions and outlook

We have here studied by holography the Coulomb drag between two strange metals and have shown how to determine the drag resistivity in such a strongly interacting system. We performed the computation within a particular model for which an analytical background solution exists and showed the important role of the plasmon modes in the drag resistivity at easily accessible temperatures. We found that the temperature scaling of the drag resistivity is governed at low temperatures by the hydrodynamic modes, whose scaling is fixed by the background solution of our holographic theory and is related to the fact that the model describes a strongly interacting system with linear-in-temperature resistivity. In particular, we showed that in the low-temperature limit the contribution from the plasmon modes is negligible and the scaling of drag resistivity follows from the scaling of the diffusion constants in the holographic density response function $\Pi(\omega, q)$, implying $\rho_D \propto T^4$ contrary to the T^2 behavior at low temperature in a Fermi liquid where the drag is governed by thermal broadening of the Fermi surface. As the temperature is raised above room temperature we found that the drag resistivity departs from the T^4 scaling due to the contribution of both the in-phase and out-of-phase plasmon modes. Here the holographic solution shows an enhancement of the drag resistivity compared to the hydrodynamic approximation, which neglects the quantum critical contribution.

The holographic model used captures various qualitative features of the low-energy

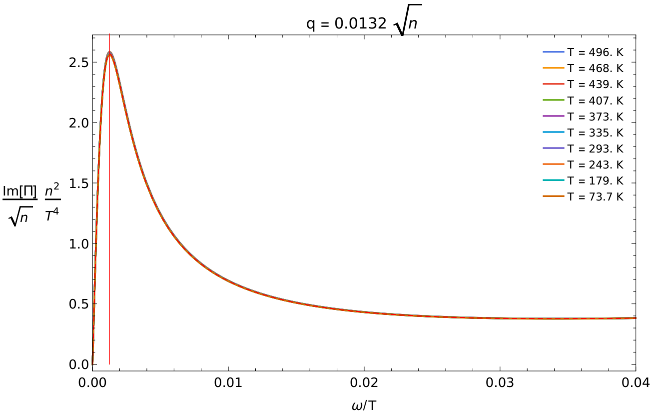

Figure 3.10: Data collapse of the imaginary part of the density-density response function at low energies, together with the behavior expected from the hydrodynamic model (dashed black line), at $q = 0.0132\sqrt{n}$

properties of the strange metal. However, we also have to keep in mind that it describes a system with a very different ultra-violet behavior compared to a laboratory cuprate material as the electronic dispersion is implicitly linearized and no lattice bandstructure is involved in the calculation. While this does not affect the emergent T^4 scaling behavior expected at low temperatures, it may affect the quantitative estimate of the drag resistivity somewhat. An important matter of future studies is the thermodynamics of the strange metal, as an analytical understanding of the observed values for the speed of sound and susceptibility is still lacking, as well as an analytical understanding of the role of the quantum critical sector in the drag resistivity. We, nevertheless, hope that the theory presented here may stimulate further experiments on drag transport to test holographic quantum matter in general and strange metals in particular.

3.A Prefactors and physical quantities

Here we explicitly show the relations between the dimensionless units used in the main text and the dimension-full variables, taking particular care in considering all the prefactors that have been set to unity in the main text for notational convenience. This makes clear the choice of parameters used to match the expected plasma frequency. In this section, we reintroduce the tilde notation for dimensionless variables, e.g. $\tilde{n} = L^2 n$. Remember that with our definition of dimensionless quantities we have that

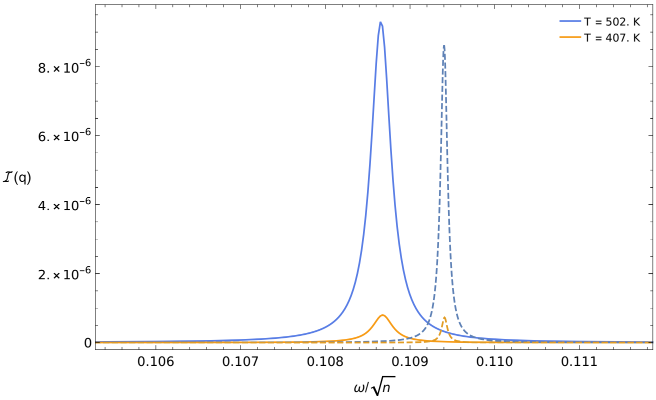

Figure 3.11: Comparison of the integrand function $\mathcal{I}(\omega, q)$ as defined in Eq. (3.12) at fixed $q = 0.066\sqrt{n}$ and high temperatures. We can see that the holographic result (solid lines) shows an enhancement of the plasmon contribution compared to the one expected from the hydrodynamic model (dashed lines).

lengths are measured in units of L, the AdS radius, energies in units of $\hbar v_F/L$ and the electric charge in units of $\hbar/Lg_F$. The action in these units then takes the form of Eq. (3.3). In order to further simplify the notation, we redefined the dimensionless action to set the prefactor $c^3L^2/16\pi\hbar G \equiv N_G$ to 1, which led to the definition of the dimensionless density as in the main text. However, the expectation values of boundary operators and, hence, boundary response functions are proportional to this unknown coefficient. To give a concrete example, using the holographic dictionary [134] that defines the chemical potential of the boundary theory as $\lim_{r\to\infty}\tilde{A}_0 \equiv \tilde{\mu}/\tilde{e}$, with $\tilde{e}$ the dimensionless electric charge, the corresponding density of the dual field theory can be computed by studying the (renormalized) boundary action to be

$$\tilde{n} = L^2 n = \frac{1}{\sqrt{3}}\frac{N_G}{\tilde{e}}\left(\frac{\tilde{\mu}}{\tilde{e}}\right)^2\sqrt{1+\frac{\tilde{e}^2\tilde{T}^2}{3\tilde{\mu}^2}}\ . \tag{3.20}$$

From now on, we redefine $\tilde{\mu}/\tilde{e} \to \tilde{\mu}$ and $\tilde{s}_0 = N_G/\tilde{e}$, in order to get rid of the dimensionless charge.

In bottom-up holography, the unknown constant $\tilde{s}_0$ is usually neglected and we are simply concerned with the qualitative behavior of the response function. By introducing the double-trace deformation that leads to plasmon modes in the system, we introduce a known scale given by the plasma frequency that we can use to uniquely determine the constant $\tilde{s}_0$. Looking at a single-layer cuprate, we have that the plasma

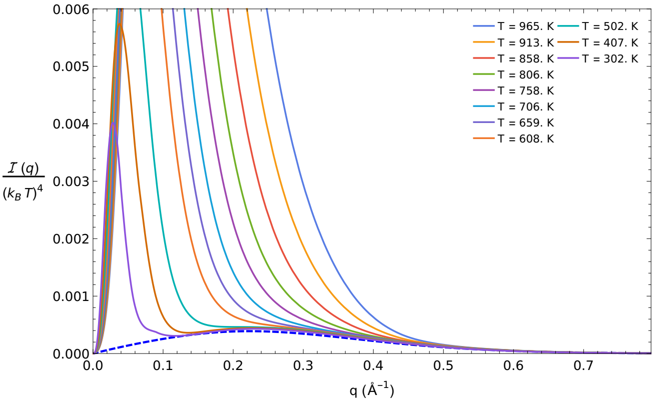

Figure 3.12: Result of the integral over frequency in Eq. (3.12) for the drag resistivity as a function of momenta rescaled with $(k_B T)^4$ for the holographic model (solid lines). We see that the contribution $\propto T^4$ that dominates at low temperatures is well captured by hydrodynamics (dashed blue line).

frequency is defined by the solution of

$$\Pi^{-1}(\omega, q) - \frac{e^2}{\epsilon}\frac{1}{2q} = 0 \ , \tag{3.21}$$

with ϵ the dielectric constant of the insulating material surrounding the layer. At low momenta, we found that the holographic model takes the hydrodynamic form in Eq. (3.14), which allows us to express the plasma frequency in terms of the Drude weight. In particular, we found that in our EMD theory the Drude weight in the units used in the main text is

$$\tilde{\mathcal{D}}(n, T) \equiv \frac{\hbar L}{v_F}\mathcal{D} = \frac{\tilde{s}_0}{\sqrt{3}}\tilde{\mu}(n, T) \ , \tag{3.22}$$

where we remind the reader that the dimensionful $\mathcal{D}$ is defined such that $\lim_{\omega\to 0}\sigma(\omega) = \pi e^2 \mathcal{D}\delta(\omega)$, and we made it explicit that $\tilde{\mu}$ is a function of the background density and temperature. In fact, for the numerical computation, it is often convenient to work at a fixed chemical potential and work with quantities that are rescaled by it, like $\tilde{\omega}/\tilde{\mu}$, $\tilde{\Pi}/\tilde{\mu}$ etc. Ultimately however, we work in a system at a fixed density and temperature, so that for every value of T and n, $\tilde{\mu}$ is determined according to Eq. (3.20), by $\tilde{\mu}(\tilde{n}, \tilde{T}) = \sqrt{\sqrt{108\tilde{s}_0^2\tilde{n}^2 + \tilde{T}^2} - \tilde{T}^4/\sqrt{6}}$. At $T = 0$ it reduces to the expressions presented in the main text in terms of $\tilde{n}$, since for $\tilde{s}_0 = 1$ we have $\tilde{\mu} = 3^{1/4}\sqrt{\tilde{n}}$. There we were only interested in the leading temperature behavior and we could ne-

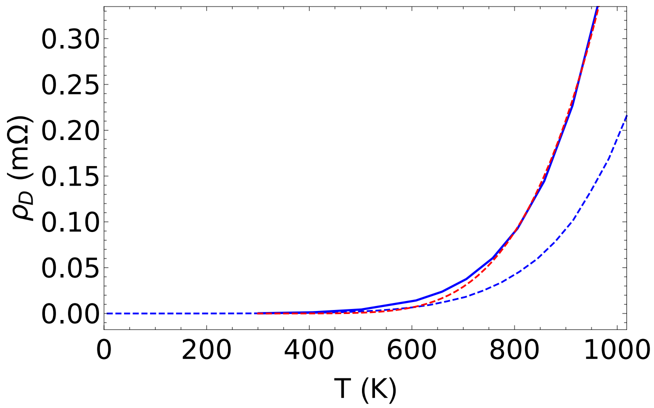

Figure 3.13: Coulomb drag behavior at large temperatures, where its behavior is determined by the plasmons, departing from the $\rho_D \propto T^4$ scaling of the low-temperature limit. Here we show the results of the holographic resistivity (solid blue line) and compare it with the hydrodynamic model (dashed blue line), showing an enhancement at high temperatures. In particular at temperature above approximately 800K the drag resistivity enters a regime where $\rho_D(T) \propto e^{-\Delta/T}$ (dashed red line), where we found $\Delta \approx 6240$K

glect the above subleading temperature correction from the chemical potential. From Eq. (3.21), we find that the plasma dispersion at low momenta is given by

$$\hbar\omega_{\rm pl}(q) = \hbar\sqrt{\frac{\mathcal{D}}{2\pi\epsilon}}\sqrt{q} = \sqrt{\frac{\tilde{s}_0\mu(n,T)}{2\sqrt{3}\tilde{\epsilon}}}\sqrt{\hbar v_F q}\ , \tag{3.23}$$

with $\tilde{\epsilon} \equiv \hbar v_F \epsilon/e^2$. Hence, for every fixed value of the density and temperature, we can determine $\tilde{s}_0$ from the plasmon dispersion.

In this paper, we aimed at modeling the cuprate layers as in Ref. [59], where they look at an (effectively) infinite stack of layers. In such a system they find that the plasma frequency for in-phase plasma excitations (i.e., when the out of plane momentum $q_z = 2\pi N$, $N \in \mathbb{N}$) obeys $\hbar\omega_{\rm pl}(q_z = 0) = 1.17$ eV. The equivalent expression for the plasma frequency in terms of the quantities defining our holographic model is

$$\hbar\omega_{\rm pl} = \hbar\sqrt{\frac{\mathcal{D}}{\pi\epsilon}}\frac{1}{\sqrt{\ell}} = \sqrt{\frac{\tilde{s}_0\mu(n,T)}{\sqrt{3}\tilde{\epsilon}}}\sqrt{\frac{\hbar v_F}{\ell}} = 1.17 \text{ eV}\ . \tag{3.24}$$

(See Ref. [96] for details of the computation). Notice that here $\mu(n,T)$ is the boundary chemical potential in dimensionful units. This is what we use to fix the scale $\tilde{s}_0$ and to translate the quantities obtain from the holographic computation in terms of SI units.

In particular, at $T = 0$ we have that

$$\sqrt{\tilde{s}_0} = 3^{1/4} \frac{\ell}{\sqrt{n}} \frac{(\hbar\omega_{\text{pl}})^2}{\hbar v_F} \frac{\epsilon}{e^2} \ . \tag{3.25}$$

Once we determined $\tilde{s}_0$, all the results obtained from the numerical computation can then be expressed in terms of SI units by fixing a value for T, n, ℓ, and v_F. Calling P_D the numerical integral for the drag in rescaled dimensionless units where $N_G = 1$, we have that the drag resistivity in Ohm is then related to P_D by

$$\rho_D = \frac{\hbar}{e^2 \tilde{s}_0^2} P_D \ . \tag{3.26}$$

Explicitely, in this paper we used $n = (0.25\text{Å}^{-1})^2 = 6.25 \times 10^{14}\text{cm}^{-2}$, $\hbar v_F = 3\text{eVÅ}$, $\ell = 6.2\text{Å}$, $\epsilon = 2\epsilon_0 = 2 \times 55.2610^{-4} e^2\text{eV}^{-1}\text{Å}^{-1}$. Fixing the in phase infinite-layer plasma frequency to be independent of temperature and equal to $\hbar\omega_{\text{pl}} = 1.17\text{eV}$ we obtain a (temperature-dependent) $\tilde{s}_0$ and a value for the holographic scale μ shown in Fig. 3.14. This last scale is what we then use to set all of the dimensionless quantities used in the numerical computation.

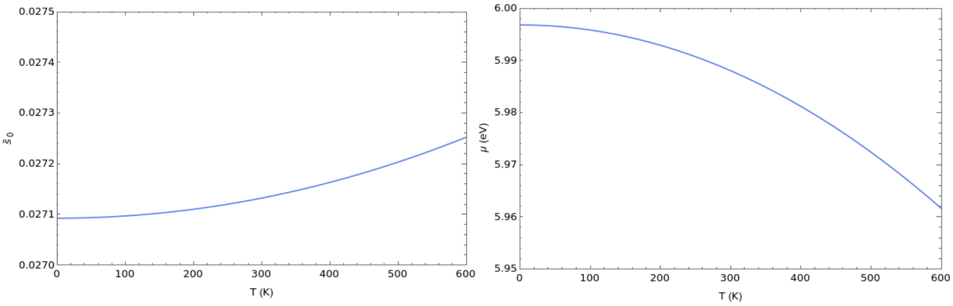

Figure 3.14: Value of the dimensionless parameters $\tilde{s}_0$ and the dimensionful chemical potential of the holographic theory μ chosen such that the plasma frequency of a layered system is fixed at all temperatures. We see that these value vary very little with temperature, with $\tilde{s}_0(T = 0) \approx 0.027$ and $\mu(T = 0) \approx 6\text{eV}$

Chapter 4

Momentum-dependent scaling exponents of nodal self-energies measured in strange metal cuprates and modelled using semi-holography

4.1 Introduction

The rich temperature versus doping diagram of the cuprate high-T_c superconductors presents a cornucopia of non-conformity [80]. In their normal state, these unusual metals have qualitatively different experimental behaviour than the Fermi liquid, with in particular the linear-in-T resistivity and its dissonant twin, the quadratic-in-T Hall angle, being among the most strange.

One intruiging possible explanation of strange metal phenomenology is that it is controlled by a strongly interacting quantum critical *phase*. If so, the immediate question follows whether their properties can be described by holographic emergence principles, as these approaches are uniquely suitable for describing such physics. Evidence for a quantum critical phase comes from high magnetic-field electrical transport experiments on overdoped cuprates [19, 6], and from laser-based Angle-Resolved PhotoEmission Spectroscopy (ARPES) on $Bi_2Sr_2CaCu_2O_{8+\delta}$ (Bi-2212), in which the normal state self-energy of the electrons in the nodal direction not only showed power-law behaviour in both ω and T, but the power varied smoothly from less than unity for underdoping, to the marginal Fermi-liquid value of unity for optimal doping [124] (a result first reported in 1999 [123]), to 1.2 for overdoping such that $T_c \simeq 0.75T_c^{max}$ [113].

Here, we explore the normal state over a much larger frequency and temperature range than before by studying overdoped samples of the single-CuO_2-plane cuprate $(Pb,Bi)_2Sr_{2-x}La_xCuO_{6+\delta}$ (Pb,Bi)-2201, using high-resolution ARPES. We uncover a *qualitatively* new facet of the self-energy of the nodal electrons, namely that it is not only a function of ω and T, but also dependent on the magnitude of the momentum away from the Fermi momentum $k - k_F$, yielding constant energy cuts through the spectral function (MDCs) with a non-Lorentzian lineshape.

After presenting the experimental data, we switch gears to test whether a quantitative theoretical description can be found using the tools of the holographic duality known as the Anti-de Sitter/Conformal Field Theory correspondence (AdS/CFT) from string theory [57, 133]. AdS/CFT approaches have been shown to successfully capture both Fermi-liquid-like [21] and non-Fermi-Liquid-like aspects of strange metallic behavior [31], including power-law self-energies with smoothly varying scaling exponents [91, 89].

Adopting a semi-holographic theoretical treatment [33], whose details are given in the Methods section, we can match its predicted k-dependent spectral function to the high-precision ARPES data across the doping range studied, for a wide energy range below the Fermi level E_F, and for momenta well away from k_F.

The combination of our experimental and theoretical results show that the k dependence of the exponents is not only experimentally detectable, but also quantifiable in sufficient detail to pose a real test for any theoretical explanation, one such theory being semi-holography.

What emerges is that, firstly, our ARPES data confirm that nodal electronic self-energies display a power law in frequency and temperature. Secondly, the scaling exponents describing the self-energies are experimentally shown to be momentum dependent. Thirdly, the observed exponents at k_F grow smoothly from unity at optimal doping towards the Fermi-liquid value of two, though this is never reached, even for non-superconducting samples. These results further strengthen the notion that the optimally and overdoped Bi-based strange metals do represent a novel quantum critical phase.

4.2 Nodal ARPES data and power-law analysis with k-independent self-energy

In Fig. 4.1 we show the imaginary part of the nodal self-energy of (Pb,Bi)$_2$Sr$_{2-x}$La$_x$CuO$_{6+\delta}$ over a large range in frequency, doping and temperature. Assuming the bare dispersion to be linear, $\varepsilon(k) = v_F(k-k_F)$, with v_F being the Fermi velocity and k_F the Fermi wave vector, the commonly made assumption of negligible k dependence - $\Sigma(k,\omega) \simeq \Sigma(\omega)$ - reduces the single-particle spectral function to a Lorentzian lineshape as a function of momentum k at each fixed frequency ω, i.e., $L(k) = \frac{W}{\pi}\frac{\Gamma/2}{(k-k_*)^2+(\Gamma/2)^2}$. Here $W(\omega)$ is the intensity, $k_*(\omega)$ the peak position, and $\Gamma(\omega)$ its width. For the results presented in the rest of this paper, $W(\omega)$ is not a key parameter and will not be discussed further. In practice, the peaks are better fit using a Voigt lineshape, the Gaussian part of which accounts for experimental resolution. In this commonly adopted framework, the imaginary part of the self-energy is then proportional to the width of the Lorentzian component as $\Sigma''(\omega) = v_F\Gamma(\omega)/2$ [123].

Confirming and extending the results in [113], the (ω,T)-dependent self-energy extracted in this way and shown in Fig.4.1 can be very well described by a remarkably simple phenomenological model dubbed the Power Law Liquid (PLL) [113], with three dimensionless parameters α, β and λ:

$$\Gamma = \frac{2\Sigma''(\omega,T)}{v_F} = G_0(\omega,T) + \lambda\frac{[(\hbar\omega)^2+(\beta k_B T)^2]^\alpha}{(\hbar\omega_N)^{2\alpha-1}} \ . \tag{4.1}$$

Here λ is a coupling constant describing the strength of the interaction, normalized to an energy scale $\hbar\omega_N = 0.5$eV for all dopings, and the parameter β sets the balance between the relative influence of temperature and frequency. $G_0(\omega,T)$ is an extra term, combining a self-energy contribution from impurity scattering, as well as electron-

4.2. Nodal ARPES data and power-law analysis with k-independent self-energy

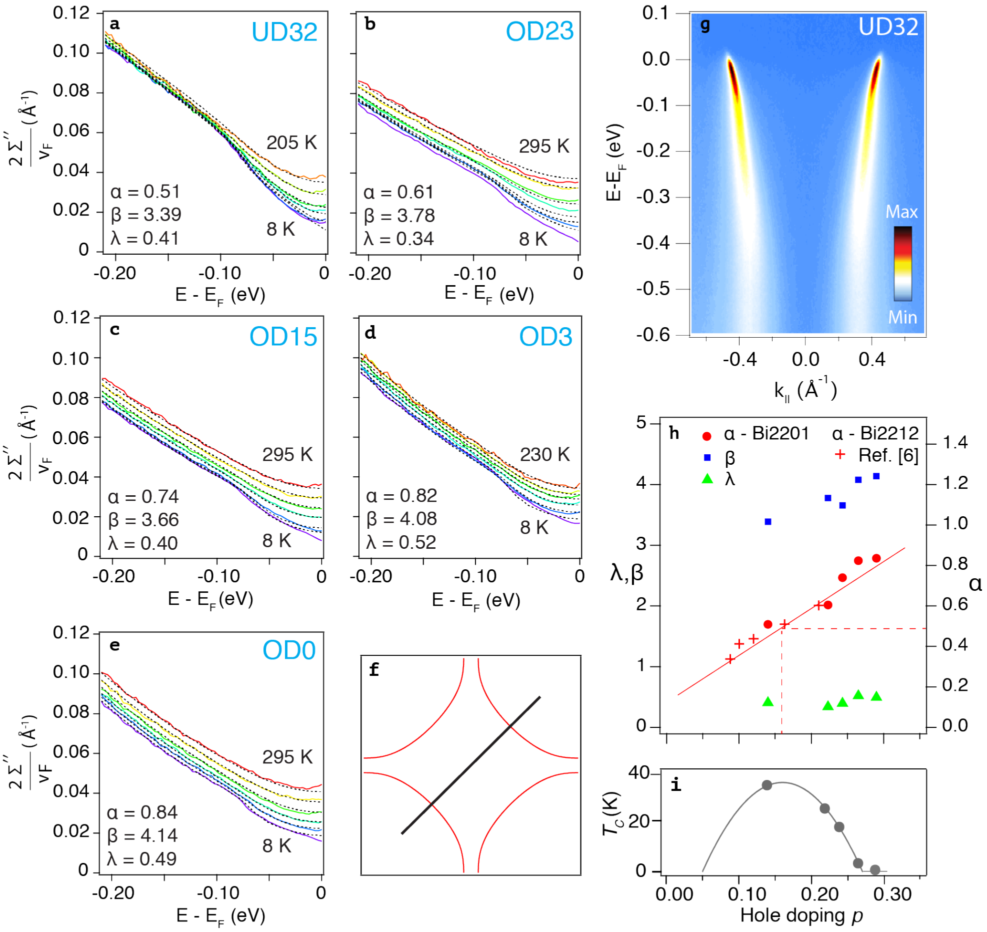

Figure 4.1: Nodal self-energy of single-CuO$_2$-layer (Pb,Bi)-2201. a-e: Temperature-dependent self-energies from ARPES for five different doping levels, extracted using symmetric Voigt fits to MDCs, plotted using colour-coded solid lines for temperature. The dashed, black lines are results to two-dimensional (in T and ω) fits employing three parameters (α, β, λ), using the power-law-liquid formalism introduced in [113] and given in Equation 1. Fitting parameters used are indicated in each data panel, and gathered together with the analogous parameters for Bi-2212 [113] in panel **h**. The red dashed lines indicate the marginal Fermi liquid ($\alpha = 0.5$ at optimal doping), which is shown above the canonical Presland dome **i** used to determine the doping level of the measured samples. Panel **g** shows a typical measured ARPES dataset, containing both the positive-k and negative-k nodal branches, along the k-space direction indicated in the schematic Fermi-surface in **f**. Table S1 in the SI lists all temperatures measured for each doping level.

phonon coupling, described in the SI[1] (S1). The electron-phonon contribution is most

---

[1] The supplementary information (SI) will be made available online when the paper is approved

clearly seen around an energy of 70 meV [13, 22], and is prominent because the normal state ARPES data presented here access much lower temperatures than those from Bi-2212 [113]. Note that Equation (4.1) describes the marginal Fermi-liquid [124] with a power of unity ($\alpha = 1/2$) at optimal doping, and the quadratic temperature and frequency behaviour of a Fermi liquid emerges when $\alpha = 1$.

Figs.4.1b-f show the experimentally extracted self-energies (coloured lines), together with the result of a two-dimensional (ω,T) fit to the data using Equation (4.1) (dashed lines). An overview of the parameters extracted from the fits is given in Fig. 4.1g, together with the parameters for Bi-2212 [113]. Compared to the latter, the ARPES data presented here cover a complementary doping range from near optimal doping ($p = 0.14$) to such overdoping that superconductivity disappears. Across this doping interval, the power increases smoothly from 1.04 ($\alpha = 0.52$) to 1.68 ($\alpha = 0.84$), meaning that even on overdoping out of the superconducting dome, the quadratic power of the Fermi-liquid ($\alpha = 1$) is not yet reached.

The continuity in α values evident in Fig. 4.1g emphasises the remarkably good agreement between the nodal self-energy behaviour in both single- and bi-layer cuprates, also illustrating that these self-energies near E_F are well described by Equation 4.1 for a temperature range spanning 200K.

4.3 Momentum-dependent power-law exponent and asymmetric ARPES MDCs

The above analysis does hinge on the aforementioned assumption of negligible k dependence: such that the spectral function part of the MDC lineshape can be well fit using a symmetric Lorentzian for each peak [77]. In Fig. 4.2a-d we show the Lorentzian fits in detail. Panel a shows that a Lorentzian spectral function gives a very good fit *close to* E_F, and yields a small residual. However, at higher binding energy, such as at 200 and 300meV, the foot of the peaks clearly show that the data (black crosses) are not captured completely by the two symmetric peaks in the fit (red lines). The experimental bottom line is that the MDC peaks in Fig. 4.2b & 4.2c are asymmetric: showing more spectral weight at large momenta $|k| > |k_*(\omega)|$, compared to $|k| < |k_*(\omega)|$ (leading to residual values of differing signs inside and outside the MDC peak pair). This behaviour cannot be captured by a fit based on Lorentzians

---

for publication.

and the power law liquid. The analysis and discussion covered by Figs. S2-S4 of the SI excludes that the MDC asymmetry comes from the non-zero curvature of an underlying 'bare band', from inhomogeneous detector response, or from strongly structured background signals. A simple yet profound possible explanation of the MDC asymmetry is then a k dependency of the electronic self-energy itself.

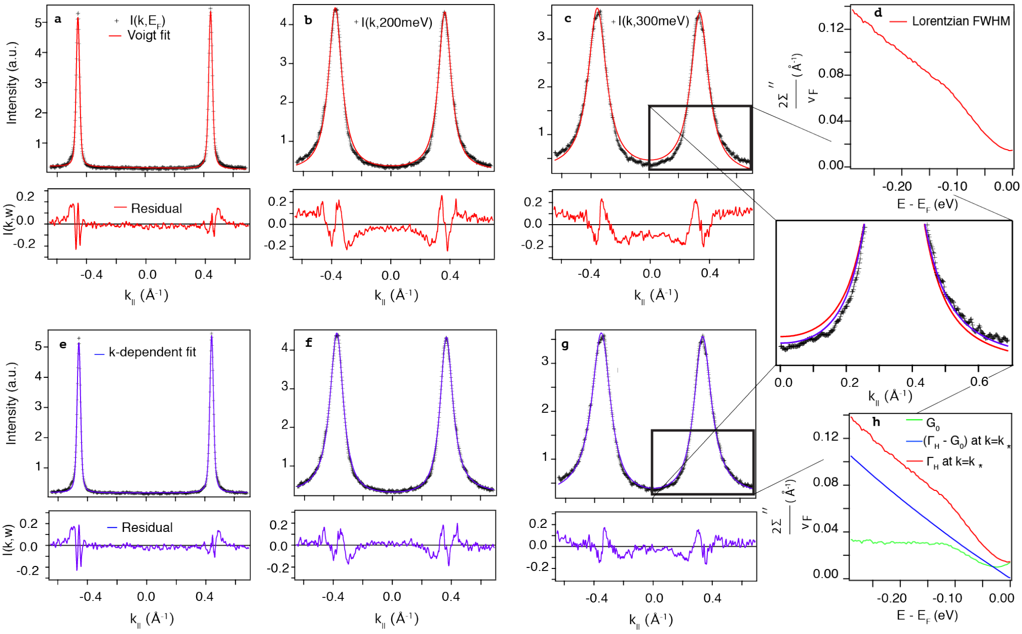

Figure 4.2: Closer look at MDC lineshapes for UD32 nodal ARPES data. a-c: a trio of MDCs at energies indicated, with symmetric peak fits in red. The residuals grow as the binding energy grows. Here **d** shows the resulting $2\Sigma''(\omega)/v_F = \Gamma(\omega)$ from the symmetric fits. **e-g**: The same three MDCs now fit in purple using our model given by Equation 4.3, including the holographically-predicted k dependence, with V set to -1. The residuals are clearly superior to the symmetric fit for energies further from E_F. **h:** The imaginary part of the self-energy $2\Sigma^{''}(k,\omega)/v_F = \Gamma_H(k,\omega)$ at $k_*(\omega)$ (red), which includes the k-dependent self-energy (blue), and the free fitting parameter G_0 (green).

Inclusion of a k-dependent self-energy, which is missing in the PLL ansatz of Equation (4.1), provides a significant experimental extension to the data-based fitness tests for aspiring theories for these materials. One model-independent approach would be to linearly expand the measured self-energy around k_F, reported in the SI (Fig. S8), which significantly enlarges the set of fitting parameters, by means of an additional frequency and temperature dependent function. Instead, we can rely on the theoretical input provided by AdS/CFT, and adjust the fitting ansatz without *any* expansion in the number of parameters.

4.4 Semi-holographic theoretical description

Physically, a semi-holographic model describes an electron that interacts with a CFT (accounting for a quantum critical state deformed by non-zero T and chemical potential) via linear coupling to a fermionic operator $\mathcal{O}$ that has a unique scaling dimension. As a result, the self-energy becomes proportional to the correlation function $\langle \mathcal{O}\mathcal{O}^\dagger \rangle(k, \omega, T)$ in the CFT. The latter can be determined from the holographic dictionary [133, 57], and automatically inherits certain scaling properties from the 'critical' CFT. To be applicable to the cuprate strange metals, the model must have a dynamical critical exponent $z \to \infty$ in order to recover the power law liquid when k is close to k_F. From this imposition of local quantum criticality, there follows a fundamental condition from the theory side that the scaling exponents *have to be momentum dependent* [32].

Here, for the CFT we use an Einstein-Maxwell-Dilaton model of holography, specifically the Gubser-Rocha model [51, 49], as it offers an analytical treatment of the gravitational spacetime. In the long-wavelength limit, within the framework of an emergent particle-hole symmetry, our semi-holography model then gives at $T = 0$:

$$\frac{2\Sigma''(k,\omega)}{v_F} = \lambda \frac{[(\hbar\omega)^2]^{\alpha(k)}}{(\hbar\omega_N)^{2\alpha(k)-1}} , \tag{4.2a}$$

$$\alpha(k) = \alpha \left(1 - \frac{k - k_F}{k_F}\right) . \tag{4.2b}$$

The semi-holographic self-energy can also be generalized to non-zero temperature [32, 49], and under our conditions is well approximated by replacing $(\hbar\omega)^2$ with $(\hbar\omega)^2 + (\beta k_B T)^2$ in Equation (4.2a). This also eases comparison to the PLL in Equation (1), and highlights the key new insight that as frequency increases, and $k \simeq k_F - \omega/v_F$ departs from k_F, a k dependence emerges in the *exponent* describing the (ω, T)-dependence of the self-energy. For low frequencies, where $k \simeq k_F$, one returns to Equation (4.1) of the PLL. The behaviour predicted by holography should leave a clear experimental fingerprint, namely that the ARPES MDCs are asymmetric: the data shown in Fig. 4.2 show this is the case.

Fig. 4.3a shows a simulated spectral function, generated using the semi-holographic self-energy shown in Figs. 4.3c & 4.3d. The resulting MDC asymmetry at non-zero energy is illustrated in Fig. 4.3b, visible as an increased intensity at the $|k| > |k_*|$ side of the peak maximum, just like in the experimental data of Fig. 4.2c. The next step is to test whether this holographic approach can yield superior quantitative fits to the ARPES data.

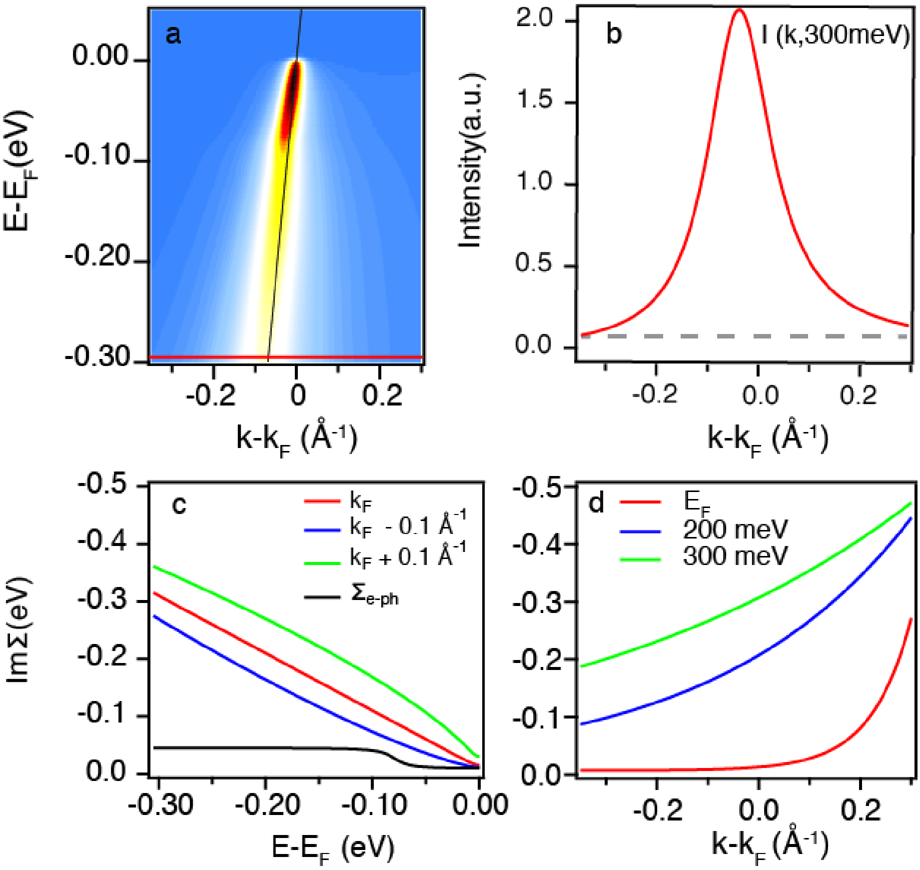

Figure 4.3: Simulated spectral function at optimal doping, using the k-dependent self-energy from semi-holography. **a**: Spectral function with a linear bare band (v_F = 4 eVÅ, k_F=0.45Å), convoluted with the experimental k resolution and **b** MDC at non-zero binding energy generated using the full ω and k-dependent self-energy plotted in panels **c** and **d** from the semi-holographic model at T=20 K. Note that **c** includes the imaginary part of a k-independent phonon self-energy.

4.5 Fitting the semi-holographic theoretical model to the ARPES data

As non-Lorentzian MDCs force a major departure from a cornerstone of ARPES data analysis methodology, we now describe how to deal with this in the analysis of real data from (Pb,Bi)$_2$Sr$_{2-x}$La$_x$CuO$_{6+\delta}$. The non-zero-T version of the self-energy with the k-dependence in Equation (4.2b), suggests a modified fit-function $L_H(k)$ at the fixed ω and T relevant for each MDC:

$$\begin{aligned} L_H(k) &= \frac{W}{\pi}\frac{\frac{\Gamma_H}{2}}{(k-k_*)^2+\left(\frac{\Gamma_H}{2}\right)^2}\ , && \text{(4.3a)}\\ \Gamma_H(k) &= G_0+\lambda\frac{[(\hbar\omega)^2+(\beta k_B T)^2]^{\alpha(k)}}{\hbar\omega_N^{2\alpha(k)-1}}\ , && \text{(4.3b)}\\ \alpha(k) &= \alpha\left(1+V\left[\frac{k-k_F}{k_F}\right]\right)\ . && \text{(4.3c)} \end{aligned}$$

$\Gamma_H(k)$ in Equation (4.3b) captures both the peak width and its asymmetry via momentum dependence built into the exponent $\alpha(k)$ in Equation (4.3c). By fixing α, β, λ and ω_N to the PLL values at low energies, only G_0 and the asymmetry parameter V remain free to vary in the fitting process for each MDC.

The Gubser-Rocha holographic model used here, however, actually *requires* that $V = -1$ for all frequencies. Thus, in this case the resulting fit function has exactly the same number of free parameters as the PLL, and is used to fit the experimental MDCs as shown using the purple lines in Fig. 4.2e-g.

Comparing Figs. 4.2b and 4.2c (PLL, k-independent) with Figs. 4.2f and 4.2g (k-dependent scaling exponents), it is clear that on adopting Equation (4.3), the residuals in the panels f and g for energies well below E_F drop, becoming as low as they were for the PLL at E_F. In particular, the zoom to Figs. 4.2c and 4.2g illustrates clearly that the asymmetry of the MDC peaks is now captured almost perfectly. Fig. 4.2h shows the total self-energy along the loci of the MDC peak-maxima in red, with the holographic, k-dependent part in blue, and the free fitting parameter G$_0(\omega, T)$ in green. The latter can be seen to automatically take on the combined form of an offset (impurity scattering) plus a step function centered at the phonon energy of 70 meV.

4.6 Testing the semi-holographic prediction

Upon determining all the free parameters in the theory (see Methods), two experimental tests of the semi-holographic results can then be performed. The first is a mild one, unconnected to the observed MDC asymmetry, and concerns the value of β, shown in Fig. 4.4a. The experimental values (blue squares) all reside in an interval between $\beta = 3 - 4$ across the doping levels studied. Those coming from our model lie between $\beta = 2 - 3$, and show a doping-dependent (generally upward) trend very similar to that of the experimental values. A detailed derivation of parameters such as β falls outside the experimental focus of this paper, and will be presented in a separate publication.

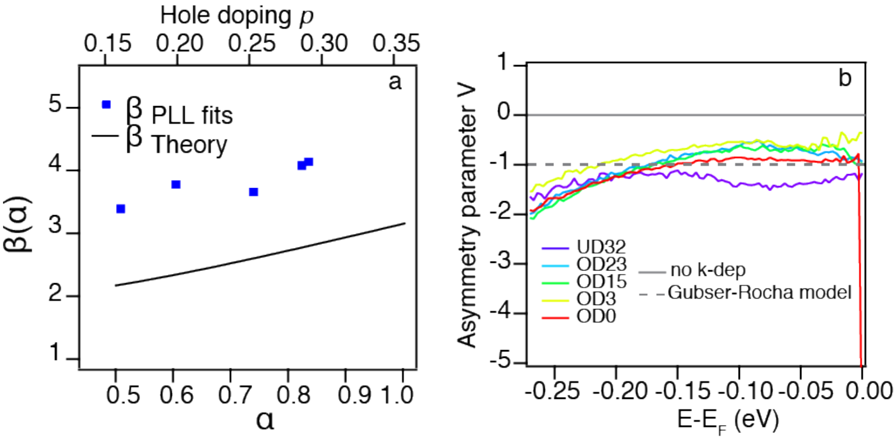

Figure 4.4: Testing the predictions from semi-holography a: Comparison between the coefficient β, determining the amount of temperature dependence in the self-energy, obtained from the PLL fit to the ARPES data (blue squares) and predicted by the holographic model (black line), as a function of the doping-dependent power α, which is translated into doping on the upper x-axis. **b:** Asymmetry parameter V of the momentum-dependent scaling exponent extracted from the experimental ARPES data over the full doping range measured at 8K, obtained by performing MDC fits to the data using Equation (4.3), where the leading scaling exponent α, the coupling constant λ and the quantity $(\hbar\omega)^2 + (\beta k_B T)^2$ are fixed. A value $V = 0$ means there is no asymmetry, and $V = -1$ is the prediction from the semi-holographic Gubser-Rocha model. The high temperature fits are shown in the SI section S6.

The second, more stringent test is given by the experimentally observed MDC asymmetry. The non-zero value of V is a non-trivial result, which is built into holography, but must be accounted for by other theoretical approaches aiming to describe the spectral function of the nodal charge carriers in cuprates. For the Gubser-Rocha model adopted here, the asymmetry parameter should have a frequency-independent value of $V = -1$. We test this by performing a second fit of the ARPES data, now leaving V as a free parameter for each ω. Fig. 4.4b shows that - with no guiding restraint at all applied to $V(\omega)$ - the experimental data yield for all doping levels, temperatures (see SI) and frequencies a value of $V \approx -1$, close to the semi-holographic prediction.

Fig. 4.4 shows that there is still some room for improvement as regards to both β and V in the current approach. Thus, these ARPES data and their parametrization presented here are an invitation to the many existing $z = \infty$ holographic models besides the analytical Gubser-Rocha model - or to completely different theoretical methods - to take the next step in capturing the observed β values and modest frequency dependence of V seen in experiment.

Before providing a discussion of other contexts in which k-dependent self energies have been discussed, we re-iterate the main results of this paper. The ω and T dependence of the electronic self-energy of nodal carriers in the normal state of the single-layer cuprate (Pb,Bi)-2201 is shown in ARPES experiments to follow a single power law with a *k-dependent scaling exponent*, yielding asymmetric, non-Lorentzian MDCs for energies away from E_F. From fits to the ARPES data from optimal doping across the whole overdoped portion of the phase diagram that work well over wide ranges in energy and temperature of more then 200 meV and 250 K, respectively, at $k = k_F$ the k-dependent power-law exponent is found to take a nearly marginal Fermi-liquid value of unity ($\alpha = 0.51$) at optimal doping, growing to 1.68 ($\alpha = 0.84$) for the most overdoped, non-superconducting system studied. For $k = k_F$, these results connect smoothly to those of [113]. However, for values $k \neq k_F$ these powers change. Such a k dependence is a key prediction from (semi)holographic models of strange metals as a quantum critical phase. The form of the k dependence and the asymmetry parameter describing its magnitude are all successfully fitted using semi-holographic single-fermion spectral functions. Importantly, any competing theoretical model for strange metals must be able to account for the observed ARPES MDC peak-asymmetry that is well described here by a momentum-dependent power-law self-energy.

There are few studies of the k dependence of the self-energy in solids. In the cuprate context, [111] and [126] present theory/modelling of possible k dependence in the self-energy resulting in a change in the dispersion velocity or arising from strong electron-phonon coupling, respectively. In a different condensed-matter realisation, k-dependent power laws have recently been observed in the zero-bias conduction anomaly in transport spectroscopy of nanowires [74], and linked to non-linear Luttinger liquid theory [66]. One might therefore wonder if there is a link between the 1D physics in the nanowire case, and the carriers in the nodal k-space direction of the quasi-2D (Pb,Bi)-2201 system that seem well described by the 1D CFT encoded semi-holographically in the AdS$_2$ infrared geometry of the $z = \infty$ models.

The results presented here herald future comparisons of the experimentally-tested, theoretical spectral function to other experimental probes such as optical and DC conductivities [70]. Alternatively, many-body condensed-matter theories can be guided by both the experimental self-energies presented here and the results from the AdS/CFT analogue, opening up possible pathways out of phenomenology and into a microscopic understanding of strange metals.

4.7 Methods

4.7.1 ARPES measurements

All ARPES data presented here were recorded at beamline I05 of Diamond Light Source, using (horizontally) linearly polarized light at a photon energy of 28 eV. Due to this chosen photon energy we can combine excellent energy resolution (12meV) with enough range in k space to measure both the negative-k and positive-k nodal branches in a single $I(k, \omega)$ image (see Fig. 4.1A), which is very helpful in distinguishing the subtle effects at play from possible complicating factors such as signal background. The energy resolution, together with the Fermi energy position - was confirmed by means of reference data from an amorphous Au film held in electrical contact with the sample. To account for resolution in the angular direction, both the Lorentzian MDC fit function used for the PLL analysis, and the L$_H$ MDC fit function from Equation(4.3) are convolved with a Gaussian of width 0.01 Å^{-1}. In the symmetric PLL case this yields a Voigt lineshape as indicated in the main text and in Fig. 4.2.

All data were recorded in swept mode, to ensure any detector-response inhomogeneity is averaged out in the energy direction, and were also confirmed to be free of detector non-linearity effects [112]. All data were recorded in the XΓX direction in the Brillouin zone.

High quality single crystals of diffraction replica-free (Pb,Bi)$_2$Sr$_{2-x}$La$_x$CuO$_{6+\delta}$, or (Pb,Bi)-2201), were grown using floating-zone techniques. Individual crystals were annealed in varying atmospheres for varying lengths of time, so as to change the oxygen content and with it the hole doping, controlling the carrier concentration and T_c. The critical temperatures were determined either via resistivity or AC-susceptibility measurements and the doping level was read off using T_c and the Presland formula [108, 4]. For the sample OD0K, $T_c \lesssim 2K \lesssim 0.05T_c^{max}$.

4.7.2 Holography and semi-holography

The Anti-de Sitter/Conformal Field Theory correspondence (AdS/CFT) links a classical gravitational theory with one additional spatial dimension to a strongly interacting quantum theory on the boundary of the extended space. In practice, it provides a systematic way to compute the response functions for a quantum theory with strong interactions, even at non-zero temperature and in the presence of a chemical potential, by means of solving a (relatively speaking) simpler problem, namely solving classical gravitational equations. For our purposes, therefore, the curved space is three dimensional and the quantum theory should describe the correlated physics of the maximally entangled fermions in the quasi-2D high-T_c cuprates [133, 57]. To be precise, holography describes the physics of a composite fermion $\mathcal{O}$ with a large number of degrees of freedom, i.e., in the so-called large-N limit. However, as we here are interested in testing theoretical predictions against spectral functions obtained through ARPES data, we ultimately want to compute the response function for an elementary fermion ψ. The solution is found within the semi-holographic framework [33], where the fermion ψ is linearly coupled to the composite fermion $\mathcal{O}$ and the Green's function describing the dynamics of ψ then acquires the form

$$G_{\psi\psi}(\omega, k) = \frac{1}{\omega - v_F(k - k_F) - g_s G^{-1}(\omega, k)} , \tag{4.4}$$

where $G^{-1}(\omega, k)$, assuming the role of the self-energy, is the two-point function of the composite fermionic operator $\mathcal{O}$, and $G_{\psi\psi}$ can be shown to be properly normalized as the Green's function of an elementary fermion [52]. The most important piece of the puzzle, the qualitative form of the complex self-energy at energies near the Fermi level, thus comes from holography. It is in this context that we compute the inverse Green's function $G^{-1}(\omega, k)$ appearing in Eq. (4.4). This is done by solving the Dirac equation on the curved gravitational background spacetime [68].

In general, as it has been done for the model in this paper, the gravitational equations needed to compute the holographic Green's function can only be solved numerically. Nonetheless, the qualitative behavior of the low-energy Green's function of such a fermionic operator can be obtained analytically and it is completely determined by the infrared properties of the theory, captured in the duality by the inner geometry of the gravitational spacetime. The electron self-energy obtained in this a way is the one we use for the nodal holes near the Fermi surface within the framework of an emergent particle-hole symmetry, and it possesses the desired (ω, T)-scaling properties, i.e., power-law exponents matching the experimental ARPES data. In particular, this implies that in the class of Einstein-Maxwell-Dilaton geometries characterized by the dynamical critical exponent $z = \infty$, and in the presence of a Fermi surface, the inverse Green's function at $T = 0$ (the low-energy behavior can be easily generalized to small non-zero temperature [49, 32]) has to assume a low-energy form near k_F [57] given by

$$G^{-1}(\omega, k) = g\omega(-\omega^2)^{\nu_k - 1/2} + \dots \ , \tag{4.5}$$

where g is constant in the limit $\omega, k - k_F \to 0$. It is important to note that the k-dependent power ν_k is solely dictated by the IR of the theory and thus is independent of any of the UV details. The lifetime of the fermionic excitations near the Fermi surface are then described by

$$\Sigma''(\omega, k) = -\frac{\lambda v_F}{2}(\omega^2)^{\nu_k} + \dots \ . \tag{4.6}$$

Theoretically, the constant $\alpha \equiv \nu_{k_F}$ in the exponent in Eq. 2b, depends on the two (dimensionless) parameters in the Dirac equation, the mass m and the charge q, that encode certain defining properties of the conformal field theory [57]. We keep the mass fixed close to the limit of $m = -1/2$ of the range allowed for by semi-holography $(-1/2 < m < 1/2)$ [52]. Then, varying only q as a function of the hole doping p, captures the doping dependence of the exponent $\alpha(p)$ seen in the experimental data, using the numerically obtained linear relationship $\alpha \approx 1.9q$. Finally, the value of λ (see Eq. 2a) leading to a match with experiment at each doping level can be obtained by adjusting the strength of the coupling g_s between the fermion ψ and the conformal field theory.

We can see that Eq. (4.5) has the same qualitative form as the semi-holographic response (4.4) for $\omega, k - k_F \to 0$. Semi-holography thus only changes the UV of the theory, i.e. the constant g, but it does not change the emergent behavior $\Sigma'' \propto (\omega^2)^{\nu_k}$. In this sense, while we showed that in our 'bottom-up' approach we possess enough tuning knobs so as to get a semi-holographic spectral function that closely resembles the one observed in the ARPES experiments, we do not know whether the values used do indeed correspond to a consistent theory of gravity. Nonetheless, our main point that the self-energy contains a momentum-dependent power is a universal feature of $z = \infty$ holographic calculations, independent of the particular UV completion applied. In fact, while the theoretical model proposed here is rooted in holography, any quantum critical theory with infinite dynamical exponent and a large-N suppression of higher-order correlation functions will be able to give rise to an effective correlation function of the same form as in Eq. (4.4) [57].

Chapter 5

Gauge/gravity duality comes to the lab: evidence of momentum-dependent scaling exponents in the nodal electron self-energy of cuprate strange metals

5.1 Introduction

Back in 1986, in one of the most exciting experimental discoveries in condensed-matter physics, the phenomenon of high-temperature superconductivity was observed for the first time in a layered copper-oxide perovskite by Bednorz and Müller [9]. Since then, other copper-oxide compounds or cuprates - a class of materials whose common trait is a layered structure of $\mathrm{CuO_2}$ planes - have been found with increasingly higher critical temperatures. This sits well above the expected limit from the BCS theory of superconductivity [8] that successfully describes the underlying physics of "conventional" superconductors. The desire to understand this phenomenon sparked a huge effort from both the experimental and the theoretical community to unveil the mystery behind the anomalous behavior of copper-oxide materials [80, 47], that eludes an explanation within the standard Fermi-liquid framework. This effort is still ongoing, underlining the challenges that these materials present due to the strongly interacting physics at play [80, 87, 116].

Peculiarities do not lie only within the superconducting phase, and the normal phase of the cuprates just above the maximum critical temperature in the phase diagram is known as the strange-metal regime. As the name suggests, this phase is characterized by a non-Fermi-liquid behavior as highlighted, for example, by an anomalous temperature behavior of the Hall angle [18] and by a linear-in-T resistivity, that does not saturate at high temperatures [23, 20, 16, 2, 88, 90] and persist at low temperatures even if superconductivity is suppressed by a magnetic field [64]. There have been a variety of attempts and techniques to model the properties of high-T_c cuprates, such as $t - J$ models, starting from the physics of the Mott insulator in the underdoped region of the cuprate phase diagram [87, 104, 99], the marginal Fermi liquid for describing the optimally doped strange metal [75, 81], and stripe phases in high-temperature superconductors [132, 30, 10, 127, 135], to mention a few. One technique, in particular, that has been used to describe a class of non-Fermi liquids that at low energies shares some of the properties of the strange-metal phase is based on the gauge/gravity (holographic) duality [34], which relates the response of a strongly interacting system to a higher-dimensional gravitational theory. With roots in high-energy and particle physics [94, 128, 48], it has proven to be a powerful tool when applied to strongly interacting condensed-matter systems to model their qualitative behavior [57, 133, 1], and also being able to describe some of the anomalous properties observed in transport experiments on cuprates [57]. Moreover, angle-resolved photoemission spectroscopy (ARPES) measurements pointed to a possible explanation of the phenomenology of the strange metal in the presence of a particular quantum critical phase that is local in space, and hence featureless in momentum [80, 113], in accordance with the marginal Fermi-liquid model. This is also well captured by the holographic realization of a strongly interacting fermion system [34, 67, 68, 91, 32, 21], that reproduces the marginal Fermi-liquid results near the Fermi surface. However, moving away from the Fermi surface these holographic models start to deviate from the completely featureless in momentum scaling of the marginal Fermi liquid, as they predict momentum-dependent scaling exponents [34, 67, 68].

Our main objective in this paper is to bring holography to the test of recent experimental ARPES measurements along the nodal line, to see what it can tell us about real samples of single-layer cuprates. In particular, we aim at verifying if its prediction of momentum-dependent scaling exponents in the electron self-energy can provide an explanation of the recently observed peak asymmetry in experimental data [119], that present a deviation from the previously proposed power-law liquid (PLL) model [113] of a momentum-independent self-energy, with an imaginary part obeying $\Sigma''_{PLL}(\omega; T=0) \propto (\omega^2)^\alpha$. Here α is a scaling exponent increasing (approximately linearly) with doping, from $\alpha = 1/2$ at optimal doping towards, but never reaching, the Fermi-liquid value of 1 [119, 103] at higher dopings. The analysis of the experimental data from ARPES measurements is performed on each momentum distribution curve (MDC), which measures the spectral function as a function of momentum at a fixed (negative) energy $\hbar\omega$. For a range of energies close to the Fermi surface, the PLL model predicts a Lorentzian lineshape for the distribution peaks as

$$\mathcal{A}(k;\omega) = \frac{W(\omega)}{\pi} \frac{\Gamma(\omega)/2}{(k - k_*(\omega))^2 + (\Gamma(\omega)/2)^2} \ , \tag{5.1}$$

where $\Gamma(\omega) = 2\Sigma''_{\mathrm{PLL}}(\omega)/v_F + G_0(\omega)$ is the full-width at half maximum (FWHM) with $G_0(\omega)$ describing contributions other than the electron self-energy to the width in the data, e.g., due to phonons, impurities, and instrument sensitivity. We define $\Sigma \equiv \Sigma' - i\Sigma''$, thus a negative imaginary part of the self-energy requires $\Sigma'' > 0$. In addition, v_F is the renormalized Fermi velocity and $k_*(\omega)$ determines the peak position $k_*(\omega) \simeq k_F + \omega/v_F$ with k_F the Fermi wave number.

In holography, a prediction, common to a large class of models proposed for the theoretical description of the strange metal, is that the electron self-energy is dominated by its frequency dependence, with the momentum dependence confined to its scaling exponent ν_k, so $\Sigma \propto \omega(-\omega^2)^{\nu_k - 1/2}$, with $\omega = \omega + i0$. Notice that in the literature this result is often quoted as $\Sigma \propto \omega^{2\nu_k}$, here however, in the range of interest to us $1/2 < \nu_k < 1$, we want to make the analytic structure of the self-energy explicit, with a branch cut everywhere on the real axis. In particular, we show that in the model analyzed in this paper we have

$$\Sigma(\omega, k; T=0) \propto \omega(-\omega^2)^{\alpha(1-(k-k_F)/k_F)} \ , \tag{5.2}$$

and we explain how this peculiar momentum dependence, that reduces to the PLL form for the sharp distribution peaks near the Fermi surface, provides a much better descrip-

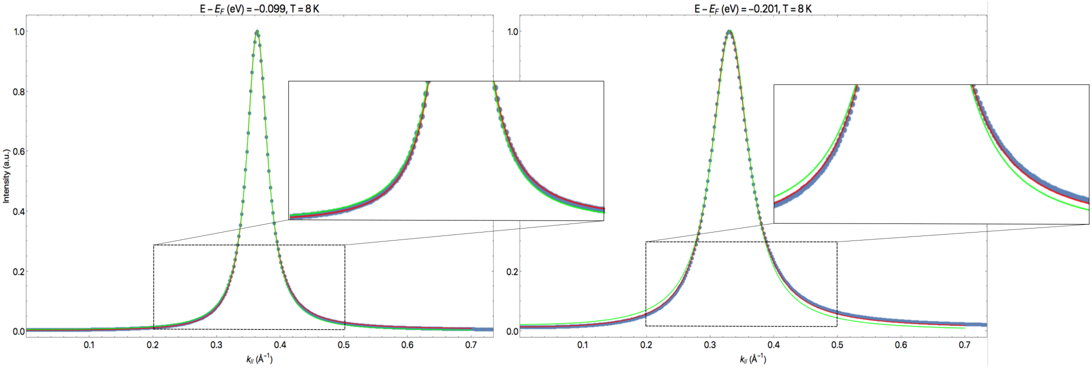

Figure 5.1: Comparison of the smoothed experimental data (blue dots) for an overdoped sample $\alpha = 0.65$ at $T = 8K$, with a Lorentzian fit based on the PLL (green line), and a fit based on the holographic prediction in Eq. (5.2) (red line). While there is little difference near the Fermi surface with $\hbar\omega = 0$ (left panel), it is evident that the holographic model accurately captures the peak asymmetry as we move away from the Fermi surface (right panel). The details of the fit are presented in section 5.5.

tion of the experimental data away from the Fermi surface. Indeed, this is found to well describe deviations from the typical symmetric Lorentzian shape of the peaks, as observed in very recent high-quality angle-resolved photoemission measurements [119], that are reproduced in Fig. 5.1, convincingly breaking the long-standing assumption of a self-energy that is completely independent of momentum. Note that, while our analysis arises from a holographic calculation of the self-energy, momentum-dependent exponents have also been theorized in a one-dimensional nonlinear-Luttinger liquid model [74]. The successful description of nodal MDCs by a momentum-dependent scaling exponent could, then, also hints at the emergence of one-dimensional physics along the nodal line.

In the hope to make this paper more accessible to a wider audience, we start first with a brief summary of holographic fermions in Section 5.2, where we introduce the gravitational background used and its main properties, and explain how to compute fermionic spectral functions in such a background. In particular, in order to make the connection with experimental results more clear, we express the holographic solution in terms of the only two energy scales of the boundary theory, namely the chemical potential μ and the thermal energy k_BT. The reader already familiar with holography might want to skip straight to Section 5.5 where the main new results are presented, and refer back to the first sections to check the notation, the conventions adopted as well as details of the derivations that led to the model given there. In Section 5.3

we then show how the low-energy behavior of the spectral function is related to the solution of the Dirac equation in the geometry of the deep interior of the spacetime, and in particular how this leads to an imaginary part of the self-energy described by momentum-dependent scaling exponents. We also explain how this gives rise to an asymmetry in the spectral function peaks. In Section 5.4 we introduce a semi-holographic construction as proposed in Ref. [52] and explain the limitations of this approach in describing quantitatively experimental data due to the non-universal real part of the self-energy. We then proceed to decouple the non-universal physics from the low-energy emergent quantum critical behavior in order to accurately model ARPES measurements on a single CuO_2-layer cuprate. The details of the modeling of the experimental data are the topic of Section 5.5, where we, in particular, explain how we need to interpret the holographic fermion response as the one for the holes with an emergent particle-hole symmetry. We also show how to change the parameters in the Dirac equation to describe different dopings in the cuprate and we finally introduce also the self-energy corrections due to the coupling to phonon degrees of freedom, so as to correctly capture the experimentally observed behavior of the MDC's at both low temperatures and higher frequencies.

5.2 Introduction to fermions in Einstein-Maxwell-Dilaton theories

In this section we summarize how to use the tools provided by the so-called AdS/CFT correspondence to compute fermionic spectral functions for a strongly interacting system. In particular, we introduce the gravitational background used for the computation and explain how it captures some key characteristics of the cuprates, as well as remind the reader how to add fermions in this background to compute the Green's function in the holography framework. Although the foundations on which this section is based can be found in Refs. [91, 68, 49], we use this section to introduce the notation used throughout the paper, with special emphasis on deriving the solution in terms of the boundary energy scales and in keeping track of dimensionful factors.

5.2.1 Gravitational background

For our background we use a 3D Einstein-Maxwell-dilaton theory [50] (where with the notation nD, we use the condensed-matter convention to denote with n the number of spatial dimensions only), that has been proposed as a holographic dual for the description of the low-energy physics of the strange-metal phase of the 2D and strongly interacting cuprates. The reasons are that it captures the linear in temperature behavior of the resistivity, it does not become unstable in the zero-temperature limit and, as will we show in this paper, it describes extremely well their fermionic response obtained by ARPES measurements. This is part of a large class of models characterized by a dynamical scaling exponent $z = \infty$ - of which the most studied one is the Reissner-Nordström background [91] - that describes an emergent low-energy quantum critical phase where, under a scaling transformation, time scales while space does not, with the deep implication that momentum becomes dimensionless under scaling and the electron self-energy is dominated by the frequency dependence. The Gubser-Rocha model considered here, is further characterized by a hyperscaling-violating exponent $\theta = -\infty$ that allows for the linear in temperature resistivity ρ and entropy S as $\rho \propto S \propto T^{(d-\theta)/z}$ in d spatial dimensions of the boundary, making it part of a subclass of models named "conformal-to-AdS$_2$" metals [133].

The Gubser-Rocha model is obtained from the gravitational action

$$S_{\text{EMD}} = \frac{c^3}{16\pi G} \int \mathrm{d}r \mathrm{d}(ct) \mathrm{d}^2x \sqrt{-g} \left[R - \frac{(\partial_\mu \phi)^2}{2} + \frac{6}{L^2} \cosh\left(\frac{\phi}{\sqrt{3}}\right) - \frac{e^{\phi/\sqrt{3}}}{4g_F^2} F_{\mu\nu}^2 \right] , \tag{5.3}$$

with r denoting the additional spacial direction of the curved bulk spacetime, R the Ricci scalar, ϕ a dimensionless scalar field known as the dilaton, and $F_{\mu\nu}$ the electromagnetic tensor with coupling constant

$$g_F^2 = \frac{c^4 \mu_0}{16\pi G} , \tag{5.4}$$

where $[\mu_0] = \text{m kg/C}^2$ is a constant with the dimension of a magnetic permittivity. Finally, L is the anti-de Sitter (AdS) radius. The equations of motion following from the action in Eq. (5.3) define a metric of the form $\mathrm{d}s^2 = e^{2\alpha(r)}(-f(r)\mathrm{d}t^2 + \mathrm{d}x^2) +$

$\mathrm{d}r^2 e^{-2\alpha(r)}/f(r)$ and are solved by

$$\begin{aligned}A_0(r) =& g_F \frac{\sqrt{3Q(r_0+Q)}}{L}\left(1-\frac{r_0+Q}{r+Q}\right) \ , \\ \phi(r) =& \frac{\sqrt{3}}{2}\log\left(1+\frac{Q}{r}\right) \ , \\ \alpha(r) =& \log\left(\frac{r}{L}\right)+\frac{3}{4}\log\left(1+\frac{Q}{r}\right) \ , \\ f(r) =& 1-\left(\frac{r_0+Q}{r+Q}\right)^3 \ ,\end{aligned} \tag{5.5}$$

with Q a positive integration constant with the dimension of a length and $r_0 \in [0,\infty)$ the horizon radius [50]. The chemical potential μ of the boundary field theory is defined through the asymptotic behavior of the bulk gauge field

$$\lim_{r\to\infty} A_0(r) = g_F \frac{\sqrt{3Q(r_0+Q)}}{L} \equiv \frac{\mu}{cq} \ , \tag{5.6}$$

with q the electric charge of the fermions introduced later and c the speed of light. At high-energies, this describes a system with a relativistic linear dispersion $\hbar\omega = \pm\hbar ck - \mu$. However, we are ultimately interested in the effective description of the electronic response in the cuprates, where near the Fermi energy the dispersion can also be linearized, but with a velocity v_F much smaller than the speed of light. Hence, we interpret the speed c in the holographic model as the (bare) Fermi velocity of the electron system near the Fermi surface. We come back to this point later on in Sec.5.5. The temperature of the boundary field theory can be computed from the black-hole horizon in the bulk spacetime

$$k_B T = \frac{c\hbar}{L}\frac{3\sqrt{r_0(r_0+Q)}}{4\pi L} \ , \tag{5.7}$$

and we can see that, contrary to the Reissner-Nordström solution, the Gubser-Rocha model has vanishing entropy, $S \propto A_{\mathrm{bh}} \propto \sqrt{r_0}$, in the zero-temperature limit, where $r_0 = 0$.

For better clarity as well as for numerical computations, we want to work with dimensionless quantities, by expressing everything in terms of physical constants and the dimensionful scale L of the theory, that is by measuring distances in units of L and energies in terms of $\hbar c/L$. We, therefore, define the dimensionless coordinates

$(\tilde{r}, \tilde{t}, \tilde{\boldsymbol{x}}) \equiv (r, ct, \boldsymbol{x})/L$, and we adsorb the gauge coupling into the field $\tilde{A}_\mu \equiv A_\mu/g_F$. The action in terms of these dimensionless coordinates and fields then becomes

$$\tilde{S}_{\text{EMD}} = \frac{c^3 L^2}{16\pi\hbar G} \int \mathrm{d}\tilde{r}\, \mathrm{d}\tilde{t}\, \mathrm{d}^2\tilde{x} \sqrt{-g} \left[R - \frac{(\partial_\mu \phi)^2}{2} + 6\cosh\left(\frac{\phi}{\sqrt{3}}\right) - \frac{e^{\phi/\sqrt{3}}}{4} \tilde{F}_{\mu\nu}^2 \right] . \quad (5.8)$$

We further define a dimensionless electric charge $\tilde{q} \equiv qLg_F/\hbar$ so that $\lim_{r\to\infty} \tilde{A}_0 = L\mu/\tilde{q}\hbar c \equiv \tilde{\mu}/\tilde{q}$, and temperature $\tilde{T} \equiv Lk_B T/\hbar c$. From now on, we will use dimensionless quantities only, unless explicitly stated otherwise, so we will drop the tilde for notational convenience.

The solutions in Eq. (5.5) can then be expressed in terms of the boundary field theory (dimensionless) chemical potential and temperature, to take the form:

$$\begin{aligned} A_0(r) =& \frac{\mu}{q} \left(1 - \frac{1 + q^2 \frac{(4\pi T)^2}{3\mu^2}}{1 + \sqrt{3} q \frac{r}{\mu} \sqrt{1 + q^2 \frac{(4\pi T)^2}{3\mu^2}}} \right) \\ \phi(r) =& \frac{\sqrt{3}}{2} \log \left(1 + \frac{1}{\sqrt{3} q \frac{r}{\mu} \sqrt{1 + q^2 \frac{(4\pi T)^2}{3\mu^2}}} \right) \\ \alpha(r) =& \log(r) + \frac{3}{4} \log \left(1 + \frac{1}{\sqrt{3} q \frac{r}{\mu} \sqrt{1 + q^2 \frac{(4\pi T)^2}{3\mu^2}}} \right) \\ f(r) =& 1 - \left(\frac{1 + q^2 \frac{(4\pi T)^2}{3\mu^2}}{1 + \sqrt{3} q \frac{r}{\mu} \sqrt{1 + q^2 \frac{(4\pi T)^2}{3\mu^2}}} \right)^3 , \end{aligned} \quad (5.9)$$

making it explicit that the solution depends only on the energy scale μ/q and on the dimensionless ratio qT/μ, as expected from the scaling symmetry of a deformed conformal field theory (CFT).

5.2.2 Holographic fermions

In order to use the tools of holography to compute the spectral function of a fermionic boundary operator $\mathcal{O}$, we need to add a Dirac action to the higher-dimensional gravitational background action S_{EMD} [91, 67, 68, 133], that, reverting back to dimensionful units for a moment, takes the form:

$$S = S_{\mathrm{EMD}} - ig_f \int \mathrm{d}r\mathrm{d}(ct)\mathrm{d}^2x\,\sqrt{-g}\bar{\psi}\left[e^{\mu}_{a}\Gamma^{a}\left(\hbar c\left[\partial_\mu + \frac{1}{4}\omega_{\mu bc}\Gamma^{bc}\right] - iqcA_\mu\right) - mc^2\right]\psi\ , \tag{5.10}$$

with $\bar{\psi} \equiv \psi^{\dagger}\Gamma^{0}$, $\Gamma^{bc} \equiv 2[\Gamma^{b}, Gamma^{c}]$, the vielbein e^{μ}_{a} is defined by $e^{\mu}_{a}e^{\nu}_{b}g_{\mu\nu} = \eta_{\mu\nu}$ and the spin connection is $\omega_{\mu bc}$, which ensures that local Lorentz symmetries are preserved and is defined as

$$\omega_{\mu cb} = \eta_{ca}\omega_{\mu}{}^{a}{}_{b} = \eta_{ca}(e^{a}_{\lambda}e^{\nu}_{b}\Gamma^{\lambda}_{\mu\nu} - e^{\nu}_{b}\partial_\mu e^{a}_{\nu})\ , \tag{5.11}$$

where $\Gamma^{\lambda}_{\mu\nu} \equiv 1/2g^{\lambda\sigma}(\partial_\mu g_{\sigma\nu} + \partial_\nu g_{\sigma\mu} - \partial_\sigma g_{\mu\nu})$ are the Christoffel symbols. Finally, g_f is a coupling constant with the dimension of an inverse velocity. Introducing the dimensionless variables of the previous section, we see that there are only two dimensionless parameters characterizing the fermions, namely $\tilde{q}$ and the dimensionless mass $\tilde{m} = mcL/\hbar$, as the action takes the form

$$\tilde{S} = \tilde{S}_{\mathrm{EMD}} - i\tilde{g}_f \int \mathrm{d}\tilde{r}\mathrm{d}\tilde{t}\mathrm{d}^2\tilde{x}\sqrt{-g}\bar{\psi}\left[e^{\mu}_{a}\Gamma^{a}\left(\left[\partial_\mu + \frac{1}{4}\omega_{\mu bc}\Gamma^{bc}\right] - i\tilde{q}\tilde{A}_\mu\right) - \tilde{m}\right]\psi\ , \tag{5.12}$$

where again, we are going to drop the tilde from now on, as we always use rescaled quantities unless explicitly mentioned otherwise.

In particular, since we are interested in a 2D boundary theory, we specified above already the case $d = 2$. In agreement with this, we now choose a representation of the Γ matrices of the form

$$\Gamma^{r} = \begin{pmatrix} \mathbb{1} & \mathbb{0} \\ \mathbb{0} & -\mathbb{1} \end{pmatrix}\ , \text{ and }\quad \Gamma^{\mu} = \begin{pmatrix} \mathbb{0} & \gamma^{\mu} \\ \gamma^{\mu} & \mathbb{0} \end{pmatrix}\ . \tag{5.13}$$

We can then decompose ψ in terms of the chirality eigenvectors of Γ^{r}, namely $\psi = \psi_R + \psi_L$ with $\Gamma^{r}\psi_R = \psi_R$ and $\Gamma^{r}\psi_L = -\psi_L$. Upon variation of the Dirac action in Eq. (5.12), we straightforwardly obtain the Dirac equation in a curved spacetime for the field ψ as

$$\left[e^{\mu}_{a}\Gamma^{a}\left(\left[\partial_\mu + \frac{1}{4}\omega_{\mu bc}\Gamma^{bc}\right] - iqA_\mu\right) - m\right]\psi = 0\ , \tag{5.14}$$

and similarly, we can obtain the equation of motion for $\bar{\psi}$. The boundary term arising from the variation of the action is given by

$$\delta S_\partial = - ig_f \int_\partial \mathrm{d}t\mathrm{d}^2x\sqrt{-h}\bar{\psi}\Gamma^r\delta\psi = \tag{5.15}$$

$$= - ig_f \int_\partial \mathrm{d}t\mathrm{d}^2x\sqrt{-h}(\bar{\psi}_L\delta\psi_R - \bar{\psi}_R\delta\psi_L)\ , \tag{5.16}$$

since terms of the form $\bar{\psi}_C\delta\psi_C = \psi_C^\dagger\Gamma^0\delta\psi_C = 0$, with $C = R, L$. Here h is the determinant of the induced metric on the boundary $h_{\mu\nu} = g_{\mu\nu} - n_\mu n_\nu$, n_μ being the normal vector orthogonal to the boundary.

If we now introduce a boundary term of the form

$$S_\partial = -ig_f \int \mathrm{d}t\mathrm{d}^2x\sqrt{-h}\bar{\psi}_R\psi_L\ , \tag{5.17}$$

the on-shell action is stationary upon imposing the boundary condition $\delta\psi_R = 0$. We then interpret the boundary value of the field ψ_R as the source of a boundary fermionic operator, with ψ_L determining its one-point function. Notice that the bulk spinor ψ has four components, half of which are related to the source, and the other half to the boundary fermionic operator for our two-dimensional theory. In order to make this split explicit, we define $\psi_\pm$ such that $\psi_R = \begin{pmatrix} \psi_+ \\ 0 \end{pmatrix}$ and $\psi_L = \begin{pmatrix} 0 \\ \psi_- \end{pmatrix}$, where $\psi_\pm$ are two-components Dirac spinors. These are not independent, but related by the Dirac equation by

$$\psi_-(r,\omega,\boldsymbol{k}) = -i\xi(r,\omega,\boldsymbol{k})\psi_+(r,\omega,\boldsymbol{k})\ , \tag{5.18}$$

where we adopted momentum-space representation for later convenience. Inserting Eq. (5.18) into the Fourier transform of the boundary action we obtain

$$S_\partial = -ig_f \lim_{\Lambda\to\infty}\int_{r=\Lambda} \frac{\mathrm{d}\omega\mathrm{d}^2k}{(2\pi)^3}\sqrt{-h}\psi_+^\dagger(r,\omega,\boldsymbol{k})\gamma^0(-i\xi(r,\omega,\boldsymbol{k}))\psi_+(r,\omega,\boldsymbol{k})\ , \tag{5.19}$$

where Λ is an ultra-violet (UV) cutoff scale.

Near the boundary (as $r \to \infty$) the mass term becomes the dominant one in the Dirac equation and ψ behaves as

$$\psi = \begin{pmatrix} \psi_+^{(0)} \\ 0 \end{pmatrix} r^{-3/2+m}(1+\dots) + \begin{pmatrix} 0 \\ \psi_-^{(0)} \end{pmatrix} r^{-3/2-m}(1+\dots) \ , \tag{5.20}$$

where the "…" stand for lower-order terms in the large-r limit and we restricted ourselves to $m \in (-1/2, 1/2)$. We can then interpret $\psi_+^{(0)} = \lim_{r\to\infty} r^{3/2-m}\psi_+$ as the source of the two-dimensional boundary Dirac operator $\bar{\mathcal{O}}_-$, with conformal dimension $\Delta = 3/2 + m$, whose one-point function is $\left\langle \bar{\mathcal{O}}_- \right\rangle = \bar{\psi}_-^{(0)}$. We then define the Green's function from the effective boundary action that can be written as

$$\begin{aligned} S_\partial =& - i \int \frac{\mathrm{d}\omega \mathrm{d}^2 k}{(2\pi)^3}\, \psi_+^{(0)\dagger}(\omega, \boldsymbol{k})\gamma^0 \left(-ig_f \lim_{\Lambda\to\infty} \Lambda^{2m}\xi(r=\Lambda,\omega,\boldsymbol{k})\right) \psi_+^{(0)}(\omega,\boldsymbol{k}) \\ =& - i \int \frac{\mathrm{d}\omega \mathrm{d}^2 k}{(2\pi)^3}\, \psi_+^{(0)\dagger}(\omega, \boldsymbol{k})\gamma^0 \left(-iG_H(\omega,\boldsymbol{k})\gamma^0\right) \psi_+^{(0)}(\omega,\boldsymbol{k}) \ , \end{aligned} \tag{5.21}$$

where we used $\langle \mathcal{O}_- \rangle = -iG_H\gamma^0\psi_+^{(0)}$ [91], so that the holographic Green's function is

$$G_H = \left\langle \mathcal{O}_- \mathcal{O}_-^\dagger \right\rangle \equiv \left(-g_f \lim_{\Lambda\to\infty} \Lambda^{2m}\xi(r=\Lambda)\gamma^0\right) \ . \tag{5.22}$$

Notice that in the mass range $-1/2 < m < 1/2$, both terms in the expansion in Eq. (5.20) are normalizable and there are, therefore, two possible quantizations. The one implicitly used above is known as *standard quantization*, where $\psi_+^{(0)}$ is the fixed source. However, in what is known as *alternative quantization* we exchange the role of coefficients, i.e., $\psi_+^{(0)}$ is now considered a dynamical field we can integrate over and we then have that ξ is proportional to the inverse of the Green's function, i.e., $G_H^{\mathrm{alt}} \equiv -G_H^{-1} = \left\langle \mathcal{O}_+ \mathcal{O}_+^\dagger \right\rangle$, where the last equality underlies that this alternative Green's function is the two-point function associated to a fermionic operator $\mathcal{O}_+$ with conformal dimension $\Delta = 3/2 - m$ [1]. As we will clarify later, it is this last interpretation of the boundary action that is used in semi-holography.

Given that we are ultimately interested in studying the response function, it is typical to derive an equation for the components of the matrix ξ directly. For definiteness, we choose a basis for the γ matrices as in Ref. [91]: $\gamma^0 = i\sigma_2$, $\gamma^1 = \sigma_1$, $\gamma^2 = \sigma_3$, with σ the Pauli matrices. Introducing the rescaled fields $\psi_\pm =$

---

[1] As you can see, the dimension of the operator in standard and alternative quantization is related by $m \to -m$, if we indeed always define the source as the leading order term in the expansion in Eq. (5.20), then changing the sign of m exchanges the roles of the coefficients as the source and operator response, effectively going from standard to alternative quantization.

$(-gg^{rr})^{-1/4}e^{-i\omega t+i\boldsymbol{k}\cdot\boldsymbol{x}}\begin{pmatrix} -iy_{\pm} \\ z_{\pm} \end{pmatrix}$ and using the rotational symmetry to set without loss of generality the momentum along the x-axis, i.e., $\boldsymbol{k} = (k, 0, 0)$, the bulk Dirac equation derived from the gravitational action in Eq. (5.10) reads

$$(\partial_r \mp m\sqrt{g_{rr}})\, y_{\pm} = \pm\sqrt{\frac{g_{rr}}{g_{xx}}}\left(k - \sqrt{\frac{g_{rr}}{-g_{tt}}}(\omega + qA_t)\right) z_{\mp} \ , \tag{5.23}$$

$$(\partial_r \pm m\sqrt{g_{rr}})\, z_{\mp} = \pm\sqrt{\frac{g_{rr}}{g_{xx}}}\left(k + \sqrt{\frac{g_{rr}}{-g_{tt}}}(\omega + qA_t)\right) y_{\pm} \ . \tag{5.24}$$

Finally, defining the field ratios $\xi_+ = y_-/z_+$, $\xi_- = z_-/y_+$, we can now show that the Green's function is

$$G_H = g_f \lim_{\Lambda\to\infty} \Lambda^{2m} \begin{pmatrix} \xi_+(r = \Lambda, \omega, k) & 0 \\ 0 & \xi_-(r = \Lambda, \omega, k) \end{pmatrix} , \tag{5.25}$$

where $\xi_{\pm}$ are solutions to

$$\partial_r \xi_{\pm} = -2m\sqrt{g_{rr}}\xi_{\pm} \mp \sqrt{\frac{g_{rr}}{g_{xx}}}\left[\left(k \mp \sqrt{\frac{g_{rr}}{-g_{tt}}}(\omega + qA_t)\right) - \left(k \pm \sqrt{\frac{g_{rr}}{-g_{tt}}}(\omega + qA_t)\right)\xi_{\pm}^2\right] , \tag{5.26}$$

with the infalling boundary conditions at the black-hole horizon for the fermionic field ψ corresponding to $\xi_{\pm}(r = r_0) = i$ at any non-zero frequency [2]. Furthermore, it follows from Eq. (5.26), that the solutions for $\xi_{\pm}$ satisfy $\xi_{\pm}^{(m)}(\omega, k) = -1/\xi_{\mp}^{(-m)}(\omega, k)$. Hence, the Green's function for $-m$, when $m \in (-1/2, 1/2)$, is simply equivalent to the Green's function in alternative quantization. We can also see that $\xi_+(\omega, k) = \xi_-(\omega, -k)$, allowing us to focus only on one component of the Green's function matrix.

The spectral function for the holographic fermion highlights the presence of a Fermi surface at a non-zero $k \equiv k_F$, as shown in Fig. 5.2 by a sharp peak at $\omega = 0$, corresponding to the Fermi energy. Depending on the m and q parameters in the Dirac equation, there can be zero, one or multiple Fermi surfaces [91, 49]. However for the values of the mass and the charge that we use in the rest of the paper we always deal with a single well-defined Fermi surface, as in the example shown in Fig. 5.3.

The physics of the Green's function near the Fermi surface is well captured by a

---

[2] In the background used in this paper, the boundary conditions at zero frequency become $\xi = \pm\sqrt{g_{xx}(r_0)}m/k - \sqrt{g_{xx}(r_0)m^2/k^2 + 1}$

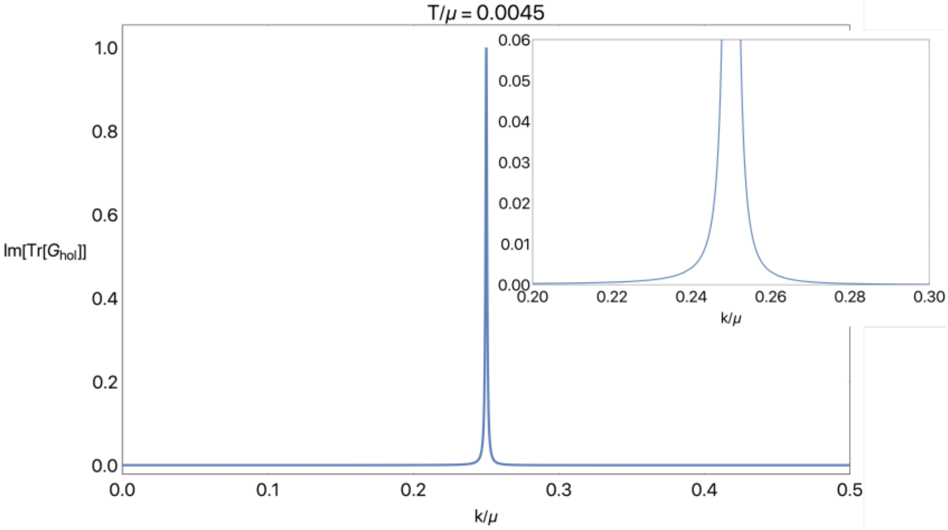

Figure 5.2: Peak in the fermionic spectral function at the Fermi energy, normalized to peak height, and a zoomed-in version (top right), showing the presence of a Fermi surface. Here we used $m = -0.49$ and $q = 0.27$.

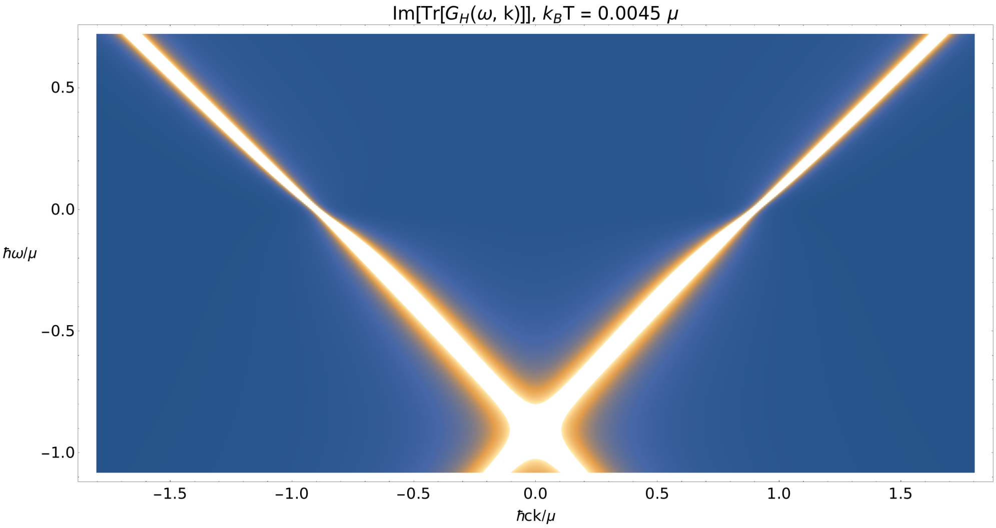

Figure 5.3: Spectral function for a fermionic operator computed from holography. It is symmetric in momentum and it shows a linear dispersion expected for a massless fermion, with the cone shifted down by the chemical potential. Here we used $m = -0.49$ and $q = 0.27$.

familiar form for the two-point function of a fermionic particle

$$G_H \simeq \frac{Z}{-\omega + v_H(k-k_F) - i\Sigma''(\omega,k)}\ , \tag{5.27}$$

with $\Sigma''(\omega,k) > 0$ governing the decay rate of the excitations and hence determining the shape of the peaks observed in ARPES experiment. For this reason, it is the main focus of this paper and we analyze it in detail in the next section. In many holographic theories, as in the Gubser-Rocha model used here, k_F, v_H, and Z can only be determined numerically, for general m and q, from the full solution of Eq. (5.26). In particular, we keep the value of $m = -0.49$ fixed throughout the paper, the reason for the choice of this particular value is mentioned in section 5.5.4, and the values for the above quantities as a function of q is shown in Fig. 5.4. We show this dependence here explicitly as it will essentially turn out to be the doping dependence of the ARPES experiments later on.

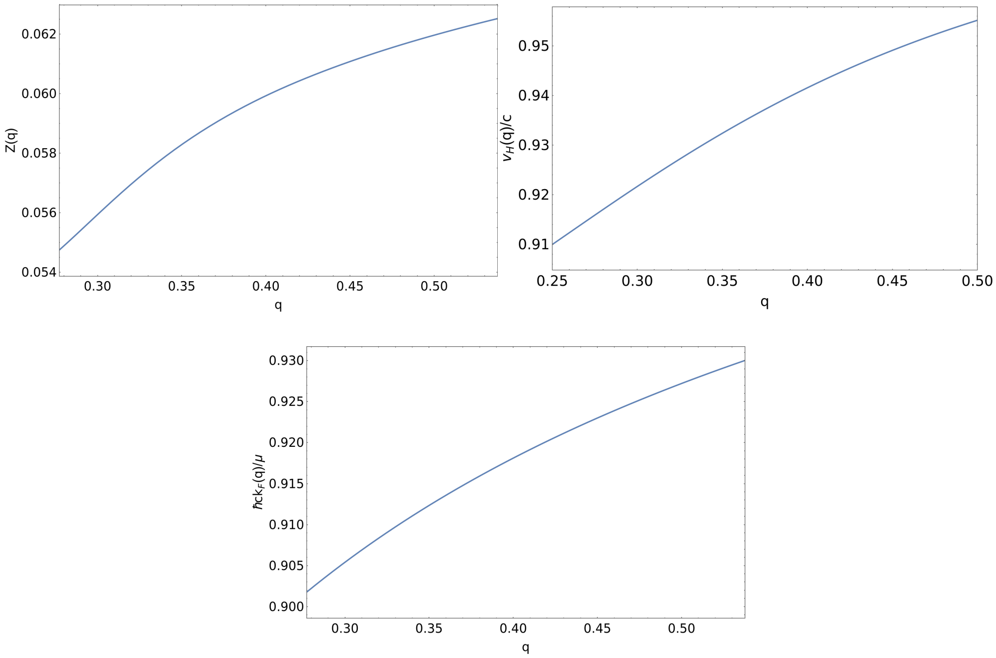

Figure 5.4: Numerical results for the dependence on the charge q of the quantities determining the Green's function near the Fermi surface. We fixed the mass $m = -0.49$ and we used a value $k_B T/\mu = 4.5 \times 10^{-3}$

5.3 Near-horizon geometry and IR emergent semi-local quantum liquid

Here we show that the near-horizon geometry implies a low-energy scaling of the zero-temperature Green's function of the form $\omega(-\omega^2)^{\nu_k - 1/2}$, where the leading momentum dependence only enters through the $k-$dependent exponent. In particular, we stress the difference between the results for the Reissner-Nordström theory, where the exponent ν_k for the fermionic spectral function depends also on the charge q and mass m of the fermionic field, and the solvable EMD background solution proposed by Gubser and Rocha [50] where the exponent depends on momentum only.

5.3.1 Near-horizon Dirac equation

The holographic duality has found a place in the toolbox of condensed-matter physicists as it allows for a qualitative description of the emergent infrared (IR) physics in strongly interacting systems governed by a universal quantum critical phase. The extra "radial" spacetime dimension in the dual gravitational theory geometrizes the energy scale of the theory, and the near-horizon geometry controls all the low-energy dissipative processes. As such, in application to condensed-matter problems, holography can be thought of as an effective field theory that describes the low-energy physics up to ultraviolet (UV) coefficients that depend on the particular UV completion, i.e., on the asymptotic (large-r in our conventions) form of the dual spacetime. That is to say $\mathrm{Im}[G_H(\omega, k; T)] \propto \mathrm{Im}[\mathcal{G}_k(\omega; T)]$, with $\mathcal{G}_k$ the IR Green's function in the regime where $T, \omega \ll \mu$. In particular then, this allows us to study the T and ω dependence of the low-energy dissipative physics of our strongly interacting fermion system by solving the Dirac equation in the geometry of the deep interior of the spacetime. This is exactly the focus of this section. In the case at hand, we show that in the emergent geometry - that is conformal to $AdS_2 \times \mathbb{R}^2$ at $T = 0$, with the AdS_2 replaced by a Schwarzschild black-hole geometry at non-zero T - the Dirac equation can be solved analytically [49]. This gives rise to a self-energy scaling $\Sigma(\omega, k) = C_k \omega(-\omega^2)^{\nu_k - 1/2}$, with $C_k \in \mathbb{R}$ and the momentum-dependent scaling exponent $\nu_k \propto q|k|/\mu$. In a narrow momentum range near k_F the scaling exponent can then be considered constant $\nu_k \simeq \nu_{k_F}$ and we immediately see that we recover the physics of the power-law-liquid self-energy proposed to describe the results of ARPES measurements on cuprates [113]. In later sections, we however argue that away from the Fermi surface, the experimentally observed peaks span a momentum range large enough to be able to observe an effect of the momentum dependence in the scaling exponent. In particular, we see that the momentum dependence implies that the peaks in the MDCs, described by a symmetric Lorentzian in the power-law liquid, become asymmetric as more spectral weight is shifted towards $|k| < |k_F|$, as also noticeable by looking closely at the tails of the distribution in Fig. 5.2. Given the importance of the deep interior of the spacetime, below we compute exactly what this form is.

In the following we are going to focus on the ξ_- component of the Green's function, hence the relevant equations from Eq. (5.14) are

$$\partial_r \begin{pmatrix} y_+ \\ z_- \end{pmatrix} = \begin{pmatrix} m\sqrt{g_{rr}} & \sqrt{\frac{g_{rr}}{g_{xx}}}k - \sqrt{\frac{g_{rr}}{-g_{tt}}}(\omega + qA_t) \\ \sqrt{\frac{g_{rr}}{g_{xx}}}k + \sqrt{\frac{g_{rr}}{-g_{tt}}}(\omega + qA_t) & -m\sqrt{g_{rr}} \end{pmatrix} \begin{pmatrix} y_+ \\ z_- \end{pmatrix} . \tag{5.28}$$

Expanding the EMD metric from Eq. (5.9), in the low-energy, low-temperature limit, to leading order in r/μ we find

$$\begin{aligned} \sqrt{g_{rr}} &\simeq \frac{1}{3^{3/8}\frac{\mu}{q^{1/4}}\left(\frac{r}{\mu}\right)^{3/4}\sqrt{1 - q\frac{(4\pi T/\mu)^2}{3\sqrt{3}}\frac{\mu}{r}}} , \\ \sqrt{\frac{g_{rr}}{g_{xx}}} &\simeq \frac{1}{\frac{\mu^2}{q}\frac{r}{\mu}\sqrt{1 - q\frac{(4\pi T/\mu)^2}{3\sqrt{3}}\frac{\mu}{r}}} , \\ \sqrt{\frac{g_{rr}}{-g_{tt}}} &\simeq \frac{1}{3^{3/4}\frac{\mu^2}{\sqrt{q}}\left(\frac{r}{\mu}\right)^{3/2}(1 - q\frac{(4\pi T/\mu)^2}{3\sqrt{3}}\frac{\mu}{r})} , \\ A_0 &\simeq \sqrt{3}\mu\frac{r}{\mu} . \end{aligned} \tag{5.29}$$

In order to compute the IR Green's function $\mathcal{G}_k(\omega, k; T)$ we now need to solve Eq. (5.28) in such a geometry. The computation for fermions in a 3D boundary theory in the $(4+1)$-dimensional generalization of the background used here was first done by Gubser *et al.* [49]. Here, however, we are interested in describing a single-layer cuprate strange metal and hence we consider a boundary theory in two spatial dimensions dual to a $(3+1)$-dimensional bulk spacetime. In the following, we go through the details of the computation for fermions in two dimensions to show that it can be recast in the same form as the one for the three-dimensional theory solved by Gubser *et al.*, to obtain the same temperature and frequency dependence, with the only difference being in the prefactor. The Dirac equation then becomes

$$r\sqrt{1-q\frac{(4\pi T/\mu)^2}{3\sqrt{3}}\frac{\mu}{r}}\;\partial_r\begin{pmatrix} y_+ \\ z_- \end{pmatrix} =$$
$$\begin{pmatrix} \frac{m}{3^{3/8}}q^{1/4}\left(\frac{r}{\mu}\right)^{1/4} & q\frac{k}{\mu}-\sqrt{q}\frac{\omega/\mu}{3^{3/4}\sqrt{r/\mu}}\frac{1}{\sqrt{1-q\frac{(4\pi T/\mu)^2}{3\sqrt{3}}\frac{\mu}{r}}}+\frac{q^{3/2}}{3^{1/4}}\sqrt{\frac{r}{\mu}} \\ q\frac{k}{\mu}+\sqrt{q}\frac{\omega/\mu}{3^{3/4}\sqrt{r/\mu}}\frac{1}{\sqrt{1-q\frac{(4\pi T/\mu)^2}{3\sqrt{3}}\frac{\mu}{r}}}+\frac{q^{3/2}}{3^{1/4}}\sqrt{\frac{r}{\mu}} & -\frac{m}{3^{3/8}}q^{1/4}\left(\frac{r}{\mu}\right)^{1/4} \end{pmatrix}$$
$$\begin{pmatrix} y_+ \\ z_- \end{pmatrix}. \tag{5.30}$$

We can immediately see an important distinction compared to the Reissner-Nordström background (see for example Ref. [68]). In the Reissner-Nordström near-horizon regime, the momentum term scales with the same power of r/μ as the terms involving the mass and charge of the fermion. On the contrary, here the mass and gauge terms are subleading in the small r/μ expansion and the IR solution then does not depend explicitly on these two quantities. In this limit, we are then left to solve the differential equation

$$r\partial_r\begin{pmatrix} y_+ \\ z_- \end{pmatrix} = \begin{pmatrix} 0 & \mathcal{F}(-\omega,k,r) \\ \mathcal{F}(\omega,k,r) & 0 \end{pmatrix}\begin{pmatrix} y_+ \\ z_- \end{pmatrix}, \tag{5.31}$$

where we defined

$$\mathcal{F}_{2D}(\omega,k,r) \equiv q\frac{k}{\mu}+\sqrt{q}\frac{\omega}{3^{3/4}\sqrt{r\mu}}\frac{1}{\sqrt{1-\frac{q}{3\sqrt{3}}\frac{(4\pi T)^2}{\mu r}}}. \tag{5.32}$$

Similarly, for a three-dimensional boundary theory we have [49]

$$\mathcal{F}_{3D}(\omega,k,r) \equiv q\frac{k}{\mu}+\frac{\omega}{2r}\frac{1}{\sqrt{1-\frac{(\pi T)^2}{r^2}}}\;. \tag{5.33}$$

By the variable redefinitions shown in table 5.1, the Dirac equation takes the same form in both boundary dimensions, namely

2D boundary theory	3D boundary theory
$\zeta = 2\sqrt{q}\frac{\omega}{3^{3/4}\sqrt{r\mu}}$ $\nu_k = 2q\frac{k}{\mu}$ $\delta_0 = \frac{2\pi T}{\omega}$	$\zeta = \frac{\omega}{2r}$ $\nu_k = q\frac{k}{\mu}$ $\delta_0 = \frac{2\pi T}{\omega}$

Table 5.1: Change of variables for the low-energy solution in a 2D and 3D boundary theory.

$$-\zeta\sqrt{1-\zeta^2\delta_0^2}\,\partial_\zeta \begin{pmatrix} y_+ \\ z_- \end{pmatrix} = \begin{pmatrix} 0 & -\zeta/\sqrt{1-\zeta^2\delta_0^2}+\nu_k \\ \zeta\sqrt{1-\zeta^2\delta_0^2}+\nu_k & 0 \end{pmatrix} \begin{pmatrix} y_+ \\ z_- \end{pmatrix} . \tag{5.34}$$

We start by carrying out the computation at zero temperature, i.e., we first set $\delta_0 = 0$. The boundary of the conformal-to-AdS$_2$ spacetime is at $\zeta \to 0$, and we can already see that the asymptotic behavior of the solution takes the form of $C_1\zeta^{-|\nu_k|} + C_2\zeta^{|\nu_k|}$. In order to put the equation in a more familiar form, it is convenient to perform a change of variables [49] as

$$\begin{pmatrix} u_+ \\ u_- \end{pmatrix} = \frac{1}{\sqrt{2}} \begin{pmatrix} 1 & i \\ 1 & -i \end{pmatrix} \begin{pmatrix} y_+ \\ z_- \end{pmatrix} \tag{5.35}$$

so that we get

$$\partial_\zeta^2 u_+ + \frac{\partial_\zeta u_+}{\zeta} + u_+\left(\frac{i}{\zeta} - \frac{\nu_k^2}{\zeta^2} + 1\right) = 0 \ , \tag{5.36}$$

$$u_- = -\frac{\zeta}{i\nu_k}(\partial_\zeta u_+ + iu_+) \ , \tag{5.37}$$

where we recognize in Eq. (5.36) the Whittaker equation with two possible solutions of the form

$$u_+(\zeta) = C\frac{i\nu_k}{\sqrt{\zeta}} W_{\pm 1/2,\nu_k}(\pm 2i\zeta) \ . \tag{5.38}$$

Near the horizon $\zeta \to \infty$, the solution behaves as $u_+ \propto e^{\mp i\zeta}$, and by imposing the infalling-wave condition at the horizon (corresponding to $e^{i\zeta}$) the solution becomes

$$\begin{aligned} u_+(\zeta) =& C\frac{i\nu_k}{\sqrt{\zeta}} W_{-1/2,\nu_k}(-2i\zeta)\ , &(5.39)\\ u_-(\zeta) =& C\frac{1}{\sqrt{\zeta}} W_{1/2,\nu_k}(-2i\zeta)\ , &(5.40)\end{aligned}$$

that in terms of the original variables is

$$\begin{aligned} y_+(\zeta) =& \frac{C}{2\sqrt{\zeta}}\left(i\nu_k W_{-1/2,\nu_k}(-2i\zeta) + W_{1/2,\nu_k}(-2i\zeta)\right)\ ,\\ z_-(\zeta) =& \frac{C}{2\sqrt{\zeta}}\left(\nu_k W_{-1/2,\nu_k}(-2i\zeta) + iW_{1/2,\nu_k}(-2i\zeta)\right)\ . \end{aligned} \tag{5.41}$$

The IR Green's function can then be extracted by expanding this exact IR solution for $\zeta \to 0$

$$\begin{aligned} \begin{pmatrix} y_+ \\ z_- \end{pmatrix} = \frac{C}{2}\Bigg[\begin{pmatrix} -1 \\ 1 \end{pmatrix} \left(\frac{(-2i)^{1+\nu_k}\Gamma[-2\nu_k]}{-\Gamma[-\nu_k]} + \mathcal{O}(\zeta)\right)\zeta^{\nu_k} + \\ \begin{pmatrix} 1 \\ 1 \end{pmatrix} \left(\frac{(2i)^{\nu_k}\Gamma[1/2+\nu_k]}{\sqrt{\pi}} - \frac{(2i)^{\nu_k}\Gamma[-1/2+\nu_k]}{2\sqrt{\pi}}\zeta\right)\zeta^{-\nu_k}\Bigg]\ , \end{aligned} \tag{5.42}$$

where we used the notation $\Gamma[x]$ for the gamma function, and we get

$$\mathcal{G}_k = i\frac{(-i)^{2\nu_k}4^{-\nu_k}\Gamma[1/2-\nu_k]}{\Gamma[1/2+\nu_k]}\zeta^{2\nu_k} r^{|2qk/\mu|}\ . \tag{5.43}$$

Explicitly we thus obtain

$$\begin{aligned} q^{2|qk|/\mu}\mathcal{G}_k^{2D}/\mu^{2|qk|/\mu} =& i(-i)^{4|qk|/\mu}\frac{\Gamma[1/2-2|qk|/\mu]}{\Gamma[1/2+2|qk|/\mu]}\left(\frac{q\omega}{3^{3/4}\mu}\right)^{4\frac{|qk|}{\mu}}\\ =& \omega(-\omega^2)^{2\frac{|qk|}{\mu}-1/2}\frac{\Gamma[1/2-2|qk|/\mu]}{\Gamma[1/2+2|qk|/\mu]}\left(\frac{q^2}{3^{3/2}\mu^2}\right)^{2\frac{|qk|}{\mu}}\ , \end{aligned} \tag{5.44}$$

$$\begin{aligned} q^{2|qk|/\mu}\mathcal{G}_k^{3D}/\mu^{2|qk|/\mu} =& i(-i)^{2|qk|/\mu}\frac{\Gamma[1/2-|qk|/\mu]}{\Gamma[1/2+|qk|/\mu]}\left(\frac{q\omega}{4\mu}\right)^{2\frac{|qk|}{\mu}}\\ =& \omega(-\omega^2)^{\frac{2|qk|}{\mu}-1/2}\frac{\Gamma[1/2-|qk|/\mu]}{\Gamma[1/2+|qk|/\mu]}\left(\frac{q^2}{16\mu^2}\right)^{\frac{|qk|}{\mu}}\ , \end{aligned} \tag{5.45}$$

where in the second line of Eqs. (5.44) and (5.45), ω has to be thought as usual as the limit $\omega + i0$. At non-zero temperature, but with $T/\mu \ll 1$, generalizing the result obtained by Gubser [49] according to the definitions in table 5.1, we find ultimately

$$q^{\nu_k}\mathcal{G}_k^{2D}/\mu^{\nu_k} = i\left(q\frac{2\pi T}{3^{3/4}\mu}\right)^{2\nu_k}\frac{\Gamma[1/2-\nu_k]}{\Gamma[1/2+\nu_k]}\frac{\Gamma[1/2+\nu_k-i\frac{\omega}{2\pi T}]}{\Gamma[1/2-\nu_k-i\frac{\omega}{2\pi T}]}\,. \tag{5.46}$$

Upon expanding the gamma functions for $\omega/2\pi T \to \infty$ we recover the zero-temperature solution in Eq. (5.44).

First, a few observations about the result just obtained. As mentioned earlier, the first peculiarity of this background compared to the Reissner-Nordström one and other dilaton models (see e.g. Ref. [17] for a review on dilaton models) is that $\nu_k \propto |k/\mu|$ with no contribution from the mass and charge of the fermion, in particular, this implies that the scaling exponent is always real and there is no pathological log-oscillatoric behavior due to a complex exponent, underling an instability at small momenta and large values of the ratio q^2/m^2 [32, 91]. Moreover, for these other backgrounds in the opposite limit of small q^2/m^2 the scaling exponent assumes the general form $\nu_k \propto \sqrt{(k/\mu)^2 + 1/\xi^2}$, with $\xi = \xi(m^2, q^2)$ setting a correlation length with the Green's function decaying (at least) exponentially as $G \propto e^{-x/\xi}$ at large $x \gg \xi$ [68]. This is not the case here as shown in Eq. (5.44).

The imaginary part of the analytical result in Eqs. (5.44) and (5.46) is finite for every value of ν_k. However, this is not the case for the real part that contains a pole for every value of momenta such that $\nu_k = 1/2 + n$, $n \in \mathbb{N}$. These divergences, though, are not present in the full Green's function, as it can be seen in Fig. 5.3, where, in the full solution obtained numerically, we observe a linear dispersion for every value of k/μ in the range of interest, according to Eq. (5.27). This is because, when the IR solution is matched with the outer solution to compute the full Green's function, these simple poles are in fact canceled by divergences in the matching coefficients [32]. Here we discuss the pole arising when $\nu_k = 1/2$ as it is the only one that concerns us in the range of momenta considered, where it is interesting to notice that in the limit $\epsilon \to 0$, with $\epsilon = \nu_k - 1/2$ there is a simple pole in the real part proportional to $-\frac{1}{\epsilon}\omega^{2\epsilon+1}$. From the matching procedure, a divergence in the matching coefficient proportional to ω/ϵ gives rise to the logarithmic term $-\omega\log(\omega^2) \simeq \omega\frac{1-\omega^{2\epsilon}}{\epsilon}$, that we indeed expect for the marginal-Fermi-liquid case $\nu_k = 1/2$ [32]. The logarithm can also be seen by noticing that for $\nu_k = 1/2$ the otherwise subleading term of the response in Eq. (5.42) has the same power as the leading term in the source. In order to fix this divergence in our expression in Eqs. (5.44) and (5.46), we could remove the simple pole in $\mathcal{G}_k$ as

$$\mathcal{G}_k(\omega;T)/\mu^{\nu_k} = i\left(\frac{-iq\omega}{3^{3/4}\mu}\right)^{2\nu_k}\frac{\Gamma[1/2-\nu_k]}{\Gamma[1/2+\nu_k]} + \frac{\sqrt{q}|\omega/\mu|}{3^{3/4}(\nu_k-1/2)}\ , \tag{5.47}$$

that does not affect the imaginary part. We stress, however, that we are primarily interested in the universal physics encoded in the imaginary part of the infrared Green's function and we won't, therefore, indulge more in the subtleties regarding the real part and we will simply assume it to renormalize the bare Fermi velocity. This is the case in the range of $\nu_k > 1/2$ we are interested in, as can be verified from the full solution.

5.3.2 Matching procedure and comparison with the ansatz

As we are ultimately interested in knowing the full Green's function, we briefly remind the reader here of the relationship between the infrared Green's function and the full one for the boundary fermionic operator $\mathcal{O}$ and we then proceed to analyze it numerically. The basic idea is that we divide the spacetime into two regions, the inner region for small r/μ where we solved the Dirac equation above, and an outer region where $r \gg \omega, T$ and we can solve the equations in a series expansion in these two quantities. For $\omega, T \ll \mu$, this two regions overlap when $\omega, T \ll r$ and $r \ll \mu$. In this overlap region we can then match the two solutions. The details of this matching procedure between the solutions to the Dirac equation in the inner and outer region of the spacetime are nicely outlined in, for example, Refs. [32, 68]. We ultimately have that the full holographic Green's function can be written as

$$G_H(\omega,k;T)\mu^{-2m} = \frac{b_+(\omega,k,T) + b_-(\omega,k,T)\mathcal{G}_k(\omega;T)\mu^{-2\nu_k}}{a_+(\omega,k,T) + a_-(\omega,k,T)\mathcal{G}_k(\omega;T)\mu^{-2\nu_k}}\ , \tag{5.48}$$

where the coefficients $b_\pm$, $a_\pm$ depend on the full spacetime and in most cases, as it is in this paper, they can only be computed numerically. They are all real and have an analytic expansion in terms of ω and T

$$a_\pm(\omega,k,T) = a_\pm^{(0,0)}(k) + \omega a_\pm^{(1,0)}(k) + Ta_\pm^{(0,1)}(k) + \cdots\ , \tag{5.49}$$

for ω, $T \ll \mu$ and similarly for $b_\pm$. The expansion coefficients depend on momentum and can be Taylor expanded as well. Notice that, from the structure of Eq. (5.48), an analogous relation holds for the Green's function in alternative quantization. In particular, we therefore expect that for small energies and temperatures we can accurately describe the imaginary part of the Green's function with a form

$$\mathrm{Im}[G_H(\omega,k;T)^{-1}\mu^{2m}] \simeq -\mathcal{C}(\omega,k,T)\mathrm{Im}\left[\mathcal{G}_k(\omega;T)\mu^{-2\nu_k}\right] \ , \tag{5.50}$$

with $\mathcal{G}_k(\omega;T)$ given in Eq. (5.46) and $\mathcal{C}$ admitting an analytical expansion in its variables where, as we are interested in describing low-energy excitations near the Fermi surface, we have $k/\mu \gg \omega/\mu, T/\mu$ and, if qk/μ is sufficiently small, we expect it to be well described by $\mathcal{C} = \mathcal{C}^{(0)} + k\mathcal{C}^{(k)} + T\mathcal{C}^{(T)} + \omega\mathcal{C}^{(\omega)} + \cdots$, with the dominant correction coming from the k dependence and only small energy and temperature-dependent corrections. We verified this numerically for different dopings, i.e., different values of the holographic fermion charge q as we soon explain, and show this in Fig. 5.5. We see that the imaginary part of the full solution is very accurately described by the IR results at all values of temperatures considered, with the coefficient $\mathcal{C}(\omega,k,T)$ linear in k as shown, for example, in Fig. 5.6 for $\alpha = 0.65$ and $qT/\mu = 0.005$. The real

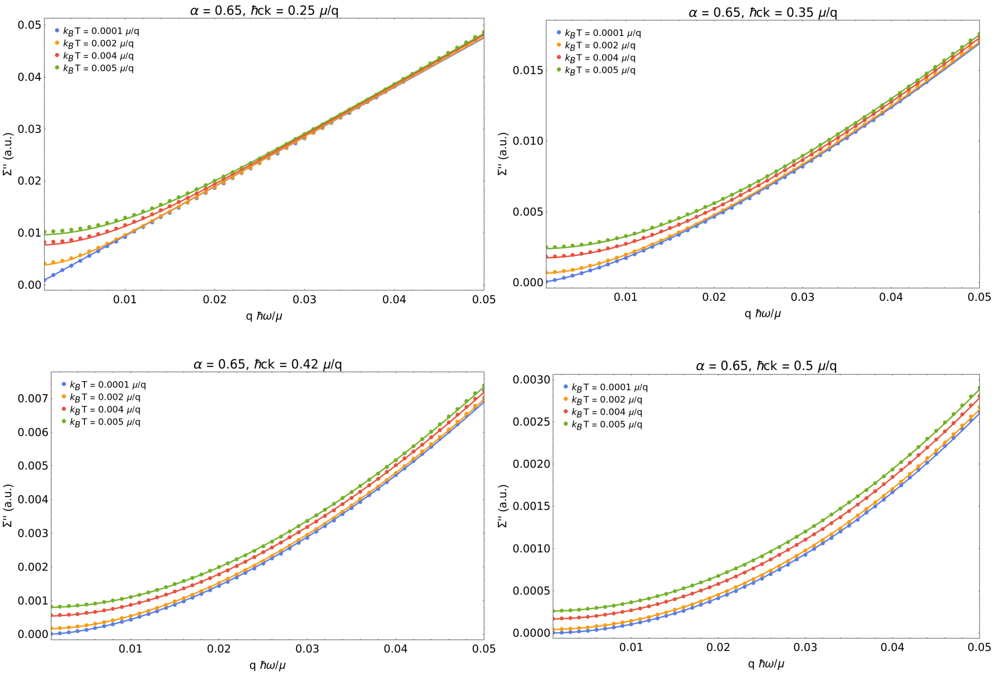

Figure 5.5: Imaginary part of the numerical self-energy (circles) for different values of fixed momentum and temperatures in the range of interest, together with a fit to the analytical low-energy result (lines). We can clearly see that the low-energy behavior of the imaginary part of the self-energy is indeed described by the $\mathrm{AdS}_2 \times \mathbb{R}^2$ solution.

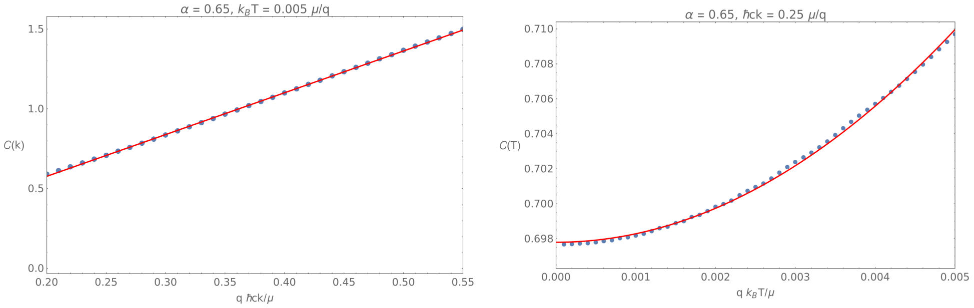

(a) Momentum dependence of the coefficient $\mathcal{C}$ with a linear fit (red line)

(b) Temperature dependence of the coefficient $\mathcal{C}$ with a quadratic fit (red line)

Figure 5.6: Example of the momentum dependence of the coefficient $\mathcal{C}$ resulting from a fit of the numerical solution at fixed temperature $T/\mu = 0.005$, with a function of the form of Eq. (5.50) with an energy-independent coefficient $\mathcal{C}(\omega, k, T) \simeq \mathcal{C}(0, k, T)$. It shows that the latter coefficient is linear in k/μ as expected from the argument in the main text, while temperature corrections are quadratic and thus negligible at sufficiently low temperatures where $\mathcal{C}(\omega, k, T) \simeq \mathcal{C}(0, k, 0)$.

part of the Green's function on the other hand cannot be understood in terms of the emergent geometry only, as it depends on the full solution and it has to be analyzed numerically.

We can further see from Eq. (5.48) that the Green's function for $\mathcal{O}$ shows a Fermi surface whenever there exists a value of momentum $k \equiv k_F$ such that $a_+^{(0,0)}(k = k_F) = 0$. Expanding the Green's function near this point we see that it can be written as

$$G_H(\omega, k; T)/\mu^{2m} \simeq \frac{b_+^{(0,0)}(k_F)}{\partial_k a_+^{(0,0)}(k_F)(k - k_F) + \omega a_+^{(1,0)}(k_F) + a_-^{(0,0)}(k_F)\mathcal{G}_{k_F}(\omega; T)\mu^{-2\nu_{k_F}}} , \tag{5.51}$$

justifying the form used in Eq. (5.27) in the previous section. We now understand that k_F/μ, as well as Z and v_H, require the full solutions and depend therefore on the UV completion of the theory, while Σ'' is, up to a prefactor, fully determined by the imaginary part of $\mathcal{G}_k$. In particular then, near the Fermi surface, we recover the PLL self-energy $\Sigma'' \propto (\omega^2)^\alpha$, proposed as a model of the cuprates strange metal, by fine-tuning the charge of the bulk fermion such that $\nu_{k_F} = 2qk_F/\mu \equiv \alpha$, with $\alpha = 1/2$ at optimal doping and increasing approximately linearly with doping towards the Fermi-liquid value of 1 [119].

The full solution start to deviate from the IR analytical behavior for small values of

$\hbar ck/\mu$, reintroducing for a moment dimensionful units. However, we are only interested in describing the MDC peaks near the Fermi momentum with $q\hbar ck_F/\mu \equiv \alpha/2 \in [0.25, 0.5)$. As noted in Sec. 5.2, we consider c as a velocity of the same order of the Fermi velocity. We can verify that this interpretation is consistent with the infrared regime $\hbar\omega, k_B T \ll \mu$ corresponding to an energy and temperature range of experimental interest. Since we have $q\hbar\omega/\mu = \alpha\hbar\omega/2\hbar ck_F$, choosing for estimation purposes a velocity $\hbar c = 4\text{eV}\text{Å}$ and $k_F = 0.5\text{Å}^{-1}$, we have that, choosing for example the largest values shown in Fig. 5.5, $q\hbar\omega/\mu = 0.05$ corresponds to an energy $\hbar\omega \in (0.2\text{eV}, 0.4\text{eV}]$ depending on the value of $\alpha \in [0.25, 0.5)$. This is also where the range of validity of the linear approximation in the dispersion observed in the ARPES measurements starts to break down and where we hence do not expect the low-energy holographic description to be valid anymore. Accordingly, the highest temperature shown is $qk_BT/\mu = 0.005$ which corresponds to the high temperatures $T \in (232K, 465K]$.

5.4 Semi-holography and effective low-energy response

As we have shown, holography provides us with a way to compute the low-energy response function of strongly interacting systems at non-zero temperature and chemical potential and for any dimensionality, a task not easily achievable with such a generality within other frameworks. However, when comparing with experimental measurements, we have to keep in mind that the holographic model considered does not fully correspond to the theory of an electron system at all energies, but it has to be regarded as yielding an effective theory capturing the low-energy behavior of a fermionic massless composite operator, whose UV behavior might be far from what is expected from a metal in the laboratory, as is also clear from the fact that the holographic Green's function presented above does not satisfy the electronic sum rule and obeys

$$\frac{1}{\pi}\int_{-\infty}^{+\infty} \mathrm{d}\omega \, \mathrm{Im}[G_H(\omega, k)] \neq 1 \; , \quad \forall k \; . \tag{5.52}$$

Here we would like to write down a low-energy effective action to decouple the dissipative physics related to the interior of the spacetime from the ultraviolet conformal field theory of the asymptotically AdS spacetime. An interpretation of the holographic results known as *semi-holography* [33, 52] considers the effective action as arising from a fermionic field χ, living on the boundary of the spacetime whose decay is controlled by the interaction with the strongly coupled sector described by the holographic fermionic operator $\mathcal{O}$, so that the effective action takes the form

$$S^{\text{eff}} = \int \frac{\mathrm{d}\omega \mathrm{d}^d k}{(2\pi)^{d+1}} (\chi^\dagger(-\hbar\omega + \epsilon(k) - \mu)\chi + g_k \chi^\dagger \mathcal{O} + g_k \mathcal{O}^\dagger \chi) + S^{\text{strong}}(\mathcal{O}) \ , \tag{5.53}$$

with g_k a momentum-dependent (assumed real) coupling constant, and S^{strong} the action from the near-horizon holographic sector, so that the Green's function for the fermion field becomes

$$G_{\chi\chi}(\omega, k) = \frac{\hbar}{-\hbar\omega + \epsilon(k) - \mu - g_k^2 \mathcal{G}_k(\omega)} \equiv \frac{1}{G_0(\omega, k)^{-1} + \Sigma(\omega, k)} \ , \tag{5.54}$$

with $-g_k^2 \mathcal{G}_k(\omega)/\hbar$ assuming the role of the electron self-energy. With the hope to extend (semi-)holography beyond just a tool for obtaining low-energy effective theories, in Ref. [52] it was further shown that by writing down an action coupling the fermion with the full holographic theory, and not only the IR emergent sector, we find

$$G_{\chi\chi}(\omega, k) = \frac{\hbar}{-\hbar\omega + \epsilon(k) - \mu + g_k^2 G_H^{-1}(\omega, k)} \underset{\omega \ll \mu}{\approx} \frac{\hbar}{-\hbar\omega + \tilde{\epsilon}(k) - \mu - \tilde{g}_k^2 \mathcal{G}_k(\omega, k)} \ , \tag{5.55}$$

and we obtain a spectral function that satisfies the electronic sum rule for masses in the range $(-1/2, 1/2)$. In fact, in this mass range, the contribution from the holographic Green's function is subleading at high energies where Eq. (5.55) reduces to that of a free fermion so that the electronic sum rule for $G_{\chi\chi}$ is satisfied, pointing to the possibility that this construction could be used to obtain in a consistent way the spectral function for a single electron in a strongly interacting theory at all energies. Notice, however, that in this way the non-universal ultraviolet physics of the holographic theory enters into the spectral function, modifying the dispersion relation and, as we will shortly show, imposing an upper limit on the lifetime of the excitations near the Fermi surface. Combining Eqs. (5.27) and (5.55) we can see in fact that the Green's function takes the low-energy form

$$\begin{aligned} G_{\chi\chi}(\omega, k) &\simeq \frac{\hbar}{-\hbar\omega(1 + g_k^2/Z) + (\hbar v_B + g_k^2 \hbar v_H/Z)(k - k_F) - i g_k^2 \mathcal{C}\,\mathrm{Im}[\mathcal{G}_k(\omega)]} \\ \mathrm{Im}[G_{\chi\chi}(\omega, k)] &\simeq \frac{\tilde{Z}}{v_F} \frac{\Gamma(\omega, k)/2}{(k - k_*(\omega))^2 + \Gamma(\omega, k)^2/4} \ , \end{aligned} \tag{5.56}$$

where $\tilde{Z} = Z/(Z + g_k^2)$, $k_*(\omega) = k_F + \omega/v_F$, $v_F(k) = v_B \frac{1+g_k^2 v_B/Z v_H}{1+g_k^2/Z}$, v_B is the bare Fermi velocity, and $\Gamma(\omega, k) = \frac{g_k^2}{v_F(1+g_k^2/Z)} \mathcal{C}\mathrm{Im}[\mathcal{G}_k(\omega)]$. We thus see that the lifetime of the electronic excitations as a function of the adjustable parameter g_k^2 is bounded from above, with a maximum as we approach the holographic result for $\lim_{g_k \to \infty} G_{\chi\chi}(\omega, k) \propto G_H(\omega, k)$. In this limit, given the small value of Z as shown in Fig. 5.4, the holographic prediction gives very sharp peaks near the Fermi surface, and cannot then offer a quantitative description of the much broader peaks measured in ARPES experiments. This is an indication that the holographic theory considered here does not provide a proper description of the electronic excitations at all energies and the UV completion of the theory, influencing the low-energy behavior through the values of Z, k_F, and v_F has to be modified if we want to write down a full theory of the cuprate strange metal valid across the entire energy range observed. This is outside the scope of our present work and we consider in what follows the semi-holographic construction as in Eq. (5.54) as we are in first instance primarily interested in understanding if there is evidence in the laboratory cuprates of the peculiar physics arising from the universal infrared behavior described by the gauge-gravity duality. Only after this question is answered affirmatively can we undertake the more challenging problem of a complete description of the theory.

We, therefore, start with the simplest approach of modeling the Green's function near the Fermi surface by

$$G_{\chi\chi}(\omega, k) = \frac{\hbar}{-\hbar\omega + \hbar v_F(k - k_F) - i g_k^2 \mathrm{Im}[\mathcal{G}_k(\omega)]} , \tag{5.57}$$

where we now consider the renormalized Fermi velocity v_F to be a k-independent adjustable parameter, incorporating the real contribution of the self-energy that renormalizes the bare velocity v_B, and the freedom in $g_k^2 > 0$ is set to match the measured peak width near the Fermi surface. In this way, the holographic input is all in the imaginary part of the electron self-energy $\hbar\Sigma''(\omega, k) \equiv g_k^2 \mathrm{Im}[\mathcal{G}_k(\omega)]$.

5.5 Comparing holography to ARPES data

The purpose of this paper is to show that the simple "semi-holographic" model described above is able to describe the energy and momentum dependence of the cuprate spectral function measured in ARPES experiments, and, in particular, we argue that it is a step forward compared to the momentum-independent self-energy of the power-law liquid as it provides a better comparison with the data at higher energies. As such, we explain here how to compare the holographic prediction to the experimental data from Ref. [119]. We start by looking at the zero-temperature solution and leave the discussion about temperature corrections, only relevant as $k_B T \simeq \omega$, to a later section.

The analysis of the electronic MDCs is based on a fit of the form of Eq. (5.1)

$$\mathcal{A}(\omega, k) = \frac{W(\omega)}{\pi} \frac{\Gamma(\omega, k)/2}{(k - k_*(\omega))^2 + (\Gamma(\omega, k)/2)^2} \ , \tag{5.58}$$

where $\Gamma(\omega, k) = 2\Sigma''(\omega, k)/v_F + G_0(\omega)/v_F$, with $G_0(\omega)$ a momentum-independent contribution usually attributed to the electron-phonon interaction and disorder. The ARPES measurements on the cuprate strange metal have generally been analyzed in a framework in which the self-energy is dominated by the frequency dependence. It has then been assumed that it could be modeled with a momentum-independent ansatz, the power-law liquid:

$$\hbar\Sigma''_{\text{PLL}} = \hbar\Sigma''_{\text{PLL}}(\omega, T) = \frac{((\hbar\omega)^2 + (\beta k_B T)^2)^\alpha}{(\hbar\omega_N)^{2\alpha - 1}} \ , \tag{5.59}$$

with $\hbar\omega_N = 0.5$eV a fixed energy scale, β a constant with an experimentally determined value around π [113], and α a doping-dependent exponent with $\alpha = 1/2$ at optimal doping and $1/2 < \alpha < 1$ as we move into the overdoped region of the phase diagram. As a first-order test of the semi-holographic prediction, according to Eq. (5.57), we simply replace the PLL's imaginary part of the self-energy with the semi-holographic result $\hbar\Sigma''(\omega, k) \equiv g_k^2 \text{Im}[\mathcal{G}_k(\omega)]$. Notice that by neglecting the real part of the self-energy this approach is independent of the UV completion of our holographic theory. One could argue that, given a non-linear momentum dependence, the real part of the self-energy should introduce some non-linearity in the dispersion relation as well as momentum dependence in $W = W(\omega, k)$ in Eq. (5.58). From the experimental fact that the peak position near the Fermi surface is well described by a linear dispersion with a phonon kink, we consider it a reasonable first step to only assume that the real part of the self-energy simply renormalizes the Fermi velocity. As previously mentioned, it is nonetheless a very interesting problem to consider the effect of a full holographic self-energy on the dispersion and normalization, but that is left for future work.

5.5.1 Particle-hole symmetry

Near the Fermi energy the MDC peaks are sharp and the holographic prediction for the imaginary part of the self-energy is well approximated by the momentum-independent form of the PLL, i.e., $\Sigma'' \propto (\omega^2)^{\nu_{k_F}}$ with the identification $\alpha \equiv \nu_{k_F} = 2q|k_F|/\mu$. In particular, we see that the value of the charge q in the bulk Dirac equation can be used to describe the doping dependence of the power-law exponent, with α approximately linear in q since the value of k_F/μ varies very little as a function of q (see Fig. 5.4). As we move away from the Fermi level, however, the observed peaks become broad enough (the FWHM is of the same order of magnitude as the Fermi momentum) that we expect to be able to notice deviations from the symmetric Lorentzian shape due to the effect of the k-dependent exponent as $\Sigma''(\omega, k, T=0) \propto (\omega^2)^{\alpha(1+(k-k_F)/k_F)}$. It is easy to see that this implies more spectral weight in the tail of the peak for $|k| < |k_*|$ as shown in an example in Fig. 5.2. This is in contrast with experimental findings along the nodal line, where the peaks appear as if they are "tilted" in the other direction, with more spectral weight for $|k| > |k_*|$. We believe that this is due to the holographic fermion in the bulk being dual to a fermionic operator for the hole, $\mathcal{O}(\omega, k) \equiv \mathcal{O}_h(\omega, k)$, hence the semi-holographic effective theory, Eq. (5.53), describes the response of a hole system, $\chi(\omega, k) \equiv \chi_h(\omega, k)$. On the other hand, ARPES measures the response of the electrons in cuprates, associated with $\chi_e(\omega, k)$. The semi-holographic spectral function, in the right panel of Fig. 5.7 is then describing the hole response in the nodal direction. The left-hand panel in Fig. 5.7 represents photoemission data and thus necessarily is in an "electron picture". Since the theory is cast in the hole picture, the red line shown in the right-hand panel shows the unoccupied hole states, which corresponds to the red line in the occupied electron states in the left panel. We thus need to identify the zero of the momentum axis with the (π, π) point, and the rotationally invariant Fermi surface at $\omega = 0$ of the semi-holographic spectral function then corresponds to the "round" Fermi surface around the (π, π) point of Fig. 5.8. Assuming, however, an emergent particle-hole symmetry near the Fermi surface, we actually identify the position of the $(0, 0)$ point along the nodal direction at $2k_F$.

Performing a particle-hole conjugation on the fermionic composite operator $\mathcal{O}_h(\omega, k) \rightarrow \mathcal{O}_e^\dagger(-\omega, 2k_F - k)$, transforms the self-energy as

$$\begin{aligned} \hbar\Sigma_h(\omega, k) = -g_k^2 \mathcal{G}_k(\omega) \rightarrow +g_{2k_F-k}^2 \mathcal{G}_{2k_F-k}^*(-\omega) = \hbar\Sigma_e(\omega, k) \\ \propto -g_{2k_F-k}^2(-\omega)(-\omega^2)^{\alpha(1-(k-k_F)/k_F)-1/2} , \end{aligned} \tag{5.60}$$

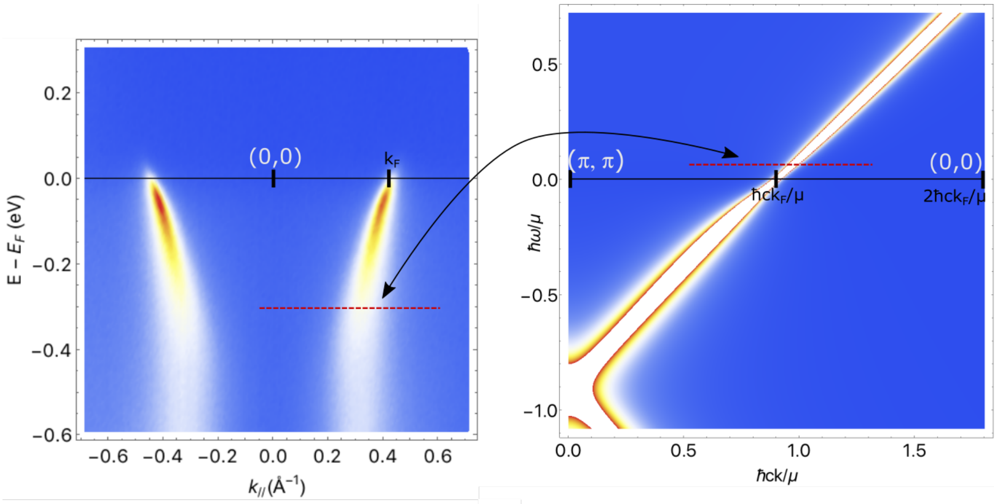

Figure 5.7: With (semi-)holography we obtain the spectral function for the holes (right panel). In an emergent particle-hole symmetry near the Fermi surface, we relate the ARPES MDC along the nodal line for the electrons in a cuprate at $E < E_F$, with momentum origin at the (0,0) point with the holographic distribution at the corresponding $\hbar\omega/\mu = (E_F - E)/\mu > 0$ (dashed red line). The origin of the momentum axis is at $2\hbar c k_F/\mu$

where we used the fact that g_k^2 is real and we dropped the absolute value in the exponent as we always consider $0 \leq k < 2k_F$. In other words, the electronic spectral function at $E < E_F$, as measured in ARPES MDCs, is described in our semi-holographic framework by the peaks for positive frequencies, as depicted in Fig. 5.7, with the momentum k measured along the nodal direction from the $(0, 0)$ point. From now on, we simply use the notation $\hbar\Sigma(\omega, k) = -g_k^2 \mathcal{G}_k(\omega)$ to refer to the self-energy for the electron as in Eq. (5.60), with the scaling exponent $\alpha(k) \equiv \alpha(1 - (k - k_F)/k_F)$.

5.5.2 Fit-function and phonon

In data collected from ARPES measurements, there is a kink in the dispersion relation, as shown in Fig. 5.9, at about $E - E_F \simeq 0.07\text{eV}$. This kink is associated with a jump in the lifetime of the excitations and it is generally attributed to the electron-phonon interaction. This gives an additional contribution to the imaginary part of the self-energy that is accounted for in the experimental fitting procedure by the addition of a momentum-independent parameter $G_0(\omega)$. As explained in more details in Ref. [119], the analysis of the experimental data is done by fitting each momentum-dependent

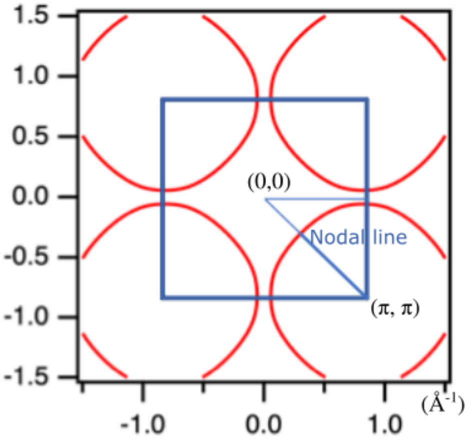

Figure 5.8: Structure of the Fermi surface. The origin of the momentum axis is set at the $(0,0)$ point, with measurements performed along the nodal line. The holographic model describes the response of the hole system from the (π,π) point, within an emergent particle-hole symmetry where the (π,π) point is assumed at $2k_F$ along the nodal direction.

curve, i.e., a slice at constant energy as for example in Fig. 5.10), with the ansatz

$$\mathcal{A}(\omega,k)=\frac{W(\omega)}{\pi}\frac{\overbrace{\frac{\lambda f_k\omega_N}{2}\left[\left(\frac{\omega}{\omega_N}\right)^2\right]^{\alpha(k)}+\frac{G_0(\omega)}{2}}^{\Gamma(\omega,k)/2}}{(k-k_*(\omega))^2+\left(\underbrace{\frac{\lambda f_k\omega_N}{2}\left[\left(\frac{\omega}{\omega_N}\right)^2\right]^{\alpha(k)}}_{\Sigma''(\omega,k)/v_F}+\frac{G_0(\omega)}{2}\right)^2}\,, \tag{5.61}$$

where λ is a doping-independent constant that is determined by a 2-dimensional fit for momenta and energies near the Fermi level, and is then fixed and does not enter as a fit parameter in the MDC fits. It is also kept fixed independently of the model used for the self-energy. In addition, $\hbar\omega_N = 0.5\text{eV}$ is an energy scale related to the microscopic details of the CuO$_2$ layer [113]. Finally, $W(\omega)$, $k_*(\omega)$ and $G_0(\omega)$ are fit functions. $W(\omega)$ is the overall normalization, that we won't discuss here, $k_*(\omega)$ the dispersion that we expect to take the form $k_*(\omega) = k_F - \omega/v_F$ plus a renormalization contribution from the phonon as explained below, and $G_0(\omega)$ accounts for the contribution to the width of the peak in the constant-energy cut through the data that does not come from

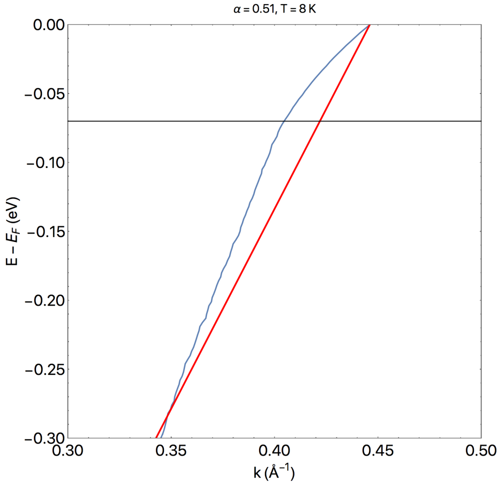

Figure 5.9: Plot of the dispersion relation from ARPES measurements along the nodal direction at optimal doping and low-temperature (blue line), and comparison with a linear disperion $E - E_F = \hbar v_F(k - k_F)$, with $v_F = 2.9\text{eV}\text{Å}$ (red line). We can see a kink in the linear dispersion around $E - E_F = -0.07$ eV.

the electron self-energy, that we expect to be well described by a model of the electron-phonon interaction. In order to check this latter ansatz, we compare the results for $G_0(\omega)$ with a simple approximation for a dispersionless phonon, with characteristic frequency obeying $\hbar\omega_{\text{ph}} = 0.07\text{eV}$, given by

$$\frac{\Sigma_{\text{ph}}(\omega)}{v_F} = \frac{G_{\text{ph}}}{2\pi} \log\left(\frac{\omega - \omega_{\text{ph}} - i\Omega}{\omega + \omega_{\text{ph}} + i\Omega}\right) , \tag{5.62}$$

with, as we will shortly see, $\Omega > 0$ even at $T = 0$, likely due to the smearing of the Fermi surface due to strong interactions in the system. This has the effect of smoothing out the step-function in the imaginary part of the phonon self-energy, as well as the kink in the dispersion.

For the PLL, $f_k = 1$ and $\alpha(k) = \alpha$, while for the semi-holographic model presented above $\alpha(k) = \alpha(1 - (k - k_F)/k_F)$ from Eq. (5.60), and from the imaginary part in Eq. (5.44) we have

$$f_k = g_k^2 \left(\frac{\omega_N \alpha}{3^{3/4} 2k_F}\right)^{2\alpha(k)} \frac{\Gamma[1/2 - \alpha(k)]}{\Gamma[1/2 + \alpha(k)]} \cos(\pi\alpha(k)) , \tag{5.63}$$

where we used the fact that $\alpha \equiv 2qk_F/\mu$ in the first prefactor. Remember that, upon reintroducing dimensionful units, this prefactor reads $\alpha\omega_N/2\hbar c k_F$. This then contains an unknown velocity that, however, can be adsorbed into the coupling constant g_k^2. Specifically, as we would like to keep the model as simple as possible, we consider a coupling $g_k^2 = \mathcal{C}_0(1/\beta_0)^{2(\alpha(k))}$, with $\mathcal{C}_0$ a momentum-independent constant that is uniquely determined by requiring that at the Fermi momentum we recover the form of the PLL, that is $f_{k_F} = 1$. Then the self-energy in Eq. (5.61) takes the form (temporarily reintroducing dimensionful quantities for clarity)

$$\begin{aligned}\frac{\Sigma''(\omega,k)}{v_F} =& \frac{\lambda\hbar\omega_N}{2}\left(\frac{\alpha\hbar\omega_N}{3^{3/4}2\hbar c\beta_0 k_F}\right)^{-\alpha\frac{k-k_F}{k_F}}\frac{\Gamma[1/2+\alpha]}{\Gamma[1/2-\alpha]}\frac{\Gamma[1/2-\alpha(k)]}{\Gamma[1/2-\alpha(k)]}\frac{\cos(\pi\alpha(k))}{\cos(\pi\alpha)}\left(\frac{\omega^2}{\omega_N^2}\right)^{\alpha(k)}, \\ \alpha(k) =& \alpha\left(1-\frac{k-k_F}{k_F}\right) .\end{aligned} \tag{5.64}$$

Here β_0 is a fixed constant independent of doping and temperature, and it does thus not introduce any extra fitting parameter compared to the PLL model. It takes a value such that $\hbar c\beta_0 \simeq 0.21$eVÅ, chosen by comparison with experimental data.

Below, in Fig. 5.10, we present the comparison of the fit to a "cleaned-up" version of data from Ref. [119] at low-temperature and near optimal doping ($T = 8K$, $\alpha = 0.51$), where the width due to the instrumental resolution and fluctuations in the data have been removed by a combination of deconvolution and smoothing respectively. We show one branch of the dispersion, but the fit is working on both branches, so as to correctly account for the overlap of the tail of each branch on the lineshape of the other. Near the Fermi surface both models provide a good fit to the data, but as we move away from E_F the semi-holographic model (red line in the figures) does a much better job in describing the data by capturing extremely well the peak asymmetry in the entire energy range where the dispersion is approximately linear. We start to see deviations from the holographic model at $\hbar\omega = E - E_F < -0.25$ eV. However, from the right panel of Fig. 5.11, one can see that this energy is one at which the approximation of a linear dispersion seems to break down. We stress again here that, while we cannot claim with certainty the origin of this observed asymmetry, many other possible simple explanations - that are not rooted in the momentum-dependence of the electron self-energy - have been analyzed and ruled out in Ref. [119]. To validate the fit procedure, we have to check that what we obtain for $G_0(\omega)$ can have a reasonable physical explanation and, in particular, whether it is consistent with the contribution from the electron-phonon interaction as per Eq. (5.62). Notice

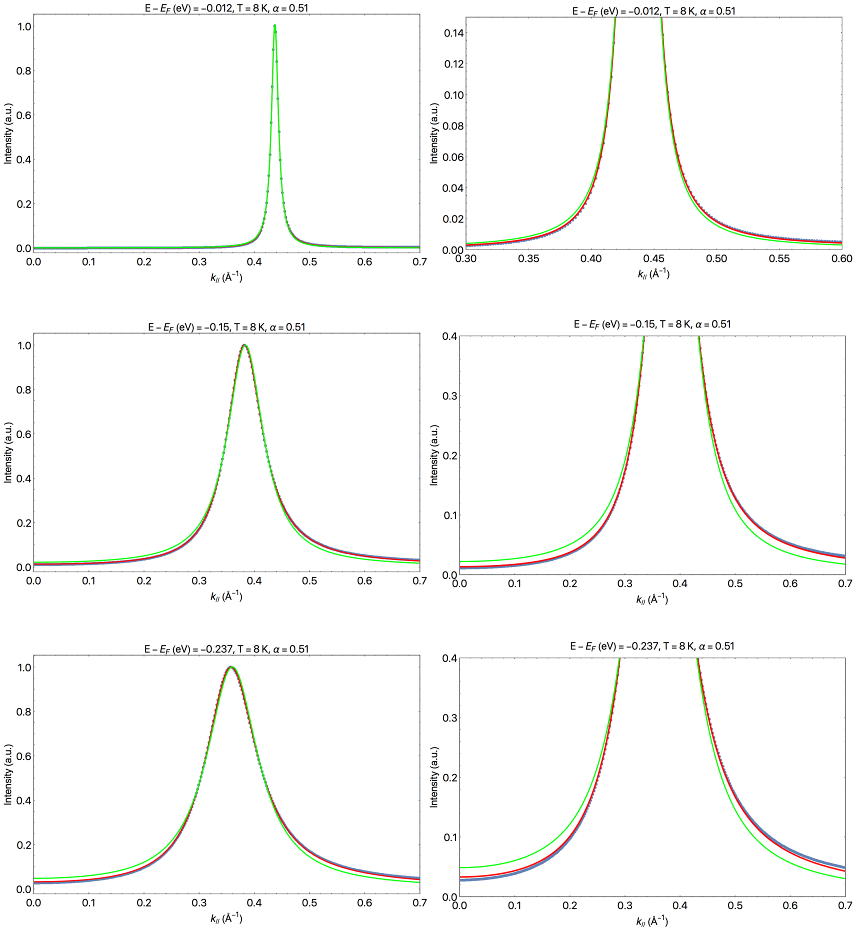

Figure 5.10: Comparison of the (smoothed) experimental MDC (blue dots) for a sample at optimal doping $\alpha = 0.51$ at $T = 8K$, with a Lorentzian fit based on the PLL (green line), and a fit based on the semi-holographic prediction for the self energy in Eq. (5.64) (red line). Near the Fermi surface both models provide a good fit, but as we move away from the Fermi surface the holographic model provides a better fit, being able to capture the asymmetry in the peak. Deep below the Fermi surface, for $E - E_F \lesssim -0.25$, we start to see deviations even for the semi-holographic model. This is, however, where we expect the low-energy approximation to break down, as is also indicated by the dispersion becoming non-linear in Fig. 5.11.

that in the way the fit is performed, the contribution of the phonon to $\Sigma''(\omega, k)$ and the dispersion relation are two independent parameters, but, within the validity of the phonon-model approximation, we expect them to be related. We therefore perform a fit of $G_0(\omega)$ for both the power-law liquid and the semi-holographic model to determine

Ω and $G_{\rm ph}$ from Eq. (5.62), and check them against the dispersion $k_*(\omega)$:

$$k_*(\omega) - k_F \overset{?}{\approx} \frac{\omega}{v_F} + \frac{G_{\rm ph}}{2\pi}\mathrm{Re}\left[\log\left(\frac{\omega - \omega_{\rm ph} - i\Omega}{\omega + \omega_{\rm ph} + i\Omega}\right)\right] \,. \tag{5.65}$$

The renormalized velocity v_F is left as a parameter in the fit for the dispersion, but we expect a value $v_F \simeq 3$eVÅ [82]. In Fig. 5.11 we show the result of the fit of this model (continuous line) to the extracted values of $G_0(\omega)$ (dots) for the PLL (green) and the semi-holographic (red) fit function. It is interesting to notice that the semi-holographic fit function, in contrast with the PLL, seems to give a description for $G_0(\omega)$ consistent with an electron-phonon model, nicely reproducing the dispersion (including the kink at $\hbar\omega_{\rm ph} = 0.07$eV) with $\hbar v_F = 2.9$eVÅ, up to energies where it ceases to be linear. While we should be careful in considering this as further evidence of the validity of the model as there could be other experimental factors influencing $G_0(\omega)$ that we might be overlooking, it is certainly satisfying to see the success of such a simple semi-holographic model with a phonon in accurately depicting the results of ARPES measurements on a single-layer cuprate. Even were the reader to be unconvinced that there is holographic physics at play in the strongly-interacting strange metal, if nothing else, the analysis presented here provides a simple and useful benchmark to compare to other theoretical models at low-temperature. A further test that is left for future work could be to check if the value found for Ω can be related to the density distribution arising from the semi-holographic Green's function $N(k) \propto \int_{-\infty}^{0} \mathrm{d}\omega \mathrm{Im}[\mathrm{Tr}[G_{\chi\chi}]]$.

5.5.3 Doping dependence

We now repeat the analysis presented above for a pair of overdoped samples at the same low-temperature $T = 8K$, and show the results in Figs. 5.14 and 5.15 for $\alpha = 0.61$ and Figs. 5.12 and 5.13 for $\alpha = 0.82$. Note that the only quantities that change with doping in the fit function Eq. (5.61) are the scaling exponent α and $k_F = k_F(\alpha)$ - both determined by a PLL fit near the Fermi surface - while all the other parameters are kept fixed. We see again, also in both overdoped cases, that the semi-holographic model provides a better description of the data at higher energies, as well as of the phonon contribution and dispersion relation [3]. The slight disagreement near the Fermi surface between $G_0(\omega)$ and the phonon model could simply arise from the fact that near E_F the approximation used for the phonon self-energy deviates the most from the Fermi-Dirac distribution with a smeared out Fermi surface, as is shown later in

---

[3] for the phonon, we considered the Fermi velocity doping independent while we allowed the coupling $G_{\rm ph}$ and the factor Ω to change with doping.

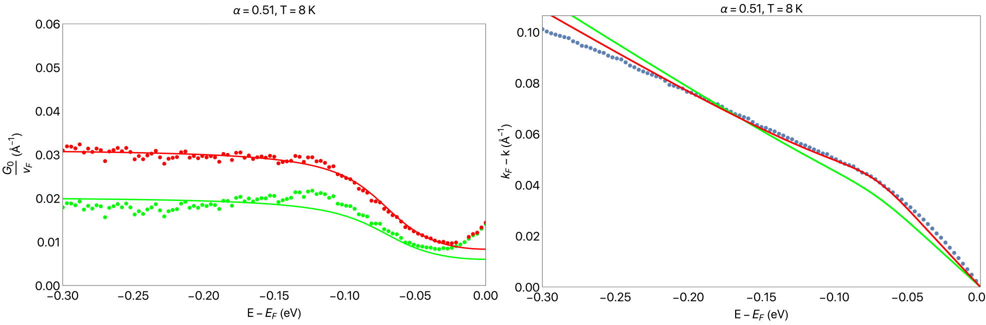

Figure 5.11: (Left) Fit of $G_0(\omega)$ in Eq. (5.61) to the electron-phonon model in Eq. (5.62) for a PLL fit function (green line), giving $G_{\text{ph}} \simeq 0.020$ and $\Omega \simeq 0.034$, and the semi-holographic one (red line), that gives $G_{\text{ph}} \simeq 0.031$ and $\Omega \simeq 0.030$ (it can be seen that there is a deviation at very small energy, probably related to some leftover disorder). (Right) Comparison between the experimentally observed dispersion relation (blue dots) with the dispersion as expected from the electron-phonon model given the parameters G_{ph} and Ω obtained from the fit. We see that the semi-holographic model provides a better fit to the dispersions with $\hbar v_F \simeq 2.9$eVÅ, while the PLL fit does not properly capture the phonon kink and gives $\hbar v_F \simeq 2.7$eVÅ.

Fig. 5.17 for the non-zero temperature example.

5.5.4 Temperature corrections

As we have seen above, the zero-temperature IR Green's function provides a compelling model to describe ARPES data at low temperatures and in the range of frequencies of interest. Moving closer to room temperatures, we want to compare experimental data with the non-zero-temperature semi-holographic prediction from Eq. (5.46). The PLL instead generalizes to

$$\Sigma''_{\text{PLL}} \propto ((\hbar\omega)^2 + (\beta k_B T)^2)^{\alpha} \ , \tag{5.66}$$

that has been shown to well capture the temperature behavior with β believed to be π, and found to lie between 3 and 4 depending on doping, see Ref. [119]. There, ARPES data were also compared with a "semi-holographic inspired" generalization - where the self-energy from the power-law liquid model was simply generalized by making the exponent momentum-dependent $((\hbar\omega)^2 + (\beta k_B T)^2)^{\alpha}/(\hbar\omega_N)^{2\alpha} \to ((\hbar\omega)^2 + (\beta k_B T)^2)^{\alpha(k)}/(\hbar\omega_N)^{2\alpha(k)}$, with $\alpha(k)$ as in Eq. (5.64) and all the other parameters kept as in the PLL. This provided an accurate description of the temperature dependence. On the other hand, the semi-holographic model seems to present a rather different

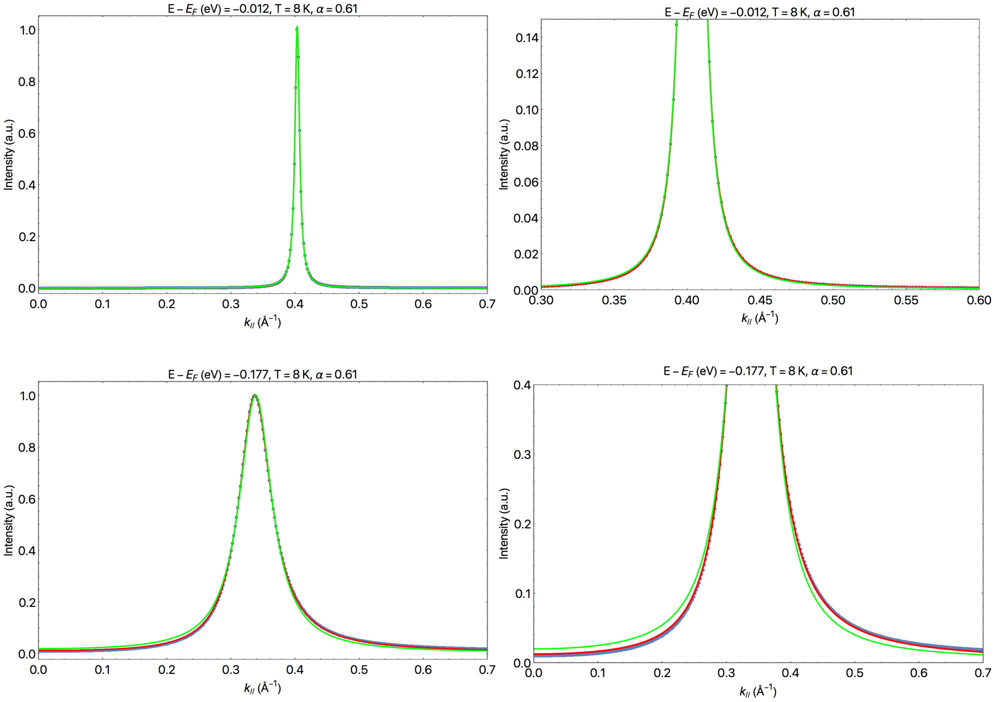

Figure 5.12: Comparison of the PLL fit (green line) and semi-holographic fit (red line) to MDC data (blue dots) for an overdoped sample with $\alpha = 0.61$ at $T = 8K$. Near the Fermi surface both models provide a good fit to the data, while further away from it the semi-holographic model accounts for the asymmetry in the peak.

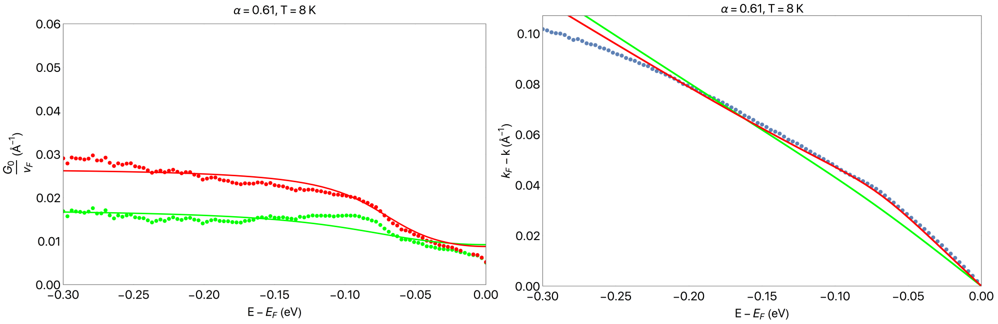

Figure 5.13: (Left) Fit to $G_0(\omega)$ with the electron-phonon model and comparision with the dispersion relation (right), for the overdoped sample with $\alpha = 0.65$. We see here as well that the semi-holographic fit function provides a description consistent with the electron-phonon model.

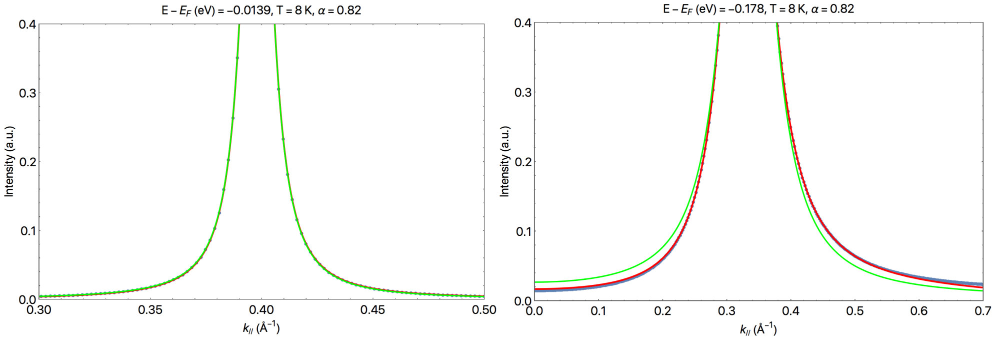

Figure 5.14: Details of the PLL fit (green line) and semi-holographic fit (red line) to MDC data blue dots for an overdoped sample with $\alpha = 0.82$ at $T = 8K$, both near and deep below the Fermi surface.

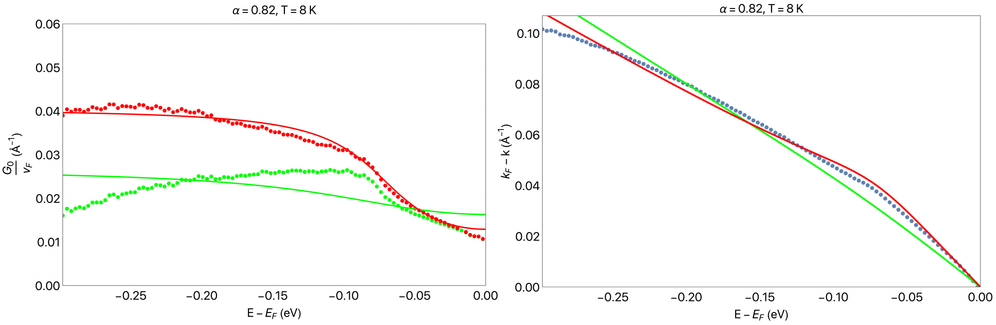

Figure 5.15: (Left) Fit to $G_0(\omega)$ with the electron-phonon model and comparision with the dispersion relation (right), for the overdoped sample with $\alpha = 0.81$.

temperature behavior as per Eq. (5.46). It is first interesting to notice that, when $\alpha(k) = 1$, the latter equation simplifies to the Fermi-liquid form

$$\mathcal{G}_k^{2D}/\mu = q\frac{4i}{3\sqrt{3}\mu^2}((\hbar\omega)^2 + (\pi k_B T)^2) \ , \tag{5.67}$$

consistent with the PLL temperature behavior. However, the factor in front of the temperature term becomes smaller for $\alpha(k) < 1$. In Fig. 5.16 we show the ratio $(\Sigma''(\hbar\omega = 0, k_B T = \epsilon, k_F)/\Sigma''(\hbar\omega = \epsilon, k_B T = 0, k_F))^{1/2\alpha}$, corresponding to β for the PLL liquid, for the semi-holographic prediction from Eq. (5.46), where $\epsilon \ll 1$. We also checked this relation numerically, where at small frequencies and especially for lower values of ν_k there are corrections to the analytical formula coming from the m and q terms in the bulk Dirac equation. We thus explored the mass parameter space

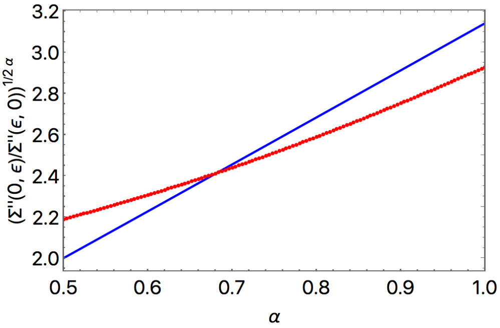

Figure 5.16: Plot of the ratio $(\Sigma''(\omega=0,k_BT=\epsilon,k_F)/\Sigma''(\omega=\epsilon,k_BT=0,k_F))^{1/2\alpha}$ from the analytical semi-holographic model (blue line), and from the full numerical solution (red line), where there are corrections dependent on the mass m in the bulk Dirac equation. In the PLL this ratio is the fit parameter β, with experimentally-determined values between 3 and 4.

between $(-1/2,1/2)$ to find the values of m that bring the ratio closest to the expected value of π even at lower ν_k. We find that this happens as we approach the lower limit of allowed mass $m=-1/2$, where, however, the temperature prefactor is still lower than the expected value for all dopings, as seen from the red line in Fig. 5.16.

Given this premise, we then do not expect the semi-holographic model to properly describe the temperature behavior, in fact, if we keep the coupling g_k fixed to the value found for the low-temperature case, we should find that the model underestimates the width of the ARPES peak for $\hbar\omega \lesssim k_bT$ compared to the prediction from the PLL. By repeating the fitting procedure explained above, we find that the semi-holographic model still accurately describes the asymmetric peak shape in the MDCs, as shown in Fig. 5.19. However, $G_0(\omega)$ departs from the expected high-temperature generalization of the electron-phonon self-energy. We generalize Eq. (5.62) to non-zero temperature by requiring that in the limit $\Omega \to 0$ the imaginary part of the model gives a good approximation of the Fermi-Dirac distribution, that is

$$\frac{\Sigma_{\rm ph}}{v_F} = \frac{G_{\rm ph}}{2\pi}\log\left(\frac{\hbar\omega-\hbar\omega_{\rm ph}-i(\hbar\Omega+4k_BT/\pi)}{\hbar\omega-\hbar\omega_{\rm ph}+i(\hbar\Omega+4k_BT/\pi)}\right), \tag{5.68}$$

where the values for $G_{\rm ph}$ and Ω are kept fixed to the ones at $T=0$. In Fig. 5.17 we show the comparison between the imaginary part of this approximation and a Fermi-Dirac distribution. This generalization gives a good description of the dispersion at higher temperatures as it can be seen in the right panel of Fig. 5.20, which compares to the experimental data at $T=205K$.

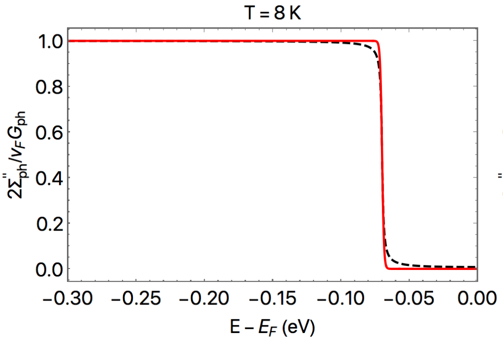

Figure 5.17: Comparison between the Fermi-Dirac distribution (red solid line) and the imaginary part of the approximation in Eq. (5.68) (black dashed line) with $\Omega = 0$.

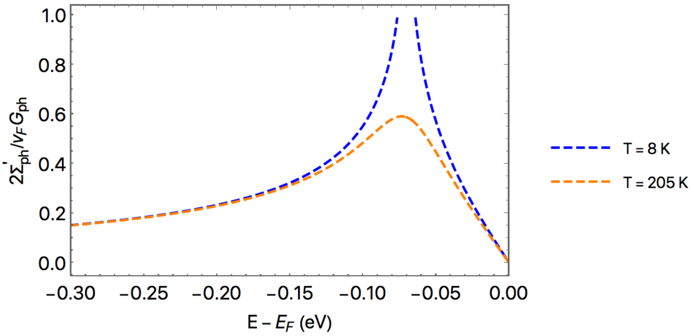

Figure 5.18: Plot of the real part of the approximation to the electron-phonon contribution in Eq. (5.68), with $\Omega = 0$. We can see a divergence at the phonon frequency $\hbar\omega_{\text{ph}} = 0.07\text{eV}$ as we approach zero temperature.

As we can see in Fig. 5.19 the contribution to $\Sigma''(\omega, k)$ that does *not* come from the electron-electron contribution to the self-energy is indeed larger than what is predicted by the simple addition of the electron-phonon interaction, as shown in Fig. 5.20. Here, we also make the comparison with the "semi-holographic inspired" model mentioned above and presented in Ref. [119] (blue line in Fig. 5.19 and blue dots in 5.20). This difference between $G_0(\omega)$ and the expected electron-phonon contribution might signal a shortcoming of the semi-holographic model considered in this paper in describing the non-zero temperature behavior of the cuprate strange metal, hinting at the necessity of searching for other models in the large class of $z = \infty$ holographic theory with a temperature behavior that more closely resembles the experimental behavior. On the other hand, it might also be that a proper description at non-zero temperature must take into account contributions to the self-energy other than the phonon that are activated at non-zero temperature, contributing to $G_0(\omega)$, or corrections to the coupling $g_k \to g_k(1 + c_1 T + \dots)$, that we did not consider here. While we believe in the importance of pointing out a possible shortcoming here, we leave a deeper analysis and identification of viable resolutions to future studies.

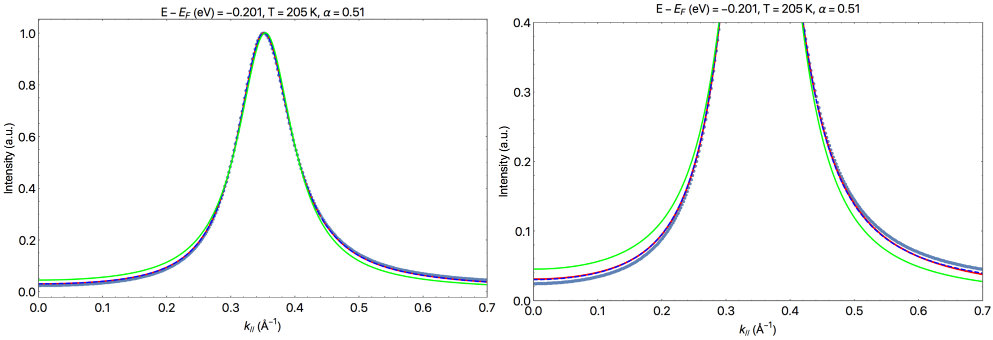

Figure 5.19: Comparison of the PLL fit (green line) and semi-holographic fit (red line) to MDC data (blue dots) for an optimally-doped sample $\alpha = 0.51$ at high temperature $T = 205K$. Here, also added for comparison, is the "holographic inspired" model of Ref. [119] (blue line). We see that the semi-holographic model still provides a better fit than the PLL to the asymmetric peak far from the Fermi surface, however, this implies a $G_0(\omega)$ that cannot be simply described by the electron-phonon model as shown in Fig. 5.20 below.

5.6 Conclusions

The main aim of this paper is to provide a simple phenomenological model that can describe the momentum distribution curves measured in high-resolution angle-resolved photoemission spectroscopy experiments on the strange metal phase on optimally-doped and overdoped single-layer cuprates. In particular, we propose a model coming from a semi-holographic theory based on the Gubser-Rocha model of the strange-metal phase, and test it on recent experimental data [119] while comparing it against the previously proposed power-law-liquid description. We find that the semi-holographic model plus an electron-phonon contribution very accurately describes the behavior of the observed spectral functions in the form of the MDCs, and provides an improvement over the power-law-liquid model in the low-temperature limit as:

- it gives a better fit to the MDC peaks over a much larger range of energy below the Fermi surface. This is because it captures an asymmetry observed in the experimental MDCs that shifts more spectral weight towards the tail of the distribution for $|k| > |k_*|$, and it reduces to the PLL result near the Fermi

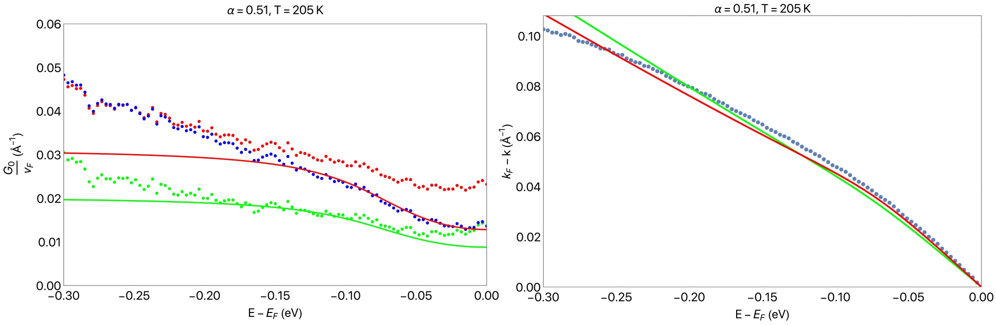

Figure 5.20: (Left) Results for $G_0(\omega)$ in Eq. (5.61) from the fit of the MDC data to a PLL fit function (green dots), the "semi-holographic inspired model" of Ref. [119], (blue dots), and the semi-holographic model (red dots) and comparison with the prediction from the high-temperature generalization of the electron-phonon model (solid lines) as in Eq. (5.68), with the parameter G_{ph} and Ω as obtained from the fit at low-temperature. While we see that in all three cases away from the Fermi surface there are contributions to $G_0(\omega)$ that are not explained by the simple model of electron-phonon interactions, the semi-holographic model also shows deviations near the Fermi surface, as expected, due to the different prediction of the temperature behavior of the electron self-energy. The deviations from the electron-phonon model are also evident in the discrepancy between the expected and measured dispersion (right).

energy where this asymmetry is too small to be observed. While there could be some alternative, non-conventional explanation of this asymmetry, we argue in favor of it coming from properties of the electron self-energy, as other possible simple causes have been analyzed and ruled out in Ref. [119].

- it is compatible with a simple model of the electron-phonon interaction that well describes - to a better degree than in the power-law liquid - both the observed dispersion relation and the contributions to the self-energy other than that from electron-electron interactions.

The most practically important implication of these results is that we can provide a phenomenological description of low-temperature momentum distribution curves in cuprates along the nodal direction with just a few fit parameters across a large range of energies and dopings. This description can be used as a benchmark to compare various theories on the self-energy in the strongly interacting cuprates. Up to a normalization we, in fact, have that

$$\mathcal{A}(\omega,k) \propto \mathrm{Im}\left[\frac{1}{k-(k_F-\frac{\omega}{v_F})-i\frac{\lambda f_k \omega_N}{2}\left[\left(\frac{\omega}{\omega_N}\right)^2\right]^{\alpha(1-(k-k_F)/k_F)}+\frac{G_{\mathrm{ph}}}{2\pi}\log\left(\frac{\omega-\omega_{\mathrm{ph}}-i\Omega}{\omega+\omega_{\mathrm{ph}}+i\Omega}\right)}\right], \tag{5.69}$$

where f_k is given in Eq. (5.63) and the only fit parameters are highlighted in red. Remember that these are constant *parameters*, in contrast with the fit *functions* $k_*(\omega)$ and $G_0(\omega)$ as in Eq. (5.61). We stress especially that - while our model is rooted in the holographic duality and that we believe these results provide good arguments in favor of the use of this technique in the description of the strange metal - the validity of the model is independent of its holographic origin. We note that momentum-dependent scaling exponents have also been predicted in a one-dimensional nonlinear-Luttinger liquid model [74], hinting perhaps at the emergence of one-dimensional physics governing the electron response along the nodal direction in copper-oxide layers.

However, we have also shown the shortcomings of the semi-holographic model adopted in this paper, in the fact that it underestimates the temperature contribution to the self-energy. However, our model is based on the specific choice of the Gubser-Rocha dual gravitational theory, which was simply dictated by the fact that it is perhaps the most simple model among the ones proposed for the description of the strange metal phase, and it allows for an analytical solution of the gravitational background. We find it already remarkable that it gives such an accurate description at low temperature, and a not-so-large discrepancy in the temperature dependence might simply point to the need for a more refined dual gravitational theory among the large class of conformal-to-AdS$_2$ metals. The differences observed at elevated temperatures might also be due to the need for a temperature-dependent coupling $g_k^2(T)$ in Eq. (5.63). This could be the topic of further research, although this would go against our main goal of providing a simple phenomenological model with as few adjustable parameters as possible. Moreover, as we have shown in Fig. 5.20, at high temperatures it appears that there are contributions to $G_0(\omega)$ that cannot simply be explained within the electron-phonon interaction, pointing to the fact that we are possibly ignoring some other effects that might change the analysis of the results if included. This is also a matter that requires further investigation in future studies.

Finally, we are careful not to claim that the momentum-dependence in the scaling exponent of the self-energy is the only possible explanation of the observed asymmetry, as there could be other factors that might generate this shift in the spectral weight, some of which, though, are carefully analyzed and ruled out in Ref. [119]. Moreover, it is important to understand that, while the asymmetry could be accounted for by simply adding an additional momentum dependence as an extra parameter in the phenomenological PLL model of the electron self-energy, the model presented here *predicts* the form of this momentum dependence, and it is far from trivial that MDC experimental results across a large range of energies can be so well described by this function, without adding any additional adjustable parameter to the PLL model.

Bibliography

[1] Martin Ammon and Johanna Erdmenger. *Gauge/Gravity Duality: Foundations and Applications.* Cambridge University Press, 2015.

[2] James G. Analytis, H-H. Kuo, Ross D. McDonald, Mark Wartenbe, P. M. C. Rourke, N. E. Hussey, and I. R. Fisher. Transport near a quantum critical point in BaFe2(As1-xPx)2. *Nature Physics*, 10(3):194–197, January 2014.

[3] Richard J. Anantua, Sean A. Hartnoll, Victoria L. Martin, and David M. Ramirez. The pauli exclusion principle at strong coupling: holographic matter and momentum space. *Journal of High Energy Physics*, 2013(3):104, Mar 2013.

[4] Yoichi Ando, Y Hanaki, S Ono, T Murayama, Kouji Segawa, N Miyamoto, and Seiki Komiya. Carrier concentrations in $\mathrm{Bi_2Sr_{2-\mathit{x}}La_\mathit{x}CuO_{6+\mathit{d}}}$ single crystals and their relation to the Hall coefficient and thermopower. *Physical Review B*, 61(22):R14956–R14959, 2000.

[5] S. S. Apostolov, A. Levchenko, and A. V. Andreev. Hydrodynamic coulomb drag of strongly correlated electron liquids. *Phys. Rev. B*, 89:121104(R), Mar 2014.

[6] J. Ayres, M. Berben, M. Čulo, Y. T. Hsu, E. van Heumen, Y. Huang, J. Zaanen, T. Kondo, T. Takeuchi, J. R. Cooper, C. Putzke, S. Friedemann, A. Carrington, and N. E. Hussey. Incoherent transport across the strange-metal regime of overdoped cuprates. *Nature*, 595(7869):661–666, 2021.

[7] S. M. Badalyan and F. M. Peeters. Enhancement of coulomb drag in double-layer graphene structures by plasmons and dielectric background inhomogeneity. *Phys. Rev. B*, 86:121405(R), Sep 2012.

[8] J. Bardeen, L. N. Cooper, and J. R. Schrieffer. Theory of superconductivity. *Phys. Rev.*, 108:1175–1204, Dec 1957.

[9] J. G. Bednorz and K. A. Müller. Possible high-T_c superconductivity in the Ba–La–Cu–O system. *Zeitschrift für Physik B Condensed Matter*, 64(2):189–193, 1986.

[10] Erez Berg, Eduardo Fradkin, Steven A Kivelson, and John M Tranquada. Striped superconductors: how spin, charge and superconducting orders intertwine in the cuprates. *New Journal of Physics*, 11(11):115004, nov 2009.

[11] Andreas Bill, H Morawitz, and V Z. Kresin. Electronic collective modes and superconductivity in layered conductors. *Physical Review B*, 68, 05 2003.

[12] Mike Blake and Aristomenis Donos. Quantum critical transport and the hall angle in holographic models. *Phys. Rev. Lett.*, 114:021601, Jan 2015.

[13] P. V. Bogdanov, A. Lanzara, S. A. Kellar, X. J. Zhou, E. D. Lu, W. J. Zheng, G. Gu, J. I. Shimoyama, K. Kishio, H. Ikeda, R. Yoshizaki, Z. Hussain, and Z. X. Shen. Evidence for an energy scale for quasiparticle dispersion in $Bi_2Sr_2CaCu_2O_8$. *Physical Review Letters*, 85(12):2581–2584, 2000.

[14] David Bohm and David Pines. A Collective Description of Electron Interactions. I. Magnetic Interactions. *Phys. Rev.*, 82:625–634, Jun 1951.

[15] David Bohm and David Pines. A Collective Description of Electron Interactions: III. Coulomb Interactions in a Degenerate Electron Gas. *Phys. Rev.*, 92:609–625, Nov 1953.

[16] J. A. N. Bruin, H. Sakai, R. S. Perry, and A. P. Mackenzie. Similarity of Scattering Rates in Metals Showing T-Linear Resistivity. *Science*, 339(6121):804–807, 2013.

[17] Christos Charmousis, Blaise Goutéraux, Bom Soo Kim, Elias Kiritsis, and Rene Meyer. Effective holographic theories for low-temperature condensed matter systems. *Journal of High Energy Physics*, 2010(11):151, Nov 2010.

[18] T. R. Chien, Z. Z. Wang, and N. P. Ong. Effect of zn impurities on the normal-state hall angle in single-crystal $yba_2cu_{3-x}zn_xo_{7-\delta}$. *Phys. Rev. Lett.*, 67:2088–2091, Oct 1991.

[19] R. A. Cooper, Y. Wang, B. Vignolle, O. J. Lipscombe, S. M. Hayden, Y. Tanabe, T. Adachi, Y. Koike, M. Nohara, H. Takagi, Cyril Proust, and N. E. Hussey. Anomalous criticality in the electrical resistivity of $La_{2-x}Sr_xCuO_4$. *Science*, 323(5914):603–607, 2009.

[20] R. A. Cooper, Y. Wang, B. Vignolle, O. J. Lipscombe, S. M. Hayden, Y. Tanabe, T. Adachi, Y. Koike, M. Nohara, H. Takagi, Cyril Proust, and N. E. Hussey. Anomalous criticality in the electrical resistivity of La2–xSrxCuO4. *Science*, 323(5914):603–607, 2009.

[21] Mihailo Čubrović, Jan Zaanen, and Koenraad Schalm. String theory, quantum phase transitions, and the emergent fermi liquid. *Science*, 325(5939):439–444, June 2009.

[22] T. Cuk, D. H. Lu, X. J. Zhou, Z. X. Shen, T. P. Devereaux, and N. Nagaosa. A review of electron-phonon coupling seen in the high-Tc. Superconductors by

angle-resolved photoemission studies (ARPES). *Physica Status Solidi (B) Basic Research*, 242(1):11–29, 2005.

[23] J. Custers, P. Gegenwart, H. Wilhelm, K. Neumaier, Y. Tokiwa, O. Trovarelli, C. Geibel, F. Steglich, C. Pépin, and P. Coleman. The break-up of heavy electrons at a quantum critical point. *Nature*, 424(6948):524–527, July 2003.

[24] Richard A Davison and Nikolaos K Kaplis. Bosonic excitations of the AdS 4 Reissner-Nordstrom black hole. *Journal of High Energy Physics*, 2011(12):37, 2011.

[25] Richard A. Davison and Andrei Parnachev. Hydrodynamics of cold holographic matter. *Journal of High Energy Physics*, 2013(6), jun 2013.

[26] Richard A. Davison, Koenraad Schalm, and Jan Zaanen. Holographic duality and the resistivity of strange metals. *Phys. Rev. B*, 89:245116, Jun 2014.

[27] Sebastian De Haro, Kostas Skenderis, and Sergey N. Solodukhin. Holographic reconstruction of spacetime and renormalization in the AdS/CFT correspondence. *Communications in Mathematical Physics*, 217(3):595–622, 2001.

[28] Mohammad Edalati, Juan I. Jottar, and Robert G. Leigh. Holography and the sound of criticality. *Journal of High Energy Physics*, 2010(10):58, Oct 2010.

[29] Mohammad Edalati, Juan I. Jottar, and Robert G. Leigh. Shear modes, criticality and extremal black holes. *Journal of High Energy Physics*, 2010(4), 2010.

[30] V. J. Emery, S. A. Kivelson, and J. M. Tranquada. Stripe phases in high-temperature superconductors. *Proceedings of the National Academy of Sciences*, 96(16):8814–8817, August 1999.

[31] T. Faulkner, N. Iqbal, H. Liu, J. McGreevy, and D. Vegh. Strange Metal Transport Realized by Gauge/Gravity Duality. *Science*, 329(5995):1043–1047, aug 2010.

[32] Thomas Faulkner, Hong Liu, John McGreevy, and David Vegh. Emergent quantum criticality, fermi surfaces, and ads$_2$. *Phys. Rev. D*, 83:125002, Jun 2011.

[33] Thomas Faulkner and Joseph Polchinski. Semi-Holographic Fermi Liquids. *Journal of High Energy Physics*, 06:012, 2011.

[34] Tom Faulkner, Nabil Iqbal, Hong Liu, John McGreevy, and David Vegh. Holographic non-fermi-liquid fixed points. *Philosophical Transactions of the Royal Society A: Mathematical, Physical and Engineering Sciences*, 369(1941):1640–1669, April 2011.

[35] Alexander L Fetter. Electrodynamics of a layered electron gas. II. periodic array. *Annals of Physics*, 88(1):1–25, nov 1974.

[36] Karsten Flensberg and Ben Yu-Kuang Hu. Coulomb drag as a probe of coupled plasmon modes in parallel quantum wells. *Phys. Rev. Lett.*, 73:3572–3575, Dec 1994.

[37] Karsten Flensberg and Ben Yu-Kuang Hu. Plasmon enhancement of coulomb drag in double-quantum-well systems. *Phys. Rev. B*, 52:14796–14808, Nov 1995.

[38] Karsten Flensberg, Ben Yu-Kuang Hu, A. P. Jauho, and Jari M. Kinaret. Linear-response theory of coulomb drag in coupled electron systems. *Phys. Rev. B*, 52:14761–14774, Nov 1995.

[39] G. W. Gibbons and S. W. Hawking. Action integrals and partition functions in quantum gravity. *Physical Review D*, 1977.

[40] B. Goutéraux and E. Kiritsis. Generalized holographic quantum criticality at finite density. *Journal of High Energy Physics*, 2011(12):36, Dec 2011.

[41] T. J. Gramila, J. P. Eisenstein, A. H. MacDonald, L. N. Pfeiffer, and K. W. West. Mutual friction between parallel two-dimensional electron systems. *Phys. Rev. Lett.*, 66:1216–1219, Mar 1991.

[42] U Gran, M Tornsö, and T Zingg. Exotic Holographic Dispersion. 2018.

[43] U. Gran, M. Tornsö, and T. Zingg. Holographic plasmons. *Journal of High Energy Physics*, 2018(11):176, Nov 2018.

[44] U. Gran, M. Tornsö, and T. Zingg. Exotic holographic dispersion. *Journal of High Energy Physics*, 2019(2):32, Feb 2019.

[45] Ulf Gran, Marcus Tornsö, and Tobias Zingg. Holographic response of electron clouds. 2018.

[46] Ulf Gran, Marcus Tornsö, and Tobias Zingg. Plasmons in Holographic Graphene. *SciPost Phys.*, 8:93, 2020.

[47] Richard L. Greene, Pampa R. Mandal, Nicholas R. Poniatowski, and Tarapada Sarkar. The strange metal state of the electron-doped cuprates. *Annual Review of Condensed Matter Physics*, 11(1):213–229, 2020.

[48] S. S. Gubser, I. R. Klebanov, and A. M. Polyakov. Gauge theory correlators from non-critical string theory. *Physics Letters, Section B: Nuclear, Elementary Particle and High-Energy Physics*, 428(1-2):105–114, 1998.

[49] Steven S. Gubser and Jie Ren. Analytic fermionic green's functions from holography. *Phys. Rev. D*, 86:046004, Aug 2012.

[50] Steven S. Gubser and Fabio D. Rocha. Peculiar properties of a charged dilatonic black hole in ads$_5$. *Phys. Rev. D*, 81:046001, Feb 2010.

[51] Steven S. Gubser and Fabio D. Rocha. Peculiar properties of a charged dilatonic black hole in AdS$_5$. *Physical Review D*, 81(4):1–12, 2010.

[52] Umut Gürsoy, Erik Plauschinn, Henk Stoof, and Stefan Vandoren. Holography and ARPES sum-rules. *Journal of High Energy Physics*, 2012(5):18, may 2012.

[53] Sean A. Hartnoll. Lectures on holographic methods for condensed matter physics. *Classical and Quantum Gravity*, 26(22), 2009.

[54] Sean A. Hartnoll, Christopher P. Herzog, and Gary T. Horowitz. Building a holographic superconductor. *Physical Review Letters*, 101(3), 2008.

[55] Sean A Hartnoll, Christopher P Herzog, and Gary T Horowitz. Holographic superconductors. *Journal of High Energy Physics*, 2008(12):15, 2008.

[56] Sean A. Hartnoll and Liza Huijse. Fractionalization of holographic Fermi surfaces. *Class. Quant. Grav.*, 29:194001, 2012.

[57] Sean A. Hartnoll, Andrew Lucas, and Subir Sachdev. Holographic quantum matter. dec 2016.

[58] S. W. Hawking and Gary T. Horowitz. The gravitational Hamiltonian, action, entropy and surface terms. *Classical and Quantum Gravity*, 1996.

[59] M. Hepting, L. Chaix, E. W. Huang, R. Fumagalli, Y. Y. Peng, B. Moritz, K. Kummer, N. B. Brookes, W. C. Lee, M. Hashimoto, T. Sarkar, J.-F. He, C. R. Rotundu, Y. S. Lee, R. L. Greene, L. Braicovich, G. Ghiringhelli, Z. X. Shen, T. P. Devereaux, and W. S. Lee. Three-dimensional collective charge excitations in electron-doped copper oxide superconductors. *Nature*, oct 2018.

[60] C. P. Herzog. Lectures on holographic superfluidity and superconductivity. *Journal of Physics A: Mathematical and Theoretical*, 42(34), 2009.

[61] N. P. R. Hill, J. T. Nicholls, E. H. Linfield, M. Pepper, D. A. Ritchie, G. A. C. Jones, Ben Yu-Kuang Hu, and Karsten Flensberg. Correlation effects on the coupled plasmon modes of a double quantum well. *Phys. Rev. Lett.*, 78:2204–2207, Mar 1997.

[62] Tobias Holder. Hydrodynamic coulomb drag and bounds on diffusion. *Phys. Rev. B*, 100:235121, Dec 2019.

[63] N E Hussey. Phenomenology of the normal state in-plane transport properties of high-t_c cuprates. *Journal of Physics: Condensed Matter*, 20(12):123201, feb 2008.

[64] N E Hussey, J Buhot, and S Licciardello. A tale of two metals: contrasting criticalities in the pnictides and hole-doped cuprates. *Reports on Progress in Physics*, 81(5):052501, mar 2018.

[65] E. H. Hwang and S. Das Sarma. Plasmon modes of spatially separated double-layer graphene. *Phys. Rev. B*, 80:205405, Nov 2009.

[66] Adilet Imambekov and Leonid Glazman. Universal theory of nonlinear luttinger liquids. *Science*, 323(5911):228, November 2009.

[67] N. Iqbal and H. Liu. Real-time response in ads/cft with application to spinors. *Fortschritte der Physik*, 57(5-7):367–384, 2009.

[68] Nabil Iqbal, Hong Liu, and Márk Mezei. Lectures on holographic non-fermi liquids and quantum phase transitions. 2011.

[69] Y. Ishii and J. Ruvalds. Acoustic plasmons and cuprate superconductivity. *Physical Review B*, 48(5):3455–3463, aug 1993.

[70] V. P. J. Jacobs, S. Grubinskas, and H. T. C. Stoof. Towards a field-theory interpretation of bottom-up holography. *Journal of High Energy Physics*, 2015(4):33, apr 2015.

[71] V. P.J. Jacobs, S. J.G. Vandoren, and H. T.C. Stoof. Holographic interaction effects on transport in Dirac semimetals. *Physical Review B - Condensed Matter and Materials Physics*, 90(4), 2014.

[72] Vivian P J Jacobs. *Dirac and Weyl semimetals with holographic interactions.* PhD thesis, Utrecht University, 2015.

[73] A. P. Jauho and Henrik Smith. Coulomb drag between parallel two-dimensional electron systems. *Phys. Rev. B*, 47:4420–4428, Feb 1993.

[74] Y. Jin, O. Tsyplyatyev, M. Moreno, A. Anthore, W. K. Tan, J. P. Griffiths, I. Farrer, D. A. Ritchie, L. I. Glazman, A. J. Schofield, and C. J.B. Ford. Momentum-dependent power law measured in an interacting quantum wire beyond the Luttinger limit. *Nature Communications*, 10(1), 2019.

[75] Y. Kakehashi and P. Fulde. Marginal fermi liquid theory in the hubbard model. *Phys. Rev. Lett.*, 94:156401, Apr 2005.

[76] Alex Kamenev and Yuval Oreg. Coulomb drag in normal metals and superconductors: Diagrammatic approach. *Physical Review B*, 52(10):7516–7527, 1 1995.

[77] Adam Kaminski and H. M. Fretwell. On the extraction of the self-energy from angle- resolved photoemission spectroscopy. *New Journal of Physics*, 6:1–7, 2004.

[78] Matthias Kaminski, Karl Landsteiner, Javier Mas, Jonathan P. Shock, and Javier Tarríoc. Holographic operator mixing and quasinormal modes on the brane. *Journal of High Energy Physics*, 2010(2), 2010.

[79] A. Karch, D. T. Son, and A. O. Starinets. Holographic quantum liquid. *Phys. Rev. Lett.*, 102:051602, Feb 2009.

[80] B. Keimer, S. A. Kivelson, M. R. Norman, S. Uchida, and J. Zaanen. From quantum matter to high-temperature superconductivity in copper oxides. *Nature*, 518(7538):179–186, February 2015.

[81] J. Kokalj, N. E. Hussey, and Ross H. McKenzie. Transport properties of the metallic state of overdoped cuprate superconductors from an anisotropic marginal fermi liquid model. *Phys. Rev. B*, 86:045132, Jul 2012.

[82] A. A. Kordyuk, S. V. Borisenko, A. Koitzsch, J. Fink, M. Knupfer, and H. Berger. Bare electron dispersion from experiment: Self-consistent self-energy analysis of photoemission data. *Physical Review B*, 71(21):1–11, 2005.

[83] Pavel Kovtun. Lectures on hydrodynamic fluctuations in relativistic theories. *Journal of Physics A: Mathematical and Theoretical*, 45(47):473001, nov 2012.

[84] Pavel K Kovtun and Andrei O Starinets. Quasinormal modes and holography. *Physical Review D - Particles, Fields, Gravitation and Cosmology*, 72(8), 2005.

[85] V. Z. Kresin and H. Morawitz. Layer plasmons and high-tcsuperconductivity. *Physical Review B*, 37(13):7854–7857, may 1988.

[86] A. Krikun, A Romero-Bermúdez, K Schalm, and J Zaanen. The anomalous attenuation of plasmons in strange metals and holography. 2018.

[87] Patrick A. Lee, Naoto Nagaosa, and Xiao-Gang Wen. Doping a mott insulator: Physics of high-temperature superconductivity. *Rev. Mod. Phys.*, 78:17–85, Jan 2006.

[88] A. Legros, S. Benhabib, W. Tabis, F. Laliberté, M. Dion, M. Lizaire, B. Vignolle, D. Vignolles, H. Raffy, Z. Z. Li, P. Auban-Senzier, N. Doiron-Leyraud, P. Fournier, D. Colson, L. Taillefer, and C. Proust. Universal t-linear resistivity and planckian dissipation in overdoped cuprates. *Nature Physics*, 15(2):142–147, November 2018.

[89] Zhidong Leong, Chandan Setty, Kridsanaphong Limtragool, and Philip W. Phillips. Power-law liquid in cuprate superconductors from fermionic unparticles. *Physical Review B*, 96(20):1–9, 2017.

[90] S. Licciardello, J. Buhot, J. Lu, J. Ayres, S. Kasahara, Y. Matsuda, T. Shibauchi, and N. E. Hussey. Electrical resistivity across a nematic quantum critical point. *Nature*, 567(7747):213–217, February 2019.

[91] Hong Liu, John McGreevy, and David Vegh. Non-fermi liquids from holography. *Phys. Rev. D*, 83:065029, Mar 2011.

[92] Andrew Lucas and Sankar Das Sarma. Electronic sound modes and plasmons in hydrodynamic two-dimensional metals. *Physical Review B*, 97(11), 2018.

[93] Andrew Lucas and Kin Chung Fong. Hydrodynamics of electrons in graphene. 30(5), 2018.

[94] Juan Maldacena. The large-n limit of superconformal field theories and supergravity. *International Journal of Theoretical Physics*, 38(4):1113–1133, Apr 1999.

[95] Donald Marolf and Simo F Ross. Boundary conditions and dualities: vector fields in AdS/CFT. *Journal of High Energy Physics*, 2006(11):085–085, nov 2006.

[96] E. Mauri and H. T. C. Stoof. Screening of coulomb interactions in holography. *Journal of High Energy Physics*, 2019(4):35, Apr 2019.

[97] Enea Mauri, Steef Smit, Mark Golden, and Henk Theodorus C. Stoof. Gauge-gravity duality comes to the lab: evidence of momentum-dependent scaling exponents in the nodal electron self-energy of cuprate strange metals. *To be published.*

[98] Wolfgang Mück. An improved correspondence formula for AdS/CFT with multi-trace operators. *Physics Letters, Section B: Nuclear, Elementary Particle and High-Energy Physics*, 531(3-4):301–304, 2002.

[99] Hidekazu Mukuda, Sunao Shimizu, Akira Iyo, and Yoshio Kitaoka. High-T_c superconductivity and antiferromagnetism in multilayered copper oxides –a new paradigm of superconducting mechanism–. *Journal of the Physical Society of Japan*, 81(1):011008, 2012.

[100] Abhishek Nag, M. Zhu, Matías Bejas, J. Li, H. C. Robarts, Hiroyuki Yamase, A. N. Petsch, D. Song, H. Eisaki, A. C. Walters, M. García-Fernández, Andrés Greco, S. M. Hayden, and Ke-Jin Zhou. Detection of acoustic plasmons in hole-doped lanthanum and bismuth cuprate superconductors using resonant inelastic x-ray scattering. *Phys. Rev. Lett.*, 125:257002, Dec 2020.

[101] Jun Nagamatsu, Norimasa Nakagawa, Takahiro Muranaka, Yuji Zenitani, and Jun Akimitsu. Superconductivity at 39 k in magnesium diboride. *Nature*, 410(6824):63–64, March 2001.

[102] B. N. Narozhny and A. Levchenko. Coulomb drag. *Rev. Mod. Phys.*, 88:025003, May 2016.

[103] John W. Negele and Henri Orland. *Quantum Many-particle Systems.* Westview Press, November 1998.

[104] Masao Ogata and Hidetoshi Fukuyama. The $t--J$ model for the oxide high-T_c superconductors. *Reports on Progress in Physics*, 71:036501, 02 2008.

[105] David Pines. A Collective Description of Electron Interactions: IV. Electron Interaction in Metals. *Phys. Rev.*, 92:626–636, Nov 1953.

[106] David Pines and David Bohm. A Collective Description of Electron Interactions: II. Collective vs Individual Particle Aspects of the Interactions. *Phys. Rev.*, 85:338–353, Jan 1952.

[107] G. Policastro, D. T. Son, and A. O. Starinets. From AdS/CFT correspondence to hydrodynamics. II. Sound waves. may 2002.

[108] M. R. Presland, J. L. Tallon, R. G. Buckley, R. S. Liu, and N. E. Flower. General trends in oxygen stoichiometry effects on Tc in Bi and Tl superconductors. *Physica C: Superconductivity and its applications*, 176(1-3):95–105, 1991.

[109] Rosario E. V. Profumo, Reza Asgari, Marco Polini, and A. H. MacDonald. Double-layer graphene and topological insulator thin-film plasmons. *Phys. Rev. B*, 85:085443, Feb 2012.

[110] Cyril Proust and Louis Taillefer. The remarkable underlying ground states of cuprate superconductors. *Annual Review of Condensed Matter Physics*, 10(1):409–429, 2019.

[111] Mohit Randeria, Arun Paramekanti, and Nandini Trivedi. Nodal Quasiparticle Dispersion in Strongly Correlated d-wave Superconductors. *Physical Review B*, 69(14):1–5, 2003.

[112] T. J. Reber, N. C. Plumb, J. A. Waugh, and D. S. Dessau. Effects, determination, and correction of count rate nonlinearity in multi-channel analog electron detectors. *Review of Scientific Instruments*, 85(4):043907, 2014.

[113] T. J. Reber, X. Zhou, N. C. Plumb, S. Parham, J. A. Waugh, Y. Cao, Z. Sun, H. Li, Q. Wang, J. S. Wen, Z. J. Xu, G. Gu, Y. Yoshida, H. Eisaki, G. B. Arnold, and D. S. Dessau. A unified form of low-energy nodal electronic interactions in hole-doped cuprate superconductors. *Nature Communications*, 10(1):5737, 2019.

[114] Aurelio Romero-Bermúdez, Alexander Krikun, Koenraad Schalm, and Jan Zaanen. Anomalous attenuation of plasmons in strange metals and holography. *Phys. Rev. B*, 99:235149, Jun 2019.

[115] Bitan Roy and Vladimir Juričić. Optical conductivity of an interacting Weyl liquid in the collisionless regime. *Physical Review B*, 96(15), 2017.

[116] D. J. Scalapino. A common thread: The pairing interaction for unconventional superconductors. *Rev. Mod. Phys.*, 84:1383–1417, Oct 2012.

[117] Matthew D Schwartz. *Quantum field theory and the standard model.* Cambridge University Press, 2014.

[118] Kostas Skenderis. Lecture notes on holographic renormalization. In *Classical and Quantum Gravity*, volume 19, pages 5849–5876, 2002.

[119] S. Smit, E. Mauri, L. Bawden, F. Heringa, F. Gerritsen, E. van Heumen, Y. K. Huang, T. Kondo, T. Takeuchi, N. E. Hussey, T. K. Kim, C. Cacho, A. Krikun, K. Schalm, H. T. C. Stoof, and M. S. Golden. Momentum-dependent scaling exponents of nodal self-energies measured in strange metal cuprates and modelled using semi-holography, 2021.

[120] T. Stauber and G. Gómez-Santos. Plasmons and near-field amplification in double-layer graphene. *Phys. Rev. B*, 85:075410, Feb 2012.

[121] Henk T. C. Stoof, Dennis B. M. Dickerscheid, and Koos Gubbels. *Ultracold Quantum Fields (Theoretical and Mathematical Physics).* Springer, 2008.

[122] Misha Turlakov and Anthony J. Leggett. Sum rule analysis of umklapp processes and coulomb energy: Application to cuprate superconductivity. *Physical Review B*, 67(9), mar 2003.

[123] T Valla, A V Fedorov, P D Johnson, B O Wells, S L Hulbert, Q Li, G D Gu, and

N Koshizuka. Evidence for quantum critical behavior in the optimally doped cuprate $Bi_2Sr_2CaCu_2O_{8+\delta}$. *Science*, 285(5436):2110–2113, 1999.

[124] C. M. Varma, P. B. Littlewood, S. Schmitt-Rink, E. Abrahams, and A. E. Ruckenstein. Phenomenology of the Normal State of Cu-O High-Temperature Superconductors. *Physical Review Letters*, 63(18):1996–1999, 1989.

[125] T. Vazifehshenas, T. Amlaki, Mojtaba Farmanbar, and Fariborz Parhizgar. Temperature effect on plasmon dispersions in double-layer graphene systems. *Physics Letters A*, 374:4899–4903, 11 2010.

[126] C. N. Veenstra, G. L. Goodvin, M. Berciu, and A. Damascelli. Spectral function tour of electron-phonon coupling outside the Migdal limit. *Physical Review B*, 84(8):21–25, 2011.

[127] Matthias Vojta. Lattice symmetry breaking in cuprate superconductors: stripes, nematics, and superconductivity. *Advances in Physics*, 58(6):699–820, 2009.

[128] Edward Witten. Anti de sitter space and holography. *Advances in Theoretical and Mathematical Physics*, 2(2):253–290, 1998.

[129] Edward Witten. Multi-trace operators, boundary conditions, and ads/cft correspondence. *arXiv*, 01 2002.

[130] Edward Witten. Sl(2,z) action on three-dimensional conformal field theories with abelian symmetry, 2003.

[131] James W. York. Role of conformal three-geometry in the dynamics of gravitation. *Physical Review Letters*, 1972.

[132] J. Zaanen, O. Y. Osman, H. Eskes, and W. van Saarloos. Dynamical stripe correlations in cuprate superconductors. *Journal of Low Temperature Physics*, 105(3):569–579, Nov 1996.

[133] Jan Zaanen, Yan Liu, Ya-Wen Sun, and Koenraad Schalm. *Holographic Duality in Condensed Matter Physics.* Cambridge University Press, 2015.

[134] Jan Zaanen, Yan Liu, Ya-Wen Sun, and Koenraad Schalm. *Holographic Duality in Condensed Matter Physics.* Cambridge University Press, 2015.

[135] Yubo Zhang, Christopher Lane, James W. Furness, Bernardo Barbiellini, John P. Perdew, Robert S. Markiewicz, Arun Bansil, and Jianwei Sun. Competing stripe and magnetic phases in the cuprates from first principles. *Proceedings of the National Academy of Sciences*, 117(1):68–72, 2020.

[136] Lian Zheng and A. H. MacDonald. Coulomb drag between disordered two-dimensional electron-gas layers. *Phys. Rev. B*, 48:8203–8209, Sep 1993.

Samenvatting

In dit proefschrift gebruiken we de ijk/zwaartekracht (holografische) dualiteit om de eigenschappen van bepaalde sterk interagerende kwantumsystemen te bestuderen. Onze grootste interesse ligt in het modelleren en beschrijven van de eigenschappen van de vreemde metaalfase van de koperoxiden, een klasse van materialen die een gelaagde structuur van CuO_2-vlakken delen en die worden gekenmerkt door sterke interacties tussen de samenstellende elektronen. Deze sterke interacties vormen de kern van de bijzondere eigenschappen van dergelijke verbindingen in vergelijking met de meer algemeen bekende metalen die onder de noemer van het goed begrepen Fermi-vloeistofkader vallen. De meest interessante van dergelijke eigenaardigheden is misschien wel dat - binnen een bepaald dopingbereik - deze verbindingen supergeleiders worden bij "hoge" temperaturen, ruim boven de limiet die wordt verwacht van de BCS-theorie. Het is echter aangetoond dat zelfs de normale fase enkele ongebruikelijke eigenschappen bezit, waardoor de naam "vreemde metaalfase" wordt gebruikt. Deze fase is de focus van ons onderzoek, omdat men gelooft dat het begrijpen ervan de deuren zou openen naar het mysterie van supergeleiding bij hoge temperaturen. Meer in detail, met het oog op de experimentele kant van de zaak, laten we in Hoofdstuk 2 zien hoe we de langeafstands Coulomb-interactie consistent kunnen introduceren in het holografische raamwerk, om in staat te zijn plasmonische excitaties te beschrijven die experimenteel zijn waargenomen in meerderelaags koperoxiden. Vervolgens gebruiken we dit om in Hoofdstuk 3 de eigenschappen van Coulomb-weerstand in een sterk interagerend tweelaagssysteem te bestuderen om aan te tonen dat het dominante gedrag bij lage temperaturen met een vierde macht schaalt met de temperatuur, afwijkend van de T^2-schaal van een Fermi-vloeistof. Bovendien geven we een schatting van de grootte van het effect bij kamertemperatuur en hogere temperaturen, in de hoop een bruikbare voorspelling te geven die in toekomstige experimenten kan worden getest. Vervolgens richten we ons in Hoofdstuk 4 op de fermionische spectrale functie, waar we momentumverdelingsfuncties analyseren die zijn verkregen door ARPES-metingen langs de knooprichting, om aan te tonen dat een asymmetrie die wordt waargenomen in de pieken consistent is met de voorspelling – afkomstig van een bepaalde Einstein- Maxwell-Dilaton (EMD) holografische theorie - van een momentumafhankelijke machtswetschaling van de elektron zelfenergie. Ten slotte gaan we in Hoofdstuk 5 dieper in op de theorie achter de holografische zelfenergie van het EMD-model, waarbij we de consistentie van de theorie met de experimentele gegevens bij energieën beneden de Fermi-energie verder controleren door een model voor de elektron-fononinteractie te introduceren, en uiteindelijk ook de beperkingen te laten zien naarmate de temperatuur stijgt.

Acknowledgments

After all these years spent working towards the results presented in this thesis, there are so many people I should acknowledge that the ones I explicitly mention here are only a small selection. Nonetheless, I surely owe a big thank you to everyone I met along the way that helped to make this long trip even just a tiny bit easier. Let me start from the top though, so, of course, thanks Henk for guiding me through this journey that we started together while I was still a student. I enjoyed working with you on the Master's thesis and I was so happy to hear I could continue doing so as a PhD! Thanks especially for always believing in me through all the ups and downs of my PhD adventure. I may not be the most talkative person you have ever met, but knowing that whenever I was going through a hard time, be it research-related or not, you were there to patiently listen and offer suggestions, always helped me to get back on track.

Then, I won't ever be able to thank my family enough. Sure you might not have helped much with the research in this thesis, but the importance of all the hours spent talking and laughing on Skype, your constant support and your ability to always cheer me up when needed is incommensurable. Mamma e babbo, you are always the first people we think of when we need to share our worst struggles and our happiest moments, and you never failed to be there for us! Marta, you were the first to go through a PhD and to experience the roller-coaster of emotions that comes with it. Without your support, especially in the final months, I honestly really believe this thesis would not exist (oh, and I cannot express enough how much I appreciated the stuffed sloth!). Claudia, having a family member living just a bikeable distance away (and I am glad you made that bike ride progressively easier by moving from Groningen to Rotterdam, before finally ending up even closer in Amsterdam) was a great way to feel a bit at home even here in the Netherlands. Spending the day together while practicing the

Italian tradition of complaining about the Dutch food and weather has always been great fun.

Thanks to Steef and Mark, collaborating with you was a pleasure and, in a moment when I was struggling a bit, seeing our theoretical results compared to real experimental data was incredibly motivating.

Francisco, I am so glad that, after two years together during the Master, we also got to share a PhD adventure in Utrecht! It was always nice to visit you in all the different places you have lived, and at some point, I should also come to Veldhoven to make "real Italian pizza" again!

Thanks to Niccolò for all the endless conversation about any random topic, it was a lot of fun and I always learned tons of new things. It was especially great to have someone to talk to while preparing a very tasty *brasato* during rainy days in Warande (although we should do it with a proper *polenta* next time).

Marco, after getting to know you when we randomly sat next to each other on our very first day of university, I was delighted to hear you were also coming to the Netherlands for your PhD! While I should have done it more often, it has always been nice to come to visit you and Ema in Eindhoven, and on this note, thanks a lot Ema for the great *carbonara* and all the nice food you made me enjoy every time I visited.

Martijn, Tim, Evi, and Thijs, Warande would have not been the same without you, I will miss the summer BBQ on the terrace. Also, Martijn, thanks for dragging me to a metal concert several years after the last one I have been to, it was great! Joey and Amber, thanks for being great housemates, I hope you will also manage to escape from Warande soon.

Luminita, thanks for being supportive. Sharing our struggles really helped to put them in perspective.

Thanks to all the people at the ITF for creating a nice atmosphere that reminded you it is not all about research and you also need to have fun sometimes. I greatly enjoyed the Planet talks, and thanks Raffaele for always ordering a lot of *pizza Tricolore*, it was by far the best one.

I also have to thank everybody that made my Master in Utrecht a lovable experience, making me forget the lack of mountains and enjoy the Netherlands more than I expected, convincing me to continue with a PhD there. A special mention to Emma for all the long entertaining conversations we had during those two years.

Thanks Chris, Lorenz, and Dion, it was a pleasure sharing the office with you, chatting about sports and differences between our countries whenever we needed a break.

Thanks to all the members of the cycling team UWTC de Volharding, training and racing with you has been a great way to disconnect from research and recharge the mental batteries while completely draining the physical ones. From spring onward, I was always looking forward to having some fun in the Tuesday and Thursday night practice races on the Nedereindse berg!

Last but not least, every single one of the “random” people that I do not even know, but that, in one way or another, got a smile out of me during all these years. None of you will ever read this thesis and most likely we won’t ever meet again, but I still need to thank all of you, as you have no idea how valuable a smile can be during a rough day.

About the author

I was born in Giussano during a hot summer day in 1992. I grew up in Inverigo, a lovely town in the north of Italy near the beautiful lake Como, surrounded by mountains where my parents used to bring me and my two sisters for a hike when we were kids[4]. I obtained my high-school diploma in 2011 from the Liceo Scientifico Galileo Galilei in the nearby town of Erba, all the while enjoying a lot of outdoor sports, falling especially in love with cycling first, and kayaking next. The latter I practiced competitively winning the Italian Championship for newcomers in 2011. Then, my adventure in physics started at the University of Milano-Bicocca where, in 2015, I obtained my Bachelor's degree.

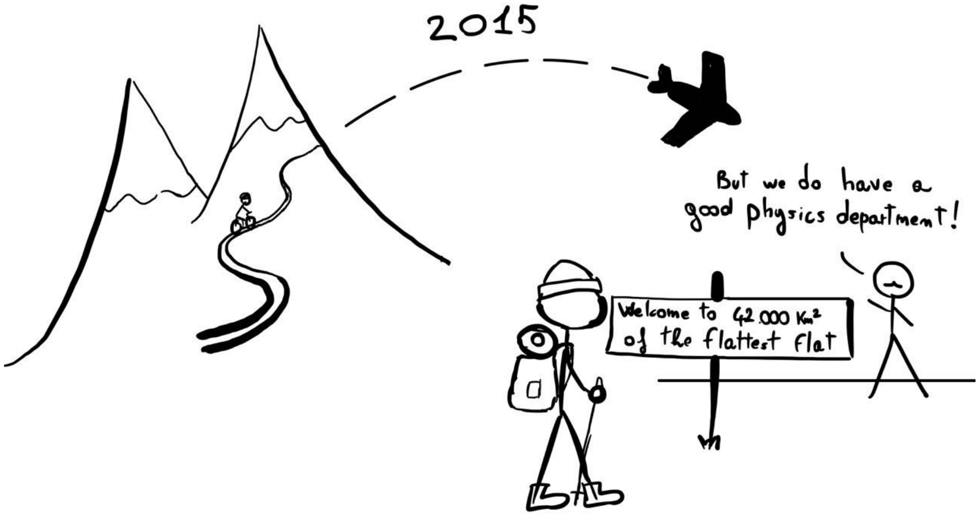

---

[4] As my mom likes to remind me, I used to enjoy running up a bit in front of them, just to run down whenever I was encountering a cow, which apparently I considered quite a scary animal as a kid.

In that same year, I moved to the Netherlands, to pursue a Master in Theoretical Physics at Utrecht University. I graduated cum laude in the summer of 2017, after completing a thesis project on a holographic model of a high-temperature superconductor under the supervision of Henk Stoof. This work was then awarded the Shell Graduation Prizes in Physics from the Koninklijke Hollandsche Maatschappij der Wetenschappen (KHMW). Just a couple of months later, I started my PhD journey under Henk's supervision at the Institute for Theoretical Physics at Utrecht University. The results of my years of research are the subject of this thesis.

While working in the Netherlands, the great bike culture and the huge number of competitive cyclists in the country reignited my passion for the sport, and I enjoyed racing and cycling all over the country as a member of the team UTWC de Volharding. Nonetheless, the more time I was spending outdoors the more I realized how much I missed being close to the mountains. In November 2022, I started a research position at the Bruno Kessler Foundation in Trento, where I work on quantum algorithms with the beautiful Dolomites in the background.